Concrete failure of headed stud fasteners exposed to fire and loaded in shear: experimental and numerical study

Von der Fakultät für Bau- und Umweltingenieurwissenschaften
der Universität Stuttgart zur Erlangung der Würde eines
Doktor-Ingenieurs (Dr.-Ing.) genehmigte Abhandlung

vorgelegt von

Kaipei Tian

aus Yichang, China

Hauptberichter: Prof. Dr.-Ing. habil. Joško Ožbolt
Mitberichter: Prof. Pietro G. Gambarova
                    Jun.-Prof. Dr.-Ing. Akanshu Sharma

Tag der mündlichen Prüfung: 18.07.2019

Institut für Werkstoffe im Bauwesen der Universität Stuttgart

2019

To my wife and son

ACKNOWLEDGEMENTS

<div align="right">
Kaipei Tian
Stuttgart, July 2019
</div>

ABSTRACT

Fire safety of structures has gained global attention in the past years. Fasteners are commonly used for connecting components to the concrete structures and play key roles for the safety of structures in fire. However, till now scarce data can be found on the fire resistance of fasteners. Eurocode 2 only gives informative recommendations and ACI 318 does not cover the fire safety design of fasteners.

In the thesis the concrete failure of headed stud fasteners before and after fire exposure is studied experimentally and numerically. Two failure modes (concrete edge failure and pry-out failure) are considered for single stud anchors and multiple-stud anchor groups. The standard fire curve ISO 834 is employed to study the effect of fire on the resistance. Numerical simulations are conducted using a thermo-mechanical model that is implemented into a three-dimensional finite element (3D FE) code. The constitutive law for concrete is the temperature dependent microplane model. The numerical results, including the temperature history profile, load-displacement response and the failure load, were verified by the experimental results. Subsequently, parametric studies are carried out.

The experimental and numerical results show that the shear capacity of headed stud anchors is strongly affected by the fire exposure. For concrete edge failure, it is confirmed that the resistance in the hot state is higher than that in the cold state. The reason is thermally induced damage as a consequence of concrete cooling. Further studies, focusing on the cold state behaviour, show that the influences of embedment depth, diameter and concrete strength on the resistance are increasing after fire exposure. On the contrary, the effect of edge distance decreases with the increase of fire duration. For pry-out failure, the influence of both concrete compressive strength and embedment depth increases with the increase of fire exposure time. The influence of fire on the concrete failure load is more than expected, the results demonstrate that the anchor behaviour is significantly reduced by the fire exposure. Especially the cooling process leads to severe loss of load capacity.

Based on the experimental and numerical results the formula for the concrete edge failure load of single anchor after fire is proposed.

The projected area for predicting the resistance of anchor groups from the resistance of single stud anchors according to CC-method is examined for concrete edge failure and pry-out failure mode. Generally, the method works for concrete edge failure after fire exposure. However, the projected area ratio should be modified for the case of pry-out failure.

KUZRFASSUNG

Der bauliche Brandschutz hat in den letzten Jahren aufgrund katastrophaler Brände weltweit stark an Bedeutung gewonnen. Befestigungen werden üblicherweise zum Verbinden von Bauteilen mit Betonkonstruktionen verwendet und spielen eine Schlüsselrolle für die Sicherheit von Konstruktionen im Brandfall. Bisher wurde jedoch der Feuerwiderstand von Verbindungselementen wenig untersucht. Der Eurocode 2 gibt nur informative Empfehlungen zu diesem Thema und der ACI 318 behandelt die Bemessung und Konstruktion von Befestigungsmitteln für den Brandfall nicht.

In der vorliegenden Arbeit wird die Versagensart Betonausbruch von Kopfbolzenverankerungen vor und nach Brandbeanspruchung experimentell und numerisch untersucht. Zwei Versagensarten (Betonkantenbruch und Betonausbruch auf der lastabgewandten Seite („pry-out")) werden für Einzel- und Gruppenbefestigungen untersucht. Die Standardkurve der internationalen Norm ISO 834 wird verwendet, um die Auswirkung von Brandbeanspruchungen auf das Tragverhalten zu untersuchen. Numerische Simulationen werden unter Verwendung eines Thermo-Mechanischen Modells für Beton durchgeführt, das in einen drei-dimensionalen Finite-Elemente-Code (3D FE-Code) implementiert wird. Das konstitutive Gesetz für Beton ist das temperaturabhängige „Microplane" Modell. Die numerischen Ergebnisse, einschließlich des Temperaturverlaufsprofils, des Last-Verschiebungsverhaltens und der Bruchlasten, werden durch die experimentellen Ergebnisse verifiziert. Anschließend wird eine umfangreiche Parameterstudie durchgeführt.

Die experimentellen und numerischen Ergebnisse zeigen, dass die Bruchlast unter Querlast von Kopfbolzenverankerungen stark von den Brandbeanspruchungen beeinflusst sind. Es wird gezeigt, dass der Widerstand im heißen Zustand höher ist als im kalten Zustand. Der Grund liegt in der thermisch bedingten Schädigung des Betons durch Abkühlung. Aus diesem Grund liegt weiterhin der Schwerpunkt der Arbeit auf dem Verhalten der Befestigungen im kalten Zustand. Es zeigt sich, dass die Einflüsse von Verankerungstiefe, Durchmesser und Betonfestigkeit auf den Widerstand nach Brandeinwirkung zunehmen. Der Effekt des Randabstands nimmt allerdings mit zunehmender Branddauer ab. Bei einem Versagen infolge Betonausbruch auf der lastabgewandten Seite („pry-out") steigt der Einfluss sowohl der Betondruckfestigkeit als auch der Verankerungstiefe mit zunehmender Branddauer. Der Einfluss der Branddauer auf die Betonbruchlast ist größer als erwartet. Die Ergebnisse zeigen, dass die Tragfähigkeit von Befestigungen unter Querbelastung durch die Brandbeanspruchung bereits nach 15 min deutlich reduziert wird. Insbesondere der Abkühlprozess führt zu einem starken Verlust der Tragfähigkeit.

Aufgrund der experimentellen und numerischen Ergebnisse wird eine Berechnungsgleichung für die Tragfähigkeit von Einzelbefestigungen bei Betonkantenbruch nach Brandbeanspruchung vorgeschlagen.

Die projizierte Fläche für die Vorhersage des Widerstands von Gruppenbefestigungen aus dem Widerstand eines Einzeldübels ohne Randeinfluss nach dem CC-Verfahren wird für Betonkantenbruch und Betonausbruch auf der lastabgewandten Seite untersucht. Prinzipiell funktioniert das Verfahren bei Betonkantenbruch nach Brandeinwirkung. Das Verhältnis der vorhandenen projizierten Flächen sollte jedoch infolge des Betonausbruchs auf der lastabgewandten Seite verbessert werden.

TABLE OF CONTENTS

Table of Contents

Table of Contents

Table of Contents

NOTATION AND TERMINOLOGY

NOTATION

$A_{c,N}$	projected area of the concrete cone for the anchorage under consideration, limited by the overlap of the individual concrete cones of adjacent anchors ($s \leq s_{cr,N}$) and the edges of the component ($c \leq c_{cr,N}$)
$A_{c,N}^0$	projected area of a single anchorage with large spacing and edge distance with the concrete cone idealised as a pyramid of height h_{ef} and base length $s_{cr,N} = 3h_{ef}$
$A_{c,N,fi(t)}^0$	idealised projection area of single anchor after fire exposure
$A_{c,V}$	projected area of the failure surface for the anchorage as defined by overlap of individual idealised failure surfaces of adjacent anchors ($s<3c_1$)
$A_{c,V}^0$	projected area of the fully developed failure surface for a single anchor idealised as a half-pyramid with height c_1 and base lengths $1.5c_1$ and $3c_1$, which equals $4.5c_1^2$
A_s	effective cross-sectional area of the headed stud anchor
c_1	edge distance measured from the longitudinal axis of the anchor perpendicular to the free edge of concrete
$c_{1,1}$	edge distance measured from the longitudinal axis of the front row anchors perpendicular to the free edge of concrete
$c_{cr,N}$	characteristic edge distance for ensuring the transmission of the characteristic resistance of a single breakout, which is $1.5h_{ef}$
c_p (C_p)	specific heat capacity
d	shank diameter of anchor
d_{max}	maximum aggregate size
d_{nom}	nominal diameter of fastener, which equates shank diameter d for headed stud
D	thermal diffusivity
e	mathematical constant
E^{20}	Young's modulus at ambient temperature $T = 20$ ℃
E_c	Young's modulus of concrete
f_c'	specified concrete compressive strength of cylinder (6×12 inch)
f_{cm} (f_c)	mean compressive strength of concrete cylinder (150×300 mm)
f_c^{20}	mean compressive strength at $T = 20$ ℃
$f_{cc,150}$	mean concrete compressive strength measured on concrete cube of $150 \times 150 \times 150$ mm at the time of the test
$f_{cc,200}$	mean concrete compressive strength measured on concrete cube of $200 \times 200 \times 200$ mm at the time of the test
f_{ck}	characteristic compressive strength of concrete cylinder
f_t	tensile strength of concrete
f_t^{20}	tensile strength at $T = 20$ ℃
f_{ctm}	mean tensile strength of concrete
$fi(t)$	fire duration in minutes

Notation and Terminology

G_F	fracture energy of concrete
$G_F{}^{20}$	concrete fracture energy at $T = 20$ ℃
H	enthalpy
h_1	spalling depth due to concrete surface spalling at high temperature
h_{ef}	effective embedment depth, designating the distance between the surface of the concrete and the end of the force transfer zone.
$k_{fi(t)}$	reduction factor of resistance due to fire exposure
k_c	coefficient for basic concrete breakout strength in tension (ACI)
$k_{c,\theta}$	reduction factor for stress-strain relationships of concrete at elevated temperatures (Eurocode 4)
k_{cp}	coefficient for pry-out strength (ACI 318)
$k_{cr,N}$	factor for concrete cone failure load in cracked concrete
$k_{ucr,N}$	factor for concrete cone failure load in uncracked concrete
$k_{u,\theta}$	reduction factor for stress-strain relationships of structural steel at elevated temperatures (Eurocode 4)
k_V	secant stiffness of load-displacement response
l_f	effective load transfer length, which is h_{ef} for anchors with constant flexural stiffness over the length of the anchor
n	total number of anchors in connection
N_b	basic concrete breakout strength in tension of a single anchor in cracked concrete (ACI 318)
$N_{u,c}^0$	concrete cone breakout strength for a single stud anchor
$N_{u,c}$	concrete cone breakout strength for multiple-stud anchor groups
$N_{Rk,c}^0$	characteristic resistance of a single fastener in case of concrete cone failure in tension
P	pressure
$P_{fi,Rd}$	fire resistance according to Eurocode 4
P_{Rd}	design shear resistance according to Eurocode 4
r_a	projected area ratio $r_a = A_{c,V}/A_{c,V}^{\ 0}$
S	surface of the unit radius sphere
$s_{cr,N}$	spacing required to allow the formation of an unrestricted concrete cone, which is $3h_{ef}$ at ambient temperature
$s_{fi(t)}$	effective size factor after fire duration $fi(t)$, which is 1.5 at ambient temperature
$S_{fi(t)}$	fracture size of anchor after fire duration $fi(t)$ (length L $\times$ width B)
T	temperature
t	time in minutes
T_0	ambient temperature
T_M	temperature of the media in which surface Γ of the solid Ω is exposed to
V	shear load
V_b	basic concrete breakout strength in shear of a single anchor in cracked concrete (ACI 318)
V_{cp}	nominal pry-out failuer load (ACI 318)
$V_{u,c}$	concrete edge failure load of a multiple-stud anchor group

Notation and Terminology

$V_{u,c}^0$	concrete edge failure load of a single stud anchor
$V_{Rk,cp}^0$	characteristic resistance of single anchor in case of pry-out failure
$V_{u,c,fi}^0$	concrete edge failure load of single anchor after fire exposure
$V_{u,cp}^0$	pry-out failure load of a single stud anchor
$V_{u,cp}$	pry-out failure load of an anchor group with multiple studs
$V_{u,c,fi}$	concrete edge failure load of anchor group after fire exposure
$V_{u,test}$	concrete edge failure load from experiment
w	crack width at peak load
z Δw	crack width at the onset of movement of LVDT (0.006 mm)
θ	crack angle with respect to concrete edge
θ_R	angle of rotation of anchor plate
θ^*	dimensionless transition temperature
$\alpha_{fi(t)}$	exponent for the influence of anchor diameter on the concrete edge failure load after fire exposure
$\beta_{fi(t)}$	exponent for the influence of embedment depth on the concrete edge failure load after fire exposure
$\gamma_{fi(t)}$	exponent for the influence of concrete compressive strength on the concrete edge failure load after fire exposure
$\gamma_{cp,fi(t)}$	exponent for the influence of concrete compressive strength on the pry-out failure load after fire exposure
$\gamma_{M,fi,v}$	partial factor for the strength of stud connectors in fire
γ_v	partial factor
Δ	Laplace-Operator
δ	displacement
δ_h	horizontal displacement
δ_{ij}	Kronecker delta
δ_{vb}	vertical displacement at the rear end of steel plate
δ_{vm}	vertical displacement at the middle of steel plate
$\dot{\varepsilon}_{ij}^{fts}(T)$	free thermal strain rate
$\dot{\varepsilon}_{ij}^{lits}(T,\sigma)$	load-induced thermal strain rate
ε_{ij}^{ft}	free thermal strain tensor
ε_{ij}^{lits}	load-induced thermal strain tensor
ε_{ij}^{m}	mechanical strain tensor
ε_N	normal microplane strain
ε_D	deviatoric microplane strain
ε_V	volumetric microplane strain
ε_{ij}	projection of macroscopic strain tensor
$\varepsilon_{fi(t)}$	exponent for the influence of edge distance on the concrete edge failure load after fire exposure
λ	concrete unit weight factor per ACI 318
λ_c	thermal conductivity
ρ	density

σ_{ij}	macroscopic stress tensor
σ_N	normal microplane stress
σ_D	deviatoric microplane stress
σ_V	volumetric microplane stress
v_c	Poisson's ratio of concrete

TERMINOLOGY

Ambient	without fire exposure
Hot state	immediately after heating
Cold state	after cooling down to room temperature
CE	concrete edge failure
Pr	pry-out failure
fm	failure mode
LVDT	linear variable displacement transducers
2c100h95d25	"2" in front of the anchor identification means fire exposure on two sides of the concrete edge; if "1" it means fire exposure on one side. "c" stands for edge distance c_1 (here $c_1 = 100$ mm), "h" stands for embedment depth h_{ef} (here $h_{ef} = 95$ mm), "d" stands for diameter d_{nom}. (here $d = 25$ mm)
G2	"G2" means anchor group with two studs
f_{cm}	$= 0.85 f_{cc,200} = 0.8 f_{cc,150}$
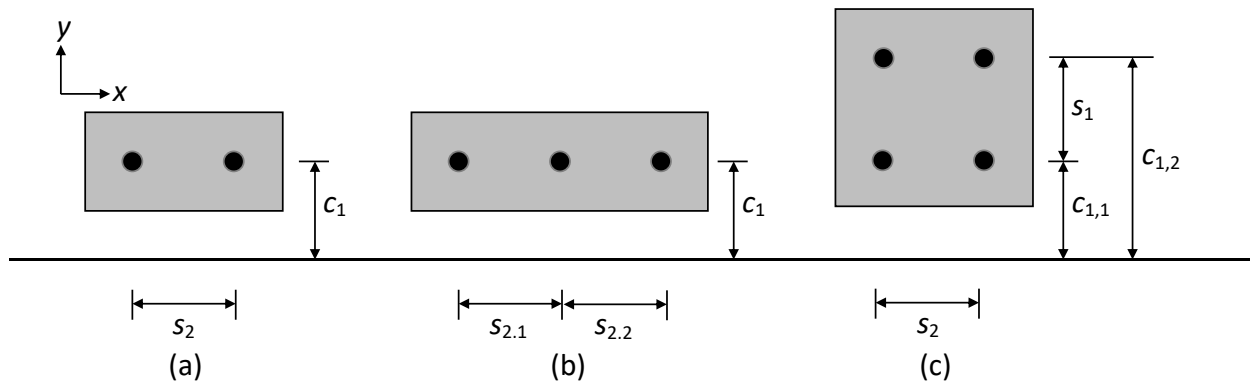
Figure 0.1 Definition of fastener spacing and edge distance for anchor groups with (a) two studs (G2), (b) three studs in a row (G3) and (c) four studs (G4).

UNITS

If not specified, SI units are used

1. INTRODUCTION

1.1. Problem statement

In the field of natural or man-made disasters, fire is one of the deadliest and most destructive events. It is unpredictable and spreads fast once occurred. When a fire engulfs a structure on a considerable scale, it is usually an unstoppable catastrophe. Fire can be triggered by collision, transportation of flammable material, leakage of gas, electrical malfunction, earthquake, and so on. After 1906 San Francisco earthquake, the post-earthquake fires erupted across the city and burned uncontrollably for three days, with practically nothing left. The Cocoanut Grove fire in 1942 killed a total of 492 lives and injured hundreds more. Many researchers believed that the reason for the collapse of the World Trade Center's twin towers in 2001 is the fire burning of the building after the aircraft impact, with fire duration of 56 minutes and 85 minutes for the WTC 2 and WTC 1, respectively. Most recently, the Grenfell Tower fire in 2017 broke out in the 24-storey flats in West London caused 72 deaths shocked the world. By each fire disaster in history, it usually caused dozens or hundreds of deaths (*Cavallini et al.*, 2007), with millions of dollars of economic loss. The focus on fire safety of structures has been thus growing globally in the past years.

Concrete, as the most widely used man made material on this planet, is recognized as a good fire proof construction material. Concrete structure is relatively safe for fire disaster due to its low thermal conductivity. It can withstand much longer duration of fire by comparing to steel structure. However, numerous studies have revealed that concrete presents mechanical property degradation and even surface spalling when subjected to fire, especially for high strength concrete. Therefore, fire engineer should pay close attention to that any local surface spalling or cracking of concrete can expose the reinforcement to high temperature and thus jeopardizes the whole structure rapidly. The degradation of mechanical property due to physically-chemically involved reactions in concrete at elevated temperatures should also be carefully considered for any concrete related structures, as well as thermally induced damage due to fire and load induced thermal strains.

Anchorages in concrete are widely used in structures for connecting various components. Building fire disaster commonly starts with the burning and falling of the claddings and attachments fastened to the main concrete structure, which has been the case in many recorded fire accidents. The destruction of claddings or curtain wall usually facilitates the spread of fire to adjacent spaces and also accelerates the fire damage of the main structure, see Figure 1.1. The fire resistance of the attachments itself is of great importance; meanwhile the fire resistance of the mechanical fasteners is structurally vital for fire safety of the whole structure. The falling of the

attachments during fire, for instance, the fire protection equipment, in particular the fire sprinkler system, would be a catastrophe for evacuating people and extinguishing fire. However, all the attached components are usually fastened to the surface or the edge of the concrete structure, where the fire damage of concrete is the most severe.

(a) (b)

Figure 1.1 (a) The Grenfell tower fire (picture from BBC news); (b) shear connection for curtain wall.

In composite or pre-fabricated structures, shear connectors between concrete and steel are important and frequently used, for example, connectors between concrete wall panels or between steel and concrete beams (see Figure 1.2). Under fire the resistance of these connections is a potential risk for the fire safety of the building structure. The failure of any structural connectors in fire may lead to first progressive and then sudden collapse of the structure.

(a) (b)
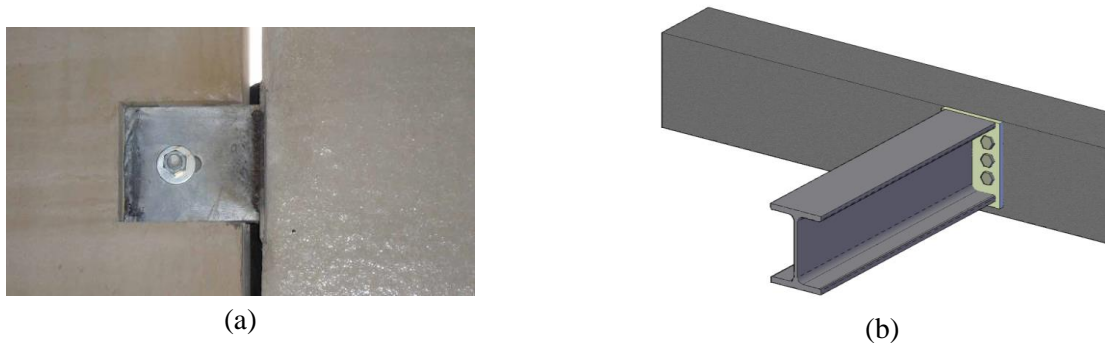
Figure 1.2 (a) Shear loaded connection between precast concrete wall panels (picture from (*National Precast Concrete Association*, 2012)); (b) connection for fastening a steel beam to a concrete beam.

Numerous investigations on concrete failure of anchors at ambient temperature exist so far. However, the load-bearing behaviour at elevated temperatures, such as fire, has barely been

investigated. Due to the softening of steel at high temperature in case of fire, steel failure might be the governing failure mode. However, if the steel parts are protected against fire or specially designed, single fastener or group of fasteners close to edge of concrete member or shallowly embedded in concrete may fail by concrete breakout because the concrete becomes extremely weak under fire scenario, especially after cooling. Therefore, to design safe and economical connections between steel and concrete it is important to understand the behaviour of fasteners under fire.

However, up to now the research on the fire resistance of fasteners in concrete is scarce. For fire safety design of fasteners, the absence of international codes is also an impediment. There are no unified fire test procedures and no commonly accepted fire design rules for fastening systems till now. The current Eurocode 2, Part 4, Annex D (*European Committee for Standardization*, 2018) gives only informative recommendations for reduction of anchor resistance for the fire exposure up to 90 minutes and 120 minutes, and in ACI 318 code (*American Concrete Institute Committee 318*, 2014) anchor resistance under fire is not yet considered.

Experimental research on fire safety of structure has been denounced as time-consuming and cost-inefficient. This is the case for the fire resistance of fasteners, because a conclusion of the resistance of fasteners relies on a large data base. A reliable numerical tool is thus needed to predict the fire resistance of fasteners. However, until now systematic numerical analyses on the fire resistance of fasteners in concrete based on verified numerical tool are not available in the literature.

1.2.   Aims and Objectives

The main objective of this thesis is to investigate the load-bearing behaviour of headed stud anchors in concrete loaded in shear under fire exposure in case of concrete failure. The concrete edge failure of anchors located close to an edge and loaded in shear towards the edge is first studied in the hot state during fire and in the cold state (residual state—after cooling down following a fire exposure). The behaviour of anchor groups with multiple headed studs undergoing concrete edge failure in the cold state is then examined. Furthermore for relatively shallowly embedded anchors away from the concrete edge of concrete slab, the pry-out failure of single anchor and anchor groups is investigated. For different anchorage configurations, parameters like concrete edge distance, embedment depth, stud diameter, concrete grade and fire durations are considered.

The experimental tests under high temperature are extremely demanding and expensive. Therefore, it is important to have an objective numerical tool. In the present thesis numerical simulations are performed using a three-dimensional (3D) thermo-mechanical (TM) model that was implemented into a three-dimensional finite element (FE) code. The constitutive law for

concrete is the temperature dependent microplane model (*Ožbolt et al.*, 2001; *Ožbolt et al.*, 2005a). Based on the experimental results the numerical model is first verified and calibrated. Subsequently, the numerical model is used to perform parametric numerical studies in order to investigate the behaviour of anchors under different fire exposure conditions. The experimental and numerical results are compared with the prediction formula based on the design code recommendation. Finally, improved formula for prediction of shear capacity of anchors is proposed.

Therefore, from the perspective of concrete edge failure and pry-out failure, considering both single anchor and anchor groups, a primary but fundamental investigation on the concrete failure capacity of headed studs after exposing to fire is experimentally and numerically presented.

1.3.   Overview of the work

Chapter 1 aims to highlight the problem statement and emphasize that the fire safety of fasteners is critical due to the role the anchors are playing in the whole structure. However, the current state of research on fire resistance of anchors in concrete after fire is scarce and correspondingly the international codes on fire safety design of anchors in concrete are insufficient.

Chapter 2 summarizes a state of the art review of the research and provisions on the concrete edge failure and pry-out failure of anchors before and after fire exposure. The characteristic of fire and developed fire curves are discussed. The hot state and cold state are explicitly defined in this chapter for differentiating the resistance after fire exposure.

Chapter 3 presents the knowledge on the physical and mechanical properties of concrete with increasing temperature. Special care is given to properties in the hot and cold state. This chapter describes the theoretical background for the thermo-mechanical modelling of concrete failure of anchors after fire exposure.

Chapter 4 discusses the results of experimental and numerical studies on the concrete edge failure of single anchors in the hot state. It is concluded that the focus should be put on the cold state resistance of anchors after fire exposure.

Chapter 5 reports the results of experimental and numerical studies on the concrete edge failure of single anchors in the cold state. A prediction formula is proposed, based on the experimental and numerical results, to calculate the concrete edge failure load of single anchors in the cold sate as a function of fire duration.

Chapter 6 presents the results of experimental and numerical investigations on the concrete edge failure of anchor groups in the cold state. The effect of multiple studs on the concrete edge failure capacity of anchors is examined through comparative analysis with Chapter 5.

Chapter 7 investigates the pry-out behaviour of anchors in the cold state experimentally and numerically.

Chapter 8 focuses on the experimental and numerical studies performed to investigate the effect of multiple studs on the pry-out capacity in the cold state, with several representative anchor group configurations.

Chapter 9 provides the concluding remarks and gives recommendations for fire safety design of fasteners in concrete.

2. STATE OF THE ART

2.1. General

The loads on fasteners are transferred to the base material by means of mechanical interlock, friction, chemical bond, or some kind of combination of these mechanisms, which induces tensile stresses in the base material. For fasteners in concrete, beyond the steel failure of anchor and the interaction failure between steel and concrete, in many cases the fastener fails because the tensile capacity of the concrete is exceeded. A number of studies, both theoretically and experimentally, have been conducted to investigate the failure mechanism of fasteners by concrete failure. The focus was on the crack propagation and corresponding resistance. The main conclusions are presented in the following sections.

2.2. Literature review and discussion

2.2.1. Resistance against concrete cone capacity (tension)

Concrete cone capacity under tension is the base for all other loading scenarios. *Eligehausen and Clausnitzer* (1983) investigated the behaviour of expansion anchors in concrete with finite element analysis. The concrete property in tension was assumed to be elastic-perfectly plastic and elastic-brittle. The obtained load-displacement curves were compared with experimental curves. Significant differences were found for the differentiation of concrete tensile profile. It was found that the number of load increments in finite element analysis had a considerable influence on the ultimate load.

Elfgren et al. (1982) numerically investigated the pull-out capacity of headed stud in concrete. It was found that the crack length at ultimate load is approximately 50% of the total length of side length of the final concrete cone. After the ultimate load was reached, the crack development becomes unstable and the final concrete cone failure pattern forms. In another report (*Elfgren and Ohlsson*, 1986) it was found that the larger the fracture energy G_f, the higher the ultimate load could present.

Sawade (1994) considered an energy based model to associate the cracking formation and widening process with energy dissipation in concrete for calculating the concrete cone capacity of headed stud anchors in concrete. Linear elastic fracture mechanics was applied and the following equation was proposed to calculate the ultimate load:

$$N_{u,c}^0 = 2.1 \cdot h_{ef}^{1.5} \cdot (E_c \cdot G_f)^{0.5} \tag{2.1}$$

Although the concrete cone capacity depends on the tensile strength of concrete, in Equation (2.1) the tensile strength f_t is reflected by the combination of Young's modulus E_c and fracture energy G_f, which is a way more realistically describing the influence of concrete mix design. It is worth noting that the ultimate load is proportional to the embedment depth h_{ef} to the power of 1.5, rather than 2, as would be according to plasticity theory.

Ožbolt (1995) investigated the load-bearing behaviour of headed stud anchors in concrete based on a non-local microplane model (*Bažant and Ožbolt*, 1990). In this analysis the embedment depths was varied from 50 mm to 2700 mm. It was found that the tensile strength of concrete solely has a minimal influence on concrete cone failure load. The concrete cone capacity, however, increases approximately proportional to $G_f^{0.5}$. The crack length when the ultimate load reached is about 40% of the side length of the concrete cone fracture envelope if small embedment depth applied; for large embedment depth the crack length is reduced to about 25% of the side length. The concrete cone slope is about 35° with respect to the concrete surface.

Experimentally measured concrete cone slope varies from test to test. On average it is about 35°, however, with increasing embedment depth it has the tendency to increase (*Zhao*, 1993).

The evaluation of large amount of experimental tests led to the development of the CCD (concrete capacity design) method (*Fuchs et al.*, 1995). For headed stud anchorage, the concrete cone failure capacity can be calculated as below:

$$N_{u,c}^0 = 15.5 \cdot h_{ef}^{1.5} \cdot f_{cc,200}^{0.5} \tag{2.2}$$

If cylinder compressive strength of concrete f_c is used:

$$N_{u,c}^0 = 16.8 \cdot h_{ef}^{1.5} \cdot f_c^{0.5} \tag{2.3}$$

where $f_{cc,200}$ is the mean concrete cube compressive strength measured on concrete cube of $200 \times 200 \times 200$ mm at the time of the test; f_c is the cylinder compressive strength measured on concrete cylinder of 150×300 mm, with $f_c = 0.85 f_{cc,200}$.

The idealized concrete cone for individual anchors under tensile load is shown in Figure 2.1.
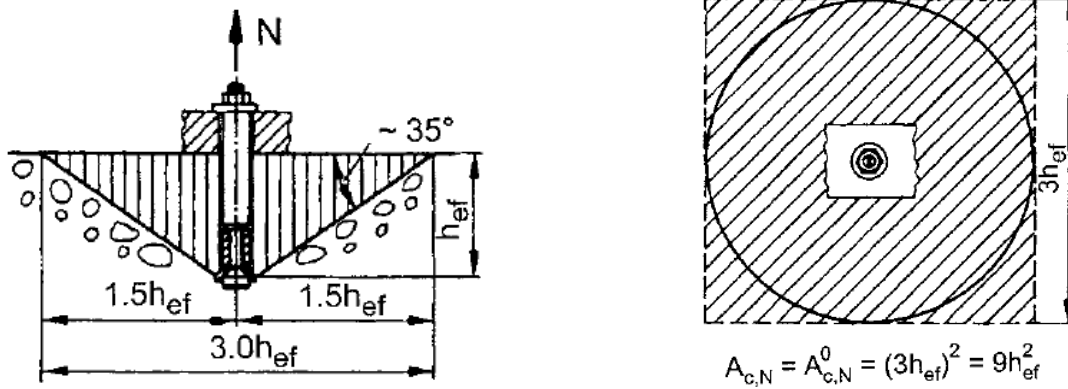
Figure 2.1 Concrete cone failure surface (*Eligehausen et al.*, 2006).

For the concrete cone capacity of multiple anchors, the group effect of anchors is taken according to the projected area ratio (*Fuchs et al.*, 1995; *Eligehausen et al.*, 2006):

$$N_{u,c} = \frac{A_{c,N}}{A_{c,N}^0} \cdot N_{u,c}^0 \qquad (2.4)$$

where

$A_{c,N}^0$ = projected area of a single anchorage with large spacing and edge distance with the concrete cone idealised as a pyramid of height h_{ef} and base length $s_{cr,N} = 3h_{ef}$;

$A_{c,N}$ = projected area of the concrete cone for the anchorage under consideration, limited by the overlap of the individual concrete cones of adjacent anchors ($s \le s_{cr,N}$) and the edges of the component ($c \le c_{cr,N}$);

$s_{cr,N}$ = spacing required to allow the formation of an unrestricted concrete cone, i.e. development of the tension resistance of one anchor according to Equation (2.2), which is $3h_{ef}$;

$c_{cr,N}$ = edge distance required to allow the formation of an unrestricted shear cone, i.e. development of the tension resistance of one anchor according to Equation (2.2), which is $1.5h_{ef}$.

For anchor groups loaded in tension the other influences, like the edge distance, eccentric loading and reinforcement are taken into account by separate factors (*Eligehausen et al.*, 2006).

8

2.2.2. Resistance against concrete edge failure under shear loads perpendicular and towards the edge

Fuchs et al. (1995) developed the CC (concrete capacity design) method and proposed the following equation to predict the concrete edge failure load of a single anchor in concrete:

$$V_{u,c}^0 = \sqrt{d_{nom}} \cdot (l_f/d_{nom})^{0.2} \cdot \sqrt{f_{cc,200}} \cdot c_1^{1.5} \qquad (2.5)$$

where

d_{nom} = the nominal diameter of fastener, which equates shank diameter d for headed stud

l_f = the effective load transfer length, which is h_{ef} for anchors with constant flexural stiffness over the length of the anchor

c_1 = is the edge distance measured from the longitudinal axis of the anchor perpendicular to the free edge of concrete.

From Equation (2.5) it can be seen that the concrete edge failure load is mainly influenced by the edge distance c_1. In analogy to the influence of embedment depth h_{ef} for anchor under tension load (to the power of 1.5), the concrete edge failure load is proportional to the edge distance to the power of 1.5 instead of 2, as it would be according to the strength theory. The influence of concrete tensile strength and fracture energy, in the equation is reflected proportional to the compressive strength $f_{cc,200}^{0.5}$. Note that this equation is mainly valid for anchor with diameter under 25 mm.

Hofmann (2005) and *Hofmann et al.* (2004) conducted a series of experiments and numerical simulations on the concrete edge failure capacity of single anchor. A more accurate equation for calculating the mean shear resistance of a single anchor in un-cracked concrete at ambient temperature is proposed as:

$$V_{u,c}^0 = 3.0 \cdot d_{nom}^{\alpha_0} \cdot l_f^{\beta_0} \cdot \sqrt{f_{cc,200}} \cdot c_1^{1.5} \qquad (2.6)$$

where $\alpha_0 = 0.1 \cdot \left(l_f/c_1\right)^{0.5}$, $\beta_0 = 0.1 \cdot (d_{nom}/c_1)^{0.2}$.

Equation (2.6) can be converted into an equation as follows:

$$V_{u,c}^0 = 3.27 \cdot d_{nom}^{\alpha_0} \cdot l_f^{\beta_0} \cdot \sqrt{f_{cm}} \cdot c_1^{1.5} \qquad (2.7)$$

where f_{cm} is the mean concrete cylinder compressive strength measured on concrete cylinder of 150×300 mm at the time of the test.

Grosser (2012) performed a review of the research on the shear loaded anchor close to concrete edge conducted by different authors. Previous proposals were found to be limited due to scarce data verification. The influence of diameter and embedment depth remained unclear and some equations could lead to overly conservative results. With this background, *Grosser* (2012) conducted a series of experimental tests and proposed the following Equation (2.8) for predicting the resistance of anchors close to edge and loaded perpendicular to the free edge:

$$V_{u,c} = 16.5 \cdot c_1{}^{4/3} \cdot \sqrt{f_{cc,200}} \cdot (0.02d + 0.5)(l_f/12d)^{c_1{}^{-0.4}} \tag{2.8}$$

For anchor groups, the shear failure load can be calculated using CC-Method by means of projected areas (*Eligehausen et al.*, 2006; *Fuchs et al.*, 1995):

$$V_{u,c} = \frac{A_{c,V}}{A_{c,V}^0} \cdot V_{u,c}^0 \tag{2.9}$$

where $A_{c,V}{}^0$ is the projected area of the fully developed failure surface for a single anchor idealised as a half-pyramid with height c_1 and base lengths $1.5c_1$ and $3c_1$, which equals $4.5c_1{}^2$; $A_{c,V}$ is the projected area of the failure surface for the anchorage as defined by overlap of individual idealised failure surfaces of adjacent anchors ($s<3c_1$); $V_{u,c}{}^0$ refers to Equation (2.6).

For anchor groups loaded in shear close to edge the other influences, like the geometry (corner and thickness of concrete slab), eccentric loading, overturning moment and reinforcement are taken into account by separate factors (*Eligehausen et al.*, 2006).

2.2.3. Resistance against pry-out failure under shear loads

Headed studs are commonly used in composite steel and concrete structures as shown in Figure 2.2. The studs are used in the central region of the concrete slab. For the general rules of design the provisions are given in Eurocode 4 Part 1-1 (*European Committee for Standardization*, 2004b).
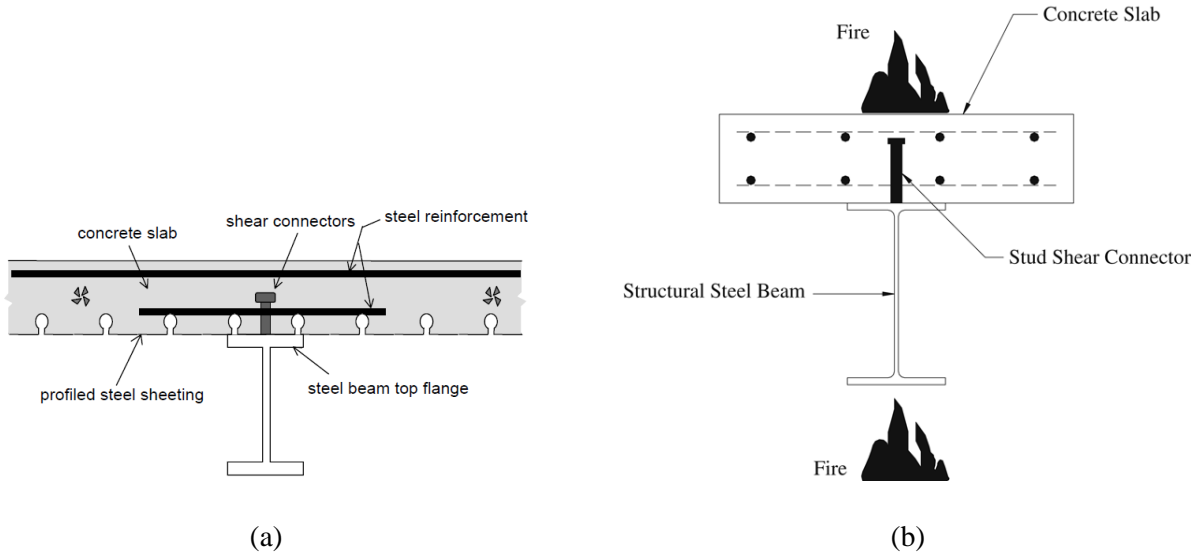
Figure 2.2 Cross-section of composite steel and concrete connection by headed studs (a) with profiled steel sheeting (*Shariati et al.*, 2012) and (b) concrete slab subjected to fire (*Mirza and Uy*, 2009).

It should be noted, however, that the research projects on the composite steel and concrete connectors are mainly focused on the push-out test as shown in Figure 2.3. In such a structure the concrete slab or the profiled steel sheeting covered concrete, for example as a floor, is closely connected by multiple headed studs which are welded on the steel beam flange. Therefore, due to the large size of the floor, the uplift and the rotation of the headed studs are restrained. The failure of the connection is either the steel failure of the stud or the crushing of the concrete and the large deformation of the stud. There is little chance the headed studs would fail in concrete cone failure as for fastener defined in Eurocode 2 Part 4. Thus, the load-slip development in the
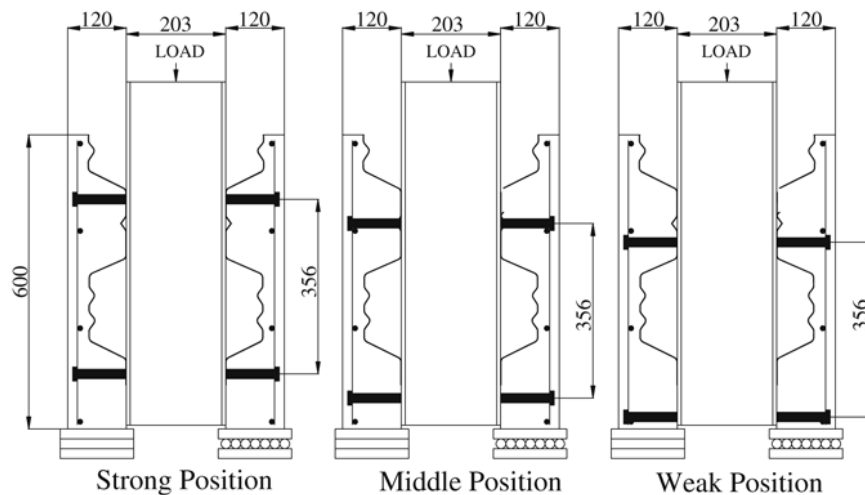
Figure 2.3 Push-out tests for composite steel and concrete connectors (*Mirza and Uy*, 2009).

11

push-out tests is significant and limitation of slip is provisioned as being no greater than 6 mm in Eurocode 4.

Early composite steel and concrete connections were investigated by using push-out tests according to the literatures (*Viest*, 1956; *Driscoll and Slutter*, 1961; *Ollgaard, J. G.; Slutter, R. G.; Fisher*, 1971)

Ollgaard et al. (1971) performed a series of push-out tests to study the failure mode, load-slip curve and ultimate load of headed stud shear connectors in normal weight and light weight concrete. It was evident that for push-out tests there are no sudden failure at the ultimate load. Although the failure was either the shearing off of the stud or the crushing of the concrete from outside observation, inside the concrete it was revealed that the pry-out fracture occurred to the front row of studs by sawing the concrete slab along the axes of the headed studs (Figure 2.4).

Comparative analyses on the influencing parameters to the ultimate load induced the following prediction equation:

$$V_u = 0.5 A_s (f_c' \cdot E_c)^{0.5} \text{ [kips]} \tag{2.10}$$

where

A_s is the effective cross-sectional area of the headed stud anchor (sq in.);

f_c' is the concrete compressive strength (ksi);

E_c is the modulus of elasticity (ksi).

Equation (2.10) was used in the AISC Specifications (*AISC Manual Committee*, 2001) and also Eurocode 4 (*European Committee for Standardization*, 2004b).
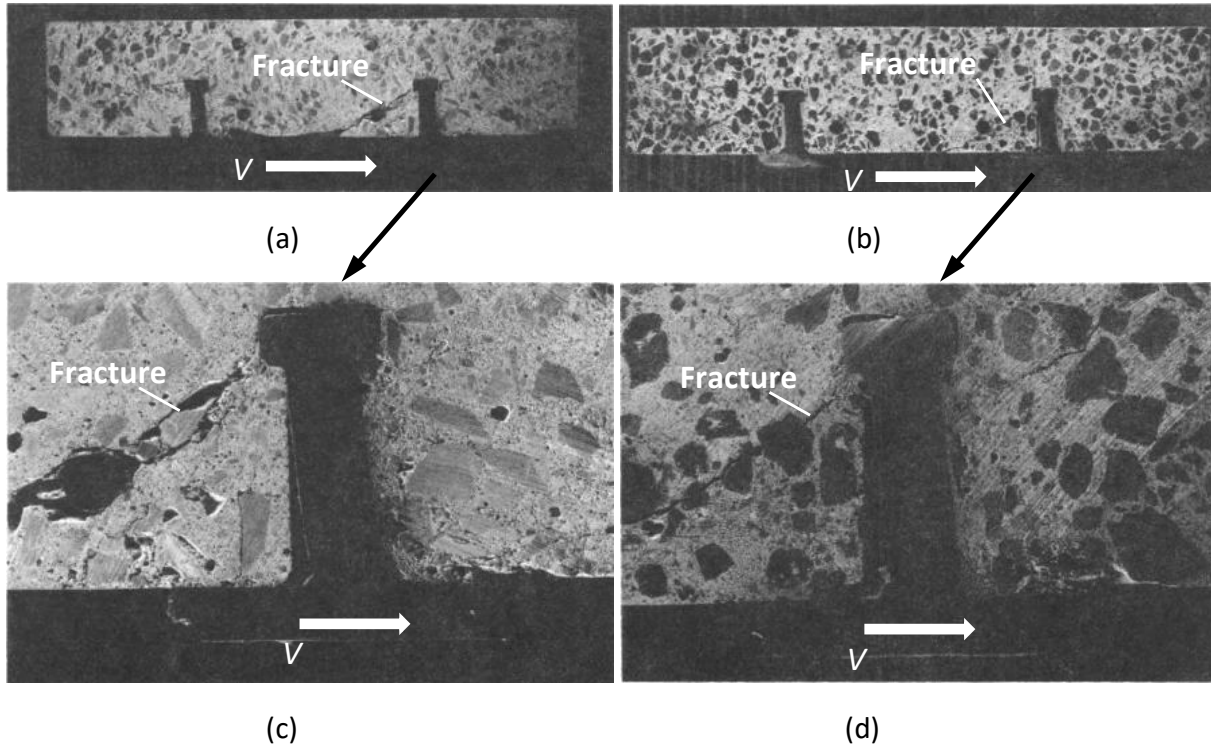
Figure 2.4 Fracture patterns observed in push-off tests. Overview of fracture of the front and rear studs: (a) normal weight concrete and (b) light weight concrete. Detailed observation of pry-out fracture pattern of front studs: (a) normal weight concrete and (b) light weight concrete. (*Ollgaard, J. G.; Slutter, R. G.; Fisher*, 1971).

The load-bearing mechanism of headed stud anchorage loaded in shear in concrete was illustrated schematically in Figure 2.5 by *Zhao* (1993). With increasing load *V*, the crushed surface shifts the centroid of resistance V_b to a position deeper along the shaft of the anchor in the concrete. Further the base plate rotates and as a result the eccentricity between the applied load *V* and resistance V_b increases. This eccentricity creates a moment which generates a compressive stress *C* between the front side of the base plate and the concrete surface and a tensile force *N* dragging the head. Friction *R* also exists against the applied force. Once the tensile force in the stud exceeds the tensile capacity associated with the maximum fracture surface that can be activated by the stud, a fracture surface originates at the back side of the head and propagates in conical shape behind the stud, see Figure 2.5b.

According to *Zhao* (1993), the pry-out capacity is determined by coefficient *k* related to the concrete cone failure in tension as follows:

$$V_{u,cp} = k_1 \cdot N_{u,c} \tag{2.11}$$

where:

k_1 = 2.0 for $h_{ef} \geq 60$ mm

k_1 < 2.0 for $h_{ef} < 60$ mm

$N_{u,c}$ is calculated according to Equation (2.2).
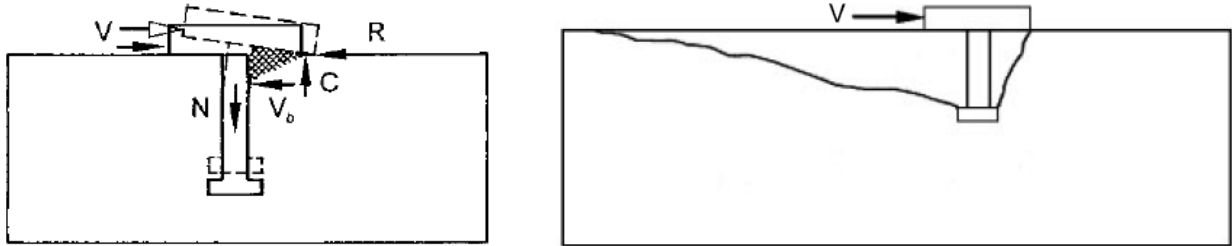
Figure 2.5 (a) Load-bearing mechanism of headed stud anchorage loaded in shear at ambient temperature; (b) crack development (*Zhao*, 1993).

It can be converted to the use of mean concrete cylinder strength f_{cm} according to Equation (2.3) as follows:

$$V^0_{u,cp} = k_1 \cdot 16.8 \cdot h^{1.5}_{ef} \cdot f^{0.5}_{cm} \tag{2.12}$$

Since the pry-out capacity is strongly related to the concrete cone capacity under tension, the pry-out failure load for anchor groups is therefore in the following form:

$$V_{u,cp} = \frac{A_{c,N}}{A^0_{c,N}} \cdot V^0_{u,cp} \tag{2.13}$$

where the calculation of the projected areas are exactly the same as for Equation (2.4).

Anderson and Meinheit (2005) created a comprehensive collection of data on the capacity of headed stud anchors located "in the field" of the concrete member under shear loading. Despite most of the data were from push-off tests, the pry-out failure mechanism was described and a literature review on the main conclusions from previous researchers was presented. The authors found that embedment depth considerably contributes to the pry-out failure capacity, which was not reflected per Equation (2.10). By using 65 tests from both push-off and pry-out testing programs, the following equation was derived for a single stud or a single y-row (y direction is the same as in Figure 0.1) of studs by using linear multi-variable regression analysis:

14

$$V_{u,cp} = 317.9\lambda n\sqrt{f_c'}\,d^{1.5}{h_{ef}}^{0.5} \text{ [lb]} \qquad (2.14)$$

where

λ is concrete unit weight factor per ACI 318;

n is total number of anchors in connection;

f_c' is specified compressive strength of concrete (psi);

d is nominal anchor diameter (in.);

h_{ef} is effective embedment depth of headed stud (in.).

In this research the authors performed eight pry-out tests for the specific purpose of examining the y-spacing influence. These data were added to the data base to examine the validity of formulas as per Equation (2.14) and ACI 318. The authors demonstrated that ACI 318 Appendix D formula was overly conservative for predicting the pry-out failure load, in particular for anchors with small h_{ef}/d ratio; while Equation (2.14) provided good correlation to prediction for all anchors with h_{ef}/d ratio less than 4.5. However, currently both in ACI 318 code (*American Concrete Institute Committee 318*, 2014) and Eurocode 2 (*European Committee for Standardization*, 2018) the design formulas for pry-out failure are still according to Equation (2.11).
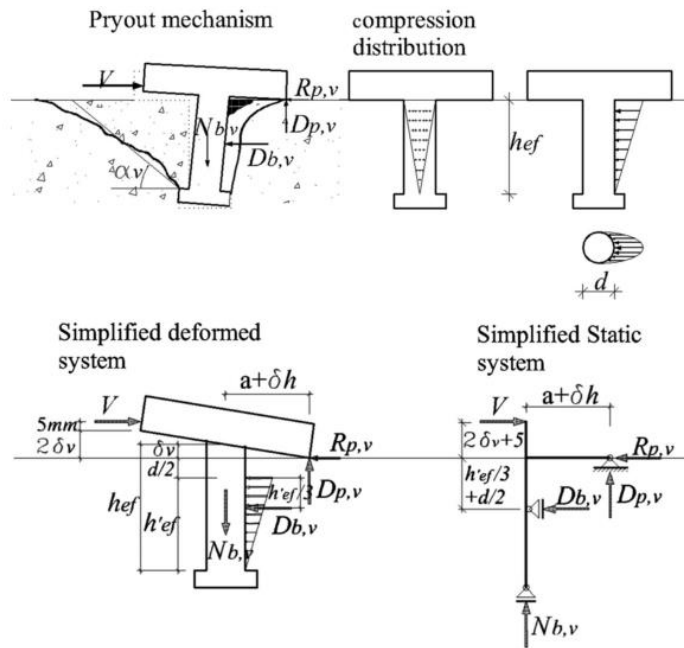
Figure 2.6 Pry-out mechanism and proposed mechanical model by *Jebara et al.* (2016).

Jebara et al. (2016) performed a series of experiments to study the effect of embedment depth h_{ef} and shaft diameter d on the pry-out capacity of headed stud anchors in concrete. The research provided useful data for the influence of anchor diameter on the pry-out failure capacity in concrete. The stress distribution along the shaft was also measured using pressure measurement film and strain gauges. The analysis finally proposed a mechanical model for pry-out failure as presented in Figure 2.6. It was found that the effect of diameter d cannot be neglected and the following equation was proposed to calculate the pry-out capacity.

$$V_{u,cp}^0 = 6 \cdot d^{0.5} \cdot f_{cc}^{0.5} \cdot h_{ef}^{1.5} \qquad (2.15)$$

For the pry-out failure of anchor groups, the following equation was proposed with different method taking the projected area into account, details can be checked in *Jebara* (2018).

$$V_{u,cp}^0 = V_{u,cp}^0 \cdot A_{p,cp}/A_{p,cp}^0 \qquad (2.16)$$

To summarize, currently the five provisions by AISC 2005, Eurocode 4 Part 1-1, the PCI handbook 6th Edition, ACI 318 Chapter 17 and Eurocode 2 Part 4 are listed in Table 2.1. All formulas are proportional to the square root of compressive strength. The main difference comes from the influence of embedment depth in different formulas, which can be seen in Figure 2.7 plotting the pry-out failure capacity predicted by different formulas as a function of h_{ef}/d ratio. The vertical axis is normalized by the calculated pry-out failure capacity according to Eurocode 4 equation. The difference between formulas with respect to the influence of embedment diameter ratio is obvious.

Table 2.1 Concrete pry-out strength by different provisions

Eq. No.	Provisions	Average formula (US units)	Average formula (SI unit)
(2.10)	AISC	$0.5A_s\sqrt{f_c' \cdot E_c}$	$0.5A_s\sqrt{f_{cm} \cdot E_c}$
	Eurocode 4	[ksi, in., kips]	[MPa, mm, N]
(2.11)	ACI 318	$2 \cdot 40 \cdot \sqrt{f_c'}h_{ef}^{1.5}$	$2 \cdot 16.8 \cdot \sqrt{f_{cm}}h_{ef}^{1.5}$
	Eurocode 2	[psi, in., lb]	[MPa, mm, N]
(2.14)	PCI 6th	$317.9\lambda n\sqrt{f_c'}d^{1.5}h_{ef}^{0.5}$ [psi, in., lb]	$317.9\lambda n\sqrt{f_{cm}}d^{1.5}h_{ef}^{0.5} \cdot 0.083$ [MPa, mm, N]
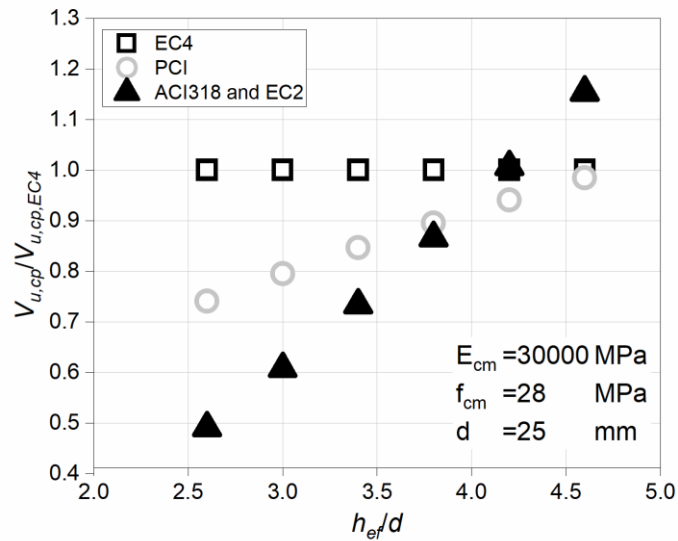
Figure 2.7 Comparison of different prediction formulas.

2.2.4. Fire load

Fire comes from a chemical reaction between oxygen and fuel which can be any sort of combustible source, for example, wood, paper, gasoline etc. Different fuel has different ignition temperature. One feature of the danger ensuing from fires is that they are self-perpetuating, which means the heat of the flame can keep the fuel itself at the ignition temperature and so it continues to burn. Another point is that it releases a lot of energy and it ignites the surrounding materials, as a consequence, the fire spreads. Fire may also produce toxic gases and smoke. It destroys property and it causes disorientation and even injuries and deaths.

Real natural fire is quickly increasing its temperature at the beginning, which can be over 200 ℃/min and is critical to many engineering materials and structures. Fire spreads rapidly and can engulf a compartment in just few minutes.

Real fires are complex phenomena that are characterized by non-uniformity and fortuitousness, being strongly dependent on the local environment. For laboratory test it is difficult to consider all influential parameters in a natural fire. Several models were developed so far to represent fire scenarios in reality. Eurocode 1 Part 1–2 (*European Committee for Standardization*, 2003) allows for the use of two different approaches for the fire curve: nominal time-temperature curves and natural fire models.

The natural fire models are simplified fire models for considering quite realistic fire scenarios in design, which takes into account the influence of the environment, density of combustible

materials, thermophysical properties of surrounding materials and ventilation conditions on the development of the fire. For this purpose the parametric fire model as described in Eurocode 1 Part 1-2 Annex A is highly recommended. For localised fire it is referring to Eurocode 1 Part 1-2 Annex C.

Nevertheless, the nominal fire curves were developed for fire resistance furnace tests of building materials and members for their classification and verification. They are more commonly used in laboratory.

The standard fire curve is also called as the ISO 834 (*International Organization for Standardization*, 1999) fire curve , which can be used for all fire design scenarios and is internationally accepted for fire resistance testing of components. This curve is based on the burning rate of the material referring to general building materials and contents, for example, paper, wood, fabric, etc. The temperature development of standard fire curve is described by the following equation:

$$T = 20 + 345log_{10}(8t + 1) \tag{2.17}$$

where *T* is the gas temperature in the fire compartment.

Eurocode 1 (*European Committee for Standardization*, 2003) describes the external fire curve, which is used for the outside of external walls or facades exposed to the plume of a fire coming from the inside of the fire compartment.

$$T = 20 + 660(1 - 0.687e^{-0.32t}) - 0.313e^{-3.8t} \tag{2.18}$$

The hydrocarbon curve (HC) is described in Eurocode 1 for the use of representing effects of hydrocarbon fire, for example, oil, gas, chemicals, etc., which has very high initial heating rate and reaches a maximum temperature of 1100 ℃. The curve is describing as follows:

$$T = 20 + 1080(1 - 0.325e^{-0.167t}) - 0.675e^{-2.5t} \tag{2.19}$$

Besides the above mentioned curves, there were several other curves developed for specific cases.

Based on the hydrocarbon curve (Equation (2.19)), in France the modified hydrocarbon curve (HCM) was developed to consider the increased safety requirements in an increased temperature situation, for example, fire in a tunnel. HCM curve reaches a maximum temperature of 1300 ℃.

$$T = 20 + 1280(1 - 0.325e^{-0.167t}) - 0.675e^{-2.5t} \tag{2.20}$$

In Germany the RABT curves were developed for train and car fires. The temperature rises rapidly up to 1200 ℃ within 5 minutes. The durations of the 1200 ℃ for car and train are 26 min and 56 min, respectively. Following is a linearly cooling branch, as shown in Figure 2.8.

By the Ministry of Transport in the Netherlands, the RWS (Rijkswaterstaat) curve was developed for the worst fire scenario, which means a 50 m³ fuel, oil or petrol tanker fire in a road tunnel. This curve is described by the following:

Time (min)	0	3	5	10	30	60	90	120	180
Temperature (^{o}C)	20	890	1140	1200	1300	1350	1300	1200	1200

All above mentioned fire curves are plotted in Figure 2.8.
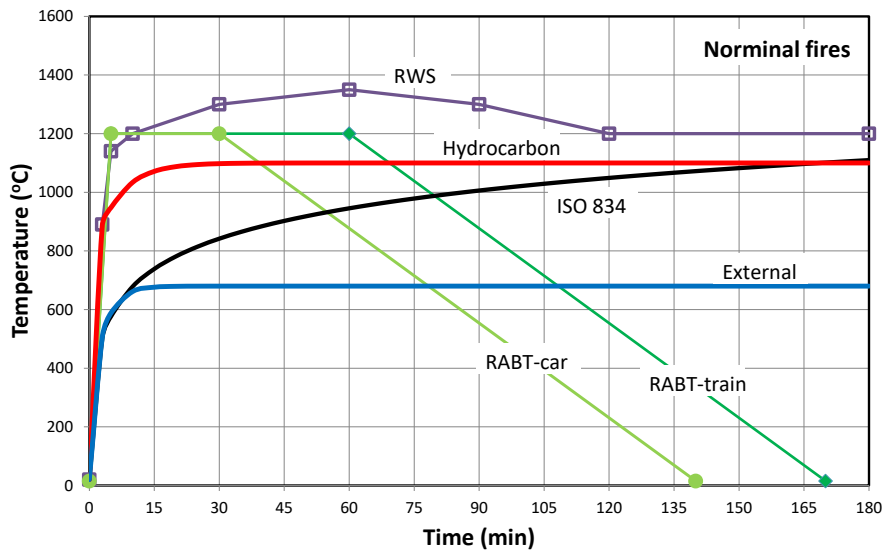
Figure 2.8 Temperature-time curves of nominal fires.

In the present study, the ISO 834 fire curve is adopted to perform the experiments and numerical analyses, due to its world-wide recognition for structural fire test. It is worthy to note that in the current codes for fire safety of structures or members usually it refers to the resistance during the fire, instead of residual capacity. However, in papers there are many discussions about the resistance of structures or materials either during fire/elevated temperature or after cooling. In the

present work both the resistance during fire and after cooling are investigated. In order to explicitly express the results, in this thesis the states are defined as shown in Figure 2.9. The ambient resistance refers to state without any fire or high temperature influence, for example, the reference tests at ambient temperature; the hot state refers to tests or results during fire, i.e. immediately after heating; the cold state stands for tests or results after the cooling of specimens to the ambient temperature, sometimes it is called as the residual resistance.
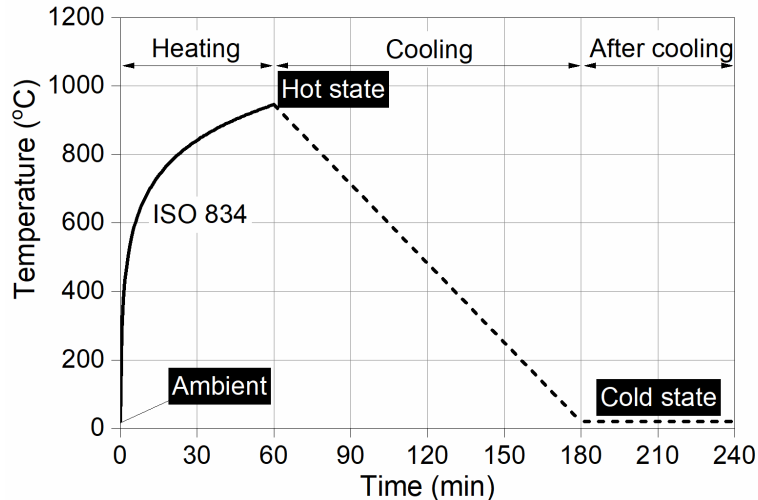
Figure 2.9 The ambient, hot state and cold state.

2.2.5. Anchorage in concrete after fire exposure

Up to now there is very limited research on the load-bearing behaviour of fasteners in concrete after fire exposure, due to the fact that fire tests are expensive, time consuming and difficult to have predictable results. Some main experiments conducted and conclusions drawn from different researchers are discussed in the following.

Tension

Due to the softening of steel at high temperature in case of fire, steel failure might be the governing failure mode (*fédération internationale du béton (fib)*, 2008). The anchor steel failure under tension and shear loads were tested in different laboratories and summarized by *Reick* (2001). Based on this the characteristic steel strengths for fasteners under fire were proposed in Eurocode 2 (*European Committee for Standardization*, 2018) for fire design purpose. However, considering fire safety in structural fire engineering the steel parts must be designed and protected against fire, which comprises protective measures of sprays, castings, intumescent

coatings, claddings, etc. (*Association for Specialist Fire Protection et al.*, 2014; *DIN Deutsches Institute für Normung*, 2016).

Concrete, a multimedia and porous composite, changes its thermophysical and thermomechanical properties due to fire exposure. Concrete breakout failure of anchors and the corresponding resistance after fire is thus more complex for fire engineering. It is known that the strength of concrete is substantially reduced with fire exposure (*Schneider*, 1982; *Zhang and Bicanic*, 2002; *European Committee for Standardization*, 2004a). This leads to strong influence on the capacity of connections between steel and concrete, namely, the load-bearing behaviour of fasteners in concrete. Particular cases are when the fasteners are located close to the edge of a concrete member and loaded in shear towards free edge or anchorages installed with shallow embedment depth and loaded in tension. After fire exposure the concrete becomes damaged, which can result in strong reduction of failure capacity of fasteners. Currently in the literature there are only limited experimental and numerical studies devoted to the residual capacity of fasteners failing in concrete under fire exposure.

Reick (2001) also performed experimental and numerical analyses of undercut and headed stud anchors under fire associated with the concrete cone capacity under tension loads. It is reported that the diameter of the concrete cone developed in case of tests after fire is larger than the diameter of the fracture cone obtained for the corresponding case at ambient temperature. The relatively rapid temperature decrease with increasing depth in the concrete corresponded to the increase of the relative concrete capacity with increasing embedment depth of the anchor. Thus, the concrete cone capacity for a fire exposure up to 90 minutes of ISO 834 fire is considered using Equation (2.21):

$$N_{u,fi(90)} = (h_{ef}/200)N_{u,c} \tag{2.21}$$

where h_{ef} stands for embedment depth in mm and $N_{u,c}$ is the concrete cone capacity at ambient temperature. This is also implemented into the current Eurocode 2 (*European Committee for Standardization*, 2018).

Ožbolt et al. (2005b) carried out numerical simulations based on 3D thermo-mechanical FE modelling on headed stud anchors with different embedment depths exposed to fire and loaded in tension. It demonstrated that the resistance of anchors with relatively small embedment depth can be significantly reduced due to fire exposure for concrete cone failure. For anchors with large embedment depth, compressive stresses may work on the anchor and leads to no reduction of capacity and even slightly higher capacity due to restraining conditions of concrete under fire were obtained. This so called confining effect was also found experimentally in the previous tests for anchors loaded in shear towards free edge under fire (hot state) (*Tian et al.*, 2016).

21

Bamonte et al. (2007) conducted experimental research on the tensile capacity of undercut fasteners installed in thermally damaged concrete. These fasteners were installed in low strength concrete, normal strength concrete and high strength concrete with various depths after exposure of the concrete to different temperature levels by electric furnace. Results showed that after reaching only 400 ℃ the pull-out capacity was roughly 20% of the values obtained from reference tests without high temperature exposure. If standard fire was applied, which means a significantly higher heating rate especially at the beginning phase, the residual capacity could be reduced further by at least 25%, depending on the embedment depth. This study also showed that the concrete grade plays only a marginal role on the residual capacity of fasteners for temperature exposure above 200 ℃.

Periškić (2009) performed extensively experimental tests and numerical simulations on the load-bearing behaviour of single anchor and anchor groups located close and away from concrete edge under tensile load at high temperatures, considering the fire exposure on one side and two sides of the edge. It was shown that for anchors located away from concrete edge, the embedment depth of anchor plays a main role on the residual capacity of anchors loaded in tension. The larger the embedment depth is, the smaller the reduction in the failure load. When the anchor is located close to an edge, the two-sided fire on the edge induces strong reduction of tensile capacity under fire exposure, which is reasonable due to the penetration of heat into concrete member from both sides of the edge.

Sharma and Bošnjak (2017) presented experimental results on the residual tensile capacity of concrete screws and undercut anchors after one hour of fire exposure. For the both types of anchors, three different embedment depths, 40 mm, 60 mm and 80 mm, were considered. It was found that the residual pull-out capacity was reduced significantly after fire exposure. At larger embedment depths, undercut anchors retain a higher percentage of their reference failure load compared to concrete screws, however, for shallowly embedded anchors the concrete screws retain a higher percentage of their reference load-carrying capacity.

Hlavička and Lublóy (2018) analysed the load-bearing behaviour of bonded anchors installed in thermally damaged concrete, with 50 mm embedment depth and 8 mm diameter. The study showed that all post-installed anchors failed in concrete cone failure, which proves a good bonding strength but thermally damaged concrete. The reduction of ultimate failure load was almost linearly reduced to about 60% and then constant. The initial reduction of resistance was not observed as severe as in other studies, which is primarily due to the following two reasons. First, the temperature rise controlled by electric furnace was initially less severe than standard fire curve ISO 834 and the final temperature reached was also lower than standard fire curve; Second, the heating was strictly localized to an area of 4*hef* surrounding the anchor, in this case confinement effect from surrounding colder concrete might occur. The authors tried to modify the formulae for predicting concrete cone failure resistance at ambient to predict the residual

resistance after fire, based on the modification of concrete compressive strength, concrete tensile strength and Young's modulus of concrete at elevated temperatures. However, by applying modified concrete properties after high temperature in the formulae for ambient condition resistance seems not to provide reasonable prediction.

Shear

From the viewpoint of heat penetration, the concrete edge failure of anchors loaded in shear towards free edge may represent the most critical case. Single fastener or a group of fasteners close to an edge of concrete member may fail by concrete edge breakout because the concrete becomes extremely weak under fire scenario, especially after cooling.

For pry-out failure of fasteners at high temperature or under fire, currently there is no data available. Nevertheless, some push-off tests with the background of fire safety of composite steel and concrete connections were reported.

Mirza and Uy (2009) conducted a series of finite element analyses on the shear connectors for composite steel-concrete connector at elevated temperature by using ABAQUS. The material property of concrete and steel are according to European codes and relevant literature. The temperature distribution were verified against experimental measurement, however, the faster temperature rise in the vicinity of the steel stud due to high thermal conductivity of steel was not reflected in the models. The load-slip curves at elevated temperatures were seen in good agreement with experimental curves. The author also reported a reduction of ultimate load by 35% compared with the ultimate load at ambient temperatures for the first 10 min of fire. The relative resistance as a function of fire duration was presented; however, the reduction formula was taken only as a function of time.

Wang (2012) applied a nonlinear three-dimensional thermo-mechanical coupled finite element model to simulate the push-out tests. The temperature profile detailed surrounding the headed studs could be obtained. It was found that the temperature in the shear studs are typically 100 to 150 ℃ higher than the surrounding concrete due to the high thermal conductivity of steel compared to concrete. Negative displacements could be observed for short period of heating due to major thermal expansion. The structural response can be well simulated. A good simulation of the slip and the deformation of the studs at elevated temperature were obtained.

Mashiri et al. (2017) investigated the post-fire load-bearing behaviour of three types shear connectors (headed stud plus two types of blind bolts) in concrete by pushout tests. The anchors have embedment depth of 100 mm and were about 20 mm in diameter. The pushout test specimens were heated up to 200, 400 and 600 °C. The reduction of resistance and the increase of ductility with elevated temperature were obvious. For both reference pushout test at ambient condition and post-fire pushout test, the main failure mode was concrete splitting, which can be

the reason for non-ideal prediction according to formulae in Eurocode 4 (*European Committee for Standardization*, 2004b), AISC (*AISC Manual Committee*, 2001) and Australian Standard AS2327.01 (*Standard Australia Limited*, 2003).

From the above it can be seen that very limited studies are devoted to the behaviour of anchors loaded in shear, close or far away from concrete edge, after fire exposure.

2.3. Design provisions-shear load

The design formulas corresponding to concrete failure are used to compute the nominal strength of a single anchor subjected to shear load. These formulas are based on the 5% fractile, which means that there is a 90% confidence level that over 95% of the failures occur above the calculated limit state for the anchor configuration. Current formulas for design referring to concrete edge failure and pry-out failure at ambient condition and for fire resistance are shortly summarized in the following.

For calculating the characteristic resistance of anchor groups, the geometrical effect of spacing as well as of further edge distances are the same as discussed previously.

2.3.1. Eurocode 2 EN 1992-4

The latest provisions in Eurocode 2 are referring to (*European Committee for Standardization*, 2018). Considering exposure to fire, the provisions are stated in the Annex D. There are three points that should be noted. First, the design method covers fasteners with a fire exposure from one side only. For fire exposure from more than one side, the design method may be used only when the edge distance satisfies the requirements: $c \geq 300$ mm and $c \geq 2h_{ef}$. Second, the concrete spalling should be prevented by appropriate measures or taken into account in the design. Third, it covers only fire classification according to EN 13501-2 (*European Committee for Standardization*, 2016) for 90 min and 120 min of fire.

Concrete pry-out failure

The development of design formula for pry-out failure is based on Equation (2.11). For pry-out failure of fasteners without supplementary reinforcement, the characteristic resistance $V_{Rk,cp}$ shall be calculated for fastenings with headed or mechanical post-installed fasteners as follows:

$$V_{Rk,cp}^0 = k_8 \cdot N_{Rk,c}^0 = k_8 \cdot k_1 \cdot \sqrt{f_{ck}} \cdot h_{ef}^{1.5} \tag{2.22}$$

with

$N_{Rk,c}^0$ the characteristic resistance of a single fastener by concrete cone failure under tension;

f_{ck} the characteristic compressive strength of concrete cylinder with 150×300 mm;

$k_1 =$ $k_{cr,N}$ for cracked concrete

       $k_{ucr,N}$ for uncracked concrete.

$k_{cr,N}$ and $k_{ucr,N}$ are given in the corresponding European Technical Product Specification. Indicative values for $k_{cr,N}$ and $k_{ucr,N}$ are $k_{cr,N} = 8.9$ and $k_{ucr,N} = 12.7$ for cast-in headed stud anchors. k_8 is a factor to be taken from the relevant European Technical Product Specification. Indicative values are $k_8 = 1$ for $h_{ef} < 60$ mm and $k_8 = 2$ for $h_{ef} \geq 60$ mm.

The characteristic resistance in case of fire for fasteners installed in concrete classes C20/25 to C50/60 should be obtained using:

$$V_{Rk,cp,fi(90)}^0 = k_8 \cdot N_{Rk,c,fi(90)}^0 = k_8 \cdot \frac{h_{ef}}{200} \cdot N_{Rk,c}^0 \text{ for fire exposure up to 90 min} \tag{2.23}$$

$$V_{Rk,cp,fi(120)}^0 = k_8 \cdot N_{Rk,c,fi(90)}^0 = k_8 \cdot 0.8 \cdot \frac{h_{ef}}{200} \cdot N_{Rk,c}^0 \text{ for fire exposure 90 to 120 min} \tag{2.24}$$

with $N_{Rk,c,fi(90)}^0$ and $N_{Rk,c,fi(120)}^0$ ($\leq N_{Rk,c}^0$) the characteristic concrete cone failure resistance of a single fastener not influenced by neighbouring fasteners or concrete edges installed in concrete strength classes C20/25 to C50/60.

Concrete edge failure

In Eurocode 2 the design formula is based on Equation (2.6), which was proposed by *Hofmann* (2005):

$$V_{Rk,c}^0 = k_9 \cdot d_{nom}^\alpha \cdot l_f^\beta \cdot \sqrt{f_{ck}} \cdot c_1^{1.5} \tag{2.25}$$

k_9 $= 1.7$ for cracked concrete

       $= 2.4$ for uncracked concrete.

The characteristic resistance of concrete edge failure for headed stud in concrete exposed to fire up to 90 minutes and 120 minutes reads:

$$V^0_{Rk,c,fi(90)} = 0.25 \cdot V^0_{Rk,c} \text{ for fire exposure up to 90 min} \tag{2.26}$$

$$V^0_{Rk,c,fi(120)} = 0.20 \cdot V^0_{Rk,c} \text{ for fire exposure 90 min to 120 min} \tag{2.27}$$

The resistance of a single anchor after 90 min and 120 min of fire exposure is equal to 17.5% and 14% of the resistance of a single anchor at ambient temperature in un-cracked concrete, respectively. In the absence of sufficient experimental data, it is not clear how reliable this formula is and if it is valid under high temperature (hot state) or also after cooling (cold state).

2.3.2. Eurocode 4 EN 1994-1-2

Compared to fasteners in concrete under fire (*European Committee for Standardization*, 2018), Eurocode 4 covers rather completed aspects for the design of composite steel and concrete connectors. In the Eurocode 4 EN 1994-1-2 (*European Committee for Standardization*, 2005b) for the structural fire design of composite steel and concrete structure, the verification of shear resistance of stud connectors under fire is achieved by applying a partial factor for the strength of material.

For the fire resistance of steel stud under fire:

$$P_{fi,Rd} = 0.8 \cdot k_{u,\theta} \cdot P_{Rd} \tag{2.28}$$

where P_{Rd} is the design shear resistance of a headed stud automatically welded as obtained per Equation 6.18 of EN 1994-1-1 (*European Committee for Standardization*, 2004b). $k_{u,\theta}$ is taken from Tables 3.2 of EN 1994-1-2 for reduction factor for stress-strain relationships of structural steel at elevated temperatures.

For the fire resistance of concrete failure under shear:

$$P_{fi,Rd} = k_{c,\theta} \cdot P_{Rd} \tag{2.29}$$

where P_{Rd} is the design shear resistance accounting for concrete failure as obtained per Equation 6.19 of EN 1994-1-1 (*European Committee for Standardization*, 2004b). $k_{c,\theta}$ is taken from Tables 3.3 of EN 1994-1-2 for reduction factor for stress-strain relationships of concrete at elevated temperatures.

In both Equations (2.28) and (2.29) for the design shear resistance P_{Rd} the partial factor γ_v should be replaced by $\gamma_{M,fi,v}$ which is the partial factor for the strength of stud connectors in the fire situation.

2.3.3. TR 020 Technical Report

TR 020 (*European Organisation for Technical Approvals*, 2004) is the early technical report describing the evaluation of metal anchor in concrete concerning resistance to fire. For the fire resistance of anchors in concrete under shear loading, the simplified design methods for determination of the duration of the fire resistance in cracked and non-cracked concrete are the same as that stated in Eurocode 2 Part 4. The test set-ups and procedures for the determination of steel failure under tension and shear and pull-out failure are clarified. However, no technical test method for concrete failure (concrete cone failure, concrete edge failure and concrete pry-out failure) is described.

2.3.4. ACI 318

Concrete pry-out failure

For a cast-in single anchor, the nominal pry-out failure load is calculated as:

$$V_{cp} = k_{cp}N_b \text{ [lb]} \tag{2.30}$$

where $N_b = k_c\sqrt{f_c'}h_{ef}^{1.5}$ [lb] (with $k_c = 24$ for cast-in anchors) is the basic concrete breakout (concrete cone failure) strength of a single anchor in tension in cracked concrete. In un-cracked concrete Equation (2.30) should be multiplied by 1.25.

Concrete edge failure

Currently in ACI 318 (*American Concrete Institute Committee 318*, 2014) the design formula is determined from the analysis in *Fuchs et al.* (1995) as per Equation (2.5). The basic concrete breakout strength (concrete edge failure) in shear of a single anchor in cracked concrete could be calculated according to

$$V_b = 7\sqrt{d} \cdot (l_f/d)^{0.2} \cdot \sqrt{f_c'} \cdot c_1^{1.5} \text{ [lb]} \tag{2.31}$$

For cast-in headed studs that are continuously welded to steel attachments and sufficient slab thickness, higher resistance could be reached according to *Shaikh and Yi* (1985). Hence in Equation (2.31) "8" should be used instead of "7". In un-cracked concrete Equation (2.31) should be multiplied by 1.4.

Currently in ACI 318 code the fire resistance and fire safety design of fasteners are not covered.

3. CONCRETE AT ELEVATED TEMPERATURES

Under fire or rapid heating, the dehydration of cementitious products, the thermal dilatation of the concrete ingredients and the build-up of water vapour can induce severe concrete damage or even thermal spalling. In order to assess the response of concrete structures and have valid model for predicting the structural response under fire or high temperature, it is important to understand the material behaviour of concrete after high temperature exposure.

Special care should be devoted to the difference between concrete properties in the hot state and in the cold state. The concrete properties are mainly influenced by the reached temperature level, the evaporation of physically bound water, the dehydration of calcium hydroxide and C-S-H, and the dissociation of calcium carbonate. However, during cooling, depends on the rate of cooling or the applied method of quenching, re-hydration process could result in "healing" as new hydration products are formed or further "damage" due to shrinkage of cement paste and aggregates.

3.1. Thermophysical properties of concrete

3.1.1. Thermal expansion

The thermal expansion of unloaded concrete is the thermal strain due to heating. It is influenced mainly by the aggregate type, water content, cement type and heating and cooling regime (*Schneider*, 1982; *Lie*, 1992). With increased temperature, the main constituents of concrete, cement paste and aggregate, behave differently. Figure 3.1a shows the thermal contraction and expansion of cement paste and rocks reported by different researchers. The hardened cement paste presents slight expansion at temperatures up to about 150 ℃. Afterwards it starts to shrink, with temperatures greater than about 200 ℃, the thermal contraction competes with thermal expansion giving a net contraction. At 800 ℃, the thermal contraction of cement stone can reach about 2%. The contraction is associated with the evaporation of water and dehydration of cementitious products at elevated temperatures (*Bažant and Kaplan*, 1996). However, rocks keep expansion at elevated temperatures. Due to the difference of rock material structure and mineral composition, different rocks expand quite differently with increasing temperature (*Harada et al.*, 1972).

Figure 3.1b shows that siliceous concretes present higher thermal expansion than calcareous concretes (*Harada et al.*, 1972; *Schneider*, 1982; *European Committee for Standardization*, 2004a). The thermal expansion of concrete increases gradually. At 573 ℃ the physical phase transformation of α-quartz to β-quartz contributes a lot to the abrupt thermal expansion of siliceous concretes. Over very high temperature of about 700 ℃, the thermal expansion remains

constant with approximately 1.3%. Due to increasing decarbonation of limestone in concrete, even a decrease in thermal expansion to zero at about 1100 ℃ can be observed (*Schneider*, 1982).

(a)   (b)
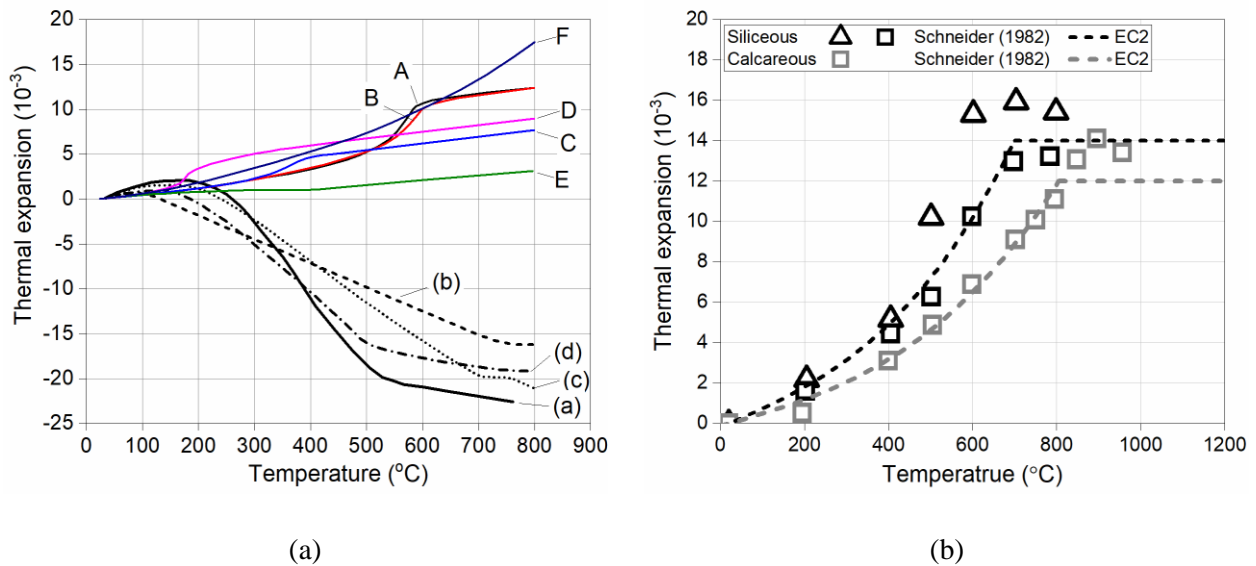
Figure 3.1 (a) Thermal expansion of cement paste: (a) Philleo (1958), (b) Harada et al. (1972), (c) Cruz and Gillen (1980) and (d) Crowley (1956), cited in *Bažant and Kaplan* (1996); and rocks: A and B (sedimentary rock), C (pyroxene, amphibolite, andesite), D (pyroxene-andesite), E (siliceous rock) and F (limestone), which are summarized by *Harada et al.* (1972). (b) Thermal expansion of concrete as a function of temperature.

3.1.2. Thermal conductivity

The thermal conductivity λ_c is defined as the ratio of the heat flux to temperature gradient. It is usually measured by means of steady-state or transient test method. The steady-state methods include the hot plate method and the hot box method, which however are not reliable for moist concretes. Transient method is thus preferable for moist concrete, for example, the hot-wire method. The thermal conductivity of concrete is mainly influenced by the type of aggregate since normally aggregates comprise 60-80% of the volume of concrete. More water in concrete leads to higher porosity, resulting in greater volume of air. As shown in Figure 3.2a, the thermal conductivity of aggregates and concretes varies in a large range at ambient condition. However, water has comparatively rather low thermal conductivity and air has the lowest. Thus, it makes sense that dense concrete has higher thermal conductivity.

With increasing temperature, the thermal conductivity of concrete decreases, see Figure 3.2b. At temperatures within 100 ℃, the thermal conductivity of concrete is little affected. Thereafter, due to the evaporation of water and the dehydration and decarbonation, a more porous material structure is developed and the thermal conductivity of normal-weight concrete decreases slightly.

Relatively large scatter of data can be attributed to different test methods and different mixtures of concrete (*Schneider*, 1988; *Lie*, 1992; *Shin et al.*, 2002). In Eurocode 2, the reduction of thermal conductivity of concrete is determined between the upper and lower limit (*European Committee for Standardization*, 2004a). It should be noted that the thermal conductivity of lightweight concrete keeps constant with low value or presents slight increase with increasing temperature according to *Harmathy* (1970).

During cooling of concrete as much as 10–20% increase of thermal conductivity was reported in fib Bulletin 38 (*f éd ération internationale du b éton (fib)*, 2007), nevertheless most of the loss of thermal conductivity is irreversible.

(a)

(b)
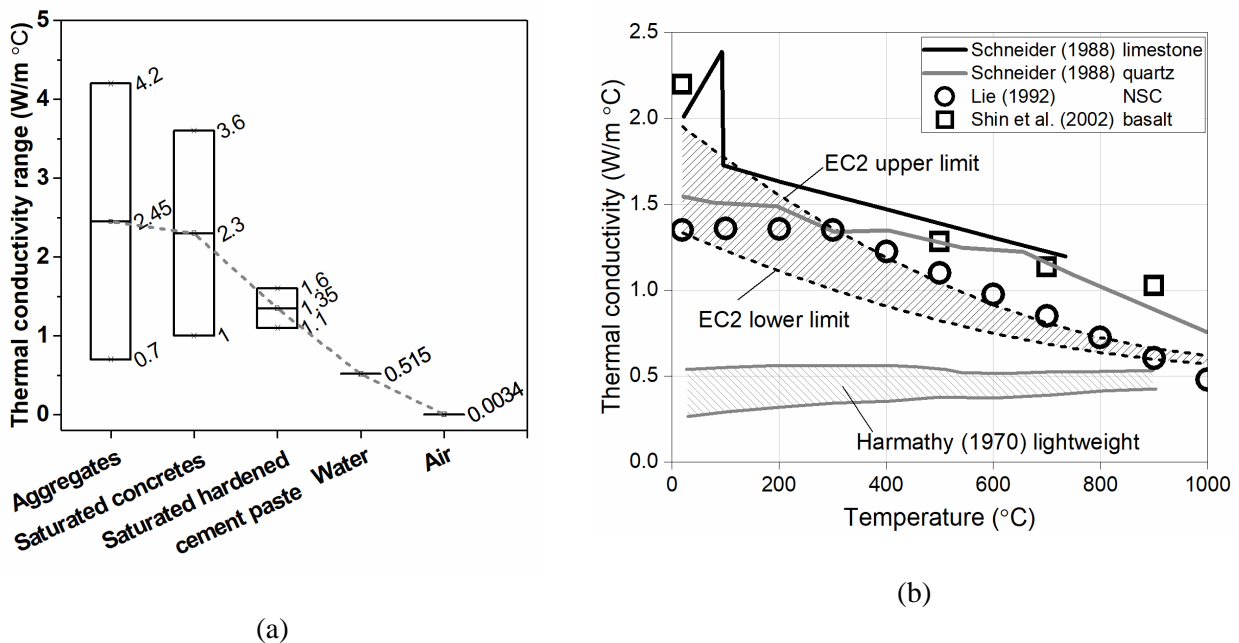
Figure 3.2 (a) Thermal conductivity of main constituents of concrete at ambient condition (data from *Khoury* (1983)); (b) Thermal conductivity of concrete as a function of temperature.

3.1.3. Specific heat capacity

The specific heat capacity is the amount of heat per unit mass that is required to change the temperature of the material by one degree. It can also be defined in terms of enthalpy H at constant pressure P (*Harmathy and Allen*, 1973):

$$C_p = (\partial H / \partial T)_P \tag{3.1}$$

where H = enthalpy, T = temperature, and P = pressure. Therefore, the evaluation of the specific heat of concrete can be complicated by the time dependent endothermic transformations during heating of concrete. Fundamentally, it can be measured by the calorimetry experiment.

Figure 3.3 shows the specific heat of normal strength concrete as a function of temperature according to different sources. Slight increase of the specific heat can be seen with increasing temperature. Lightweight concrete (pumice aggregates) seems to have relatively small value of specific heat at high temperature according to *Harmathy and Allen* (1973). Nevertheless, the specific heat of concrete is not only little affected by the mineralogical character of the aggregate but is also not very sensitive to the proportion of aggregate because the specific heat of the aggregates are very similar to that of the cement stone (*fédération internationale du béton (fib)*, 2007). In Eurocode 2 the specific heat capacity is differentiated by the moisture content 0%, 1.5% and 3% from temperature 100 to 200 °C. In this temperature range the strong vaporization of free water consumes a lot of heat due to the high specific heat of water (4.29 kJ/kg °C).
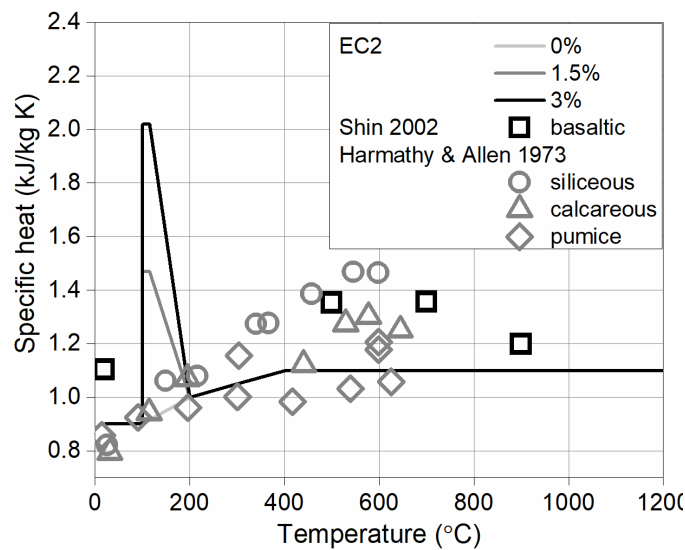
Figure 3.3 Specific heat of concrete as a function of temperature.

3.1.4. Thermal diffusivity

The thermal diffusivity D expresses the rate of flow of heat for a material under transient thermal conditions. It defines the speed of heat propagation by conduction during temperature change. Experimentally it can be tested by Angstrom method or the flash method. The thermal diffusivity D can be calculated by dividing the thermal conductivity λ_c with the volumetric specific heat which is the product of specific heat capacity C_p and density ρ as:

$$D = \lambda_c/(\rho C_p) \ [\text{m}^2/\text{s}] \tag{3.2}$$

Figure 3.4a shows the change of thermal diffusivity of concrete with increasing temperature. The solid lines indicate the thermal diffusivity of concrete calculated from Equation (3.2) according to the upper limit and lower limit of the thermal conductivity of concrete in Eurocode 2 (Figure 3.2b) and corresponding density and specific heat. The data for the thermal diffusivity of siliceous and calcareous concretes are generally between the upper and lower limits according to Eurocode 2 (*Harada et al.*, 1972; *Harmathy and Allen*, 1973). Aggregates do not seem to influence the thermal diffusivity a lot. Lightweight concrete, however, shows much lower thermal diffusivity. The thermal diffusivity of normal-weight concrete remarkably decreases for temperature up to about 500 ℃, due to largely reduced thermal conductivity and slightly increased specific heat at the same temperature range. Over 600 ℃ it is seen that both normal weight and lightweight concrete have a thermal diffusivity approximately being equal to 0.33 mm^2/s.
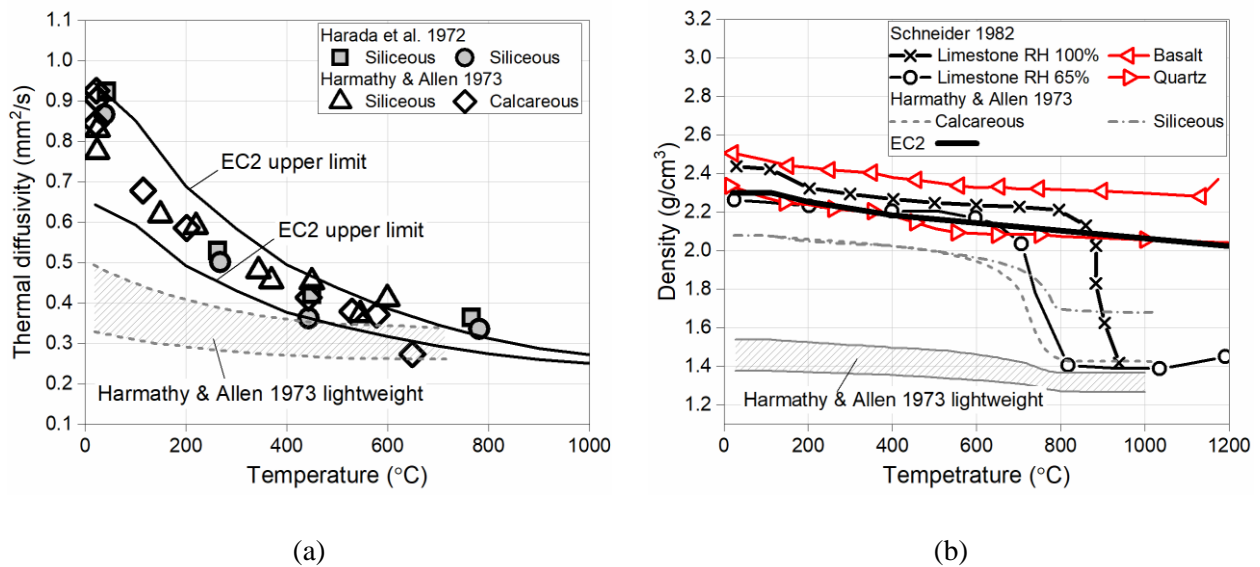
Figure 3.4 Thermal diffusivity (a) and density (b) of concrete as a function of temperature.

3.1.5. Density

The change of density ρ of concrete with increasing temperature is associated with the mass reduction due to vaporization of free water, loss of chemically bound water, dehydration of C-S-H products and decarbnotaion of $CaCO_3$. The thermal dilation and change of porosity also have influence on the density. Figure 3.4a shows a comparison of density of concrete at elevated temperatures reported by different sources (*Harmathy and Allen*, 1973; *Schneider*, 1982; *European Committee for Standardization*, 2004a). The initial reduction of density up to about

700 ℃ is rather moderate. Thereafter, the decarbonation of carbonate aggregates (limestone) leads to sharp reduction of density. The curve referring to Eurocode 2 is rather simplified for both siliceous and calcareous concretes. According to *Harmathy and Allen* (1973), lightweight concretes with many types of lightweight aggregates (expanded slag, expanded shale, expanded clay and pumice) show slight reduction of density with increasing temperature.

3.2. Thermo-mechanical properties of concrete

3.2.1. Uniaxial compressive stress-strain response

After temperature exposure, a complete understanding of stress-strain curve is required for developing an appropriate model for predicting the concrete structure response in fire numerically. The measurement of the stress-strain curves under compression after fire exposure has gained considerable attention in the past (*Schneider*, 1976; *Schneider*, 1988; *Chang et al.*, 2006; *Bamonte and Gambarova*, 2012; *Neuenschwander et al.*, 2017).

Several models based on experimental data have been developed to represent the stress-strain responses. Figure 3.5a shows a comparison of various models: *Anderberg and Thelandersson*, (1976), *Li and Purkiss* (2005) and *European Committee for Standardization* (2004a). With increasing temperature the peak load is largely reduced and the strain at peak load is increased. The ductility of concrete is also increased with increasing temperature.

(a)   (b)
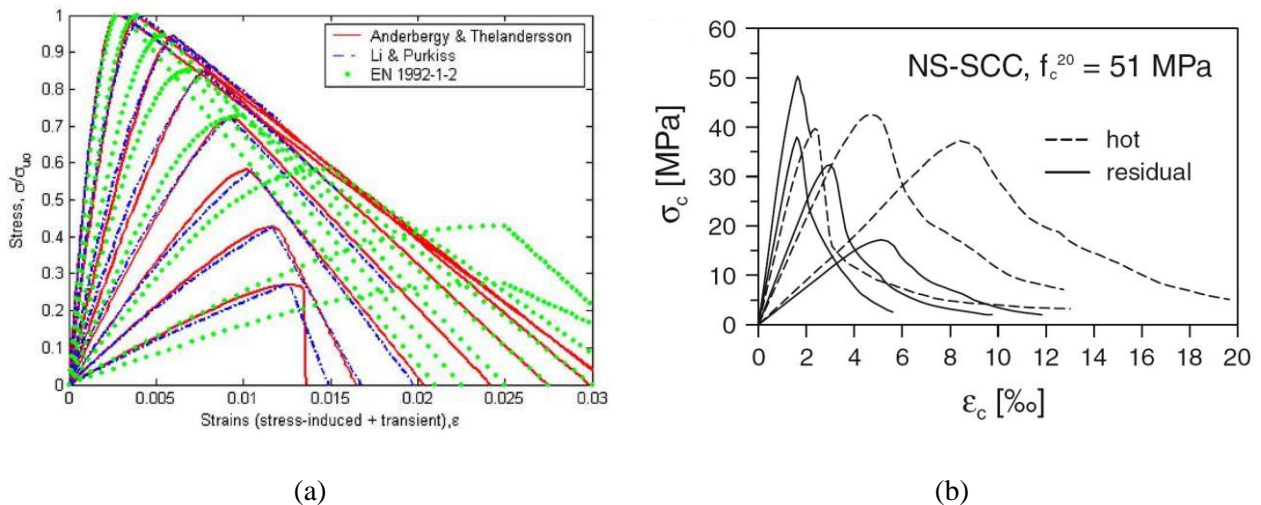
Figure 3.5 Stress-strain curves of concrete under uniaxial compression after different temperatures. (a) Models (*Li and Purkiss*, 2005); (b) hot vs. cold (residual) (*Bamonte and Gambarova*, 2012).

Measurement of a complete stress-strain curve at elevated temperature and after cooling is difficult. So far very little effort has been made to compare directly the stress-strain curves in the

hot and cold state. Figure 3.5b shows a comparison between the hot and cold curves for self-compacting concrete after high temperature exposure. It is seen that the initial ascending branch is stiffer in the cold state than that in the hot state for relatively low temperature, however, for very high temperature, the hot state response is slightly stiffer. In the tests performed by *Torić et al.* (2013) for high strength concrete, the residual stress-strain responses are always less stiff than the corresponding curve in the hot state.

3.2.2. Compressive strength

Concrete compressive strength of normal strength concrete suffers degradation after high temperature exposure, due to the evaporation of water, loss of bond strength between aggregate and cement paste, dehydration of the hydrated cement products, thermal cracking and so on. Up to temperature of 300 ℃, compressive strength was reported to be unaffected. After this temperature, compressive strength decreases with increasing temperature. The loss of compressive strength at elevated temperatures depends on the concrete mixture of aggregate, the heating-cooling regime, the test conditions, and so on. *Abrams* (1971) performed a series of experiments to study the influence of aggregate type (carbonate, siliceous, and sanded lightweight), test procedure (heated without load and tested in the hot state, heated with load and tested in the hot state, and heated without load and tested after cooling), and original strength of concrete (23 to 45.5 MPa). For the tests with load, pre-load to ultimate load ratios 0.25, 0.40 and 0.55 were applied; it was found that specimens stressed during heating, the so called transient state compressive strength, retained the highest strengths at high temperatures, which had strengths 5 to 25 percent higher than those specimens tested unstressed during heating. For the effect of aggregates, concrete made with carbonate or sanded lightweight aggregates kept higher strength at rather high temperature (see Figure 3.6a). After cooling, the residual strength of all concrete types turned out to be much lower than the hot state strength (see Figure 3.6b). This is due to severe thermally induced damage of concrete during the cooling process. The way of cooling has a noticeable influence on the residual strength according to *Lee et al.* (2007). It should be noted that maximum difference is reached for temperature ranging from about 400 to 700 ℃. After this temperature the difference between hot state strength and cold state strength is small. The normalized decrease of the compressive strength at high temperature is little, or not at all, affected by concrete initial strength.

Schneider (1982) studied the degradation of concrete compressive strength of normal strength concrete considering different aggregates, i.e. limestone, quartz and expanded clay, see Figure 3.6a. It was shown that the compressive strength was not affected apparently up to 300 ℃. At higher temperature the strength is tremendously reduced.

The values for siliceous and calcareous concrete in Eurocode 2 Part 1-2 are also plotted in Figure 3.6a. Typically, the compressive strength increases slightly up to 200 ℃ and then decreases

gradually up to 400 ℃. Beyond this temperature the compressive decreases dramatically. After 800 ℃, less than 20% of original strength is left.

(a)   (b)
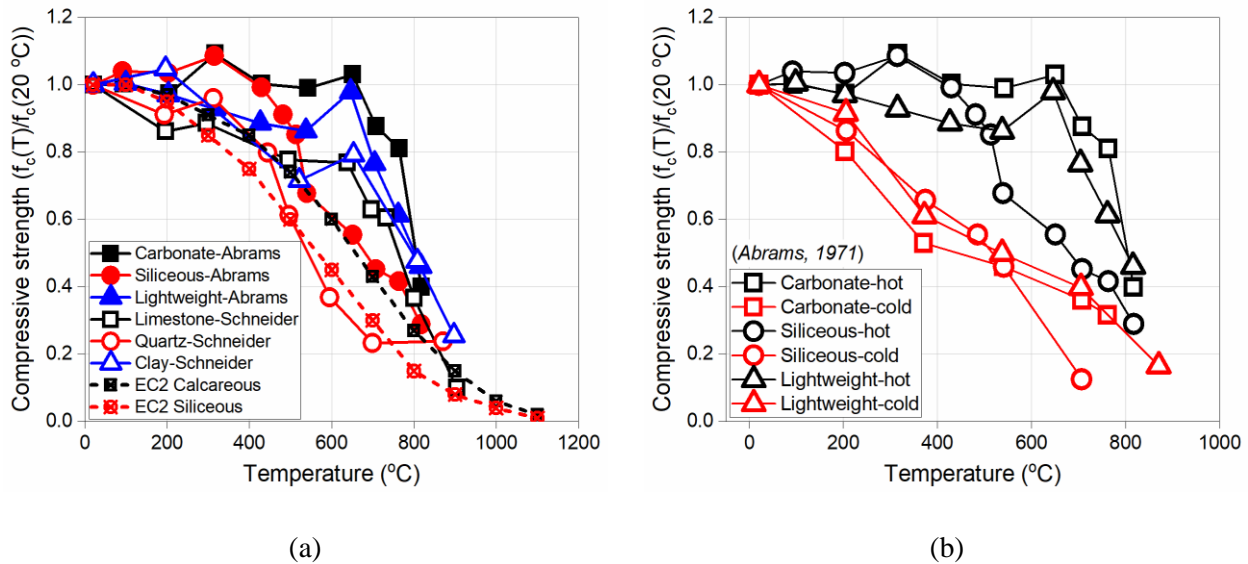
Figure 3.6 Compressive strength of normal strength concrete as a function of temperature. (a) Values for hot state strength; (b) comparison between the hot state and cold state strength.

3.2.3. Young's modulus

Figure 3.7 shows the reduction of Young's modulus of normal strength concrete with increasing temperature. The Young's modulus decreases monotonically. In contrast, the compressive strength can maintain its original strength up to 300 ℃ before an obvious reduction (see Figure 3.6). Over 300 ℃ less than 20% of original Young's modulus is left.

In Figure 3.7 a significant scatter of the data can be seen. It was reported that the aggregate type has a strong influence on the Young's modulus of concrete at elevated temperatures (*Schneider*, 1982). Lightweight aggregate indicate the lowest decrease of the modulus of elasticity and siliceous aggregate the highest (*Schneider*, 1988).

The comparison of the Young's modulus obtained from hot state test and cold state test is illustrated in Figure 3.7b. It is obvious the residual Young's modulus after cooling is much lower than that tested in the hot state. It should also be noted that the Young's modulus in the cold state is significantly influenced by the method of cooling. Water cooling brings in much severer loss concerning Young's modulus than slow cooling in controlled conditions. Generally, faster cooling contributes to a more severe decrease of the stiffness (*Lee et al.*, 2007).

36
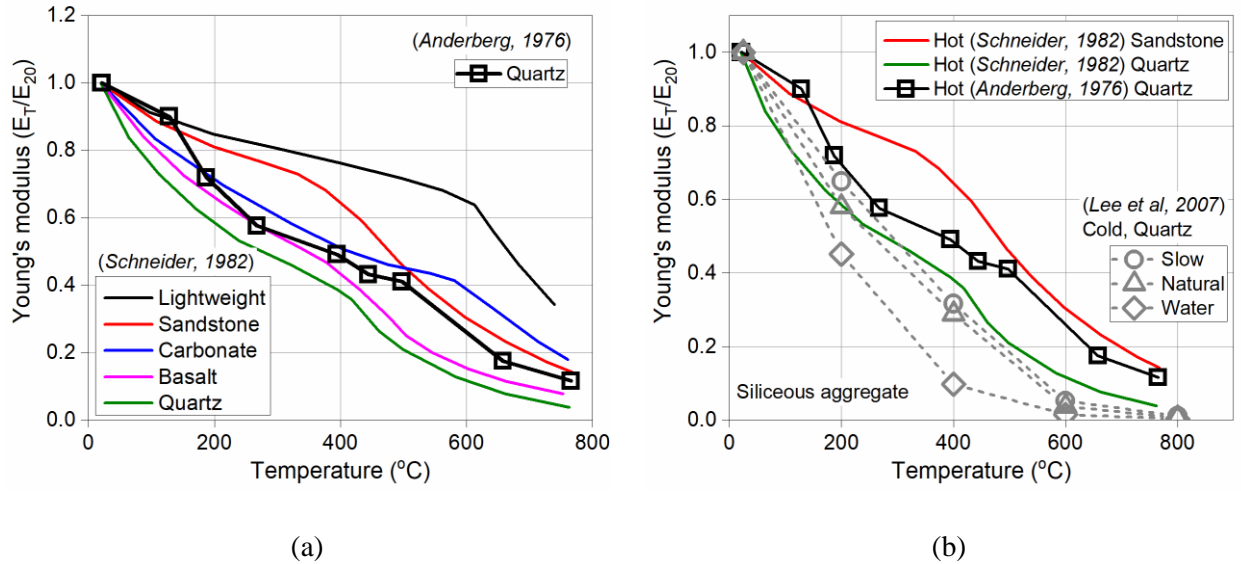
Figure 3.7 Young's modulus of normal strength concrete as a function of temperature. (a) Values for hot state; (b) comparison between values for hot and cold state.

3.2.4. Tensile strength

In the design of reinforced concrete structures, tensile strength of concrete is usually neglected and instead the capacity of steel under tension is utilized. Concrete has relatively low tensile strength, which can be less than 10% of the compressive strength. Consequently, concrete tensile strength has been little investigated at high temperatures. However, the fasteners in concrete mainly make use of the tensile strength of concrete. It is therefore important to understand the evolution of concrete tensile strength with increasing temperature.

The relative reduction of tensile strength with increasing temperature is plotted in Figure 3.8a. *Harada et al.* (1972) showed that the tensile strength of concrete containing limestone aggregate is more affected by the temperature than the concrete containing sandstone aggregate. Tests conducted by *Anderberg and Thelandersson* (1976) on concrete with quartz aggregates present good agreement with those results with sandstone aggregates. In the Eurocode 2 Part 1-2 it is assumed that up to 100 °C the tensile strength is unaffected and it decreases linearly to zero at 600 °C (*European Committee for Standardization*, 2004a).

Figure 3.8b presents a comparison of the evolution of tensile strength of normal strength concrete tested in the hot and cold state with increasing temperature. It is seen that the hot state strength is slightly larger than the cold state strength. However, they follow very similar reduction tendency. It is worthy to note that experimental results showed that the cold state tensile strength is generally the same as the hot state strength for high strength concrete ($fc \approx 90$ MPa) and the cold

state strength is even higher than the hot state strength for ultra-high strength concretes (fc ≈ 160 MPa) (*Felicetti et al.*, 2000)

(a)   (b)
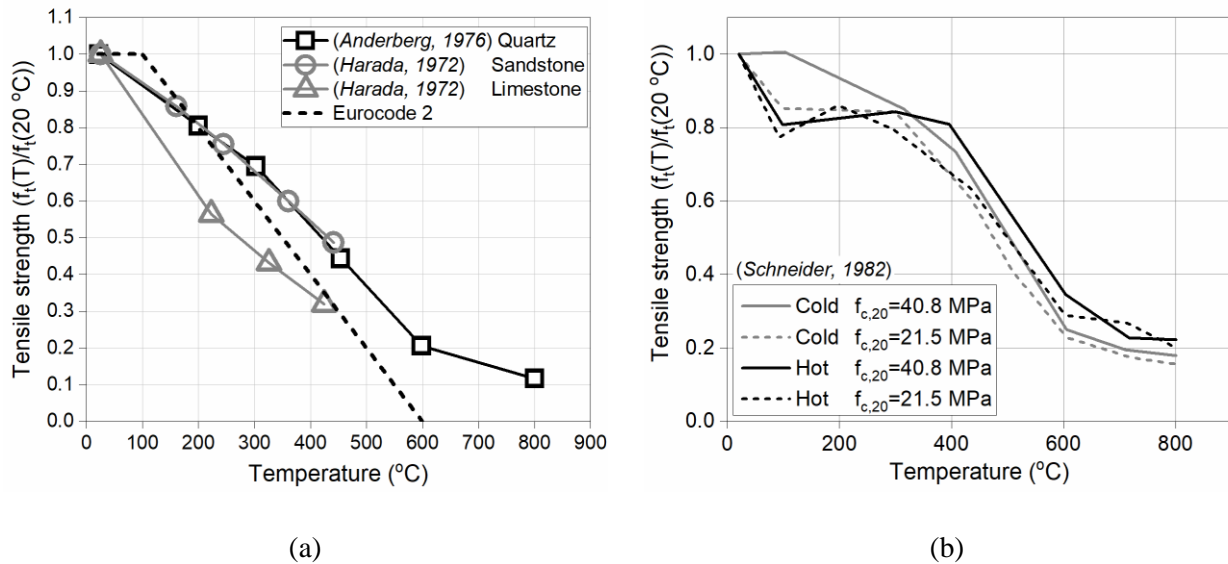
Figure 3.8 Tensile strength of normal strength concrete as a function of temperature. (a) Values for hot state; (b) comparison between values for hot and cold state.

3.2.5. Fracture energy

The fracture energy is defined as the amount of energy necessary to create one unit area of crack. It is usually measured by means of stable three-point bending tests on notched concrete beams (*Kluwer Academic Publishers*, 1985) or wedge-splitting test (*Brühwiler and Wittmann*, 1990), in which the applied load and the crack mouth opening displacement (CMOD) need to be monitored continually. This makes an appropriate measurement in the hot state difficult and no data of fracture energy in the hot state could be found. At ambient temperature, many discussions have been conducted on the fracture energy of concrete (*Bažant and Becq-Giraudon*, 2002; *Bažant and Kazemi*, 1990; *Wittmann*, 2002). The influence of high temperature on the fracture energy of concrete can only be evaluated after cooling, i.e. in the cold state.

Yu et al. (2013) performed the wedge-splitting test to investigate the temperature on the fracture energy of concrete. The temperature considered ranging from ambient to 600 °C. Figure 3.9a shows the effective load on crack development as a function of the CMOD after exposing the concrete specimens to different temperatures. It is seen that the peak load is reduced with increasing temperature.

Baker (1996) and *Zhang and Bicanic* (2002) studied the influence of high temperature on the fracture energy of concrete by conducting the three-point bending tests. Both of them observed

that the fracture energy increased with increasing temperature and then decreased, with maximum values at 300 °C. High strength concrete always showed higher value of fracture energy than normal strength concrete. All the data mentioned are plotted in Figure 3.9b and generally they follow the same tendency.

(a)   (b)
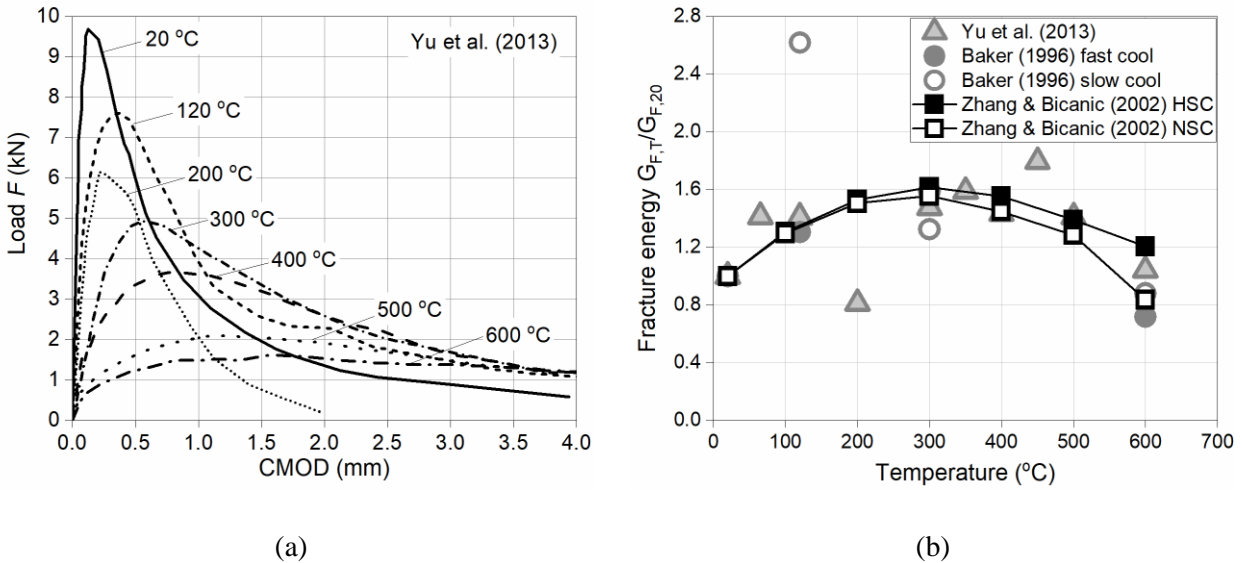
Figure 3.9 (a) Effective load as a function of CMOD after exposing concrete to various temperatures; (b) relative fracture energy as a function of temperature from different researchers.

3.2.6. Poisson's ratio

The influence of high temperature on the poisson's ratio of concrete has been investigated by several researchers. The poisson's ratio decreases from around 0.18 at ambient condition with increasing temperature. *Zhang and Bicanic* (2002) reported that high strength and normal strength concrete reduced their poisson's ratio in a similar way. *Luccioni et al.* (2003) tested the influence of different cooling regime on the reduction of concrete poisson's ratio. Cooling with spurts of cold water led to obviously larger reduction of poisson's ratio of concrete than those cooled naturally in the air. *Bahr et al.* (2013) used new testing techniques, the Impulse Excitation Technique, to obtain the poisson's ratio of concrete after high temperature exposure. Based on the tested data a model was proposed to calculate the temperature-dependent poisson's ratio. All the results are presented in Figure 3.10. A relatively large scatter of the data can be seen is due to different testing techniques and conditions.
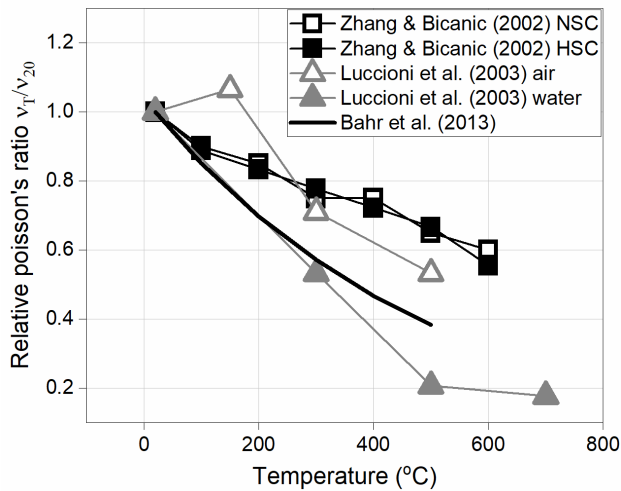
Figure 3.10 Relative poisson's ratio of concret as a function of temperature.

3.3. Thermal strain

The thermal strains of concrete at elevated temperatures can be divided into free thermal strain and load induced thermal strain.

3.3.1. Free thermal strain (FTS)

The free thermal strain (FTS, ε_{th}) stands for the strain that is developed when unloaded concrete is under heating. Since the thermal strain measurements are performed with unsealed specimens, the free thermal strain includes shrinkage. Figure 3.11 shows the free thermal strain of cement and concrete made with different coarse aggregates as a function of temperature. It is seen that the aggregates type and the proportion of aggregates in concrete affect the free thermal strain the most. The free thermal strain is also a nonlinear function of temperature. Pure cement stone shows contraction at temperatures above 150 to 400 ℃ (*Schneider*, 1988). The α to β inversion of quartz at about 573 ℃ induces the rapid expansion for concrete with quartz aggregate.

The free thermal strain is partly irreversible. For temperatures less than 400 ℃, residual thermal dilatation can be observed. Whereas, over 400 ℃ residual contraction could be observed (*Schneider*, 1988; *Hager*, 2004).
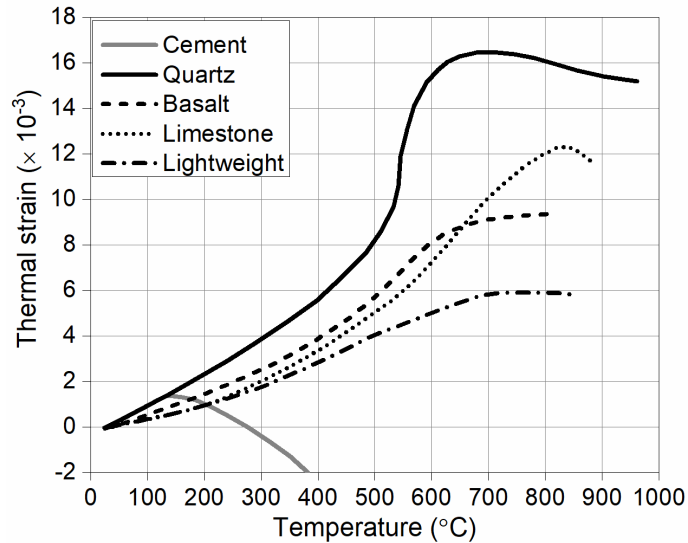
Figure 3.11 Free thermal strain of cement and concrete with different aggregates (*Schneider*, 1988).

3.3.2. Load induced thermal strain (LITS)

At any given temperature, the load induced thermal strain (LITS) is the difference between the free thermal strain (measured on unstressed/unloaded specimens) and the strain measured on specimens subjected to a constant load applied prior to the heating process (*fédération internationale du béton (fib)*, 2007). Figure 3.12 shows the strain-temperature curves of concrete specimens heated while loaded with 0%, 10%, 20% and 30% load. The difference between the loaded and unloaded is the LITS. It is obvious that the higher the load ratio results in the greater LITS. The free thermal strain is sensitive to the type of aggregate, however, *Khoury* (2006) stated that LITS is relatively insensitive to the type of aggregate and cement. The reason is that LITS originates from the C-S-H gel. Only over temperature 450 °C, the aggregate shows some influence on the LITS. The aggregate content by volume in the range of 0 to 75% indeed has remarkable influence on the LITS. According to *Hager* (2004), the difference in heating rate (1 °C/min and 5 °C/min) showed a pronounced influence on the LITS. Faster heating induces less LITS by comparing to slower heating, since the concrete specimen might be not thoroughly penetrated by heat during rapid heating. According to *Gernay* (2012), LITS increases almost linearly up to 400 °C, however, it increases much more rapidly at higher temperatures (see Figure 3.12b).

LITS comprises several components: transitional thermal creep (TTC), drying creep, time-dependent creep and changes in elastic strain (*Khoury et al.*, 2002), the initial elastic strain on loading is excluded. The sum of TTC and drying creep is called the "transient creep" and it is by far the largest component of LITS in unsealed mature concrete. The transient creep is

41

irrecoverable, i.e. it occurs only during first time heating under load. It is predominantly temperature-dependent and not time-dependent, especially for fire scenarios which last only hours.

Based on the meso-scale simulations of concrete, it has been shown that the main reason for LITS is the interaction between free thermal strain and load induced damage of cement paste (*Bošnjak*, 2014).
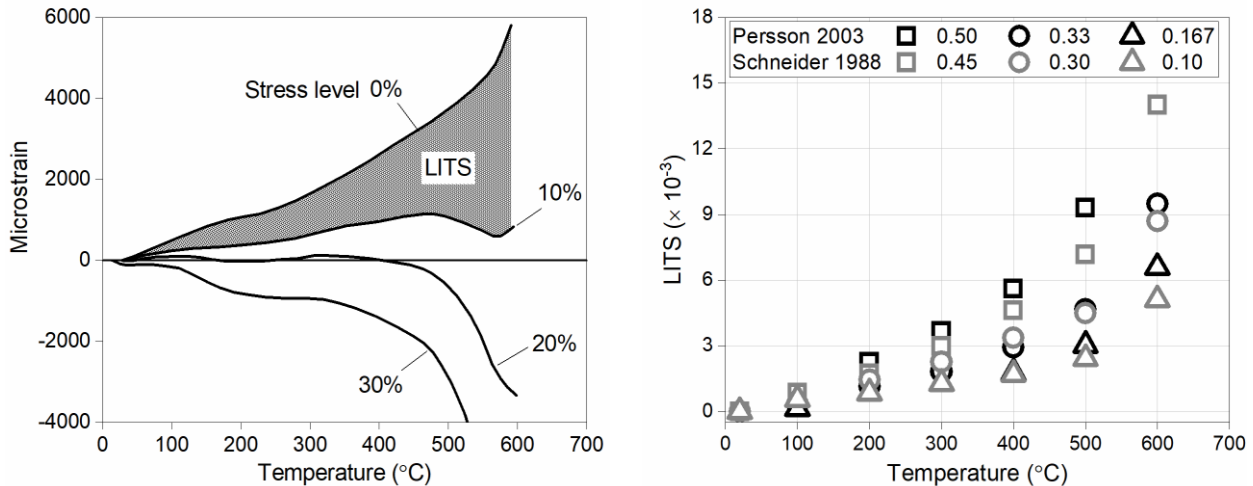
Figure 3.12 (a) LITS for concrete heated with 1 ℃ /min under 0%, 10%, 20% and 30% load, in the figure the LITS for 10% load is explicitly marked (*Khoury*, 2006); (b) LITS as a function of temperature under different load ratios, presented by *Gernay* (2012) based on experimental data from *Schneider* (1988) and *Persson* (2003).

3.4. Thermo-mechanical model for concrete

For analysing concrete structures it is important to have reliable numerical tool which is able to realistically simulate the mechanical behaviour of concrete. In the past different constitutive models and methods were proposed: linear- and non-linear fracture mechanics, continuum damage mechanics, plasticity theory, microplane model, and others. Among these models, the microplane model has been shown to be a reliable tool to describe concrete behaviour (*Bažant and Prat*, 1988; *Bažant and Ožbolt*, 1990).

In the present work the thermo-mechanical model for concrete is based on the temperature dependent microplane model (*Ožbolt et al.*, 2005b; *Ožbolt et al.*, 2005a).

3.4.1. Microplane model for concrete with relaxed kinematic constraint

Microplane model was originally proposed by *Taylor* (1938) and then applied for metal plasticity with the name "slip theory". Further it was used for non-softening behaviour of rocks and soils by *Zienkiewicz and Pande* (1977). Bažant et al. contributed main development of Taylor's idea to suffice for strain-softening brittle-plastic behaviour of concrete and defined the term "microplane" (*Bažant*, 1984; *Bažant and Gambarova*, 1984; *Bažant and Prat*, 1988).

In the microplane model the material response is calculated based on the monitoring of stresses and strains in different pre-defined directions. With the integration of the microplane stresses and strains in a thermodynamically consistent way, it is possible to calculate the macroscopic stress tensor from a known macroscopic strain tensor. The constitutive framework is similar to discrete type of the models (e.g. random particle model) with the difference that the model is formulated in the framework of continuum mechanics. The physical concept behind the microplane model was discussed by *Taylor* (1938) and *Mohr* (1900). In the microplane model the material is characterized by the relation between stress and strain components on planes of various orientations. These planes may be imagined to represent the damage planes or weak planes in the microstructure, such as those that exist at the contact between aggregate and cement matrix (see Figure 3.13a). Unlike phenomenological models for concrete (e.g. plasticity or damage based models), which are based on tensor invariants, in the microplane model the tensorial invariance restrictions need not be directly enforced. Superimposing, in a suitable manner, the responses from all the microplanes automatically satisfies them.

| (a) | (b) | (c) |
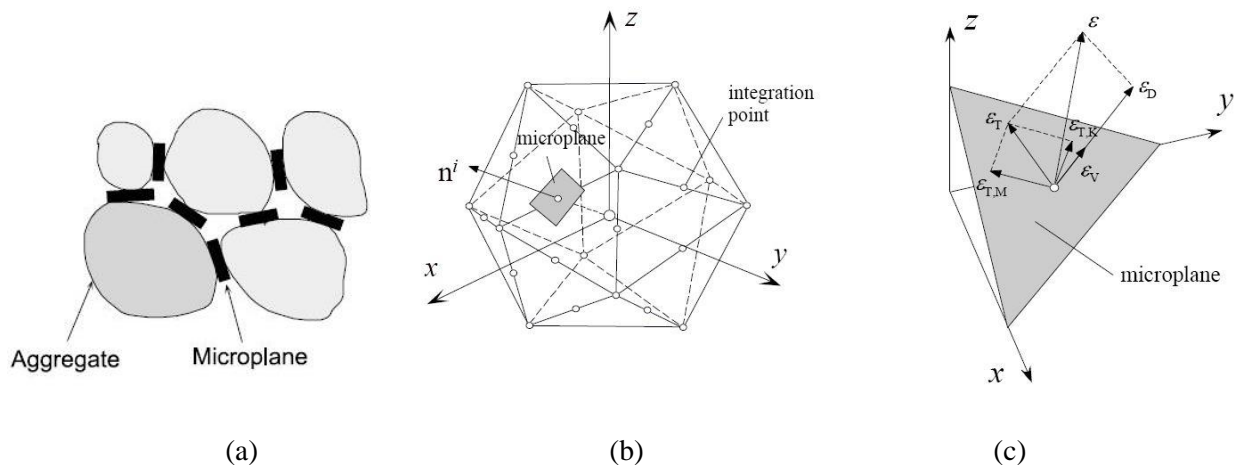
Figure 3.13 Microplane model: (a) load transfer over a number of idealized contact planes; (b) FE integration point with 21 microplanes; (c) decomposition of strain vector on the specified microplane. (*Ožbolt et al.*, 2001; *Ožbolt et al.*, 2011)

The used microplane model (*Ožbolt et al.*, 2001) is based on the so-called relaxed kinematic constraint concept. Each microplane is defined by its unit normal vector components n_i (Figure 3.13b). Microplane strains are assumed to be the projections of macroscopic strain tensor ε_{ij} (kinematic constraint). On the microplane normal (σ_N, ε_N) and two shear stress–strain components (σ_K, σ_M, ε_K, ε_M) are considered.

To realistically model concrete, the normal microplane stress and strain components have to be decomposed into volumetric and deviatoric parts ($\sigma_N = \sigma_V + \sigma_D$; $\varepsilon_N = \varepsilon_V + \varepsilon_D$) (Figure 3.13c). Unlike most microplane formulations for concrete, which are based on the kinematic constrain approach, to prevent unrealistic model response for dominant tensile load and to prevent stress locking phenomena, in the present model kinematic constrain is relaxed. Based on the micro-macro work conjugacy of volumetric-deviatoric split and using pre-defined microplane stress-strain constitutive laws, the macroscopic stress tensor is calculated as an integral over all possible, pre-defined, microplane orientations:

$$\sigma_{ij} = \sigma_v \delta_{ij} + \frac{3}{2\pi} \int_S \left[\sigma_D \left(n_i n_j - \frac{\delta_{ij}}{3} \right) + \frac{\sigma_k}{2} \left(k_i n_j + k_j n_i \right) + \frac{\sigma_M}{2} \left(m_i n_j + m_j n_i \right) \right] dS \qquad (3.3)$$

where S denotes the surface of the unit radius sphere, δ_{ij} is Kronecker delta, and k_i and m_i are directions of the shear components.

Theoretically, the larger the number of microplanes, the more accurate the results are. An excess of microplanes, however, will obviously require more computational work. A good balance between the accuracy of results and corresponding computational time involves 21 microplanes according to *Bažant and Oh* (1986) (Figure 3.13b). To account for large strains and large displacements, Green-Lagrange finite strain tensor is used. Furthermore, to account for the loading history of concrete, the co-rotational Cauchy stress tensor is employed. For more details with respect to the features and various aspects related to the finite strain formulation of the microplane model, readers may refer to *Bažant et al.* (2000) and *Ožbolt et al.* (2001).

3.4.2. Transient thermal analysis

Based on the constitutive law for heat flow and conservation of energy, the equation which describes temperature distribution in continuum of volume Ω reads:

$$\lambda_c \Delta T(x, y, z) - c\rho \frac{\partial T}{\partial t}(x, y, z) = 0 \qquad (3.4)$$

where T is temperature (K), λ_c is thermal conductivity (W/mK), c is the specific heat (J/kgK), ρ is mass density (kg/m^3) and Δ is Laplace-Operator.

The surface boundary condition has to be satisfied as:

$$\lambda_c \frac{\partial T}{\partial \boldsymbol{n}} = \alpha(T_M - T) \tag{3.5}$$

where $\boldsymbol{n}$ is normal to the boundary surface Γ, α is transfer or radiation coefficient (W/m^{2}K) and T_M is temperature of the media in which surface Γ of the solid Ω is exposed to, for instance the air temperature. In order to solve the problem by finite element method, Equations (3.4) and (3.5) have to be written in weak form. More details can be found in *Ožbolt et al.* (2005a) and *Ožbolt et al.* (2008).

3.4.3. Decomposition of strain tensor

As discussed in Section 3.3, the total strain tensor ε_{ij} due to stress in concrete subjected to high temperature is decomposed as:

$$\varepsilon_{ij} = \varepsilon_{ij}^m(T,\sigma) + \varepsilon_{ij}^{ft}(T) + \varepsilon_{ij}^{lits}(T,\sigma) \tag{3.6}$$

where ε_{ij}^m is the mechanical strain tensor, ε_{ij}^{ft} is the free thermal strain tensor, ε_{ij}^{lits} is the load-induced thermal strain tensor.

The mechanical strain in general can be decomposed into elastic, plastic and damage part. In the present model these strain components are obtained from the constitutive law (microplane model).

The free thermal strain is thus expressed as a function of temperature as follows (*Periškić*, 2009):

$$\dot{\varepsilon}_{ij}^{fts}(T) = \alpha \dot{T} \delta_{ij} \tag{3.7}$$

$$\alpha = \begin{cases} \dfrac{6.0 \times 10^{-5}}{7.0 - \theta}, & 0.0 \leq \theta \leq 6.0 \\ 0, & 6.0 < \theta \end{cases}$$

where $\theta = (T - T_0)/100$ °C.

45

Figure 3.14a shows a comparison of the free thermal strain as a function of temperature obtained experimentally and predicted by the model.

The LITS is a function of both stress level and temperature. In the present study, the model for LITS is taken according to *Periškić* (2009), which is based on experimental data from *Zhang and Bicanic* (2002) (see Figure 3.14b). LITS develops in the opposite direction of free thermal strain, therefore, it contributes significantly to the relaxation and redistribution of thermal stresses in concrete at elevated temperatures.

$$\dot{\varepsilon}_{ij}^{lits}(T,\sigma) = \frac{\sigma}{f_c^{20}} \beta \dot{T} \tag{3.8}$$

$$\beta = \begin{cases} 2A\theta + B & , & 0.0 \le \theta \le \theta^* = 4.5 \\ 2C(\theta - \theta^*) + 2A\theta^* + B, & \theta^* < \theta \end{cases}$$

where θ^* is a dimensionless transition temperature between the two expressions (470 ℃) and θ is calculated the same for Equation (3.7). These two expressions are introduced to account for abrupt change in behaviour detected in the experiments. Constants A, B and C are obtained experimentally and set as $A = 0.0005$, $B = 0.00125$ and $C = 0.0085$.

(a)   (b)
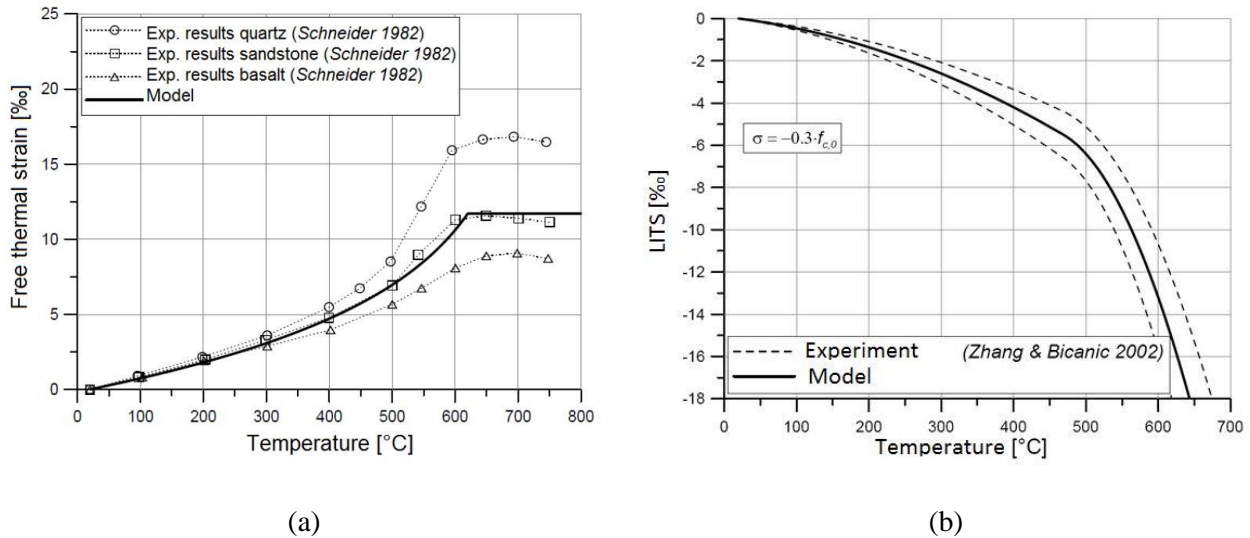
Figure 3.14 Comparison of (a) the free thermal stain and (b) the LITS in the experiment and model (*Periškić*, 2009).

3.4.4. Thermal-mechanical coupling

The mechanical properties of concrete are temperature dependent, which has been discussed in Section 3.2 from many aspects. In the present temperature dependent microplane model, the variation of the mechanical properties of material is realized by coupling the temperature profile through the transient thermal analysis, as presented in Section 3.4.2. The model for the temperature dependent mechanical properties, i.e. compressive strength, tensile strength, Young's modulus and fracture energy, are specified in the following.

In the nonlinear finite element analysis, the thermal and mechanical properties are defined for each time step Δt. In the present model, when studying the mechanical part of the problem, thermal properties are assumed to be constant and the opposite, when studying the thermal part the mechanical properties are constant.

Compressive strength

In the present model the compressive strength is assumed to be constant up to 300 ℃ considering discussions in Section 3.2.2. Thereafter, the compressive strength decreases linearly. The model is proposed by *Periškić* (2009):

$$f_c(T) = \max(\omega_{t,f_c}) f_c^{20} \tag{3.9}$$

$$\begin{cases} \omega_{t,f_c} = 1.0 & , \quad 0.0 \leq \theta \leq 2.8 \\ \omega_{t,f_c} = 1.43 - 0.153\theta, & 2.8 < \theta \end{cases}$$

where f_c^{20} is uniaxial compressive strength at $T = 20$ ℃; θ is calculated the same for Equation (3.7) and the same in the following.

Figure 3.15a shows a comparison of the experimental data and prediction by Equation (3.9).

Tensile strength

The tensile strength of concrete is considered to decrease linearly as per:

$$f_t(T) = \max(\omega_{t,f_t}) f_t^{20} \tag{3.10}$$

$$\omega_{t,f_t} = 1.0 - 0.13\theta$$

where f_t^{20} is uniaxial tensile strength at $T = 20$ ℃.

Figure 3.15b shows a comparison between the experimental data and the prediction by Equation (3.10).

(a)

(b)
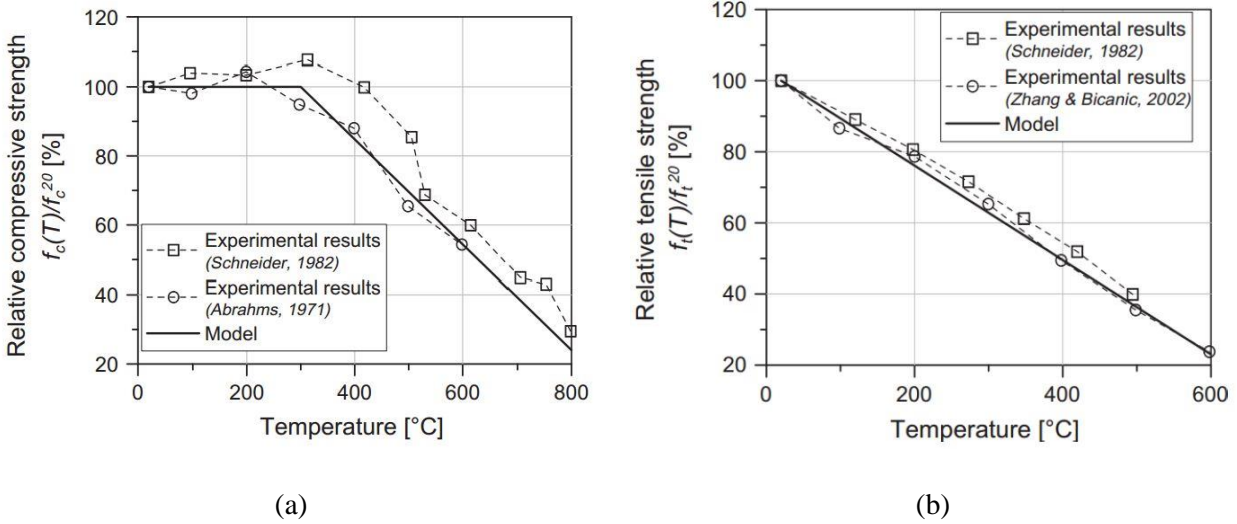
Figure 3.15 Comparison of experimental data and the model for (a) relative compressive strength and (b) relative tensile strength as a function of temperature (*Periškić*, 2009; *Ožbolt et al.*, 2014).

Young's modulus

Experimental data from *Schneider* (1982) about the influence of temperature on the Young's modulus of concrete showed a nonlinear relationship. In the present model, the Young's modulus as a function of temperature proposed by *Stabler* (2000) is applied as follows:

$$E(T) = \left(1 - \max\left(\omega_{t,E}\right)\right) E^{20} \tag{3.11}$$

$$\begin{cases} \omega_{t,E} = 0.2\theta - 0.01\theta^2, & 0.0 \leq \theta \leq 10 \\ \omega_{t,E} = 1, & 10 < \theta \end{cases}$$

where E^{20} is Young's modulus at ambient temperature $T = 20$ °C.

Figure 3.16a shows a comparison between the experimental data and the prediction by Equation (3.11).

Fracture energy

Based on data from *Zhang and Bicanic* (2002), the influence of temperature on fracture energy of concrete is taken according to *Perišklć* (2009):

$$G_F(T) = \max(\omega_{t,G_F}) \, G_F^{20} \tag{3.12}$$

$$\begin{cases} \omega_{t,G_F} = 1.0 + 0.407\theta - 0.07272\theta^2 \,, & 0.0 \leq \theta \leq 2.8 \\ \omega_{t,G_F} = 0.917 + 0.467\theta - 0.0833\theta^2, & 2.8 < \theta \end{cases}$$

where G_F^{20} is concrete fracture energy at ambient temperature $T = 20$ ℃.

Figure 3.16b shows a comparison between the experimental data and the prediction by Equation (3.12).

(a) (b)
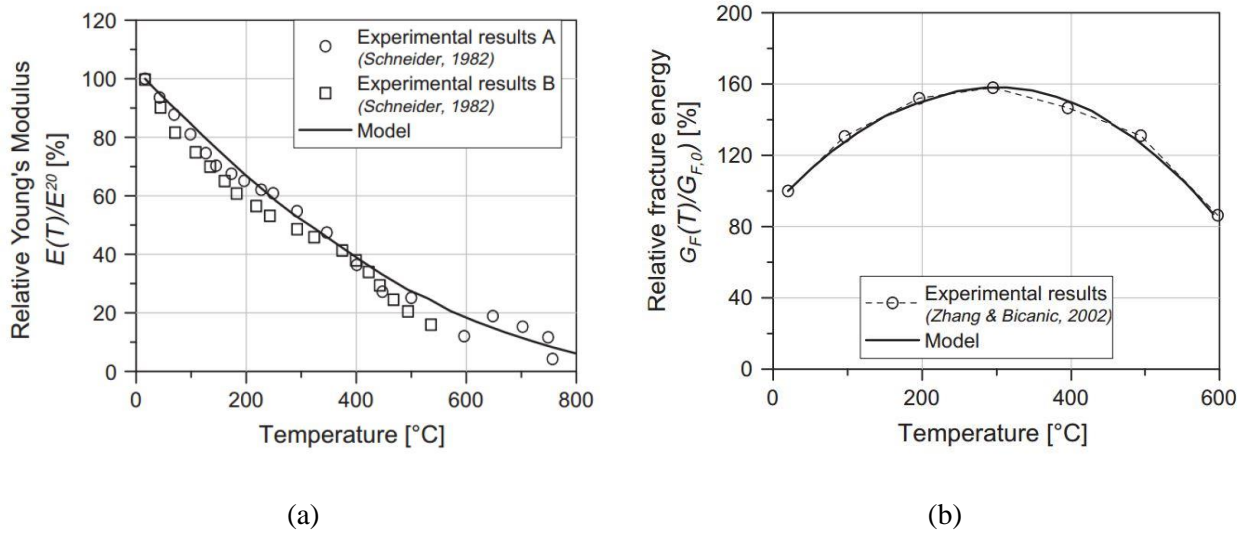
Figure 3.16 Comparison of experimental data and the model for (a) relative Young's modulus and (b) relative fracture energy of concrete as a function of temperature (*Perišklć*, 2009; *Ožbolt et al.*, 2014).

3.5. Temperature dependent steel model

In the hot state, the strength of steel degrades pronouncedly with increasing temperature (*Kordina and Meyer-Ottens*, 1981). According to *Harmathy* (1993), at 650 ℃ only 20% and 10% of original strength is left for hot-rolled and cold-drawn steel, respectively. In the model the reduction of Young's modulus and yield strength is accounted for as plotted in Figure 3.17.

(a)   (b)
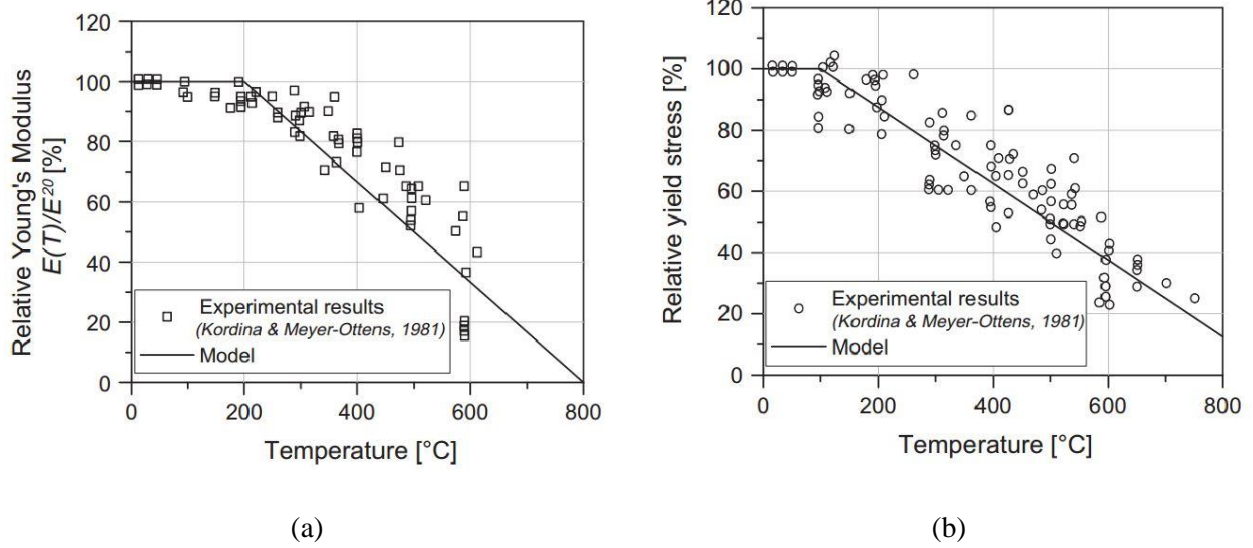
Figure 3.17 Comparison of experimental data and the model for (a) relative Young's modulus and (b) relative yield strength of steel as a function of temperature in the hot state (*Ožbolt et al.*, 2014).

Studies on the residual strength of steel after cooling show that, unlike concrete, steel can recover its yield strength depending on the type of steel (*Takeuchi et al.*, 1993; *Felicetti and Meda*, 2005). (*Felicetti and Meda*, 2005) showed that the residual strength of deformed bars are up to 550 ℃ almost completely recovered. Furthermore, the residual Young's modulus of steel is equal to the value of virgin steel. Figure 3.18 shows the recovery of the yield stress of steel as implemented in the model.
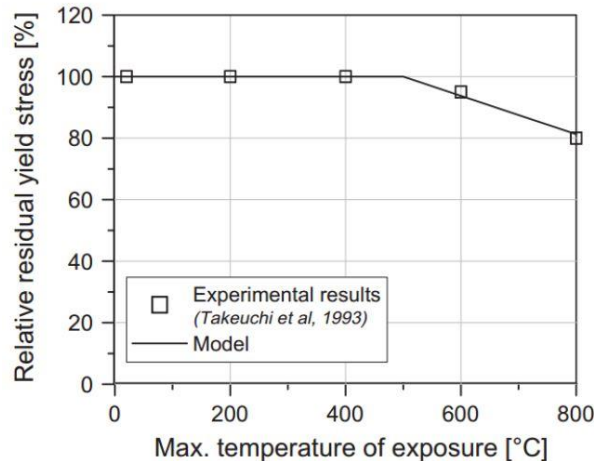
Figure 3.18 Comparison of experimental data and the model for relative residual yield strength of steel as a function of temperature in the cold state (*Ožbolt et al.*, 2014).

50

4. PRELIMINARY EXPERIMENTAL AND NUMERICAL STUDY FOR CONCRETE EDGE FAILURE UNDER FIRE

4.1. Scope

Very scarce experimental and numerical data exists on the shear resistance of anchors after fire. In this experimental program, the anchors were installed close to the edges of concrete slabs and were tested in the furnace immediately after heating (without cooling), i.e. in the hot state. The residual capacities of anchors were also tested after cooling down the concrete slabs, i.e. in the cold state, to compare with the resistance in the hot state. Considering that the fire tests are costly and time-consuming, the main aim of the test program was to obtain representative shear resistances of single anchors for the hot state. Only 90 min of fire duration was adopted to perform the fire test, considering in the current code 90 min and 120 min of fire are covered (*European Committee for Standardization*, 2018). The results of the tests are later used to verify the numerical model. After the validation of the model, further numerical studies were conducted and results were compared with the code. The experimental and numerical work has also been described in *Tian et al.* (2018).

4.2. Anchors

The experimentally tested fastener consists of a headed stud, a steel plate and a nut (see Figure 4.1). The dimensions of the headed studs were taken according to ISO 13918 (*International Organization for Standardization*, 2008). Three different edge distances ($c_1 = 50$ mm, 100 mm and 150 mm), two anchor diameters ($d = 16$ mm and 25 mm) and two embedment depths ($h_{ef} = 45$ mm and 95 mm) were investigated. The furnace temperature is over 1000 ℃ after heating up to 90 min according to ISO 834 fire. Normally used structural steel begins to soften around 420 ℃ and loses 90% of its initial strength above 800 ℃ (*European Committee for Standardization*, 2005a). Therefore, the special high-temperature resistant steel 1.4828 according to EN 10095 (*European Committee for Standardization*, 1999) was used to prevent steel failure in the fire tests carried out at high temperature. The mechanical and thermal properties of steel 1.4828 are summarized in Table 4.1. Other anchors, tested after cooling (the cold state), were made of standard structural steel S235J2.

51
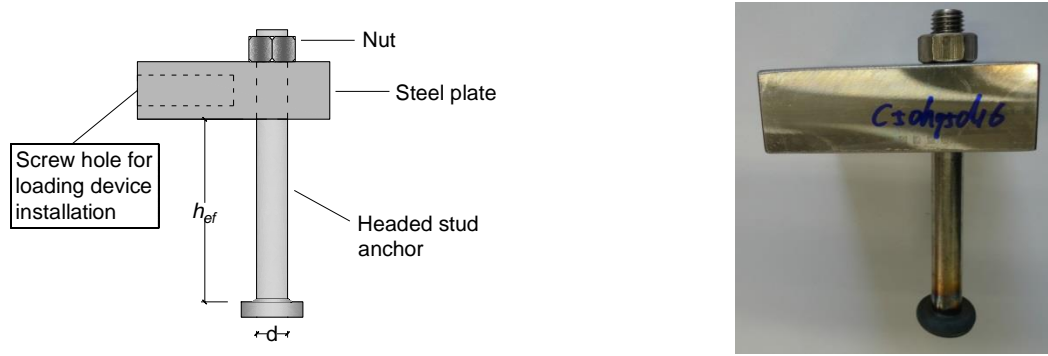
Figure 4.1 Headed stud anchor and steel plate.

4.3.   Concrete specimens

It is known that high strength concrete is more prone to explosive spalling at high temperatures than normal strength concrete (*Khoury*, 2000; *Ali et al.*, 2011). One of the main reasons for concrete spalling is the build-up of pore pressure in concrete. Low-grade concrete has higher water to cement ratio, porosity and permeability than that of high strength concrete, which means more connected pores and vaporizable free water. Therefore, the built-up vapour pressure can be relieved and the concrete is less sensible to high temperature spalling (*Kalifa et al.*, 2000; *Mindeguia et al.*, 2010; *Ju et al.*, 2017). In order to assure concrete failure and to prevent explosive spalling, in the tests the low quality concrete (C12/15, Eurocode 2) was used. The water/cement ratio of the concrete was 0.80 (EN 206-1 (*European Committee for Standardization*, 2013b) and DIN 1045-2 (*DIN Deutsches Institute für Normung*, 2008b)). After casting of concrete members the specimens were kept at room temperature for three months to let the moisture inside the concrete to evaporate as much as possible. The mechanical and thermal properties of concrete are summarized in Table 4.1. The compressive strength and density were tested according to European standards EN 12390-3 (*European Committee for Standardization*, 2009b) and EN 12390-7 (*European Committee for Standardization*, 2009c), respectively. The

Table 4.1 Material properties

Material	Young's modulus E (GPa)	Poisson's ratio v_c	Uniaxial compressive strength f_{cm} (MPa)	Tensile strength f_{ctm} (MPa)	Fracture energy G_F (J/m^2)	Heat conductivity λ_c (W/mK)	Heat capacity c_p (J/kgK)	Weight density ρ (kg/m^3)
Concrete C12/15	27	0.18	12	1.6	30	1.33	900	2300
Steel 1.4828	200	0.33	-	550-750	-	18.00	500	7900
Protection board	1.2	0.18	2.4	3.1	10	0.083	0.95	450

other properties were taken in accordance with Eurocode 2 (*European Committee for Standardization*, 2011; *European Committee for Standardization*, 2004a).

Figure 4.2 shows schematically the fire exposure on the concrete edge from the top and front sides, and also the shear loading direction. As shown in Figure 4.2a the front face was insulated by a fire protection board to assure one side fire only, i.e. heating on the top side of the concrete member. The material properties of the protection board, which were provided by the manufacturer, are listed in Table 4.1. In Figure 4.2b the specimen was exposed to fire on two sides of the concrete edge. In order to apply the load in the hot state after 90 min of fire exposure, the specimen was designed as shown in Figure 4.2c. The top slab (L1 $\times$ W1 $\times$ H1 = 2900 $\times$ 600 $\times$ 210 mm) and the vertical concrete slab (L2 $\times$ W2 $\times$ H2 = 1850 $\times$ 300 $\times$ 690 mm) were partly connected, i.e. there are two openings at the top of the vertical slab. Note that these two slabs were cast simultaneously with the same concrete class and they were connected by steel bars inside the concrete material. The length of the openings on top of the anchors A and B was 5 times the edge distance of respective anchors, and they were designed according to the guideline for approval tests for the use of anchors in concrete (*European Organisation for Technical Approvals*, 2012). The two ends of the top slab were then put on the furnace wall and were supported inside the furnace. The top slab served as a part of the roof of the furnace. In this way, anchors A and B (see Figure 4.2c) could be loaded in shear in vertical direction, perpendicular to the free edge, over the steel rod connecting to the loading setup on top of the specimen (outside of the furnace).
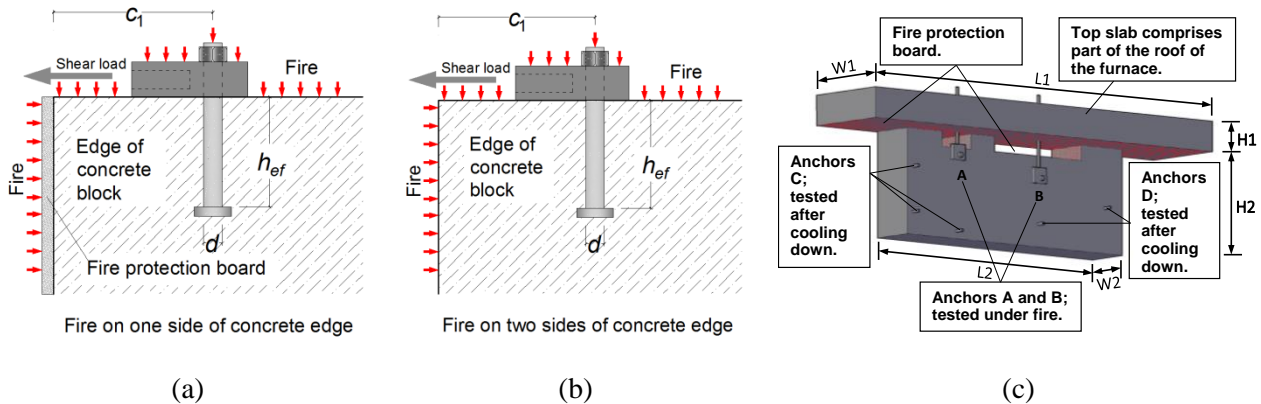
Figure 4.2 Applied fire and loading for: (a) fire on one side of concrete edge, (b) fire on two sides of concrete edge and (c) concrete specimen.

Along the bottom and sides of the vertical concrete member, additional anchors C and D, which have the same edge distance c_1, embedment depth h_{ef} and diameter d as anchors A and B, respectively, were cast in (see Figure 4.2c). These anchors were always exposed to fire on two sides and loaded in shear towards free edge after cooling down the specimen (i.e. cold state). In total 12 specimens (Figure 4.2c) were made and all tested configurations of anchors are

summarized in Table 4.2. For each of them, at least three tests were repeated to get the representative result of the experimental test. Reference tests at ambient conditions were also conducted for the relevant anchors (see Table 4.2) installed in one concrete slab with dimension of $1500 \times 1500 \times 300$ mm (length $\times$ width $\times$ thickness). For each reference test configuration in Table 4.2, two tests were repeated to compare with results obtained according to Eurocode 2. Note that for the shear loading after cooling and the reference tests, the support span was kept as 5 times of the edge distance of the corresponding anchor.

Table 4.2 Anchorage configuration

Embedment depth	Diameter	Fire effect		Edge distance	
Fire tests under 90 min ISO834						
95	16	One side	50	100	-
95	16	Two sides	50	100	-
95	25	One side	50	-	150
95	25	Two sides	-	-	150
45	25	One side	150	-	
Reference tests at room temperature						
95	16	-	50	-	-
95	25	-	50	-	150
45	25	-	150	-	-

To obtain the thermal profile around the anchorage, the time-temperature response was monitored by using Type-K thermocouples with ± 1.5 °C tolerance up to 1000 °C. Figure 4.3 shows the positions of thermocouples, which were embedded at various positions inside the concrete specimen. The thermocouples were fixed using thin steel wire. For each anchor configuration the temperature profile was measured twice.
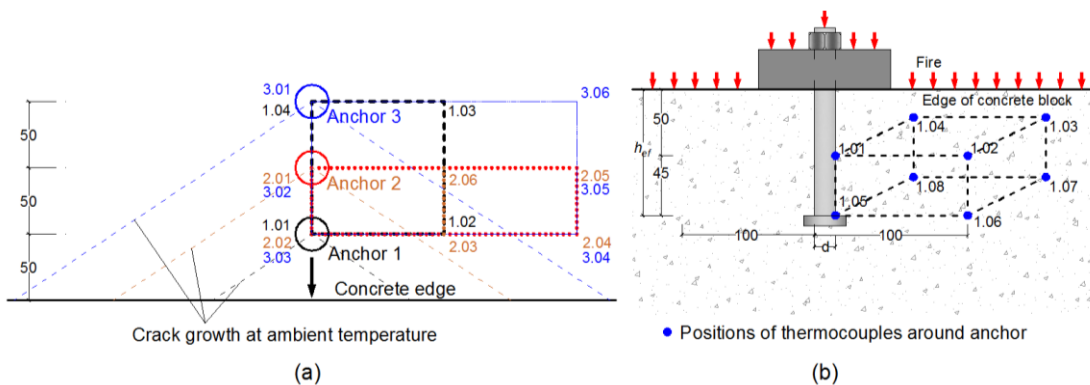
Figure 4.3 Thermocouples layout (measures is mm).

4.4. Test procedure

The tests were conducted at the fire safety laboratory (Material Testing Institute, MPA), University of Stuttgart. The concrete specimens were first placed along the wall of the furnace, as shown in Figure 4.4a. Subsequently, the steel plate and steel rod were installed (see Figure 4.4b). The thermocouples for monitoring the furnace temperature and for recording the temperature field inside the concrete were connected to the respective data logger. On top of the specimen the loading setups were then placed for each anchor to be tested in the hot state. The anchors were loaded by using hydraulic cylinders. Finally, the middle section of the furnace was closed with additional fire resistant covers.

(a)   (b)

Figure 4.4 (a) Specimen layout and (b) anchor connection for shear loading in hot state.

According to EN 1990 (*European Committee for Standardization*, 2002) and the Technical Specification (*European Committee for Standardization*, 2009a), the calculated design load for the anchors: c50h95d16 ($c_1 = 50$ mm, $h_{ef} = 95$ mm and $d = 16$ mm), c50h95d25, c100h95d16, c150h45d25 and c150h95d25 were 3.08 kN, 3.38 kN, 7.42 kN, 11.81 kN and 13.48 kN, respectively. Before the fire exposure, the anchors were preloaded with these loads. Note that for the tests in cold state the anchors were not preloaded.

The fire tests were carried out according to ISO 834 (*International Organization for Standardization*, 1999), with fire duration of 90 min. After 90 min heating the temperature was kept constant and the anchors were loaded in the hot state up to failure. The recorded temperature history in the furnace and around the anchors (thermocouple positions are shown in Figure 4.3 as an example) is shown in Figure 4.5. As can be seen, the temperature was well controlled and within the allowable range according to EN 1363-1 (*European Committee for Standardization*,

2012). After all of the relevant anchors were loaded and results were recorded, the burners were all shut off. The specimens were cooled down to the ambient temperature naturally.
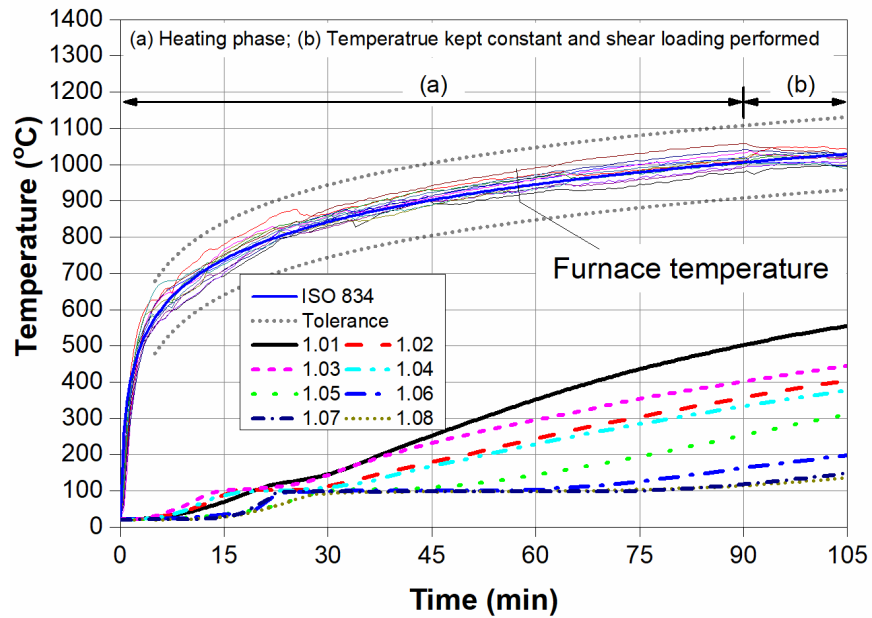
Figure 4.5 Temperature rise in the furnace and around the anchor.

The residual capacities of anchors (post-fire tests) along other edges of the specimens were then tested at ambient temperature (the cold state) in the laboratory. As shown in Figure 4.6, hydraulic cylinders were used for loading the anchors. The applied load was monitored by the load cells.
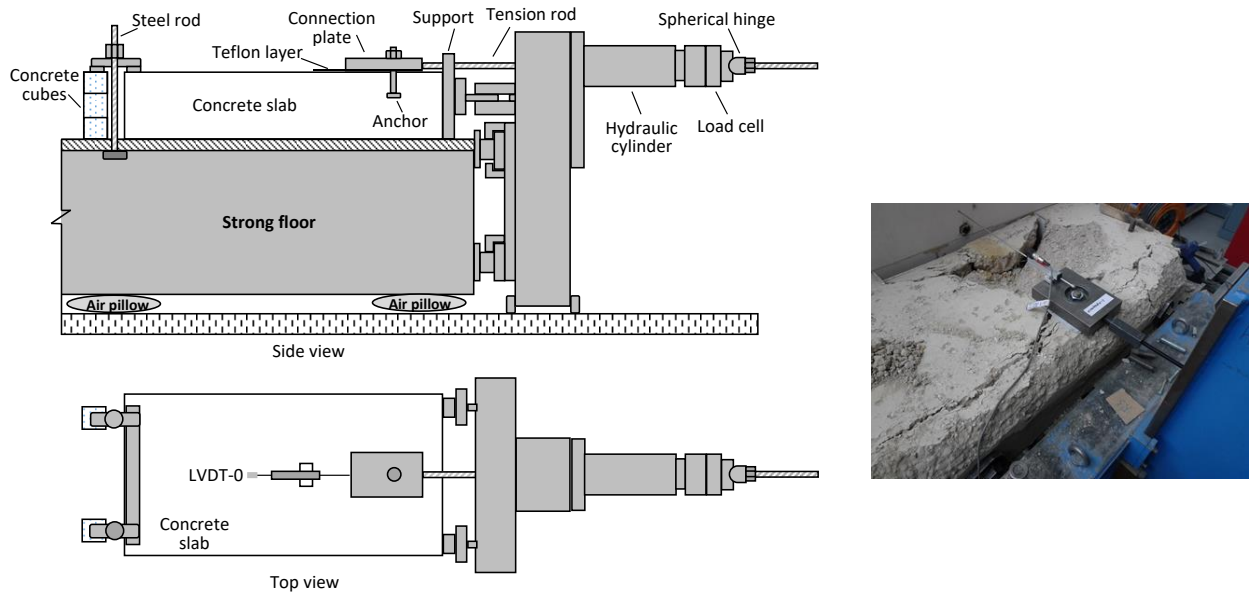
Figure 4.6 Detail of the test setup in the laboratory.

56

4.5. Experimental results

4.5.1. Fracture pattern

During the 90 min of heating, no explosive spalling of concrete was observed. After cooling down to the ambient temperature, the concrete specimens were severely damaged, as can be seen from Figure 4.7. The failure of anchors loaded in the hot state resulting in the typical concrete edge failure. Damage at the rear side of the anchor was also observed. The concrete member was damaged along other free edges, especially at the bottom edge. For anchors with edge distance $c_1 = 50$ mm (c50h95d16 and c50h95d25) and $c_1 = 150$ mm (c150h45d25 and c150h95d25), the failure pattern under fire (hot state) was mainly a semi-conical failure of concrete edge (see Figure 4.8). The cracks started to propagate at an angle of approximately 30° with respect to free edge and propagated towards the corner of the openings. The concrete edge failure was observed in all tested anchor configurations except one type of anchor with concrete edge distance of 100 mm and diameter of 16 mm (2c100h95d16, hot state), which failed in a mixed mode of concrete edge failure and yielding of anchor shaft (see Figure 4.9). In this case the cracks started at an angle of around 20° with respect to free edge. The results of experimental tests indicated that if the edge distance is larger or equal to 100 mm and duration of fire is 90 min, the diameter of the anchor should be greater than 16 mm. For all anchors the failure depth at the front face of the edge developed to about 1.5 to 2 times of the edge distance.

Figure 4.7 Specimen after fire exposure up to 90 min.
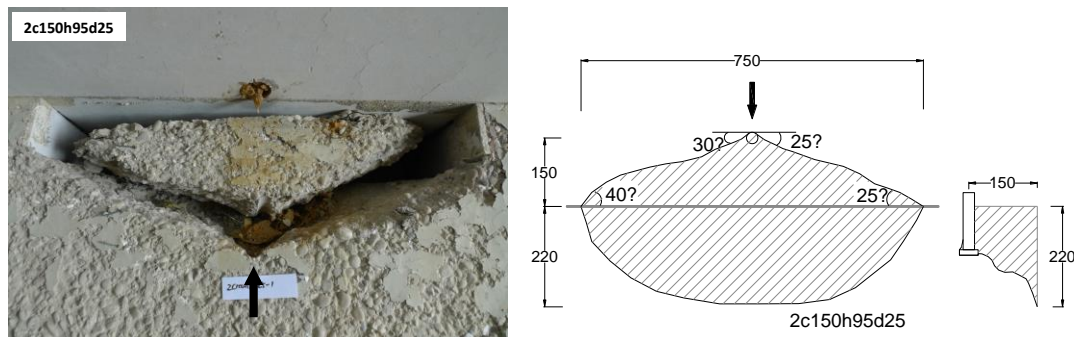
Figure 4.8 Failure pattern of c150h95d25 tested under 90 min of fire (hot state).

57
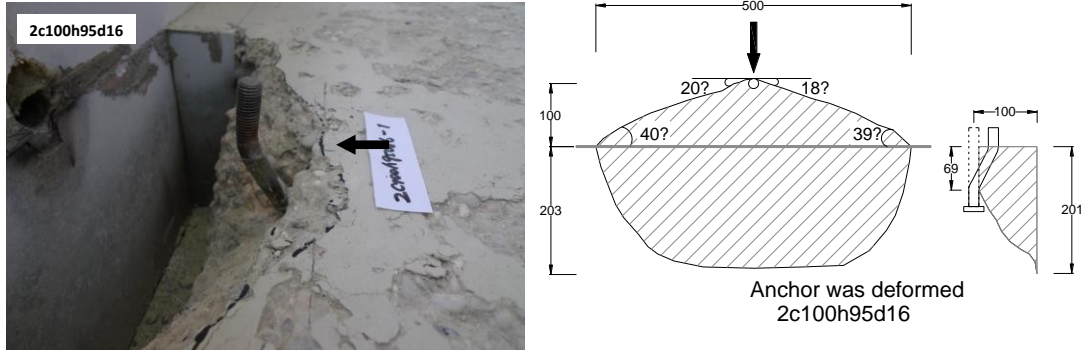
Figure 4.9 Failure pattern of c100h95d16 tested under 90 min of fire (hot state).
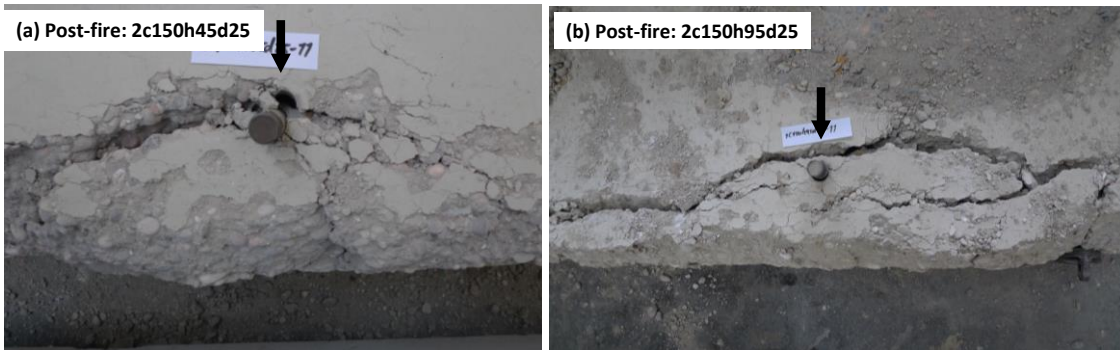
Figure 4.10 Failure pattern of 2c150h45d25 and 2c150h95d25 tested after cooling of 90 min fire exposure (cold state).

Figure 4.10 shows the failure modes of post-fire tests in the cold state ("2" in front of the anchor name indicates heating from both sides of the concrete member). Compared to the half cone failure pattern of reference test at ambient temperature, the fractures in the cold state are more randomly distributed. In all cases the failure was due to the failure of concrete, and no yielding of steel was observed.

4.5.2. Load-displacement behaviour

Because of technical reasons the load-displacement curves were not measured in the hot state. Figure 4.11 shows typically measured load-displacement curves at ambient temperature (reference) and after 90 min of fire (cold state). It can be seen that for all anchor diameters and edge distances the anchors after exposing to fire show significant reduction of stiffness and resistance.

(a)

(b)
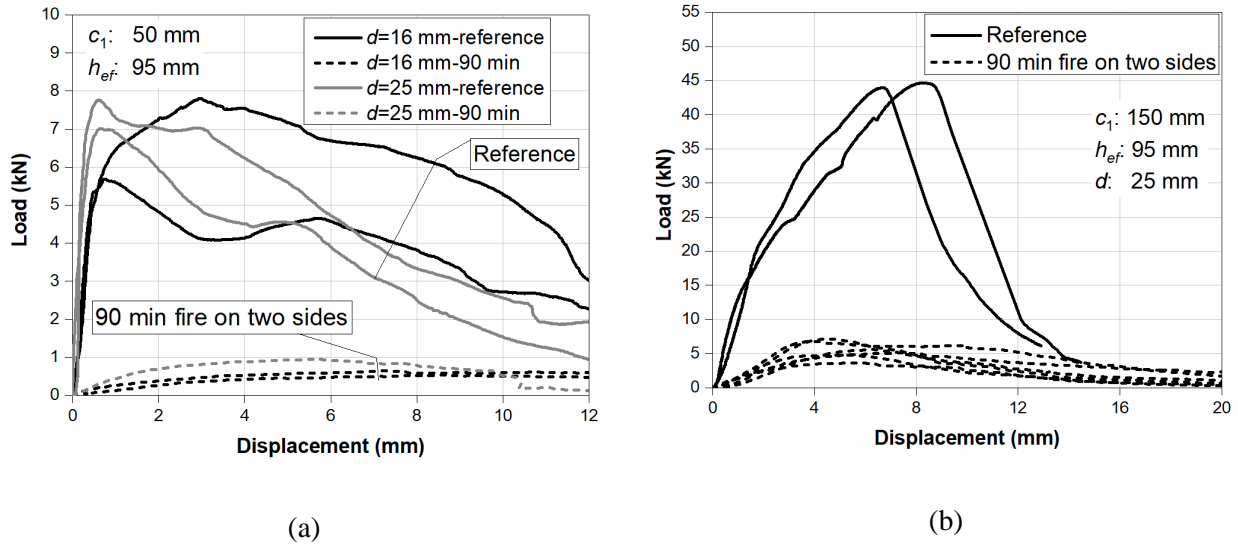
Figure 4.11 Load-displacement curves of reference tests and post-fire tests: (a) c50h95d16 and c50h95d25 and (b) c150h95d25.

Figure 4.12 shows load-displacement curves of anchors tested after cooling with different diameters and different edge distances. From Figure 4.12a it can be seen that the anchors with larger diameter behaves obviously stiffer than the anchor with smaller diameter after 90 min of fire exposure. In Figure 4.12b the influence of edge distance on the load-displacement curve is shown. As expected, with increase of edge distance the load-bearing response is much stiffer. However, the scattering of measured curves is increasing with the increase of edge distance. This is mainly due to the different extent of cracks and damage of the concrete member close to the edge after cooling.

(a)

(b)
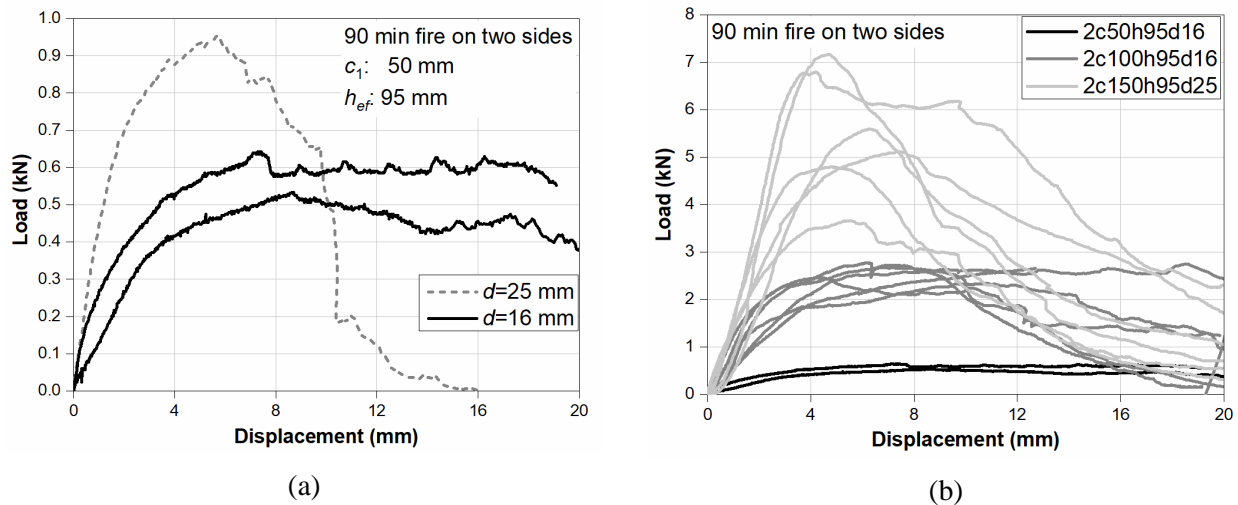
Figure 4.12 Load-displacement curves from post-fire tests: (a) effect of diameter and (b) effect of concrete edge distance.

The influence of the embedment depth on the load-displacement curves of anchors after cooling is shown in Figure 4.13. It can be seen that larger embedment depth results in stiffer response, however, the scatter is larger than that if the embedment depth is smaller. This may due to that the deeper inside the concrete the less thermal damage is induced.
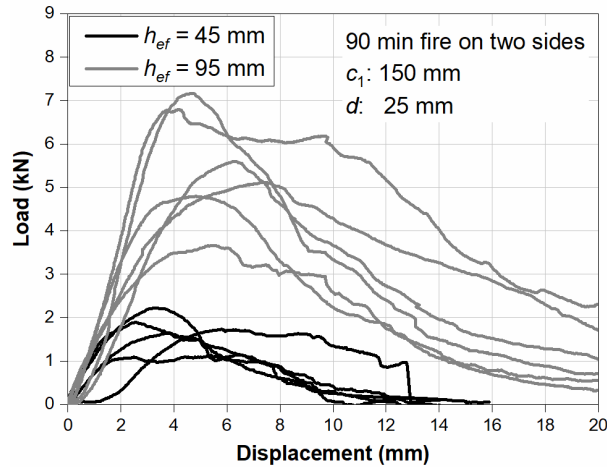
Figure 4.13 Load-displacement curves of anchors with different embedment depths.

4.5.3. Peak load

The peak loads from reference tests at ambient temperature, tests after 90 min of fire (hot state) and post-fire tests after cooling down (cold state) are summarized in Annex A Table A.1 . The corresponding displacements at peak loads and failure modes are also indicated.

(a)

(b)
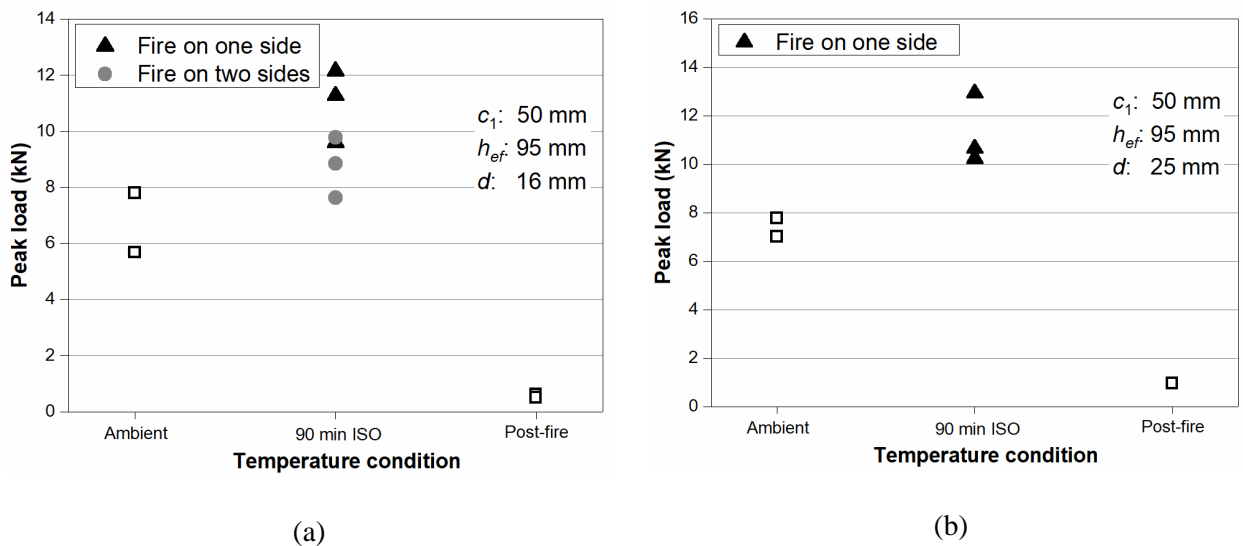
Figure 4.14 Resistance under fire load for anchor configurations: (a) c50h95d16 and (b) c50h95d25

Figure 4.14 shows the resistance as a function of temperature for the anchors with the smallest edge distances of 50 mm for two different diameters (i.e. c50h95d16 and c50h95d25). The results are unexpected, i.e. it can be seen that compared with the reference resistance the resistance of anchors with edge distance of 50 mm in the hot state increased 63% and 30% for fire exposure on one side and two sides, respectively (see Figure 4.14a). The load capacity of anchor exposed to fire on one side is 26% higher than that under two sides of fire exposure. Similar increase of load capacity was observed for the anchor c50h95d25 (see Figure 4.14b). However, after cooling the specimens, the load carrying capacities of anchors exposed to fire on two sides were reduced to only 8% ($d = 16$ mm) and 13% ($d = 25$ mm) of the corresponding reference resistances at ambient temperature.
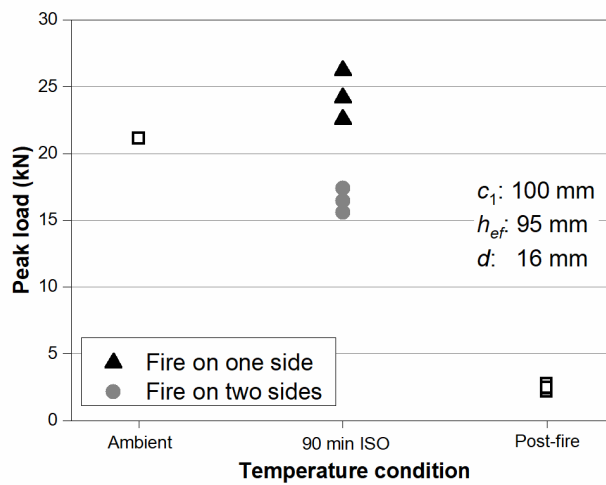
Figure 4.15 Resistance under fire load for anchor configuration c100h95d16.

(a)   (b)
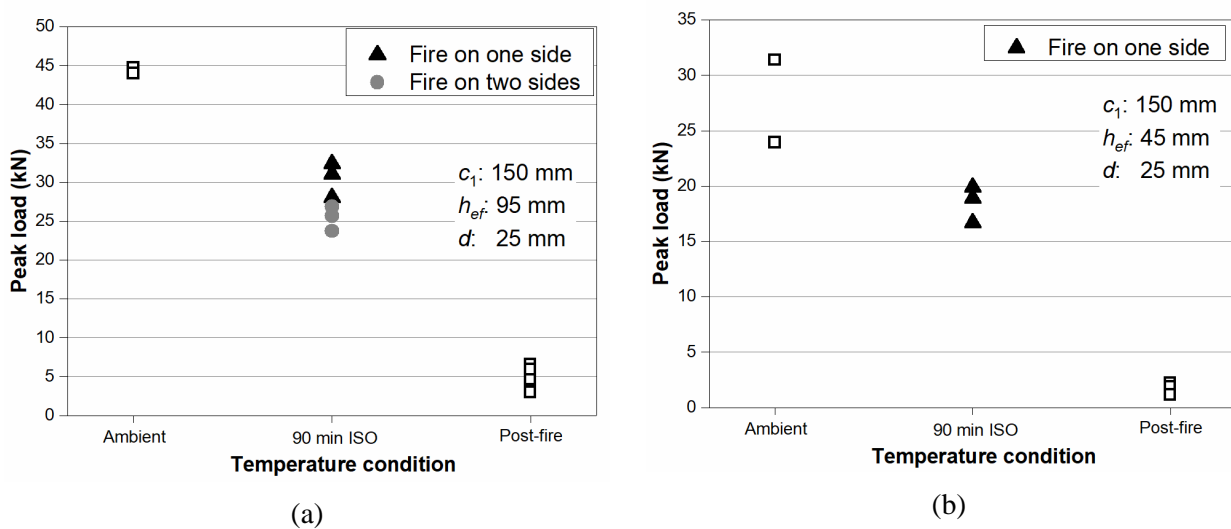
Figure 4.16 Resistance under fire load for anchor configurations: (a) c150h95d25 and (b) c150h45d25.

61

In Figure 4.15 and Figure 4.16 the results are shown for the edge distances $c_1 = 100$ mm and 150 mm, respectively. Unlike the anchors with the smallest edge distance of 50 mm, by increasing the edge distances to 100 mm and 150 mm, the load carrying capacity for the hot state decreases compared to the corresponding reference resistance. By comparing Figure 4.16a and b, it seems the peak load in the hot state is reduced for concrete edge distance of 150 mm regardless of the embedment depth. The resistance in the cold state is significantly reduced compared to the reference resistance, which happens the same as for $c_1 = 50$ mm.

The resistance shown in Figure 4.14 to Figure 4.16 are normalized to the uniaxial compressive strength of 14.61 MPa, based on the square root function. From the Figures it is obvious that the anchors with relatively small edge distance in hot state have the resistance that is even higher than the reference resistance at ambient temperature. As already mentioned above, this is unexpected since the concrete after 90 min of heating is damaged, and the resistance of anchors should be reduced compared to the reference resistance. As confirmed through numerical analysis, the increase of the peak load under fire ($c_1 = 50$ mm), or only moderate decrease ($c_1 = 100$ mm), is due to the confinement effect. Namely, since the top of the concrete slab (see Figure 4.2c) was not exposed to fire, relatively large temperature induced compressive stresses parallel to the free concrete edge were generated. These stresses considerably increased the shear resistance of anchors with small edge distance loaded in the hot state. Further away from the free edge the anchor is located, the weaker is the effect of the temperature induced confinement stress. This will be discussed below in the framework of numerical analysis. It is worth noting that in practical engineering there are frequently some confinement effects, for example at positions of a structure curved or grooved concrete edges exist, which should be taken into account in the fire safety design of anchors.
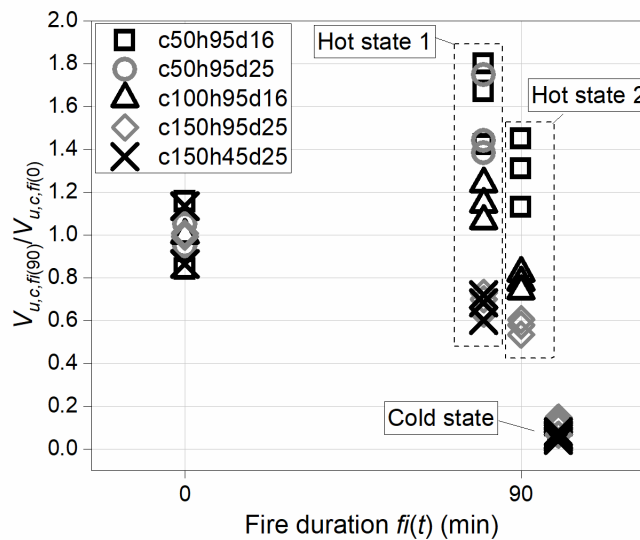
Figure 4.17 Relative resistance of anchors after fire exposure in the hot and cold state.

In contrast to the hot state, in the cold state the resistance in comparison to the reference resistance is strongly reduced for all edge distances (see Figure 4.17). On average, for all anchors only 10% of the reference resistance remained. Due to the cooling process the confinement stresses are released. Because of the inhomogeneity of the temperature field (e.g. surface of the concrete cools faster than the concrete inside the slab), through the cooling process additional damage of concrete can be generated. The damage after cooling can even be more severe if in the hot state the confinement effect is strong.

4.5.4. Summary

In the experimental program a fire test for 90 min of ISO 834 fire was performed on anchors failing in shear. The concrete specimens and anchorage configurations were designed so that the anchors could be loaded in shear towards the free edge in the hot state immediately after 90 min of fire. It is found that for the resistance in the hot state, the anchors with small edge distance of 50 mm exhibits increased resistance compared to the reference resistance at ambient temperature. This is due to the confining effect of the non-heated side of the slab. With larger edge distance (100 and 150 mm), due to the reduced confinement effect it is found that the resistance in the hot state decreases compared to the reference resistance value.

After cooling from 90 min of ISO 834 heating, about 10% on average of the reference resistance is remained for all tested anchors.

As illustrated in Figure 4.17, the present experimental results clearly show that for the resistance of anchors, which fail due to the concrete edge failure rather than the steel failure, the cold state resistance is relevant. The concrete edge exposed to fire on two sides has relatively lower resistance than that exposed to fire only on one side. Therefore, more attention should be devoted to the cold state resistance. As will be discussed later, these experimental results are also confirmed through numerical simulations.

4.6. Verification of numerical model

The experimental tests are numerically simulated by using 3D FE code MASA (*Ožbolt*, 1998). As the constitutive law for concrete, the thermo-mechanical microplane model is used (*Ožbolt et al.*, 2005a). The analysis is carried out in order to verify and calibrate the model and to better understand the behaviour of fasteners exposed to high temperature.

4.6.1. Discretization

The finite element discretization (see Figure 4.18) is performed according to the geometry and boundary conditions from the experimental tests by employing 4-node constant strain solid finite

elements. The connection between steel and concrete is performed by using contact elements that can transfer only compressive contact forces. To assure mesh size independent results, the regularisation based on the crack band method is used (*Bažant and Oh*, 1983). The properties of concrete and steel employed in the analysis are the same as specified in Table 4.1. The temperature dependent thermal properties of concrete and steel are taken according to Eurocode 2 EN 1992-1-2: Part 1-2 (*European Committee for Standardization*, 2004a). Since the aim of the analysis was to investigate the failure of concrete, the behaviour of steel was assumed to be linear elastic.

Figure 4.18a shows the finite element discretization for modelling single headed stud anchors loaded in the hot state after 90 min of fire exposure towards the free edge. The geometry of the model is exactly the same as the corresponding anchor configuration in the experiment. Figure 4.18b shows the finite element discretization for modelling the concrete edge failure resistance at ambient temperature as reference and also the resistance in the cold state.

(a)   (b)
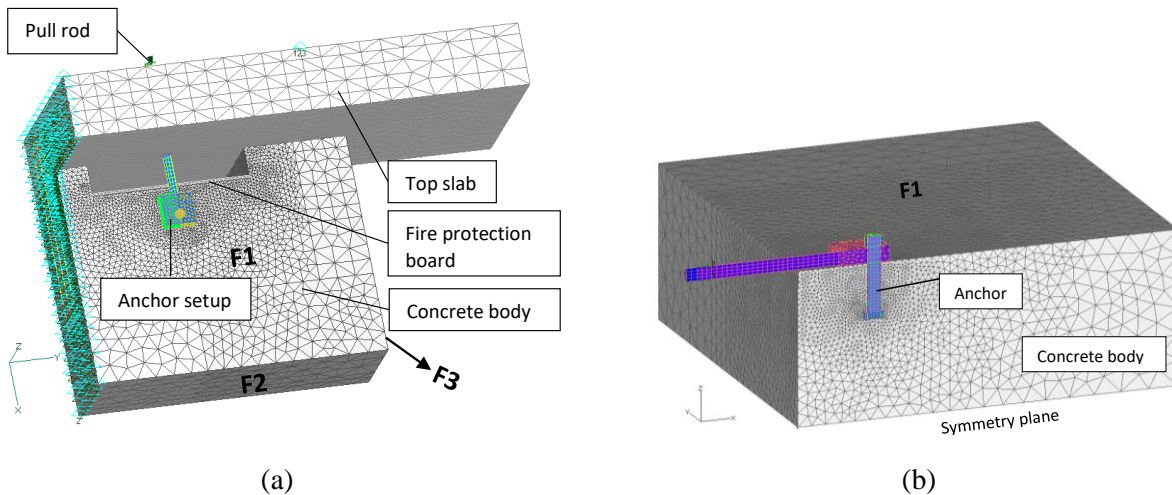
Figure 4.18 (a) Finite element discretization for validation of the experiment at 90 min of fire and (b) simulation of anchors in the cold state.

4.6.2. Temperature profile

The concrete surfaces (F1, F2 and F3 in Figure 4.18a), including the front face of the edge if fire exposure on two sides, were heated by applying heat flux of 28 W m^{-2} on the outer (exposed) faces of finite elements and temperature values according to ISO 834 fire curve on the surface nodes. The heating interval was set as 1 min per step up to 90 min of heating, followed by a linear cooling to ambient temperature (20 °C) with the same interval that was lasted for 120 min. The typical temperature history curves obtained from the experiment and the finite element analysis for anchors are shown in Figure 4.19. It can be seen that the FE model reasonably well predicts temperature profile of concrete subjected to one and two sides of fire (see Figure 4.19a).

Figure 4.19b and c show the temperature field in concrete for anchors 2c50h95d16 and 2c150h95d25 for 90 min of heating according to ISO 834, respectively. It is obvious that the anchor with relatively large edge distance of 150 mm and the surrounding area of its head are still out of the heat penetration at the time when the maximum environmental temperature has already reached. In contrast, the anchor with small edge distance of 50 mm is fully located in the heat penetration area. This will result in a much higher resistance for anchor with large edge distance.
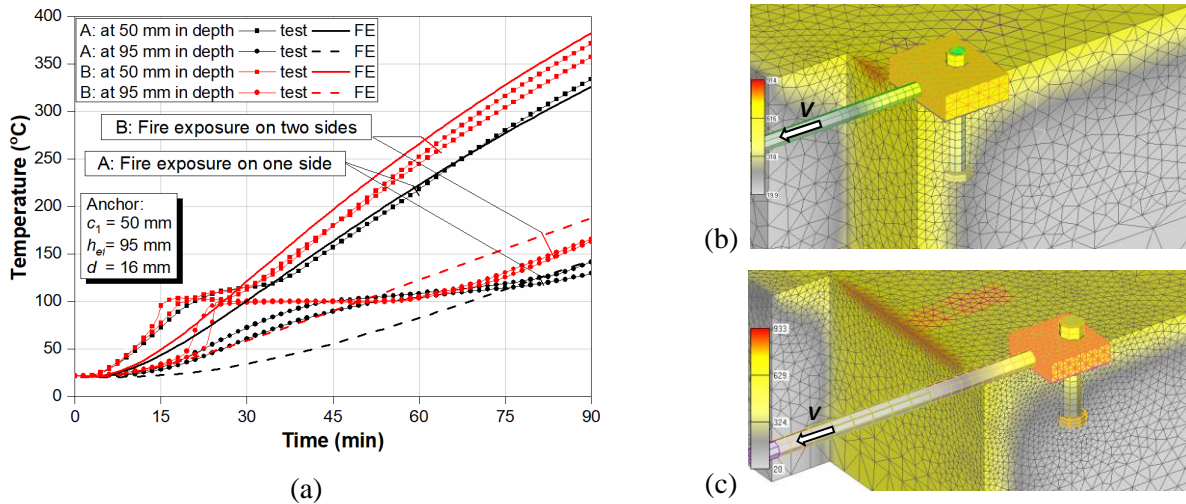
Figure 4.19 (a) Temperature rise around anchor c50h95d16 in concrete; Temperature field for anchor (b) 2c50h95d16 and (c) 2c150h95d25 for fire exposure of 90 min.

4.6.3. Load-displacement behaviour and crack development

Figure 4.20a shows typical numerically predicted and experimentally measured load-displacement curves for the reference tests at ambient temperature. The numerical results are obtained by employing the 3D FE discretization shown in Figure 4.18b. As can be seen, the numerically predicted and experimentally measured peak loads are in good agreement, however, the numerical analysis shows stiffer response, i.e. the peak load is reached at lower displacement. This can be attributed to the local damage of concrete, which cannot be accounted for in the macroscopic finite element analysis. The typical crack patterns obtained experimentally and numerically are shown in Figure 4.20b and they are very similar indeed.

(a)

(b)
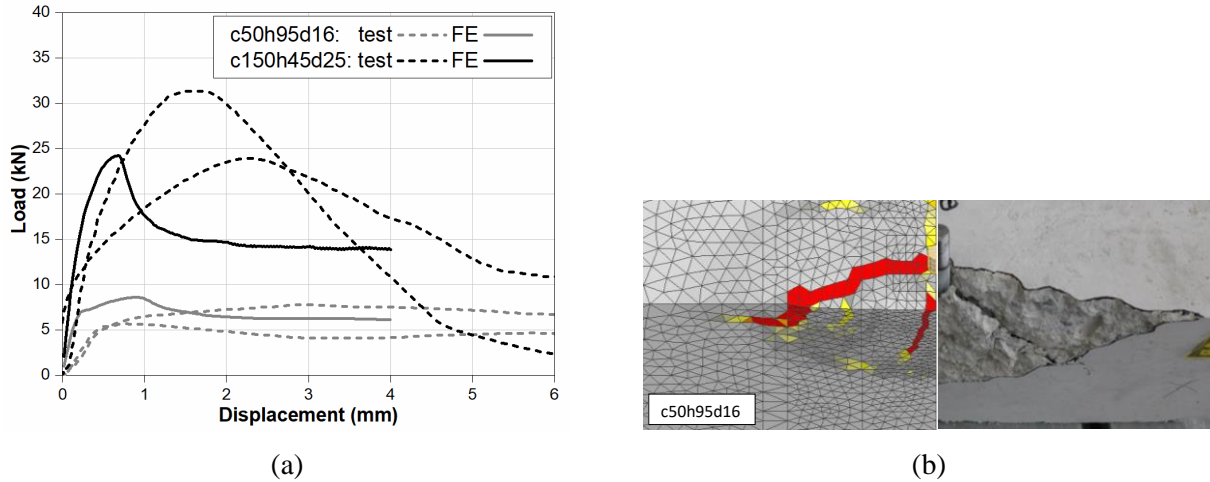
Figure 4.20 (a) Load-displacement curves, experiment vs. FE analysis and (b) predicted and observed failure modes (ambient temperature).
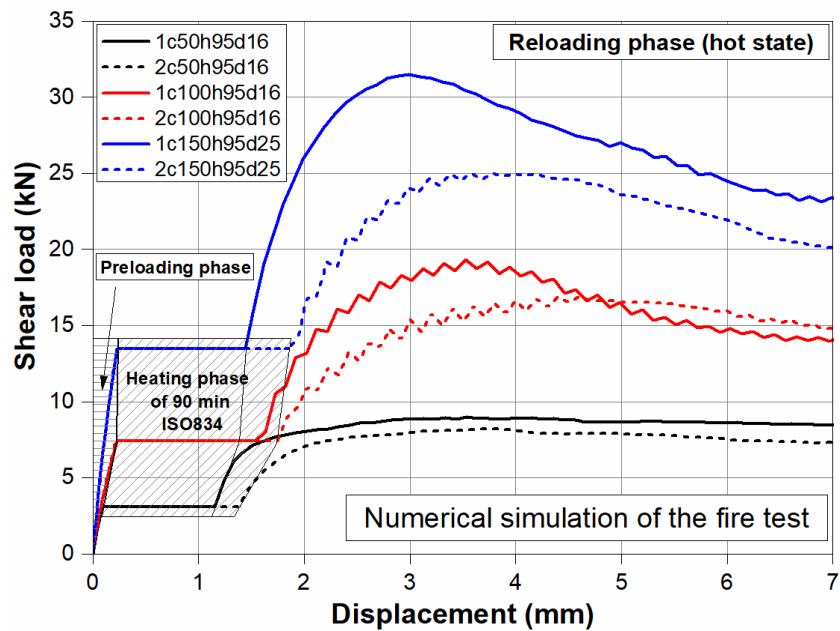
Figure 4.21 Typical load-displacement curves for hot state loading ("1" and "2" in front of the anchor name indicates fire on one side and two sides of the concrete edge, respectively).

The simulation of the shear failure in the hot state is performed using the finite element discretization shown in Figure 4.18a. The loading procedure is exactly the same as in the experimental test. Firstly, the anchor was preloaded to design load and keep constant, then heating was conducted until 90 min and following the cooling phase. Afterwards the anchors were loaded until failure. The typical numerically predicted load-displacement curves for anchors loaded in the hot state are shown in Figure 4.21. As mentioned above, these curves were not

66

measured in the experiments. It can be seen that during fire exposure of 90 min the displacements increase due to the thermally induced strains and damage of concrete. After the reloading phase, it can be seen that the fire load from two sides yields stronger reduction of resistance. The numerical model can realistically simulate the phases in the fire test.

The typical temperature induced damage of concrete and failure mode obtained numerically and observed in experiments are shown in Figure 4.22. It is shown that not only the computed cracks around the anchor due to shear loading agree well with the experimental measurement, but also the thermal cracks due to heating at the right down side of the specimen nicely correlate. Both numerically and experimentally, the cracks are initiated at the back side of the anchor and propagate towards the corners of the opening. The half-cone diameter B is approximately 5 times of the edge distance and its depth H at the front face is approximately 1.5 to 2 times of the edge distance. The angle (θ) of the concrete half-cone measured with respect to the free edge is around 30 degrees.
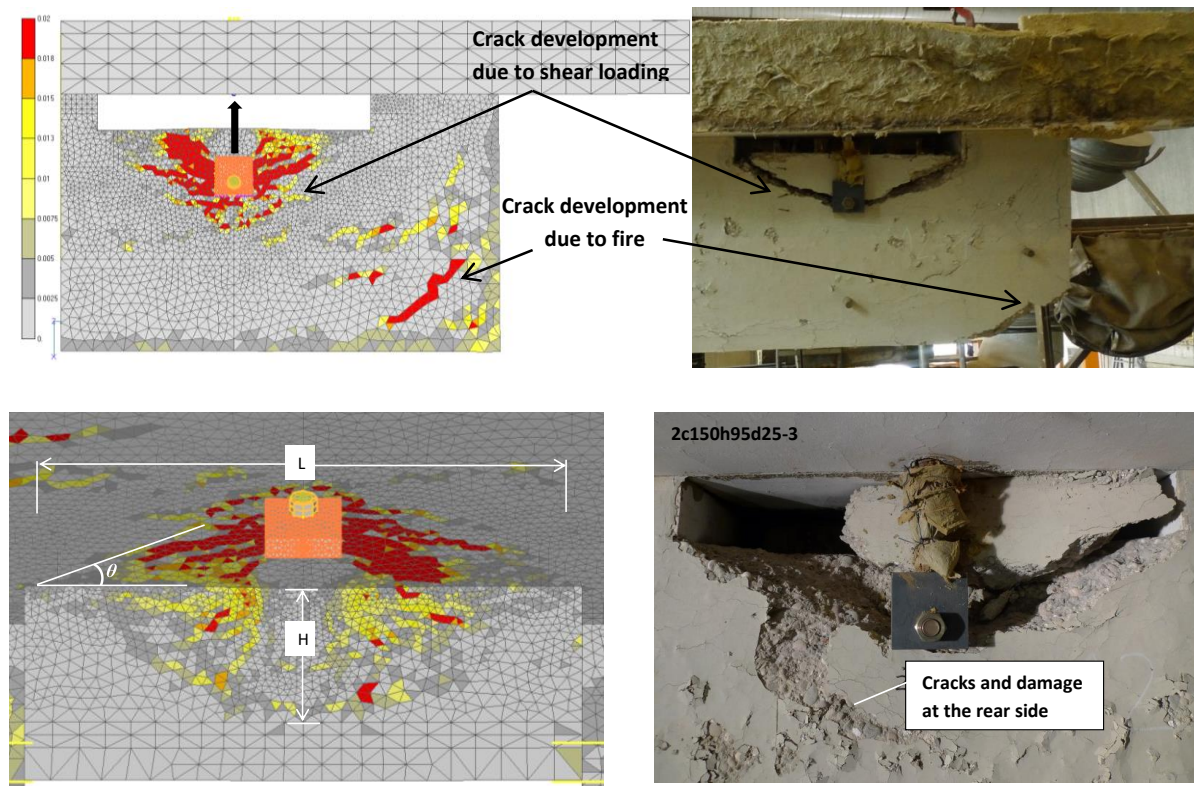
Figure 4.22 The typical temperature induced damage of concrete and failure mode, FE analysis (left) and experiment (right).

The numerical simulations for the cold state were performed using the FE model shown in Figure 4.18b. The same as in the experimental tests the anchors close to the free edge were exposed to 90 min fire, cooled down to ambient temperature and then loaded in shear up to failure. These

anchors were not preloaded and they were not experimentally tested in the hot state. However, the numerical simulation was performed for both cases, cold and hot state, i.e. the verification of the model is performed only for cold state whereas the prediction is carried out for the hot state.

4.6.4. Peak load

Numerically obtained resistance of the anchors are listed in Annex B Table B.1 . All peak loads obtained numerically and experimentally are shown and compared in Figure 4.23 as a function of edge distance (Figure 4.23a) and embedment depth (Figure 4.23b). The comparison between experimental results and numerical predictions shows that the model is able to realistically replicate the resistance of fasteners under shear load at ambient temperature (comparing with both test data presented as empty triangles and design code formula presented in dashed lines in Figure 4.23), after 90 min of fire exposure (hot state) and after cooling (cold state). Figure 4.23a shows that increasing edge distance increases the resistance, however, after cooling only slight increase is observed with larger edge distance. Both experimentally and numerically obtained resistances in the hot state for relatively small edge distance are higher than the reference resistance at ambient condition. However, for larger edge distances the resistance decreases compared to the reference value. Numerical analysis confirms that the increase of the peak load under fire for $c_1 = 50$ mm, or only slight reduction for $c_1 = 100$ mm, is due to the confinement effect. Since the top slab (see Figure 4.2c) was not exposed to fire, relatively large temperature induced compressive stresses parallel to the free concrete edge were generated. The principal compressive stresses are shown in Figure 4.24 for anchors with small (a) and large (b) edge distances. As can be seen from Figure 4.24a for small edge distance, the compressive struts are formed in the loading direction of the anchor against the connections to the top slab. This is due to the relatively small distance between the anchor position and the confining zone (red zone in Figure 4.24). Further away from the free edge where the anchor is located, the weaker is the effect of the temperature induced confinement stress and no compressive strut can be formed, i.e. there are no compressive stresses along the free edge (see Figure 4.24b). In contrast to the results obtained for anchors loaded in the hot state, numerically predicted and experimentally measured resistance of anchors loaded in the cold state decreases significantly compared to their reference resistance. This can be attributed to the release of confining stresses because of cooling and significant damage of concrete due to fire impact.

(a) (b)
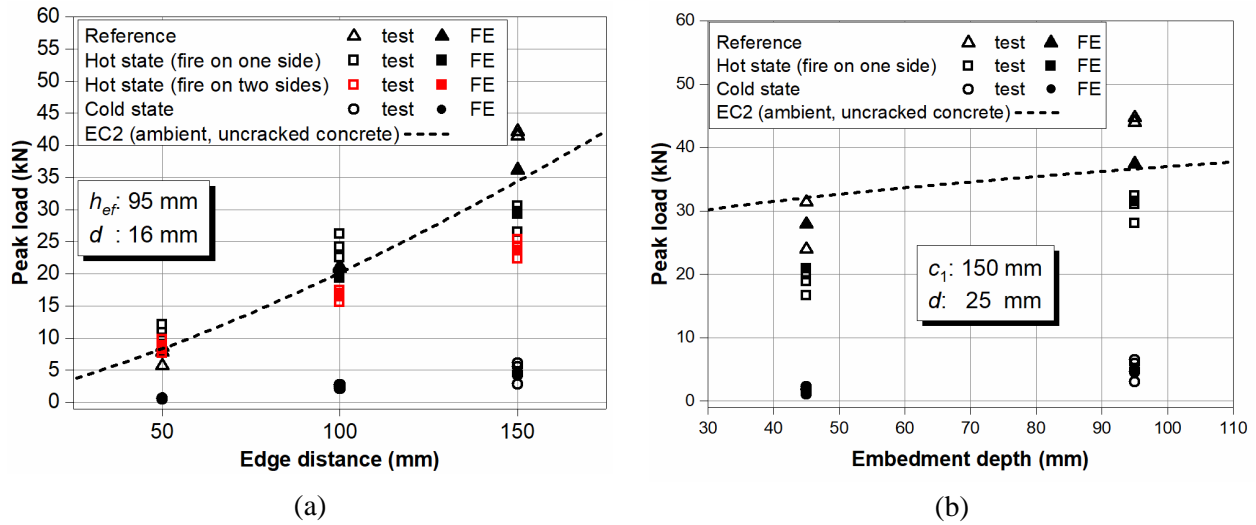
Figure 4.23 Experimentally and numerically predicted resistance for hot and cold state: (a) function of edge distance and (b) function of embedment depth.

(a) (b)
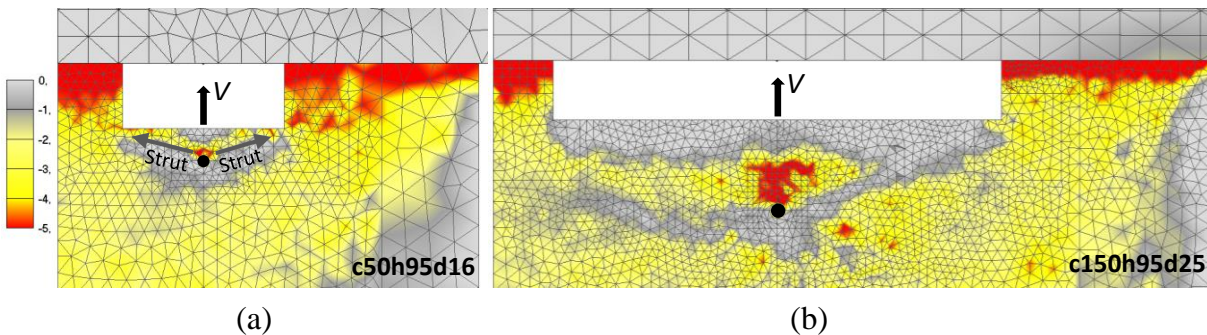
Figure 4.24 Compressive stress distribution for anchors (a) with small edge distance and (b) large edge distance.

As expected, Figure 4.23b shows that with larger embedment depth the shear resistance of anchors after cooling becomes relatively high. However, compared to the effect of the edge distance on the shear resistance, the influence of embedment depth is not strong in all conditions.

The above experimental and numerical results showed that the temperature induced confinement effects can significantly influence the resistance of fasteners in the hot state. Obviously for design the relevant resistance is that obtained from unconfined specimen, as the simple finite element model shown in Figure 4.18b. This is valid for the hot and cold states. Therefore, in Figure 4.25 all the experimental and numerical results obtained only for unconfined specimens heated from both sides, for hot and cold state are shown. Furthermore, the results are compared with the reference resistance at ambient temperature and the design code formula.

69

From Figure 4.25, it can be seen that the most critical case corresponds to the resistance obtained for the cold state, i.e. after the concrete specimen is cooled down to the ambient temperature and then tested. For such a case the reduction of resistance compared to the reference resistance in un-cracked concrete is approximately 90%. It can be seen that the current design formula overestimates the numerically and experimentally obtained resistance for cold state. Furthermore, it can be seen that the resistance for the hot state, obtained only numerically, is higher than that of the cold state, and it is obviously underestimated by the current design formula. The reduction of the resistance in the hot state compared to the reference resistance in un-cracked concrete is approximately 62%. The reason for smaller reduction in the hot state is due to the fact that cooling causes additional thermally induced damage of concrete, which leads to additional degradation of shear resistance of fasteners. Finally in Figure 4.25 numerically predicted peak loads in the hot state and with only one side of heating are also shown. As expected, the resistance is higher than when both sides of the concrete member are exposed to fire.
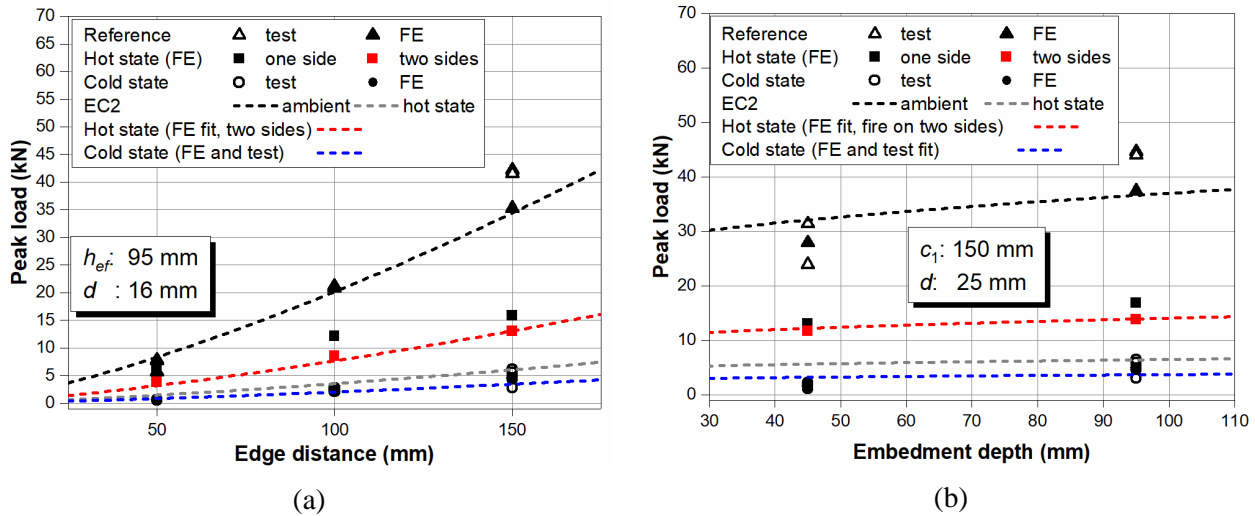
Figure 4.25 Experimentally and numerically predicted resistance for hot and cold state of confinement free specimens: (a) function of edge distance and (b) function of embedment depth.

4.7. Summary

In the present study the results of experimental and numerical investigations on a single headed stud anchors close to concrete edge loaded perpendicular to free edge in shear under elevated temperature are presented and discussed. Reference tests at room temperature, the tests at 90 min of fire (hot state) and tests after 90 min of heating and subsequent cooling were performed (cold state). The tests were also numerically simulated in order to verify and calibrate the numerical model. Based on the presented results the following can be concluded. (1) The employed numerical model is able to realistically replicate experimental tests. This is observed for the temperature distribution, failure mode and resistance. (2) The failure load of reference test at

ambient temperature agrees very well with the design code formula according to Eurocode 2 and numerical results. (3) It was found that for the anchors with relative small edge distance tested at hot state, the resistance is even larger than that for the reference test at room temperature. As confirmed in the numerical study, the reason is due to the influence of the thermally induced confinement compressive stresses as a consequence of the geometry and thermal boundary conditions. The same analysis without confinement effect exhibited significant reduction of the resistance. (4) The analysis shows that the shear resistance of anchors in the hot state is higher than the same resistance for the cold state. (5) The design prediction formula underestimates resistance for the hot state, however, it overestimates the experimental and numerical results for the cold state. (6) The results of the study indicate that the cold state resistance is relevant for concrete edge failure of anchors close to free edge. Therefore, it would be possible that for the hot state the failure of steel could be critical.

On the basis of this preliminary study, it is worth focusing on the shear resistance of anchors regarding concrete edge failure in the cold state. And fire exposure on both sides of the concrete edge is critical. Thus, in the following chapter, experimental and numerical studies are conducted to consider higher grade of concrete and also anchor groups loaded in shear after different fire durations.

5. INVESTIGATION OF SINGLE HEADED STUD ANCHORS LOADED TOWARDS FREE EDGE IN THE COLD STATE

5.1. Scope

In this chapter the load bearing capacities of headed stud anchors loaded in shear perpendicular to the free edge after fire exposure of 0 min (reference), 15 min and 60 min of standard fire curve ISO 834 are experimentally and numerically investigated. The effect of concrete edge distances c_1 of 75 mm, 100 mm and 150 mm, together with the influence of different concrete compressive strength f_{cm} of grade C20/25 and C40/50, nominal diameter d_{nom} of 16 mm, 25 mm and 32 mm, and embedment depth h_{ef} of 70 mm, 95 mm and 140 mm on the load-bearing behaviour of the anchors at various durations of fire were carried out firstly. The experimental work is also described in *Tian et al.* (2018).

After evaluating the experimental results, numerical analyses are performed with respect to the same anchor configurations as in the experiments. The experimental and numerical results are compared to verify the numerical models. Following that, numerical parametric study is carried out based on the verified models and a formula for prediction of concrete edge failure capacity is proposed.

5.2. Anchors and configurations

(a)   (b)
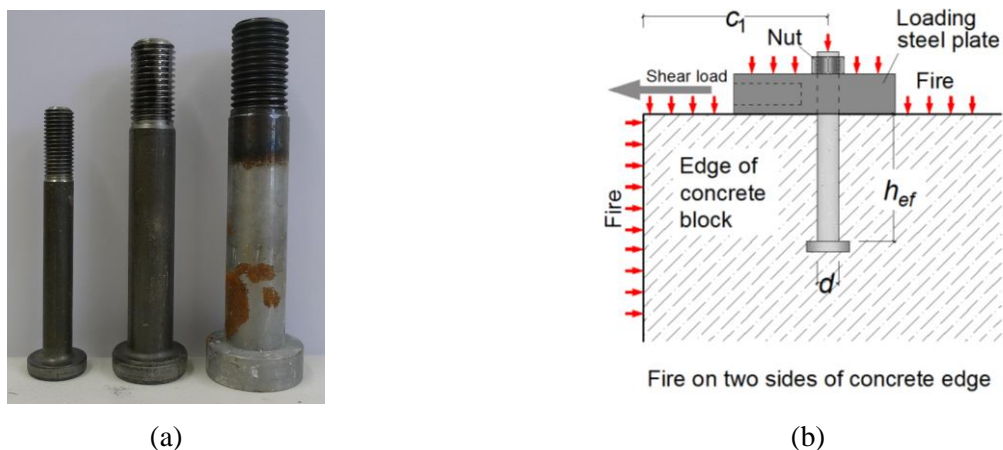
Figure 5.1 (a) Headed stud anchors used in the present study; (b) anchor configuration and applied fire on two sides of the concrete edge.

The headed stud anchors, as shown in Figure 5.1a, were produced using structural steel S235J2. The production of the headed stud corresponding to the materials, mechanical properties and dimensions according to EN ISO 13918 (*International Organization for Standardization*, 2008). The typical anchor configuration used in the tests is shown in Figure 5.1b. It consists of a headed stud anchor cast-in concrete with an edge distance c_1 and having an embedment depth h_{ef}. A steel plate with internally threaded hole to connect the loading device is used to apply the load in shear perpendicular to the free edge. Different edge distances (c_1 = 75 mm, 100 mm and 150 mm), shaft diameters (d = 16 mm, 25 mm and 32 mm) and embedment depths (h_{ef} = 70 mm, 95 mm and 140 mm) under two-sided fire exposure are investigated.

The actual configurations of the anchors tested are listed in Table 5.1. Each has been repeated three times to verify reproducibility of the results. Altogether, 50 tests were performed for examining concrete edge failure in the cold state.

Table 5.1 Anchorage configurations

Identification	Edge distance c_1 (mm)	Embedment depth h_{ef} (mm)	Diameter d (mm)	Concrete grade	Fire duration $fi(t)$ (min)
2c100h70d16	100	70	16	C20/25	15; 60
2c100h95d16	100	95	16	C20/25; C40/50	0; 15; 60
2c100h140d16	100	140	16	C20/25; C40/50	0; 15; 60
2c75h95d25	75	95	25	C20/25; C40/50	15; 60
2c100h95d25	100	95	25	C20/25; C40/50	0; 15; 60
2c150h95d25	150	95	25	C20/25; C40/50	0; 15; 60
2c100h95d32	100	95	32	C20/25	15; 60

[*] Number 2, c, h and d in the identification stands for fire exposure from two sides of the concrete member, edge distance, embedment depth and diameter, respectively.

5.3. Concrete specimen

The dimensions of the concrete slabs were designed according to guideline ETAG 001 (*European Organisation for Technical Approvals*, 2012). Considering that no previous post-fire experimental experiences and standard post-fire test procedures currently exist for metal anchors in concrete, the slabs were designed in a conservative way ensuring a full development of the

concrete edge breakout. Sufficient member thickness $h > 2h_{ef}$ and $h > 2c_1$ were considered to avoid the influence of the thicknesses of the member and the support distances of $7c_1$ were provided to exclude the influence of the supports on the concrete edge failure resistance. It should be noted that under ambient conditions, a support distance of $4c_1$ is considered sufficient to allow the development of full breakout body. However, after the exposure to fire, since the breakout body could be larger, due to the presence of the cracks and different mechanical properties of concrete, a support distance of $7c_1$ was considered as appropriate.

Table 5.2 Material properties

Material	Grade	Room temperature: at the time of the fire test				After cooling	
		E-modulus (GPa)	Uniaxial compressive strength $f_{cc,150}$ (MPa)	Tensile strength f_{ctm} (MPa)	Weight density ρ (Kg/m^3)	Uniaxial compressive strength $f_{cc,150,\,fi(15)}$ (MPa)	Uniaxial compressive strength $f_{cc,150,\,fi(60)}$ (MPa)
Concrete	C20/25: Charge 1	27	36.92	2.84	2262	33.62	-
Concrete	C20/25: Charge 2	27	34.53	2.94	2264	-	8.51
Concrete	C40/50: Charge 1	30	54.52	3.1	2264	47.22	-
Concrete	C40/50: Charge 2	30	59.12	3.77	2280	-	9.67

* $fi(15)$ and $fi(60)$ represent 15 min and 60 min of ISO 834 fire duration, respectively.

The anchors were first fixed at the bottom side of the wooden moulds (formwork) (see Figure 5.2a), which guarantees a flat and even surface for all the anchors cast-in, then the fresh concrete was poured in the moulds. The concrete mix were designed according to DIN 1045 (*DIN Deutsches Institute für Normung*, 2008a; *DIN Deutsches Institute für Normung*, 2008b). Concrete grades C20/25 and C40/50 were used. Since higher strength concrete presents higher risk of explosive spalling under fire, polypropylene fibre (pp fibre) with moderate dosage of 1 kg/m^3 (roughly 0.1% by volume) was added to the mixture of C40/50 to mitigate the risk of explosive spalling. However, no fibres were added to the concrete of grade C20/25. The compressive strength, tensile strength and modulus of elasticity were tested according to European standards EN 12390-3 (*European Committee for Standardization*, 2009b), EN 12390-6 (*European Committee for Standardization*, 2010) and EN 12390-13 (*European Committee for*

Standardization, 2013a), respectively. The material properties obtained from the tests are summarized in Table 5.2.

To optimize the use of the space of the furnace in the fire test facility, the specimens were placed as shown in Figure 5.2b. They were grouped in pairs of two slabs each standing back to back with an insulation material (rockwool) in between to prevent heat penetration on the back side of the slabs. In total, ten slabs comprising 7 slabs of C20/25 and 3 slabs of C40/50 were arranged in the furnace for each fire test. As can be seen in Figure 5.2, two single anchors were cast at each vertical edge of the slabs, plus one at the top edge. These anchors were exposed to two-sided fire. The ones at the bottom edges were subjected to only one-sided fire, which will be used for comparative analysis in further investigations. The anchors located in the central region of the slabs were used to perform pry-out tests, which will be discussed in Chapter 7 and 8.

(a)   (b)
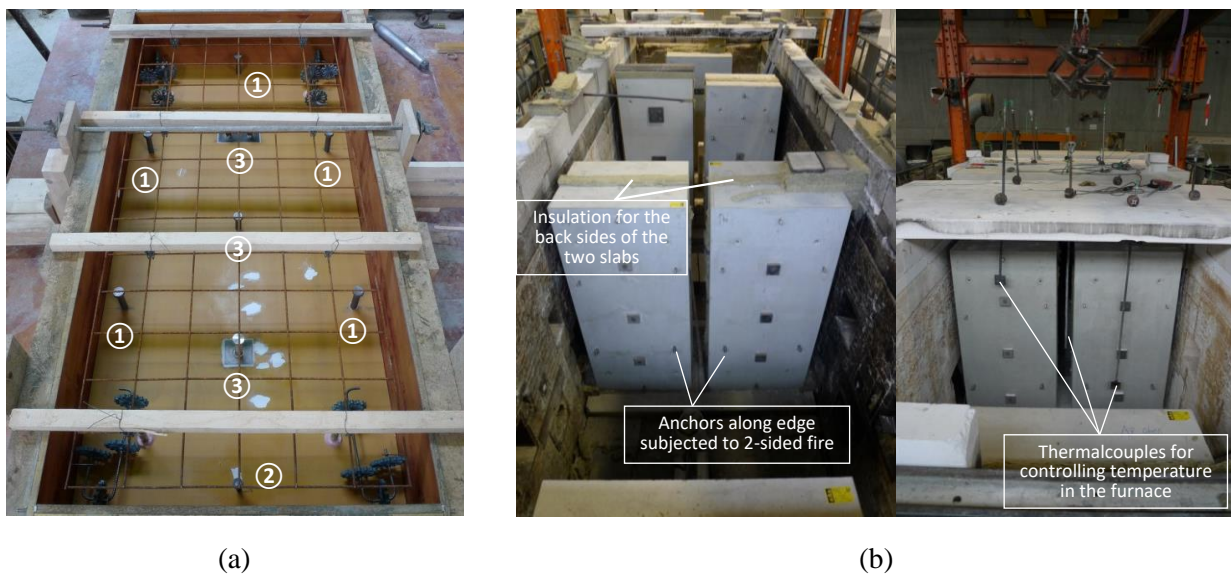
Figure 5.2 (a) Positions of anchors: ① indicates anchors installed near edge and subjected to two-sided fire; ② indicates anchors close to edge but subjected to only one-sided fire; ③ indicates anchors installed in-the-field for pryout failure in further study; (b) layout of the concrete slabs in the furnace.

To measure the temperature rise inside concrete specimens, thermocouples were fixed at positions inside the specimens as shown in Figure 5.3. A typical concrete specimen has dimension $1000 \times 400 \times 2200$ mm ($L \times W \times H$) (note that the figure is for the half size—one symmetry plane). When the fire started, the front, top and left faces of the specimen were heated. For distances of 200 mm and 250 mm away from the top end and bottom end, respectively, and in the middle of the height, the thermocouples were fixed along the direction perpendicular to the front face. The anchors under consideration in the experimental program were installed with embedment depths in the range of 50 mm to 150 mm. Therefore, the first thermocouple was fixed 50 mm away from the front face and the following were 100 mm away from each other. For each

fire test, 15 min or 60 min of fire duration, one concrete specimen with concrete grade C20/25 and another with concrete grade C40/50 were designated for inside temperature rise measurement. These measurements are used to obtain the temperature distribution and to verify the thermal parameters for numerical temperature profile.
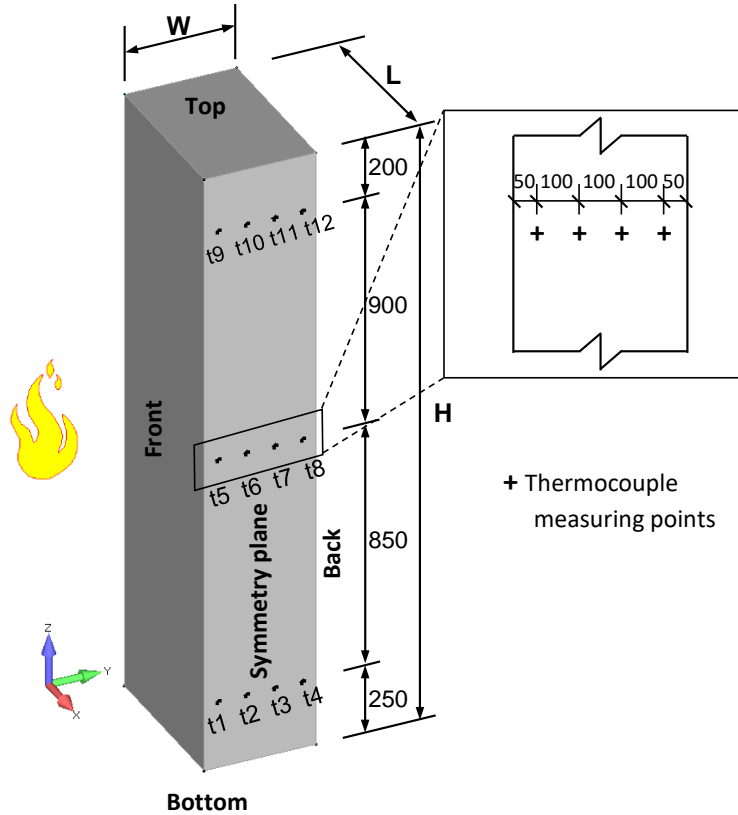
Figure 5.3 Sketch for the temperature rise measurement inside the concrete specimen (unit: mm).

5.4. Fire tests

The fire tests were conducted at the fire test facility of the Material Testing Institute (MPA), University of Stuttgart, according to EN 1363-1 (*European Committee for Standardization*, 2012). After covering the furnace with slabs and starting the fire, the thermocouples arranged at various levels inside the furnace were employed to monitor and control the temperature rise *T* according to ISO-834 (*International Organization for Standardization*, 1999):

$$T = T_0 + 345\log(8t + 1) \tag{5.1}$$

where T_0 is the ambient temperature (24 °C), *t* represents the time in minutes. Two fire durations of 15 min and 60 min were used for all anchor configurations described in Section 5.2. After reaching the target duration, the burners were shut off and the specimens were cooled down to the

ambient temperature naturally. As can be seen in Figure 5.4a, the variation of furnace temperature with time satisfies the requirements within the given tolerances.

(a)

(b)
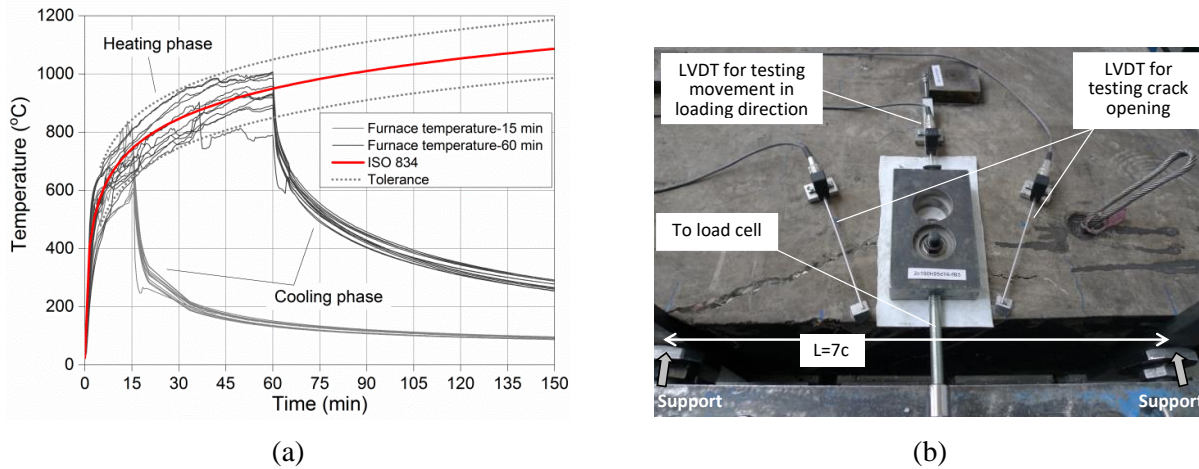
Figure 5.4 (a) Temperature rise in the furnace for 15 min and 60 min of ISO 834 fire and (b) shear loading set-up after cooling the specimen.

5.5.   Test setup
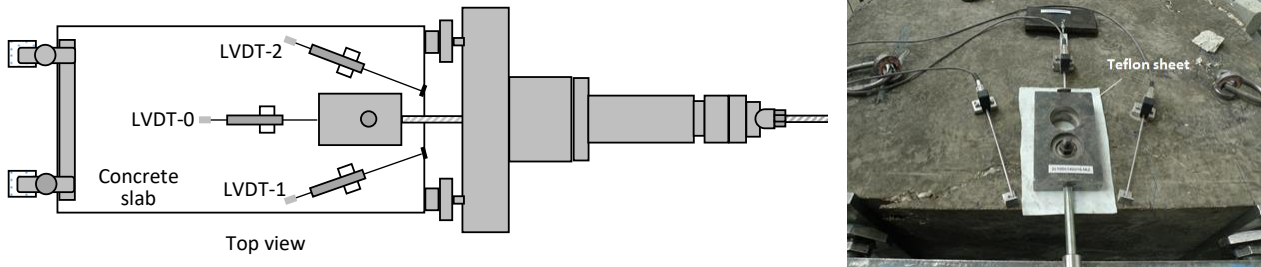
Figure 5.5 Test setup and loading configurations.

After cooling, post-fire tests were performed. The loading configuration was basically the same as shown in Figure 4.6. Through the threaded rod, the steel plate was connected to the load cell which was equipped with the hydraulic cylinder for loading. A friction reducing Teflon sheet was used between the steel plate and the concrete surface. At the rear side of the anchor, one linear variable displacement transducer (LVDT-0) was used to measure the displacement δ in the loading direction. Two more LVDTs (LVDT-1 and -2) were glued to the concrete member to determine the crack openings, which was not configured for the tests in Chapter 4. According to *Grosser* (2012), on the front face of the concrete edge normally no crack is developed. In the test program, no measurement was applied at the front face of the edge. The support distance was

kept to be 7 times of the edge distance to avoid any influence of the supports on the resistance. Figure 5.5 depicts the test setup and the loading scenario.

5.6. Test results and discussion

In the following the experimental results are evaluated to analyse the influence of fire exposure on the load-bearing behaviour of anchors by concrete edge failure.

5.6.1. Fire effect on the concrete slab

The fire exposure led to significant deterioration of the concrete slabs. Even though, concrete spalling due to fire is mainly associated with the high strength concrete, spalling was observed in the slabs of grade C20/25, see right in Figure 5.6a and b. The explosive spalling took place only in the central region of the slabs. Thus, the anchors used to investigate the concrete edge failure were not affected by the spalling. On average, the spalling depth was measured as about 15 mm. The maximum spalling depth was about 25 mm for the C20/25 slabs for fire durations of 15 min and 60 min. It is worth noting that the spalling phenomena happened only within the first 10–15 min of heating, when the heating rate was quite high according to ISO 834 fire. The reason for spalling can be attributed to the high density of concrete and higher water content at the bottom side of casting. No spalling was observed in the slabs of grade C40/50 due to the presence of PP fibres (see left in Figure 5.6a and b).

| (a) | (b) |

Figure 5.6 Fire effect on the concrete specimens after (a) 15 min and (b) 60 min of ISO 834 fire.

5.6.2. Concrete edge failure mechanism after fire exposure

In order to extend the concrete capacity (CC) method for considering the shear resistance of fasteners after fire, it is important to understand the concrete edge failure mechanism. According

to *Eligehausen et al.* (2006), at ambient temperature the idealized shape of a typical breakout body of concrete for anchorages installed close to an edge and subjected to a shear load perpendicular to the edge is shown in Figure 5.7a. The cracks propagate at an angle of approximately 35 °, measured with respect to the concrete edge. At the front face of the edge the crack develops to a depth of approximately 1.5 times the edge distance. The reference tests at ambient temperature agree with these observations. However, after fire exposure the failure pattern was found mostly a combination of concrete edge failure (CE) and pry-out (Pr) failure. As shown in Figure 5.8, the concrete slab is after fire exposure extremely damaged, which leads to irregular development of the cracks when the anchor is loaded in shear towards the free edge. The angle θ is significantly smaller than 35 °. The crack initiation angle, with respect to concrete edge, was observed mostly less than 10 ° and the cracks propagate to the position of the supports, which means the crack length is much larger than $3c_1$ as in the case of ambient temperature. Therefore, the critical spacing between the supports should be increased at least to $4c_1$ while considering the fire resistance of the anchors. *Reick* (2001) observed similar behaviour for the anchors subjected to fire and loaded in tension.

(a)　　　　　　　　　　　(b)　　　　　　　　　　　(c)
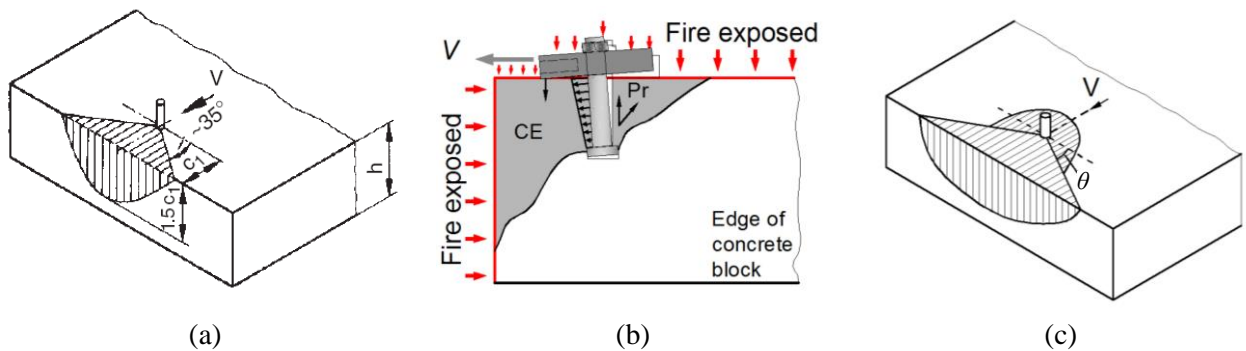
Figure 5.7 Concrete failure pattern: (a) at ambient condition; (b) and (c) after fire exposure.
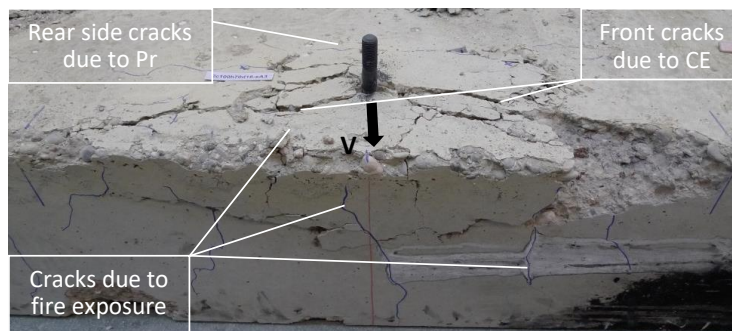
Figure 5.8 Concrete edge failure in combination with pry-out failure of anchors close to edge loaded in shear after fire exposure.

More importantly, due to thermally induced damage of concrete, pry-out failure was visually inspected to occur at the rear side of all the anchors tested, see Figure 5.7b and c. This indicates a

different failure mechanism for anchorages close to edge and loaded perpendicular to edge in shear after fire. The cracks start in front of the upside of the shaft and after peak load is attained, cracks appear on the rear side of the head and pry-out failure occurs. Thus, the peak resistance is controlled still by concrete edge failure, but this finding may stand for a rather ductile failure for anchors exposed to fire.

5.6.3. Fire effect on the load-displacement behaviour
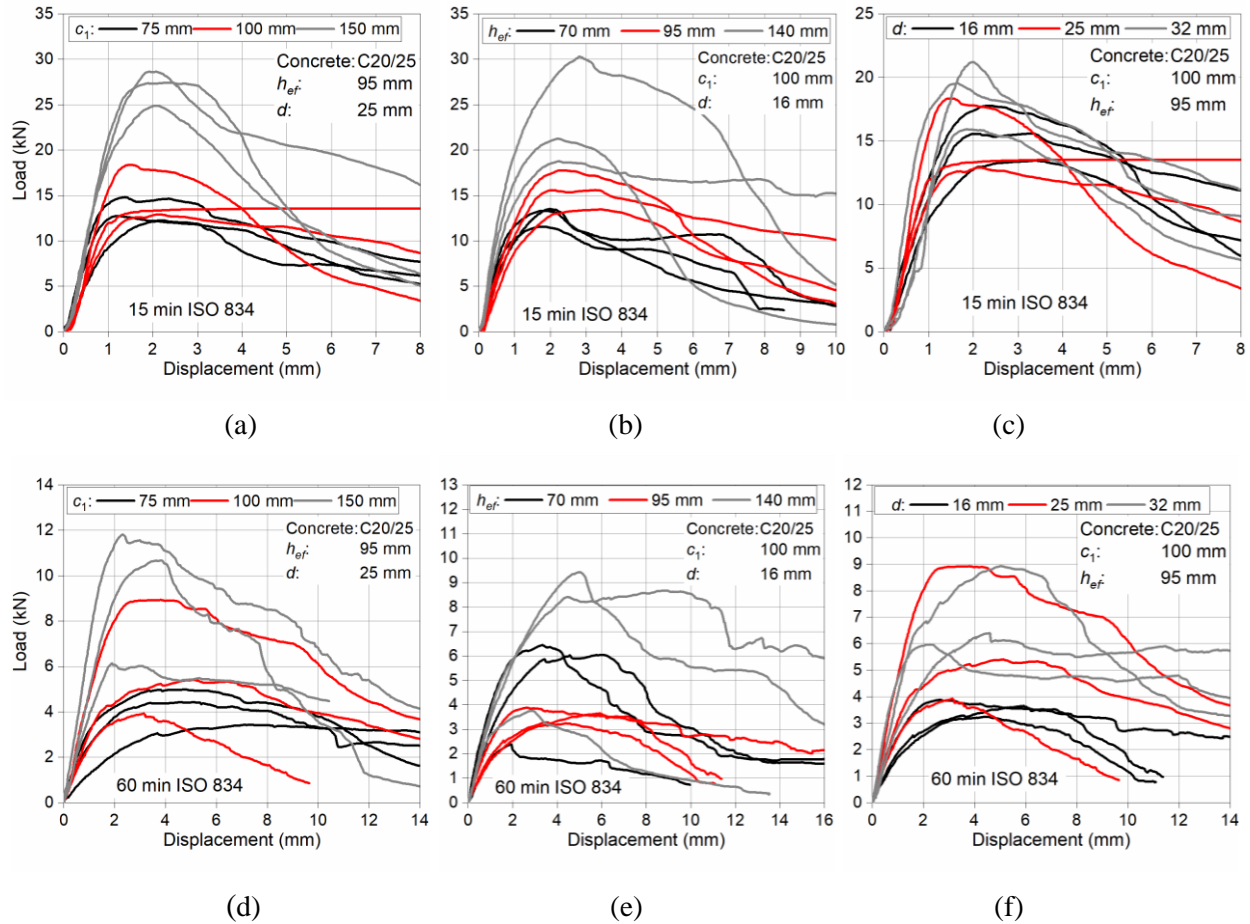
Figure 5.9 Load-displacement curves of anchors after 15 min and 60 min of fire exposure with respect to different: (a) and (d) edge distance; (b) and (e) embedment depth; (c) and (f) diameter.

In structural design, ductile failure mode rather than brittle failure is considered to be desirable. The load-bearing behaviour of anchorages has long been understood as associated with various levels of deformation and stiffness, which defines a brittle failure or a ductile failure. However, the implementation of deformation criteria in anchor design is still largely a theoretical exercise (*Silva*, 2007). The deformation and stiffness are especially significant for calculating the load distribution or redistribution to the individual anchors in anchor groups, which are mostly applied in practice. After fire exposure, the stiffness becomes even more important factor for influencing

the load redistribution in the fastening system, for example, the group of anchors used in a steel-concrete composite frame considering fire safety. Therefore, the study on the complete load-displacement behaviour of the anchors becomes significant.

Figure 5.9 shows the load-displacement curves of anchors in concrete grade C20/25 after 15 min and 60 min of fire exposure. It can be seen that the edge distance c_1 and embedment depth h_{ef} have relative large influence on the load-displacement behaviour of anchors after both 15 min and 60 min of fire. The influence of diameter d is considerable after 60 min of fire but it is not obvious for anchors after 15 min of fire. In general, after 60 min of fire exposure the load-displacement tends to be more ductile.

Typical load-displacement curves obtained from the post-fire tests are plotted in Figure 5.10 with respect to different fire exposures. The curves are characterized by three branches: the first branch almost linear up to 50% of the ultimate load, which generally defines the secant stiffness of the anchor in shear (*Grosser*, 2012); the second branch with increasing curvature to the peak load; the third descending branch after attaining the peak load. From Figure 5.10a for configurations 2c100h95d16 in concrete C20/25 and Figure 5.10b for 2c150h95d25 in concrete C40/50, it is clear that with longer fire exposure the three branches become unclear and the stiffness is lower. However, the differences of initial stiffness upon loading are remarkable for cases without fire exposure, 15 min and 60 min of fire duration.

(a)   (b)
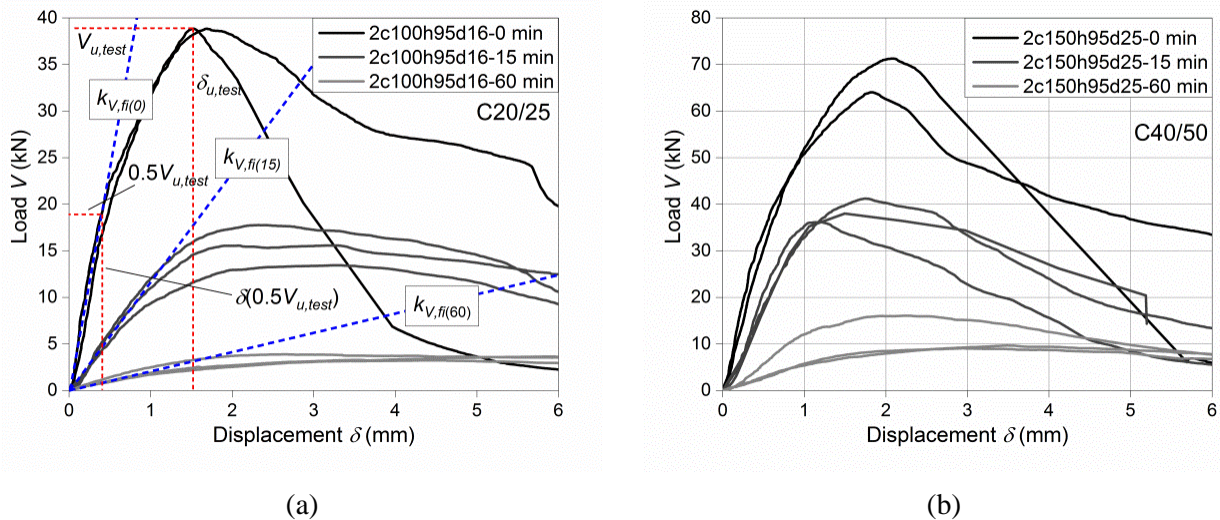
Figure 5.10 Fire effect on the load-displacement behaviour of headed stud anchors loaded in shear perpendicular to free edge after different fire durations: (a) 2c100h95d16 in concrete C20/25 and (b) 2c150h95d25 in concrete C40/50.

The secant stiffness, corresponding to the first branch $k_{V,\,fi(t)} = 0.5Vu,fi(t)/\delta(0.5Vu,fi(t))$, are plotted as a function of shaft diameter d, embedment depth h_{ef} and edge distance c_1 in Figure 5.11 to Figure 5.13. The obvious ductile response of anchors after fire exposure is principally due to

the fact that the tensile strength is more reduced than the fracture energy. Since the brittleness of concrete is linear proportional to the fracture energy and inverse proportional to the square of tensile strength, the increase of temperature induced damage leads to more ductile response.

Grosser (2012) conducted a comprehensive analysis on anchors arranged close to concrete edge and loaded perpendicular to the free edge in concrete C20/25. It was found that the embedment depth has no influence on the shear stiffness of anchors and the edge distance may only have limited effect on the shear stiffness. The shear stiffness k_V was mainly influenced by the anchor diameter d. The reference tests performed in this work confirm these findings (see Figure 5.11).

Figure 5.12a and b show the influences of shaft diameter d on the shear stiffness of anchors after 15 min and 60 min of fire duration, respectively. In the diameter range from 16 mm to 32 mm, it is seen that the diameter plays insignificant role and only slight increase of stiffness is attained with increasing diameter. The effect of diameter on stiffness after fire exposure is largely reduced compared to that at room temperature (see Figure 5.11). This is attributable to the already presented damage in concrete due to fire. For concrete grade of C20/25, the shear stiffness is around 14.4 kN/mm and 3.3 kN/mm after 15 min and 60 min fire duration, respectively. For concrete grade of C40/50, this value increases slightly up to 25.4 kN/mm and 5.7 kN/mm after 15 min and 60 min fire exposure, respectively. Comparing the mean stiffness values at room temperature of around 40 kN/mm for $d = 16$ mm and around 60 kN/mm for $d = 32$ mm, the reduction in stiffness due to fire is significant.
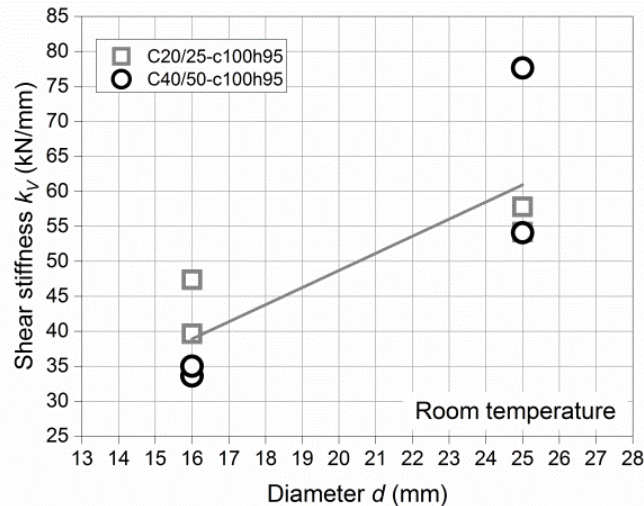
Figure 5.11 Influence of diameter on the shear stiffness of anchors at room temperature.

(a)   (b)
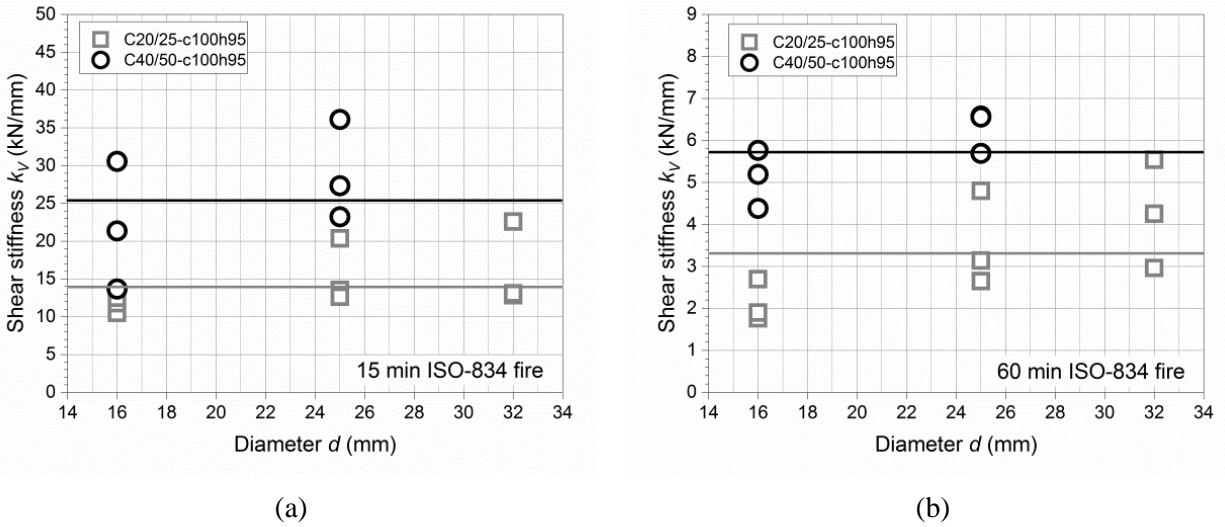
Figure 5.12 The shear stiffness of anchors as a functions of diameter d after (a) 15 min and (b) 60 min of fire exposure.

Figure 5.13a and b show the change of the shear stiffness with increasing embedment depth h_{ef} after 15 min and 60 min of fire, respectively. The embedment depth makes no obvious impact on the stiffness with respect to 15 min and 60 min of fire exposure. However, it is notable that the concrete C40/50 exhibits higher stiffness than concrete C20/25, which is about 15.3 kN/mm and 2.75 kN/mm for C20/25 after 15 min and 60 min of fire, respectively, and 22.4 kN/mm and 5.0 kN/mm for C40/50 after 15 min and 60 min of fire, respectively. These differences seem to diminish for large embedment depth $h_{ef} = 140$ mm.

(a)   (b)
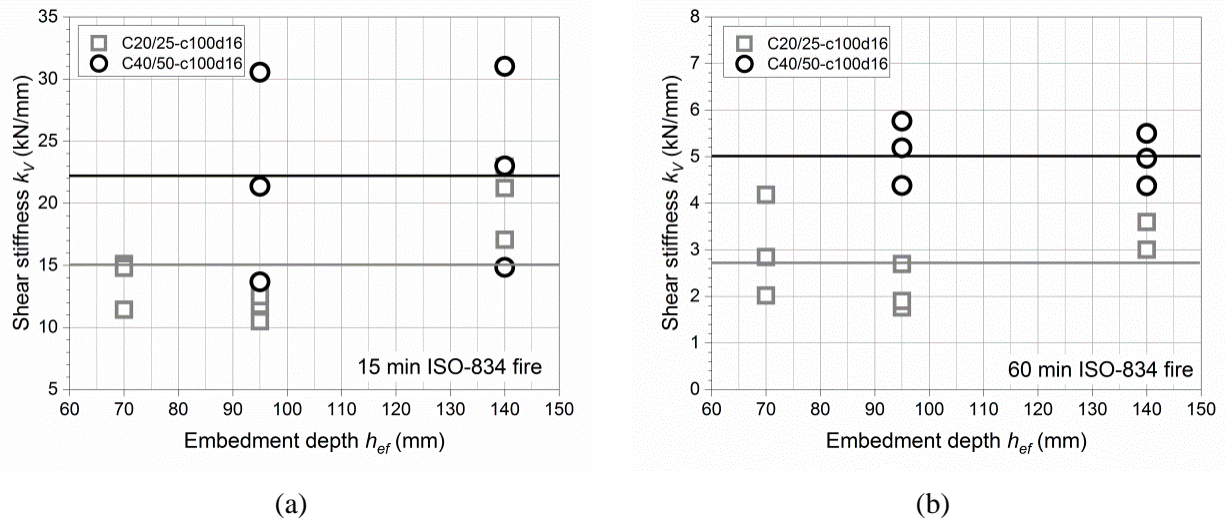
Figure 5.13 The shear stiffness of anchors as a function of embedment depth hef after (a) 15 min and (b) 60 min of fire exposure.

83

In Figure 5.14 the shear stiffness is plotted as functions of the edge distances c_1 after 15 min and 60 min of fire exposure for $d = 25$ mm. The results show a very strong influence of the edge distance on the shear stiffness of the anchors after exposing to fire. This is in contrast to the findings reported by *Grosser* (2012), who found that at room temperature the shear stiffness of anchors is dependent mainly on the anchor diameter rather than the edge distance. In this study it is found that after exposing to fire the stiffness increases almost linearly with increasing edge distance. Higher concrete grade C40/50 exhibits larger value of stiffness compared to that of concrete C20/25. Nevertheless, the trend lines are parallel to each other. This tendency can be depicted for C20/25 as following Equation (5.2) and (5.3). For C40/50 Equations (5.2) and (5.3) should be multiplied with constants 1.64 and 1.55, respectively, to obtain the value of shear stiffness after 15 minutes and 60 minutes of fire exposure.

$$k_{V,fi(15)} = 0.125c_1 + 4.30 \text{ for C20/25} \tag{5.2}$$

$$k_{V,fi(60)} = 0.038c_1 - 0.31 \text{ for C20/25} \tag{5.3}$$

(a)   (b)
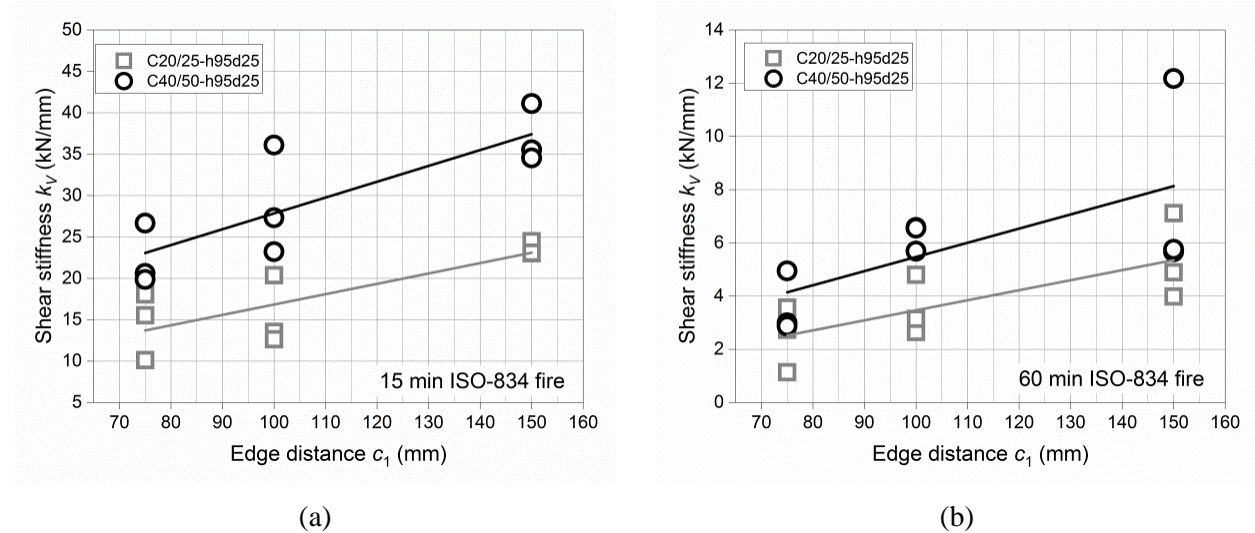
Figure 5.14 The shear stiffness of anchors as a function of edge distance after (a) 15 min and (b) 60 min of fire exposure.

All the test results clearly indicate a strong reduction of shear stiffness with increasing fire duration, regardless of edge distance, embedment depth, shaft diameter and concrete grade. The available data are summarized in Figure 5.15a and plotted as a function of fire duration $fi(t)$. It is shown that the shear stiffness reduces non-linearly and the reduction can be expressed using an exponential function as:

$$k_{V,fi(t)} = k_{V,fi(0)}e^{-0.045fi(t)} \tag{5.4}$$

Accordingly, the displacement at peak load $\delta_{u,test}$ increases with the reduction of shear stiffness, i.e. with the increasing fire duration (see Figure 5.15b).

In summary, fire exposure leads to strong reduction of shear stiffness. Without fire exposure, diameter is the main factor influencing the shear stiffness. However, after fire exposure, edge distance, instead of diameter, plays a more important role in the shear stiffness. For each fire exposure, higher concrete grade indicates slightly larger value of shear stiffness.

(a)   (b)
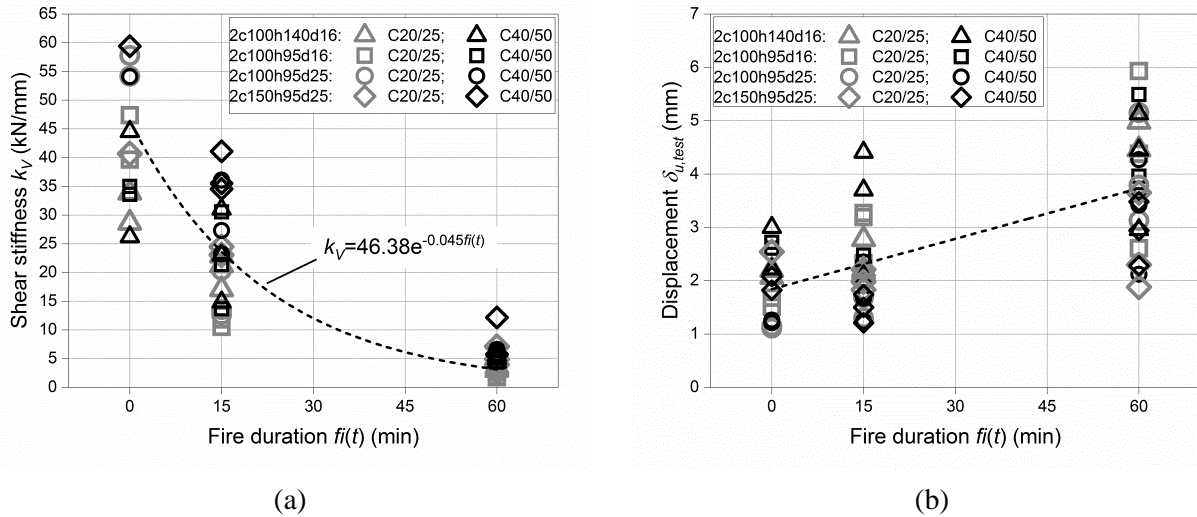
Figure 5.15 The shear stiffness plotted as a function of fire duration; (b) the displacements corresponding to ultimate load versus fire duration.

5.6.4. Crack propagation

Figure 5.16 shows typically the crack development curve of anchors with different edge distance after 15 min of fire. Crack width w1 and w2 corresponds to the LVDT-1 and LVDT-2 in Figure 5.5. It can be seen that the cracks w1 and w2 propagate symmetrically in the loading process regardless of the edge distance. When the peak load is reached, it seems that all anchors have the same level of crack openings. Obviously, the final crack width is much smaller than the displacement δ measured by LVDT-0. The readings of LVDTs was found to start increasing from zero at $\Delta w = 0.006$ mm on average. This value is taken as criterion for the start of cracking. The load level corresponding to Δw is marked in Figure 5.16 for different edge distances. It is worthy to know the percentage of load reached when the cracks start, which are presented in Figure 5.17 to Figure 5.19.
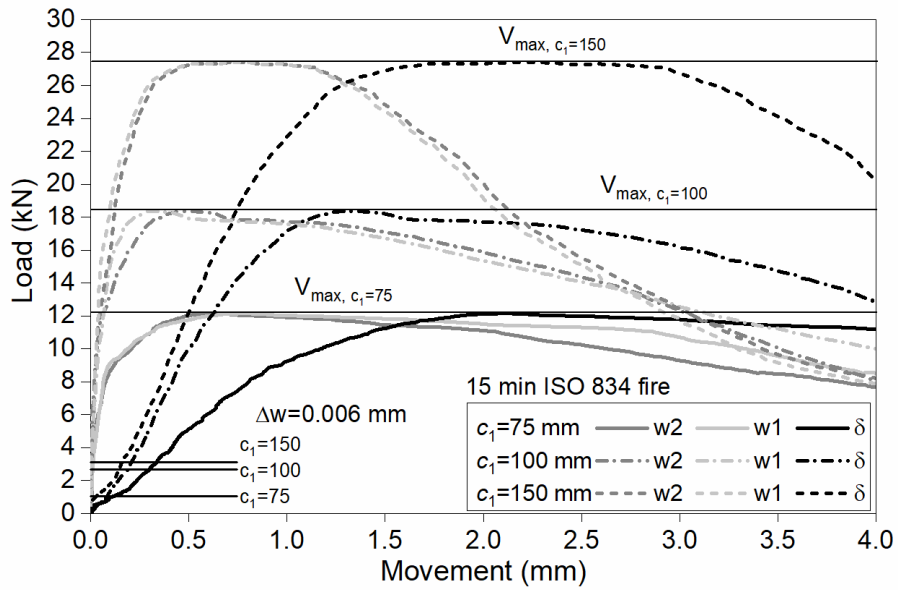
Figure 5.16 Typical crack development of anchors with different edge distance after 15 min of fire exposure.

Figure 5.17 shows the load percentage when the cracking onset as a function of the edge distance. The load seems not to be changed with different edge distances. At ambient temperature, cracking starts at 41% and 48% on average of the peak load for the concrete grades C20/25 and C40/50, respectively. After 15 min of fire exposure, cracking starts at 17% and 23% of the peak load for concrete C20/25 and C40/50, respectively. This ratio is 11% for both concrete grades after 60 min of fire duration.

(a)

(b)
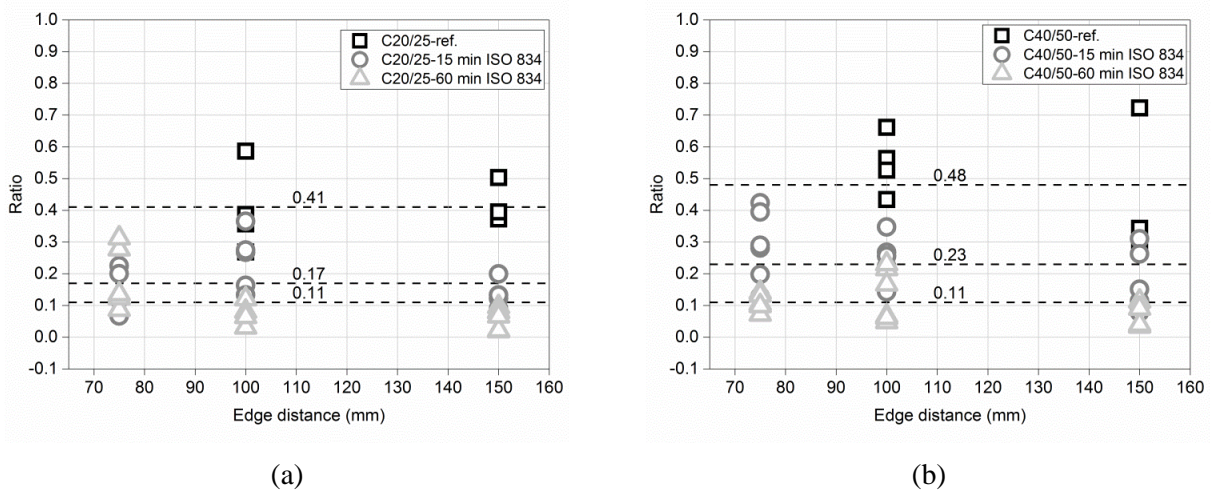
Figure 5.17 Load percentage at onset of cracking as a function of edge distance in concrete grade (a) C20/25 and (b) C40/50. Anchor $h_{ef} = 95$ mm; $d = 25$ mm.

Figure 5.18 shows the load percentage at the onset of cracking as a function of embedment depth. The load percentage seems not to be changed with embedment depth but the scattering is higher for the embedment depth of 140 mm. At ambient temperature, the cracking starts at 50% and 57% of the peak load for concrete grade C20/25 and C40/50, respectively. After 15 min of fire exposure, the cracking starts at 27% and 23% of the peak load for concrete C20/25 and C40/50, respectively. This ratio is 13% and 20% for concrete grade C20/25 and C40/50 after 60 min of fire, respectively.
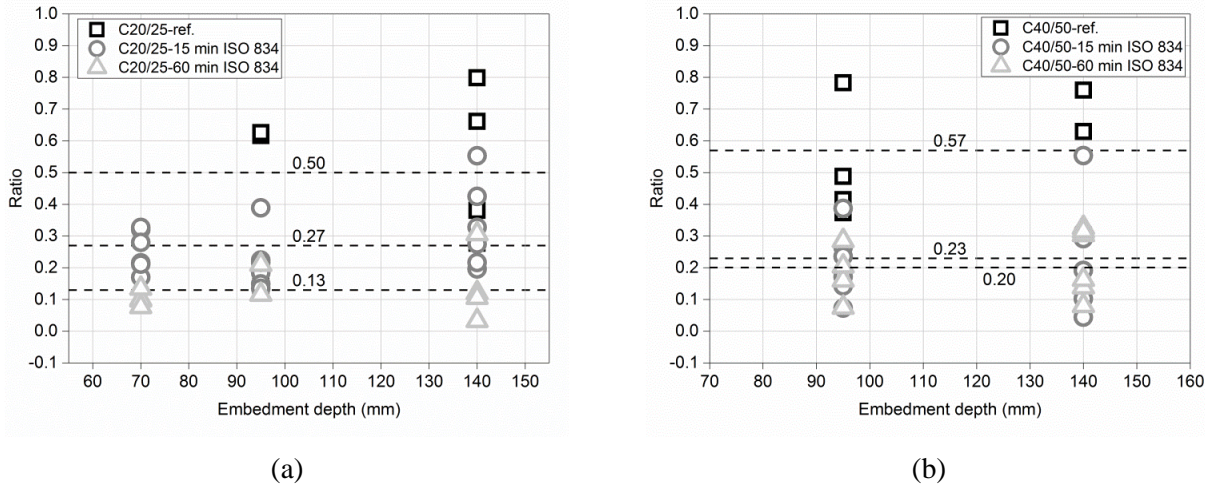
Figure 5.18 Load percentage at the onset of cracking as a function of embedment depth in concrete grade (a) C20/25 and (b) C40/50. Anchor $c_1 = 100$ mm; $d = 16$ mm.

Figure 5.19 shows the load percentage at the onset of cracking as a function of diameter. The load percentage seems to decrease slightly with increasing diameter in concrete C20/25. At ambient temperature, cracking starts at 43% and 53% of the peak load for concrete grade C20/25 and C40/50, respectively. After 15 min of fire exposure, cracking starts at 22% of the peak load for the both concrete grades. This load ratio is 12% and 15% for concrete grade C20/25 and C40/50 after 60 min of fire, respectively.

(a) (b)
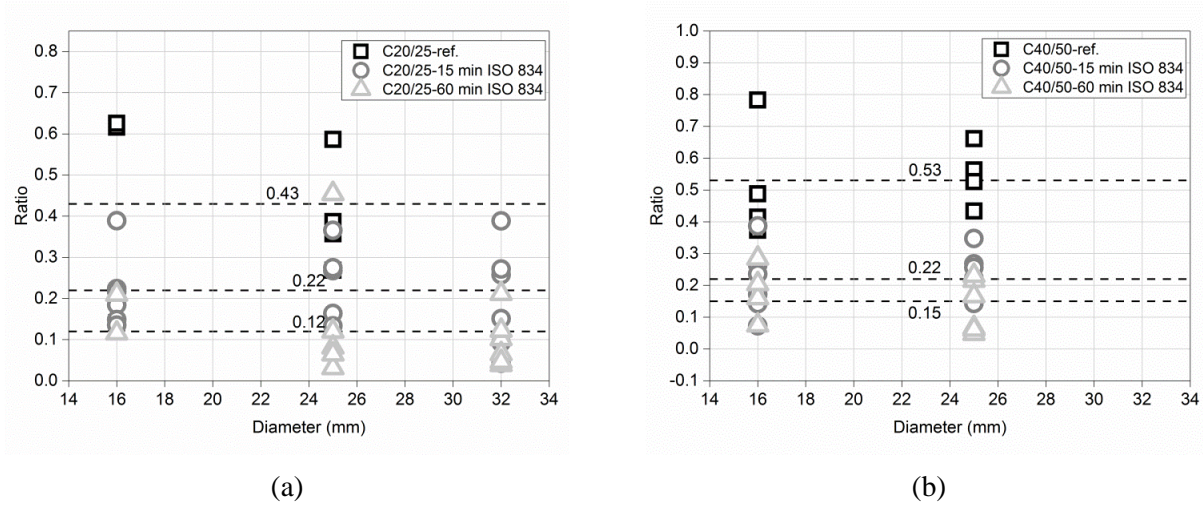
Figure 5.19 Load percentage of anchors at the onset of cracking as a function of diameter in concrete grade (a) C20/25 and (b) C40/50. Anchor $c_1 = 100$ mm; $h_{ef} = 95$ mm.

Figure 5.20 shows the ultimate crack width at peak load as a function of edge distance for different fire durations. At ambient condition and after 15 min of fire exposure, the ultimate crack width is generally at the same level. It is on average 0.28 mm and 0.32 mm for concrete C20/25 and C40/50 at ambient condition, respectively. After 15 min of fire, it is 0.49 mm and 0.58 mm for concrete C20/25 and C40/50, respectively. After 60 min of fire, the reduction is observed for concrete C20/25. On average the ultimate crack width is 2.05 mm and 1.65 mm for concrete C20/25 and C40/50, respectively.

(a) (b)
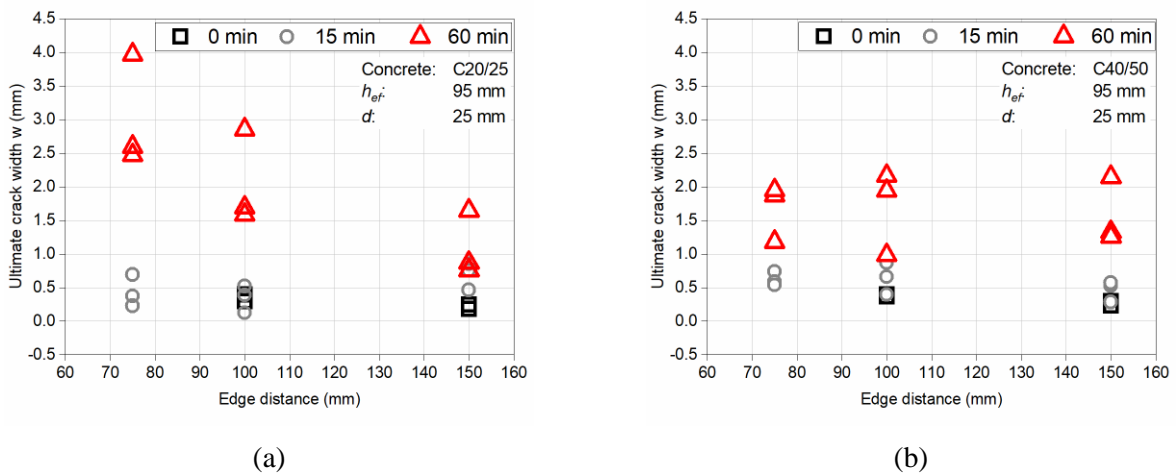
Figure 5.20 Ultimate crack width at peak load versus edge distance in concrete grade (a) C20/25 and (b) C40/50.

Figure 5.21 shows the ultimate crack width as a function of the embedment depth for different fire durations. It is seen that the ultimate crack width is independent of the embedment depth. However, with increase of fire exposure, the ultimate crack width increases gradually. It is on

average 0.31 mm and 0.22 mm for concrete C20/25 and C40/50 at ambient condition, respectively and after 15 min of fire it is 0.83 mm and 0.77 mm, respectively. After 60 min of fire, the ultimate crack width is equal to 2.04 mm and 2.32 mm for concrete C20/25 and C40/50, respectively.

(a)   (b)
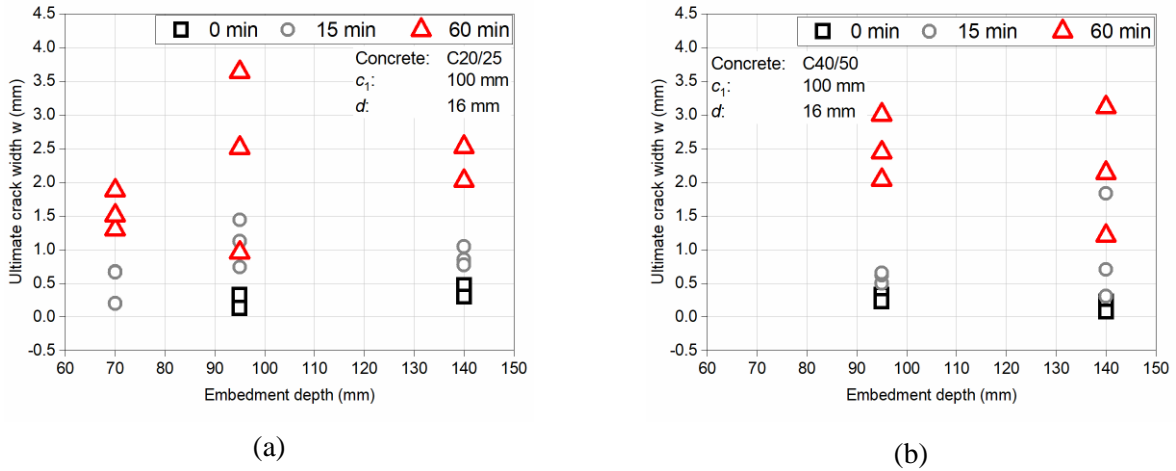
Figure 5.21 Ultimate crack width at peak load versus embedment depth in concrete grade (a) C20/25 and (b) C40/50.

Figure 5.22 shows the ultimate crack width as a function of anchor diameter for different fire durations. The ultimate crack width is generally constant for different diameters, however, it increases with increase of fire exposure. It is on average equal to 0.25 mm and 0.33 mm for concrete C20/25 and C40/50 at ambient condition, respectively, and after 15 min of fire, it is 0.61 mm and 0.62 mm, respectively. After 60 min of fire, on average the ultimate crack width is equal to 2.15 mm and 2.10 mm for concrete C20/25 and C40/50, respectively.

(a)   (b)
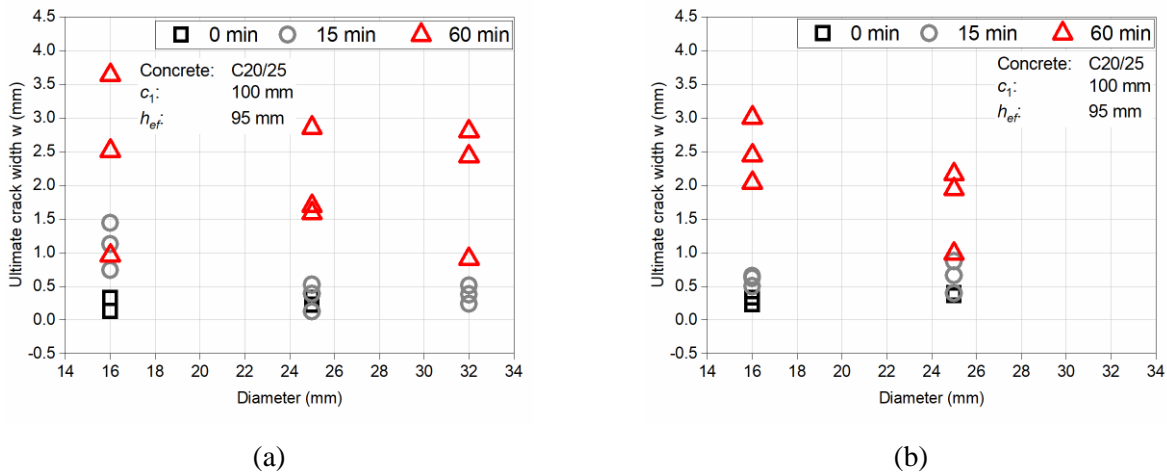
Figure 5.22 Ultimate crack width at peak load versus diameter in concrete grade (a) C20/25 and (b) C40/50.

89

Figure 5.23 shows the ultimate crack width of anchors loaded towards the free edge as a function of fire duration for concrete C20/25 and C40/50. The ultimate crack width is obviously increasing with the increase of fire duration. However, with the increase of fire duration, the wide scatter of the data is observed. At ambient condition the average value of ultimate crack width is 0.28 mm with standard deviation SD = 0.10 and coefficient of variation COV = 36%. After 15 min of fire the ultimate crack width is ranging from 0.13 mm to 1.84 mm with 0.63 mm on average (SD = 0.34, COV = 54%), and after 60 min of fire the ultimate crack width is ranging from 0.76 mm to 3.97 mm with 1.99 mm on average (SD = 0.79, COV = 40%).
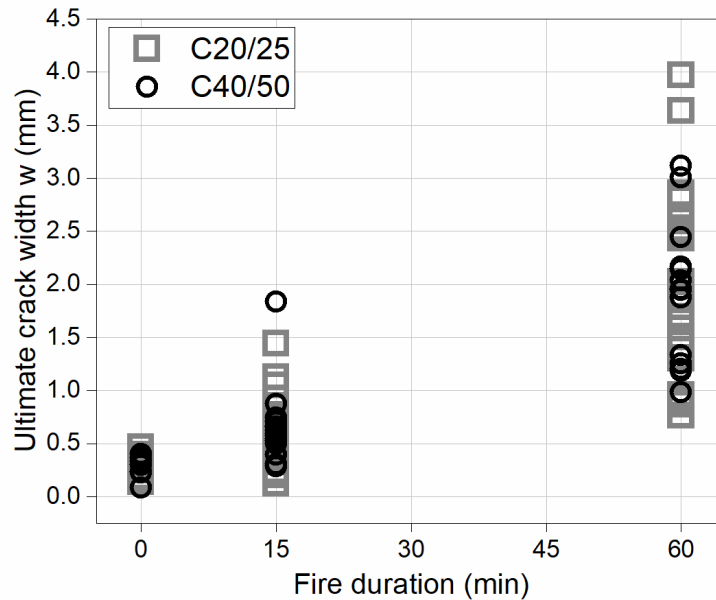
Figure 5.23 Ultimate crack width at peak load as a function of fire duration.

5.6.5. Peak load at ambient temperature

The reference peak loads obtained at ambient temperature are compared with the relevant prediction Equations (2.6), (2.8) and (2.31) according to Eurocode 2, *Grosser* (2012) and ACI 318, respectively (see Figure 5.24). It is shown that these equations can predict the shear resistance very well. Equation (2.6) (Eurocode 2) gives the best relative agreement with the experimental results, with the mean value of 1.06 (SD = 0.1; COV = 10.36%). Equation (2.6) also gives more distinctly the influence from the aspects of anchor diameter d_{nom}, embedment depth h_{ef}, concrete compressive strength $f_{cc,200}$ and edge distance c_1 on the resistance compared to the others.
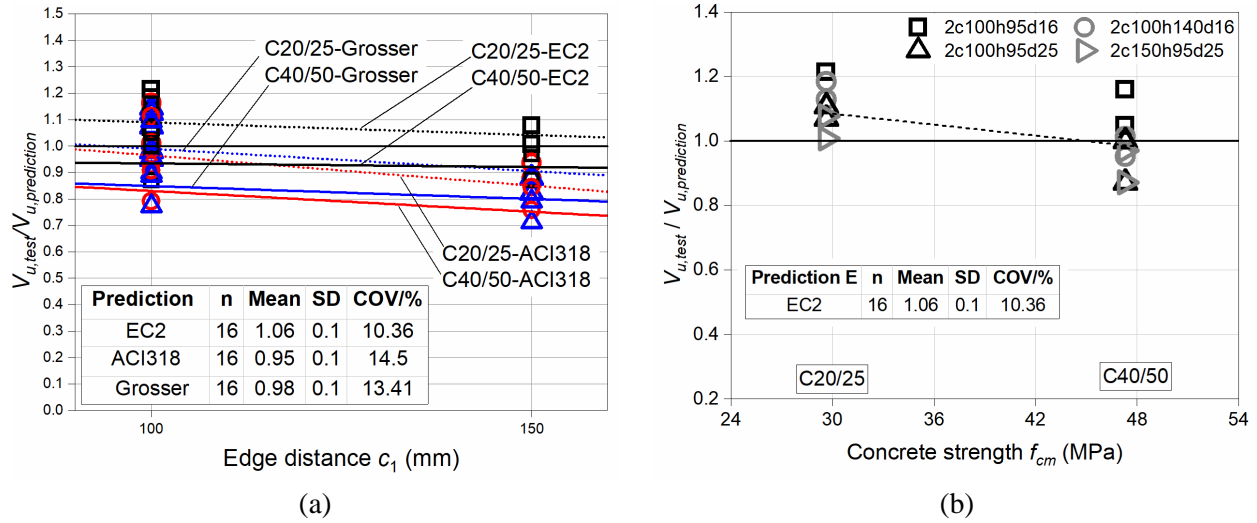
Figure 5.24 Ratio between measured and calculated (by different prediction equations) concrete edge failure loads at ambient temperature as a function of (a) edge distance and (b) concrete strength.

Figure 5.25 shows the influence of concrete compressive strength and shaft diameter on the concrete edge failure resistance of anchor at ambient temperature. In the current code, the resistance is proportional to the concrete compressive strength to the power of 0.5, which is higher than the power of about 0.3 obtained in the test (see Figure 5.25a). For the influence of diameter, the experimental results show good agreement with the conclusion in the current code, which is proportional to the diameter to the power of 0.1 (see Figure 5.25b).
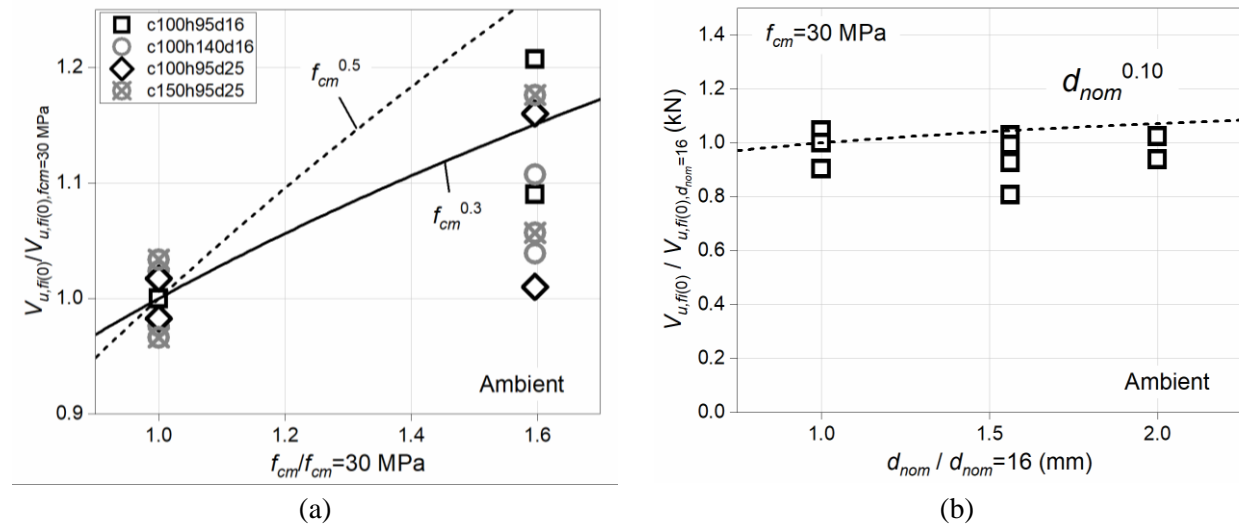
Figure 5.25 Influence of (a) concrete strength and (b) diameter on the relative peak load at ambient temperature.

In Figure 5.26 is shown the influence of edge distance and embedment depth on the concrete edge failure resistance of anchors at ambient temperature. The experimental results indicate that the resistance is proportional to the edge distance to the power of 1.3, which is slightly lower than the power of 1.5 from the current code (see Figure 5.26a). The influence of embedment depth is seen to be the same as in the current code and proportional to the power of 0.07 (see Figure 5.26b).

(a)   (b)
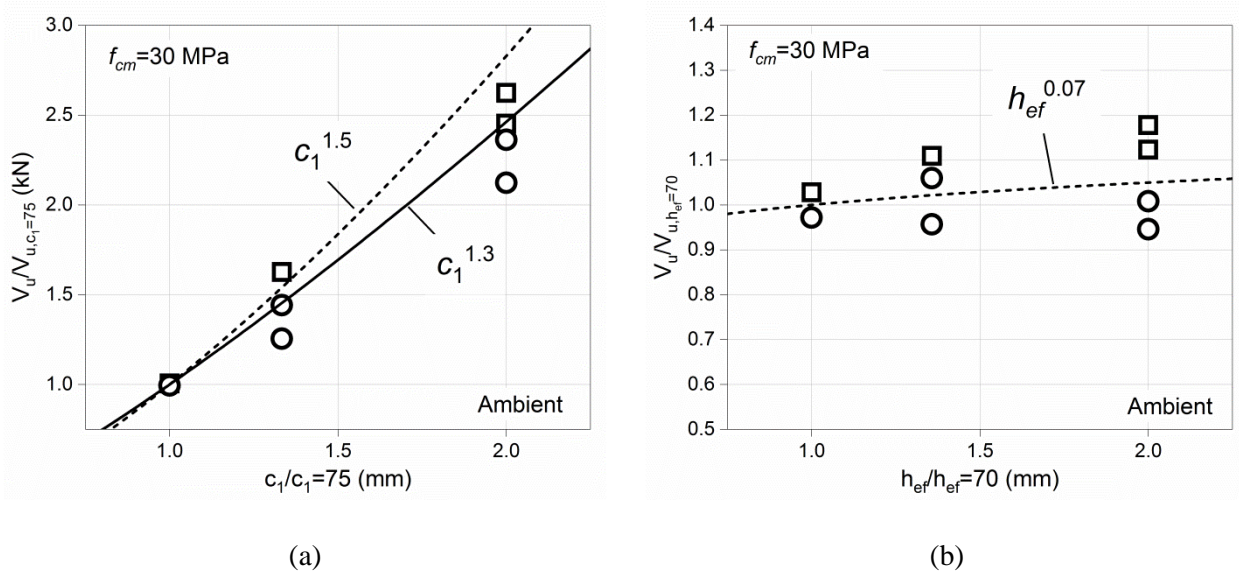
Figure 5.26 Influence of (a) edge distance and (b) embedment depth of anchors on the relative peak load at ambient temperature.

5.6.6. Peak load after 15 min ISO-834 fire

After 15 min of fire exposure, the influence of concrete compressive strength and shaft diameter of anchor on the relative resistance is shown in Figure 5.27a and b, respectively. It can be seen that the influence of concrete grade on the peak load is proportional to the concrete compressive strength to the power of 0.75, which is slightly higher than the power of 0.5 at ambient temperature according to current code. In Figure 5.27b, the influence of the shaft diameter on peak load is proportional to the power of 0.15 (for $h_{ef}/c_1 = 0.95$). This is higher than the value of $\alpha_0 = 0.1$ in Equation (2.6) for the same h_{ef}/c_1 ratio.

(a)   (b)
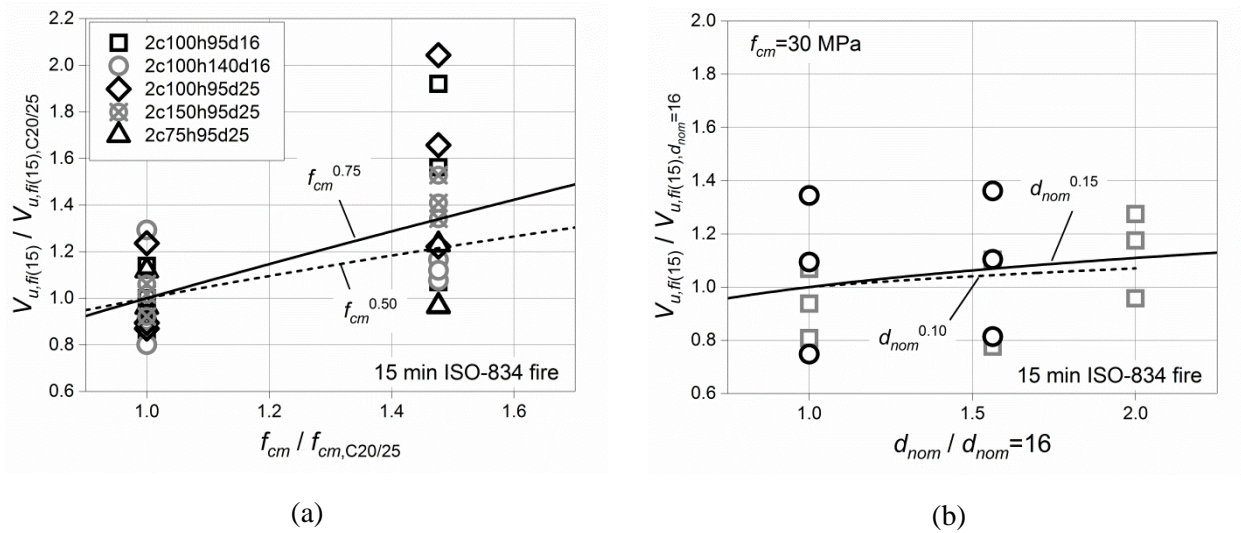
Figure 5.27 Influence of (a) concrete strength and (b) nominal diameter of anchor on the relative peak load after 15 min fire exposure.

Figure 5.28 shows the influence of the embedment depth and the edge distance of anchors on the relative resistance. It can be seen that the embedment depth has relatively large effect on the peak load, which is proportional to the embedment depth to the power of 0.69, excluding one outlier data point this value is 0.3 (see Figure 5.28a). However, the value for the ambient temperature is much smaller ($\beta_0 = 0.07$ in Equation (2.6)). In Figure 5.28b, the influence of edge distance on peak load is shown to be proportional to the power of 1.24, which is smaller than that of 1.5 for ambient temperature.

(a)   (b)
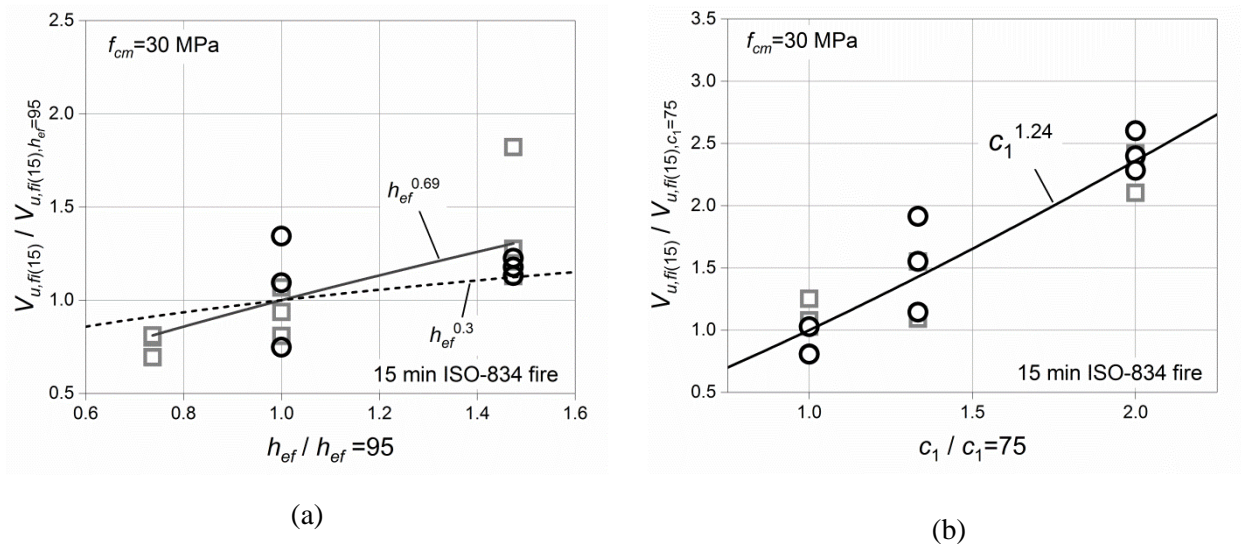
Figure 5.28 Influence of (a) embedment depth and (b) edge distance of anchor on the relative peak load after 15 min fire exposure.

93

5.6.7. Peak load after 60 min ISO-834 fire

Figure 5.29a and b show the variation of relative peak load for fire duration of 60 minutes. The scatter of data becomes relatively large due to severe thermal damage of concrete. From Figure 5.29a, it is seen that the relative peak load is increasing proportionally to the concrete compressive strength to the power of 0.8. The shaft diameter has strong influence on the increase of resistance, which increases in proportion to the power of 0.84, after excluding the highest scattering data points (Figure 5.29b).

(a) (b)
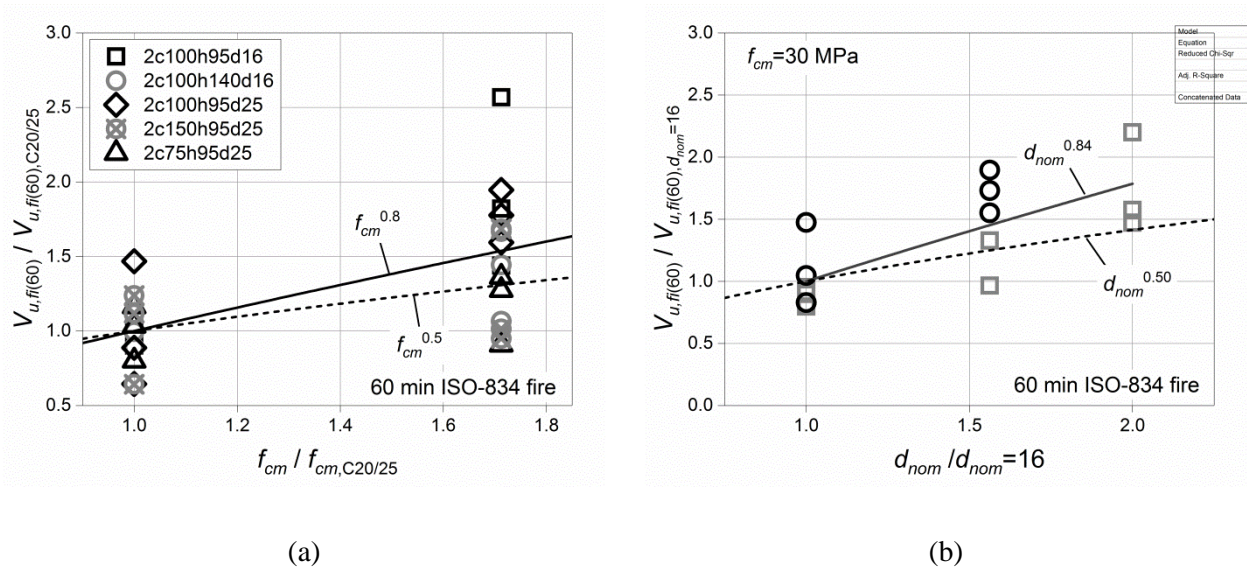
Figure 5.29 Influence of (a) concrete strength and (b) nominal diameter of anchor on the relative peak load after 60 min of fire exposure.

The influence of the embedment depth and the edge distance on the resistance is depicted in Figure 5.30. The peak load increases with increasing embedment depth to the power of 1.67 (see Figure 5.30a), which is much higher than the exponent obtained for 15 minutes of fire (0.75). This indicates that the greater the thermal damage in concrete is, the greater is the influence of the embedment depth on the concrete edge failure resistance. This could be explained by considering the fact that the concrete further away from the edge suffers less thermal damage. Therefore, the resistance of anchors with larger embedment depths is higher.

For different edge distances, the peak load increases in proportion to the power of 1.21 (Figure 5.30b). It is interesting to note that the influence of edge distance on the peak load seems to be independent of the fire duration. The exponent for ambient temperature (1.5) becomes slightly less after exposing to fire (1.24 for 15 minutes and 1.21 for 60 minutes). This is the opposite to the observations made for the initial stiffness of anchors, where the edge distance had a

significant influence in cases after fire exposure, however, had almost no influence in the cases at ambient temperature. All experimental results are summarized in Annex A Table A.2 .

(a)   (b)
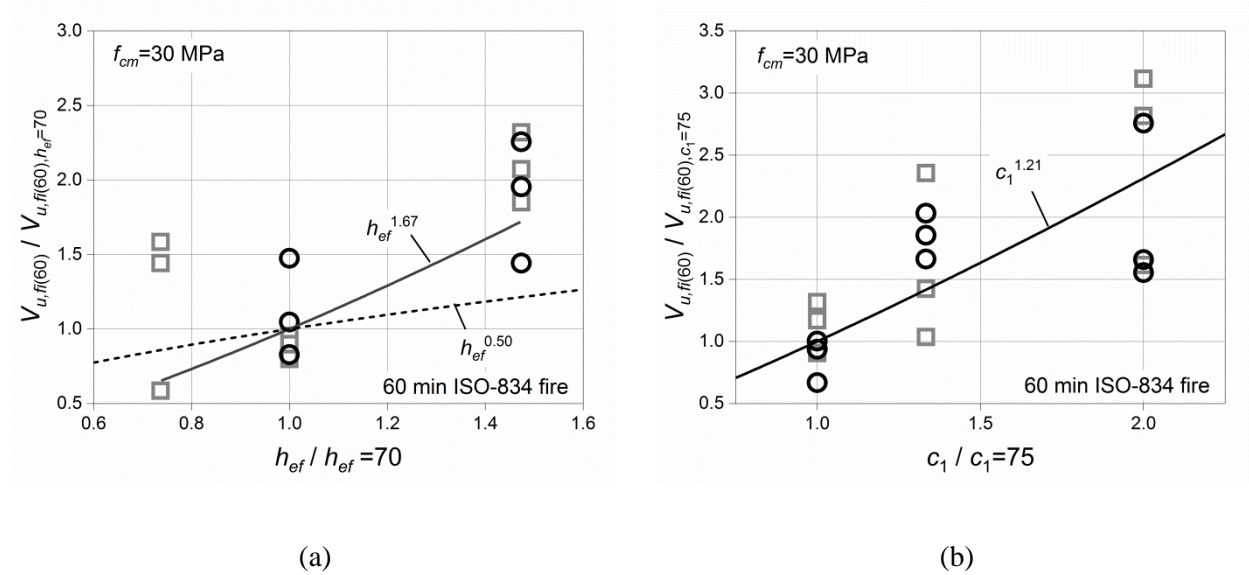
Figure 5.30 Influence of (a) embedment depth and (b) edge distance of anchor on the relative peak load after 60 min of fire exposure.

5.7.   Numerical study of concrete edge failure of single stud anchor after fire exposure

As described in Chapter 5.3, the temperature profile was monitored experimentally at specific positions in the concrete slab, rather than closely around the installed anchors. In this chapter the numerical analysis is performed to verify the temperature rise and drop inside concrete slab at the corresponding positions in the experiments. Furthermore, parametric study is performed numerically on the concrete edge failure of single headed stud anchors and the numerical results are compared with experimental results. Finally a formula is proposed to predict the concrete edge failure capacity of single headed stud anchor after fire exposure.

5.7.1.   Finite element model for concrete edge failure simulation

Figure 5.31 shows the geometry, boundary condition and finite element discretization of the model for concrete edge failure simulation after fire exposure. In principle the numerical model is a replica of the laboratory test to the geometry and boundary conditions. For the discretization, four-node finite elements are used for concrete specimen and the steel plate, and eight-node finite elements are used for the headed stud and the pull rod. In the numerical modelling, the heating area is designed sufficiently to cover the zone of concrete in which edge failure is taking place.

95

At the top face of the slab, the heating covers a rectangular area of $3c_1 \times 3.5c_1$ in size (see Figure 5.31a). For very small edge distance of 75 mm, it is $4c_1$ in the x direction. The heating at the front face covers a rectangular area with length of $3.5c_1$ in y direction for all anchors.

(a)   (b)
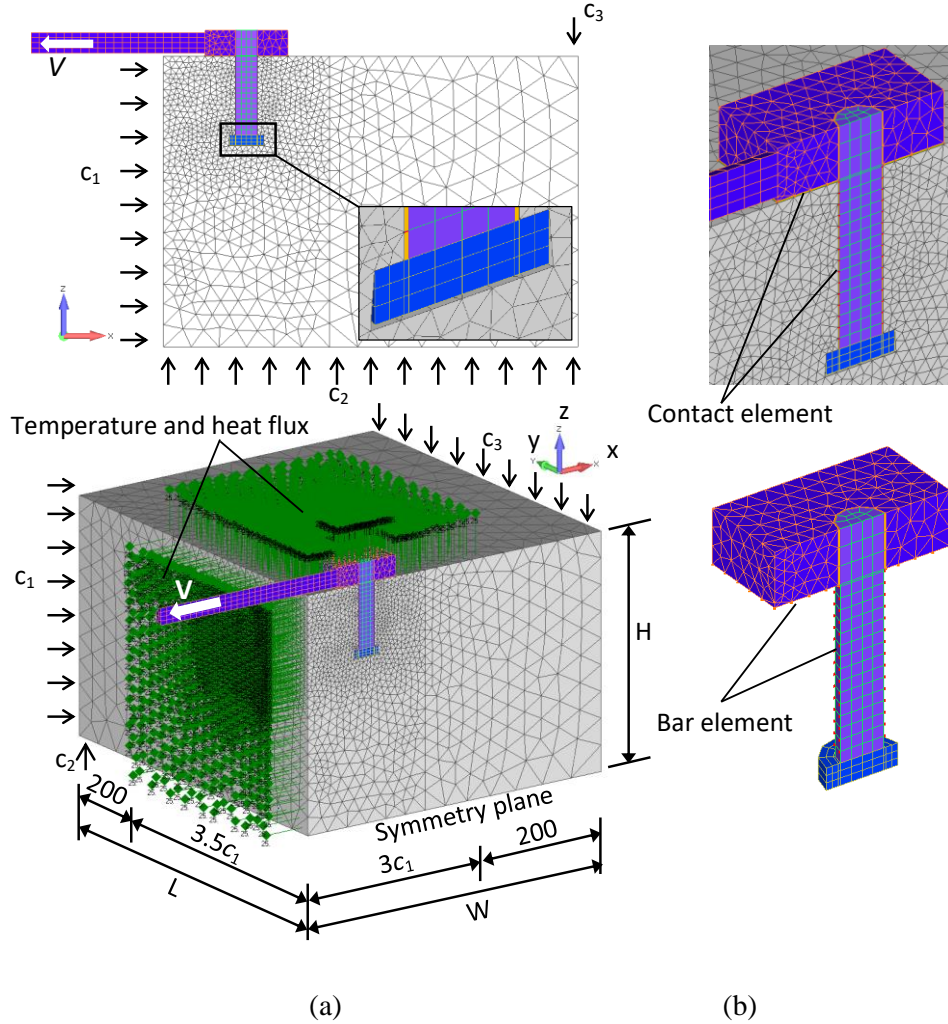
Figure 5.31 Geometry, boundary condition and finite element discretization of the model for concrete edge failure simulation.

The numerically simulated configurations of anchors for concrete edge failure after fire exposure are listed in Table 5.3. The numerical simulations are performed for all the cases subjected to testing. In addition, the geometry for $c_1 = 200$ mm, concrete grade C12/15 and fire durations of 30 min and 90 min, which were not considered in the experiments, were also simulated.

Table 5.3 Configuration for numerical modelling of concrete edge failure of single headed stud anchors

c_1 (mm)	h_{ef} (mm)	d (mm)	Concrete grade	Fire duration $fi(t)$ (min)
100	70 95 140	16	C12/15; C20/25; C40/50	0; 15; 30; 60; 90
75 100 150 200	95	25	C12/15; C20/25; C40/50	0; 15; 30; 60; 90
100	95	32	C12/15; C20/25; C40/50	0; 15; 30; 60; 90

5.7.2. Material property and loading regime

In the numerical analysis three concrete grades are considered (C12/15, C20/25 and C40/50) to study the influence of concrete strength on concrete edge failure capacity. The Young's modulus E, mean value of cylinder compressive strength f_{cm}, tensile strength f_{ctm} and mass density of concrete ρ are according to the experimental tests. The Possion's ratio v_c is kept constant as 0.18 for all. The fracture energy of concrete G_F in the numerical analysis is considered according to the CEB-FIP Model Code (*fálération internationale du báton (fib)*, 1993) as follows:

$$G_F = (0.0469d_{max}^2 - 0.5d_{max} + 26)(f_{cm}/10)^{0.7} \qquad (5.5)$$

where d_{max} is the maximum aggregate size in mm. The material properties of concrete used in the numerical simulation are summarized in Table 5.4.

Table 5.4 Material properties of concrete before fire exposure

Material	Young's modulus E (GPa)	Poisson's ratio v_c	Uniaxial compressive strength f_{cm} (MPa)	Tensile strength f_{ctm} (MPa)	Fracture energy G_F (J/m^2)	Heat conductivity λ_c (W/mK)	Heat capacity c_p (J/kgK)	Weight density ρ (kg/m^3)
C12/15	25	0.18	12	1.6	30	1.33	900	2223
C20/25	27	0.18	30	2.9	60	1.49	900	2267
C40/50	30	0.18	47	3.4	70	1.64	900	2280

It should be noted about the change of thermal properties of concrete with increasing temperature. According to Eurocode 2 general rules for structural fire design (*European Committee for Standardization*, 2004a), the thermal conductivity of concrete lie between the upper limit and lower limit, see Figure 5.32a. Higher concrete grade means lower water to cement ratio according to the design of concrete mixture (*Kosmatka et al.*, 2002; *European Committee for Standardization*, 2013b) and at the same time has higher value of weight density, which leads to higher value of thermal conductivity comparing to that of lower concrete grade. Therefore, the thermal conductivity of concrete grade C12/15 is assumed to be the same as the lower limit in Figure 5.32a. Concrete grade C40/50 takes the average value of upper limit and lower limit. Concrete grade C20/25 takes the average value of concrete grade C12/15 and C40/50. The specific heat capacity of concrete are assumed to be the same for all concrete grades and are taken according to Figure 5.32b.

The material properties of steel are taken as: Young's modulus 200 GPa, Poisson's ratio 0.33, thermal conductivity 18 W/m·K, Specific heat capacity 500 J/kg·K and mass density 7900 kg/m^3.

<div align="center">(a)   (b)</div>
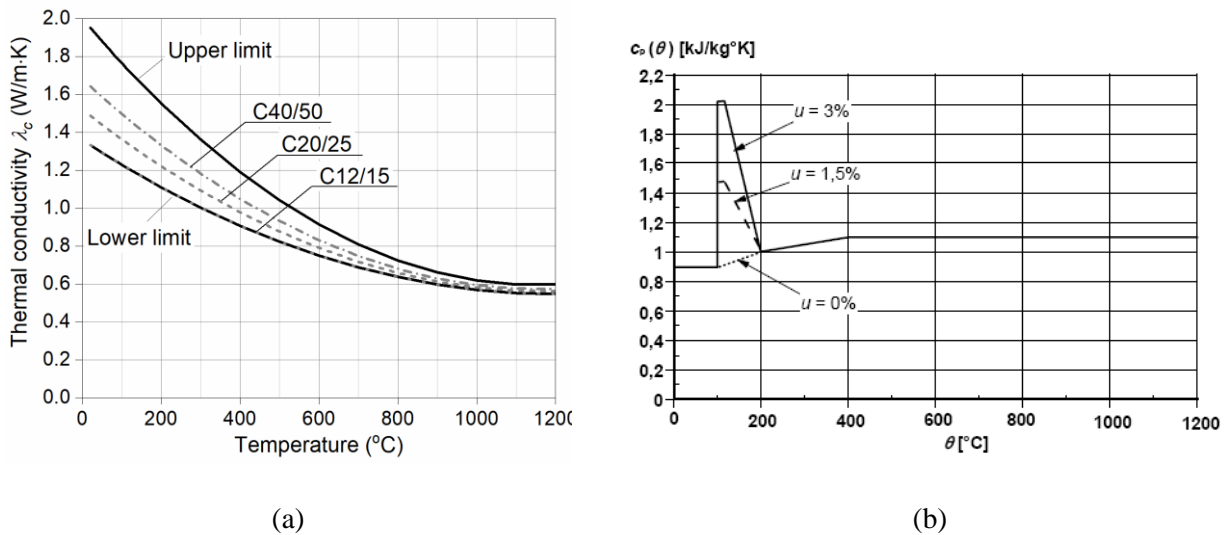
Figure 5.32 (a) Thermal conductivity of concrete as function of temperature; (b) specific heat as function of temperature (taken from Eurocode 2 Part 1-2 (*European Committee for Standardization*, 2004a)).

The fire loads are illustrated in Figure 5.33. For the sake of good replication of furnace temperature, the temperature curves for 15 min and 60 min of heating are direct simulation of the experimental heating and cooling curves. Then the curves for 30 min and 90 min of fire are similar to the curves for 15 min and 60 min of fire. The heating phases always follow standard ISO 834 fire curve. The shear load on anchor was realized by applying displacement controlled load towards free edge.
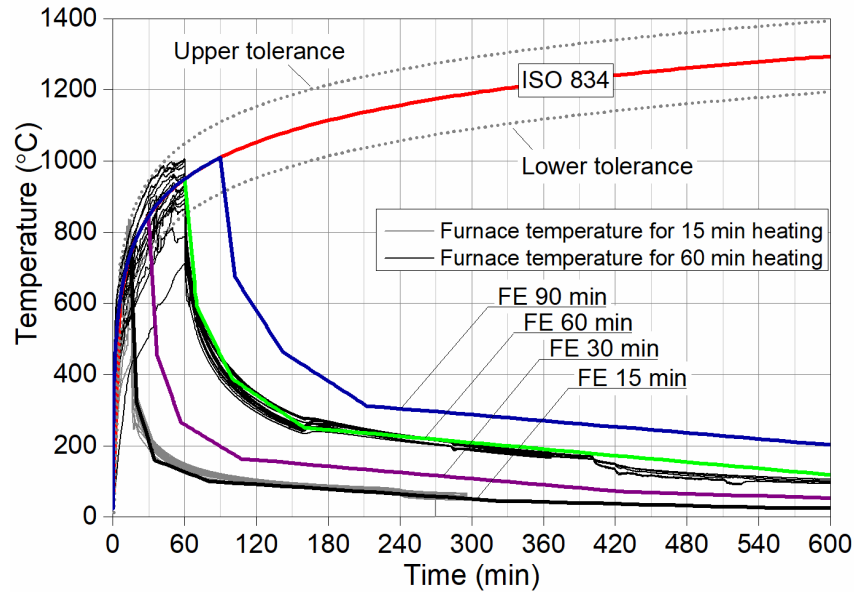
Figure 5.33 FE temperature curves for different heating and cooling regimes.

5.7.3. Numerical verification of temperature distribution in concrete slab

In this section the temperature profiles at positions as shown in Figure 5.3 are numerically verified with concrete slab models. Since in the tests the measured temperatures at those positions represent the temperature distributions in all the other relevant concrete slabs, the numerical verification of temperature distribution in the concrete slabs is the fundament for the temperature distribution analysis around anchors installed close to specimen edge and far away from specimen edge.

5.7.3.1. Finite element model

To save computing time, the temperature at the top of the concrete specimen is modelled according to Figure 5.34a, to which the positions of thermocouples are 200 mm away from the top surface of the specimen. The FE model is exposed to fire from the top, front and right side (three-sided fire). The fire exposure in the middle of the height of the specimen and at the bottom of the specimen (see Figure 5.3) is modelled as shown in Figure 5.34b. The FE model is therefore exposed to fire only from the front and right side (two-sided fire). The temperature curves for positions t5–t12 are compared with their counterparts in the experiments. Note that temperature curves for positions t9–t12 are compared directly with their corresponding positions at the top surface of the experiment (see Figure 5.3). The positions t5–t8 in the thermal analysis are compared with experimental pairs t1/t5, t2/t6, t3/t7 and t4/t8 in the experiment, since in the middle and at the bottom of the specimen, as shown in Figure 5.3, the fire conditions are the same.

(a)   (b)
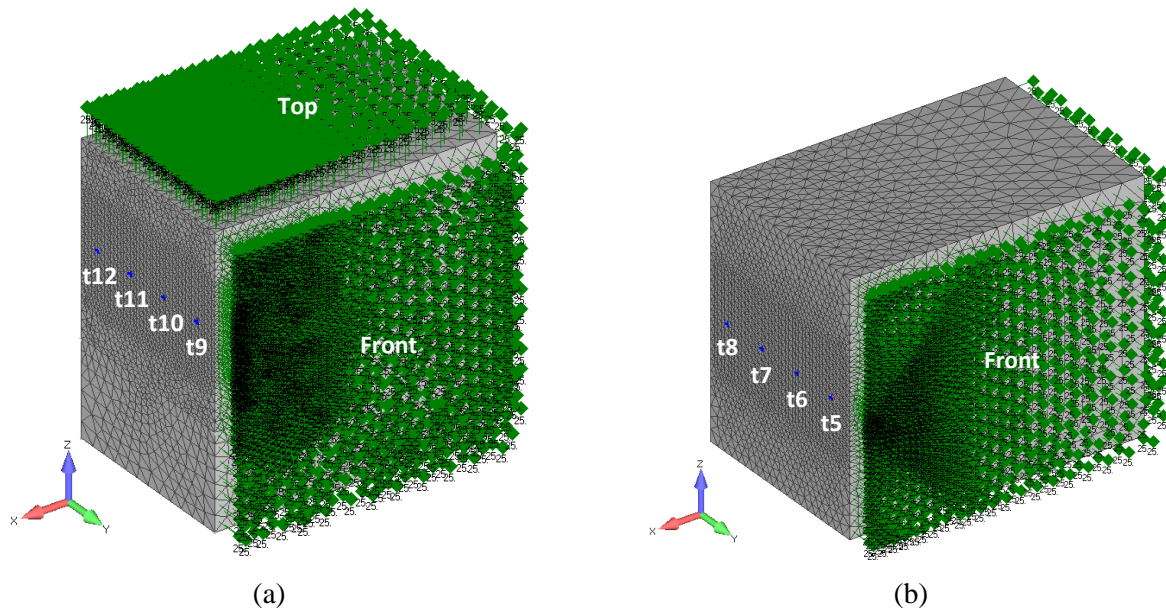
Figure 5.34 FE models for verification of temperature rise inside concrete. (a) Three-sided fire; (b) two-sided fire.

(a)   (b)
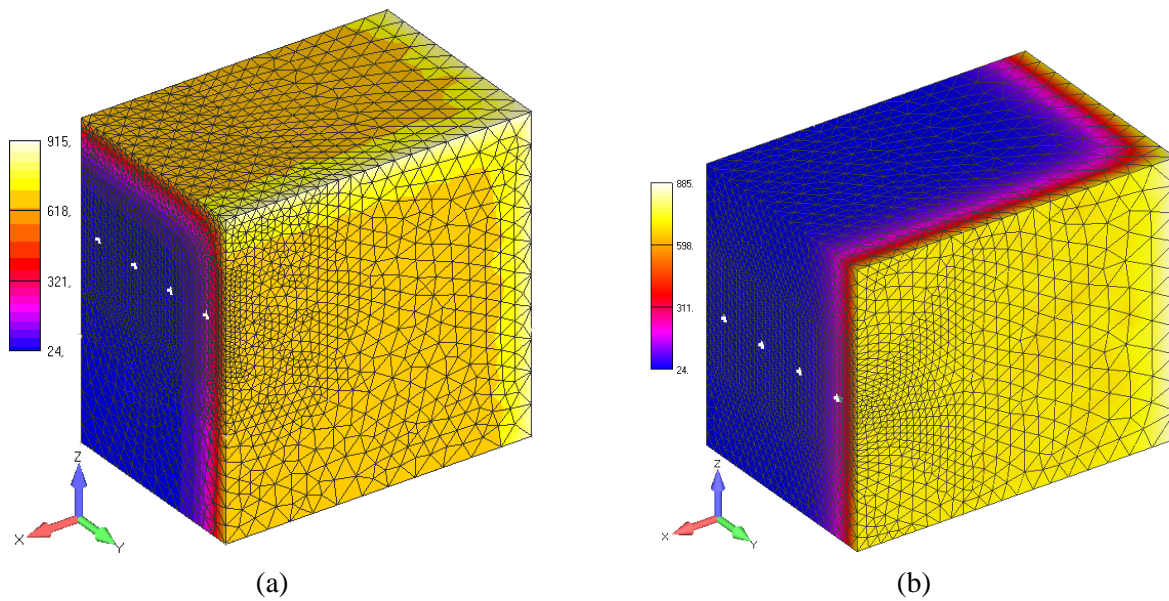
Figure 5.35 Temperature distribution obtained numerically after 60 min of heating. Concrete grade: C20/25.

5.7.3.2.   Temperature verification

Figure 5.35 shows the numerical temperature distribution for concrete grade C20/25 after 60 min of heating. For three-sided heating in Figure 5.35a and two-sided heating in Figure 5.35b the maximum temperature reaches 915 °C and 885 °C, respectively.

Figure 5.36 shows comparison of numerical temperature curves with experimental temperature curves at the corresponding measuring points after 15 min of heating. Figure 5.36a and b compare the temperature profiles in concrete C20/25 for three-sided fire and two-sided fire, respectively. The numerical curves agree very well with temperature measurements at each depth. Figure 5.36c and d show temperature profiles in concrete C40/50, which also show good agreement with the experimental data.

(a)   (b)

(c)   (d)
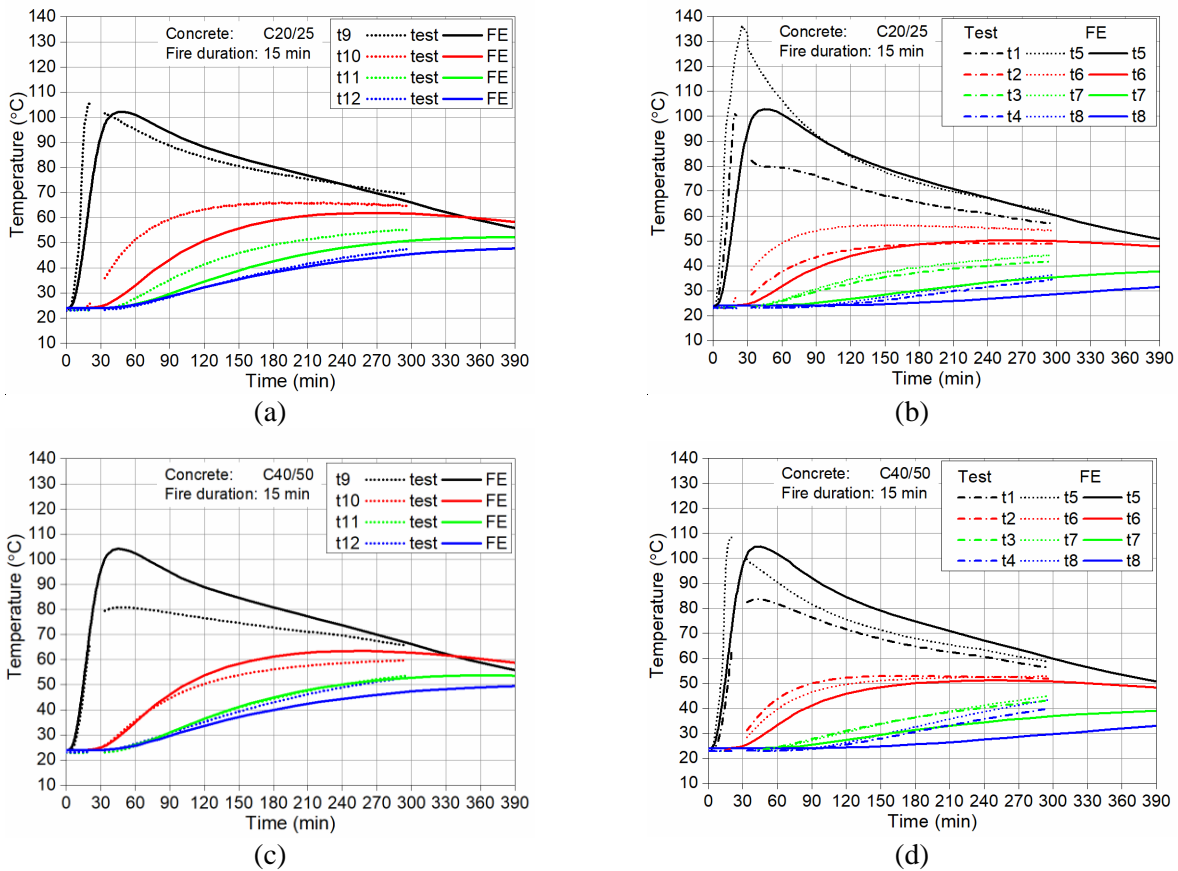
Figure 5.36 Temperature verification for 15 min ISO 834 fire. (a) Three-sided fire and (b) two-sided fire for concrete grade C20/25; (c) three-sided fire and (d) two-sided fire for concrete grade C40/50.

In Figure 5.37 is shown the comparison between numerical temperature curves and experimental temperature curves for 60 min of heating, in which (a) and (b) are for concrete C20/25, and (c) and (d) are for concrete grade C40/50. It can be seen that the temperature is well described numerically in shallow regions (close to the heated surfaces) for three-sided heating; however, in

deep regions (far from the heated surfaces) the numerical results overestimate the experimental results (see Figure 5.37a and c). From Figure 5.37b and d, it shows that the numerical curves give good agreement with the experimental measurements for two-sided heating.

Having in mind the complexity of the problem and the differences between the theoretical and experimental boundary conditions, the agreement between measured and calculated temperature profile is reasonably good.

(a)

(b)

(c)

(d)
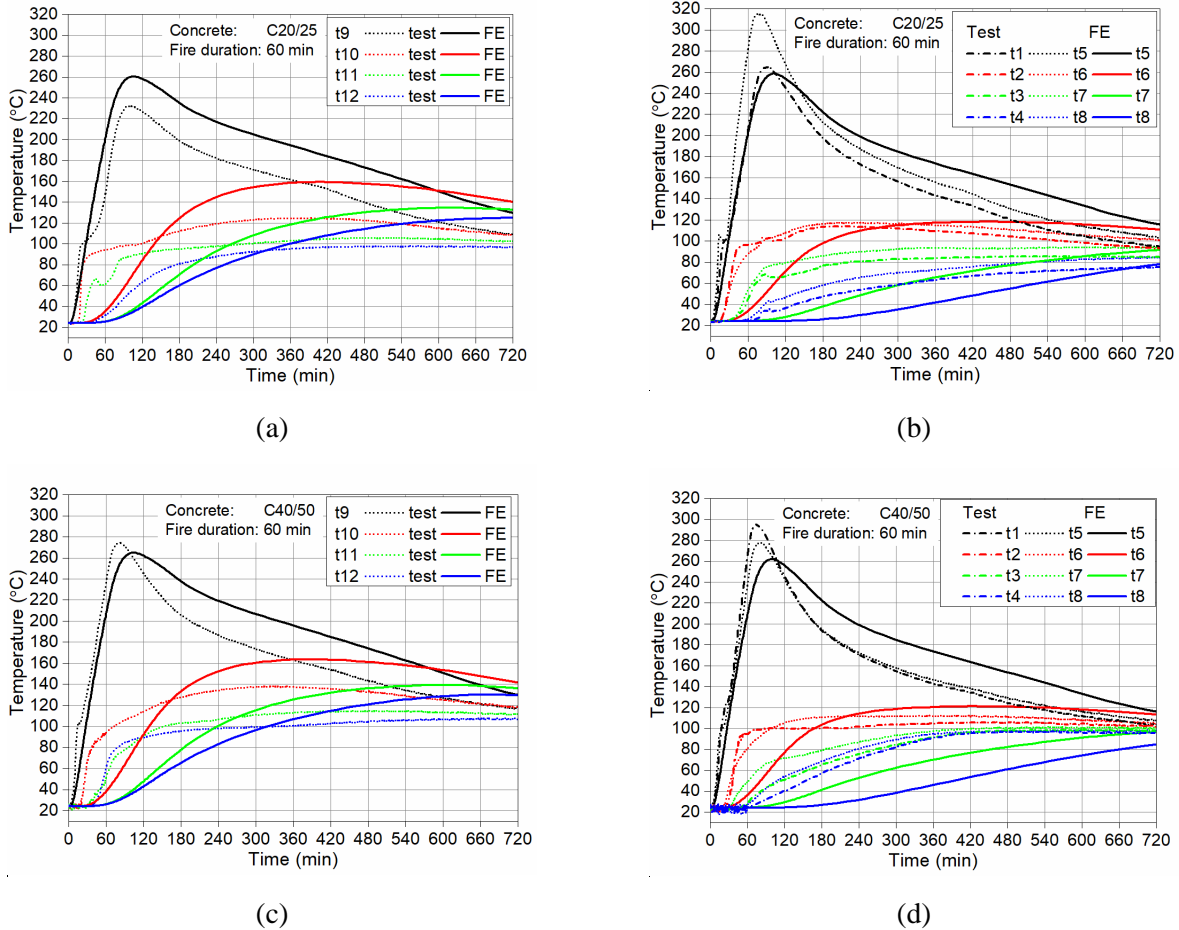
Figure 5.37 Temperature verification for 60 min ISO 834 fire. (a) Three-sided fire and (b) two-sided fire for concrete grade C20/25; (c) three-sided fire and (d) two-sided fire for concrete grade C40/50.

5.7.4. Temperature distribution around anchor

Figure 5.38 shows typical temperature distribution of anchors with edge distance of 75 mm and 150 mm after exposing to fire. For anchors with the same embedment depth, the temperature field around the anchor is mainly affected by the edge distance, due to the heating from the front face. After 30 min of fire exposure, the temperature penetration reaches the head of anchor with edge

distance of 75 mm, which happens to anchor with edge distance of 150 mm only after 60 min of fire.

$fi(t)$ (min)	(a) 2c75h95d25; C20/25	(b) 2c150h95d25; C20/25
15		
30		
60		
90		
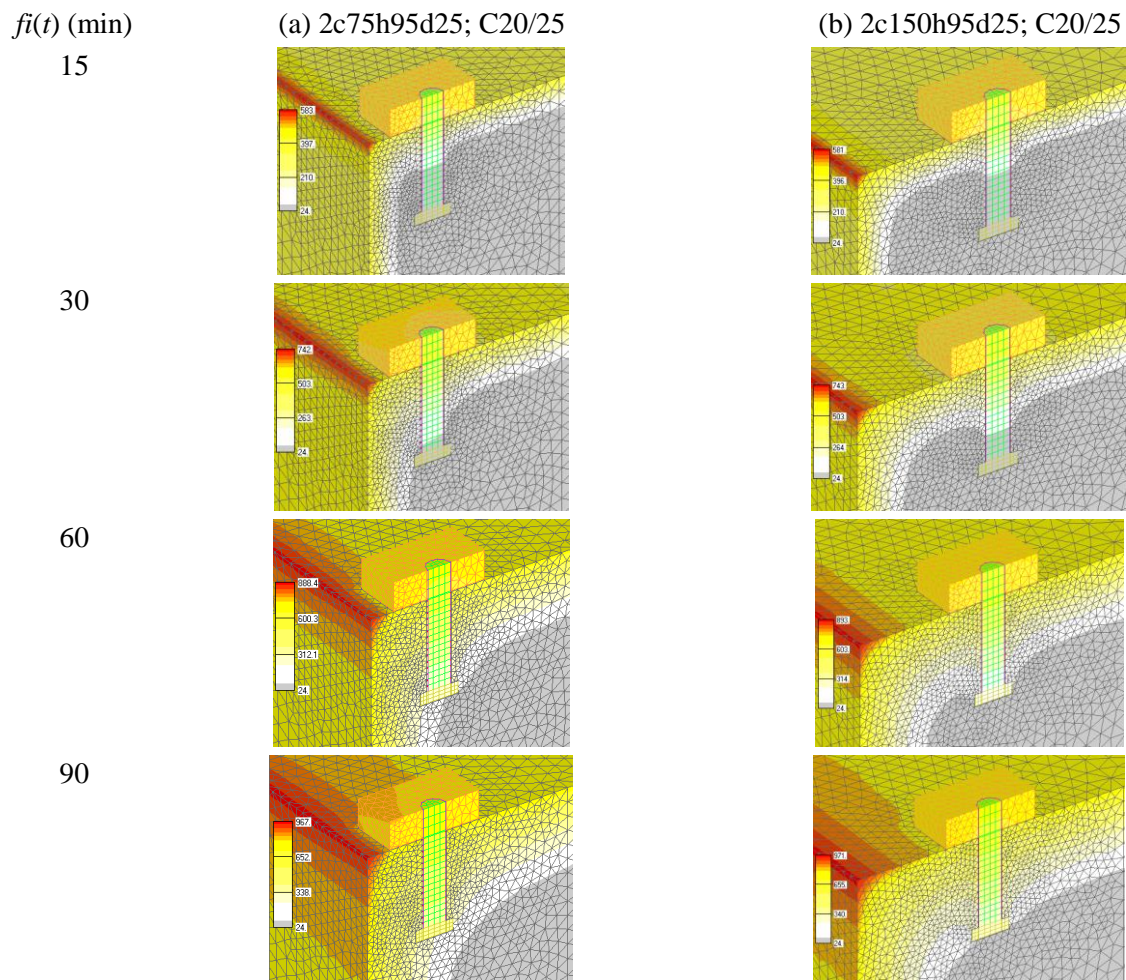
Figure 5.38 Numerical temperature distribution of anchors embedded in concrete C20/25 exposed to fire on both sides of the edge. (a) Edge distance c_1 = 75 mm; (b) Edge distance c_1 = 150 mm.

5.7.5. Typical failure mode

In Figure 5.39 are shown the numerical fracture patterns for anchor with edge distance of 75 mm (2c75h95d25) loaded towards free edge after fire exposure. The figures indicate the fractures at
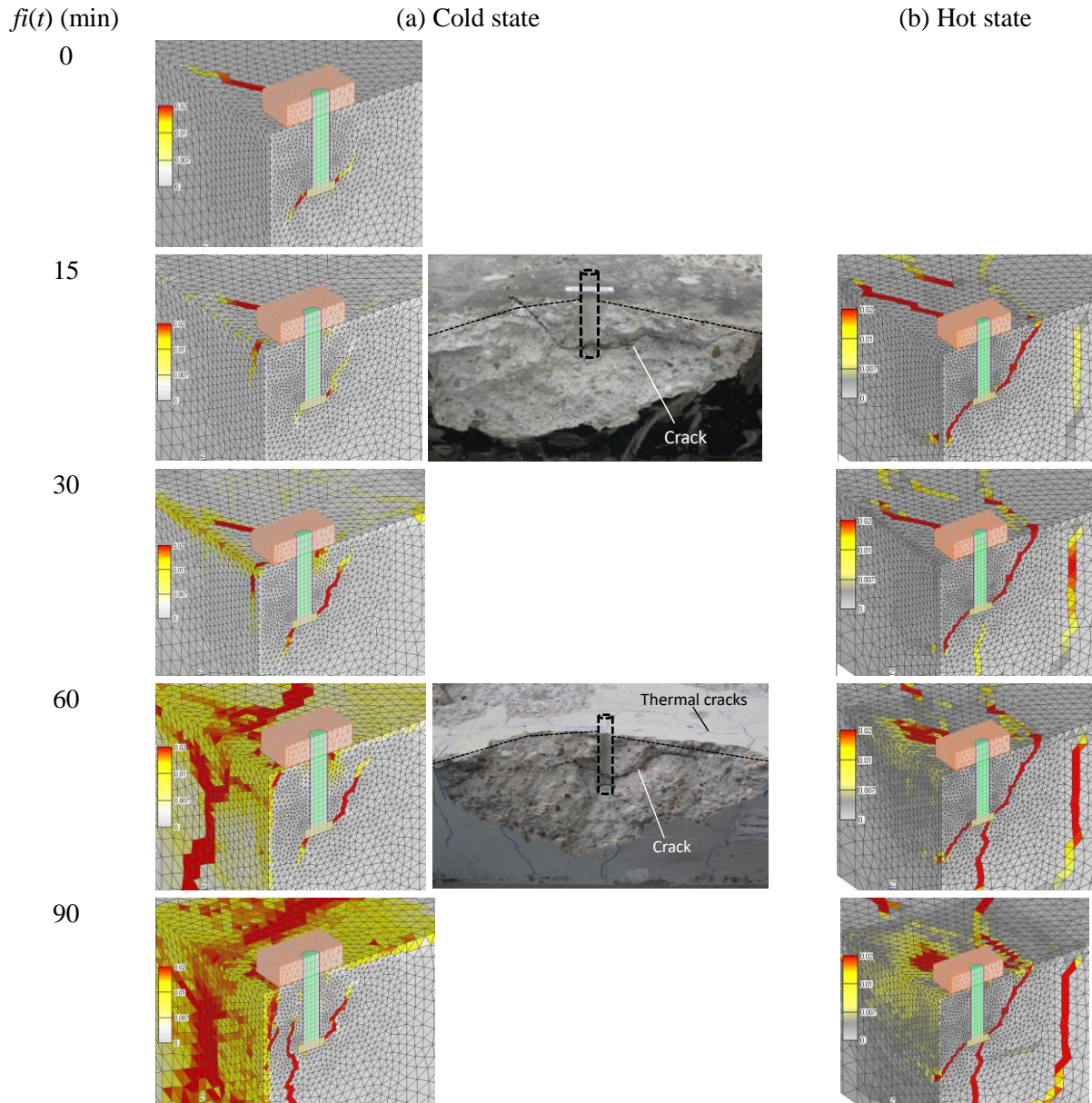
Figure 5.39 Numerical fracture patterns of anchor 2c75h95d25 loaded in shear in concrete C20/25 after different fire durations. (a) Cold state – FE and test; (b) hot state. Loading direction: towards free edge.

the peak loads. Fracture patterns after 15 min and 60 min of fire exposure obtained experimentally are also presented in Figure 5.39a to compare with corresponding numerical fracture patterns. It can be seen that the comparison indicates a good agreement with each other. At ambient temperature and after 15 min of fire, the fracture for the cold state loading starts at the position of the upper side of the shaft. The crack at the rear side of the head is initiated afterwards. However, after prolonged fire duration, both cracks are developing almost at the same time and cracks on the surface are widely spread. For the cracks in the hot state loading, it can be seen that they are developing basically at the same time. It can be clearly seen that the damage of concrete

104

for the cold state is higher than for the hot state. Consequently, crack patterns are slightly different and, as will be shown later, the resistance is for the cold state lower than for the hot state.

5.7.6. Load-displacement curve

5.7.6.1. Verification analysis

Figure 5.40 shows the comparison between the numerical and experimental load-displacement curves after fire exposure. The load-displacement curves for anchors with different edge distance are shown. It can be seen that the numerical curves predict stiffer response than the experimental curves, especially for the anchor with small edge distance. As stated previously, this can be attributed to the local damage of concrete, which cannot be accounted for in the macroscopic finite element analysis. Nevertheless, the peak loads are very well predicted and this is also true for the ductility of the load-displacement response.
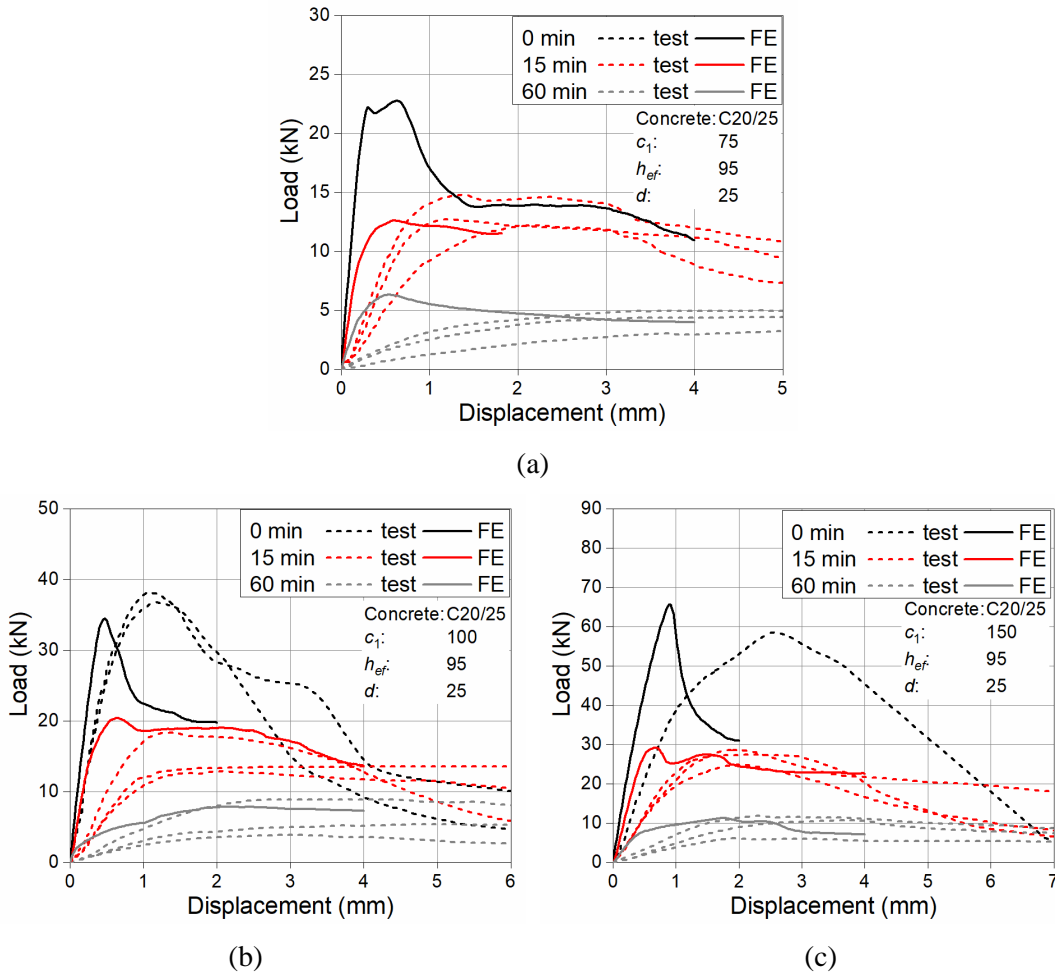
Figure 5.40 Comparison between numerical and experimental load-displacement curves at ambient temperature, after 15 min and 60 min of fire exposure in concrete grade C20/25. (a) 2c75h95d25; (b) 2c100h95d25; (c) 2c150h95d25.

To further verify the numerical prediction, Figure 5.41 shows the comparison between the numerical and experimental load-displacement curves after fire exposure for the anchors with large embedment depth of 140 mm (Figure 5.41a), large diameter of 32 mm (Figure 5.41b) and for concrete grade C40/50 (Figure 5.41c). The same as shown in Figure 5.40, stiffer load-displacement response can be seen, especially for anchor with large diameter of 32 mm (see Figure 5.41b). Moreover, the peak loads and the general load-bearing behaviour at ambient temperature and after fire exposure are reasonably well predicted by the numerical models. Therefore, the numerical parametric studies are further carried out to study the influence of parameters specified in Table 5.3.

(a)

(b)

(c)
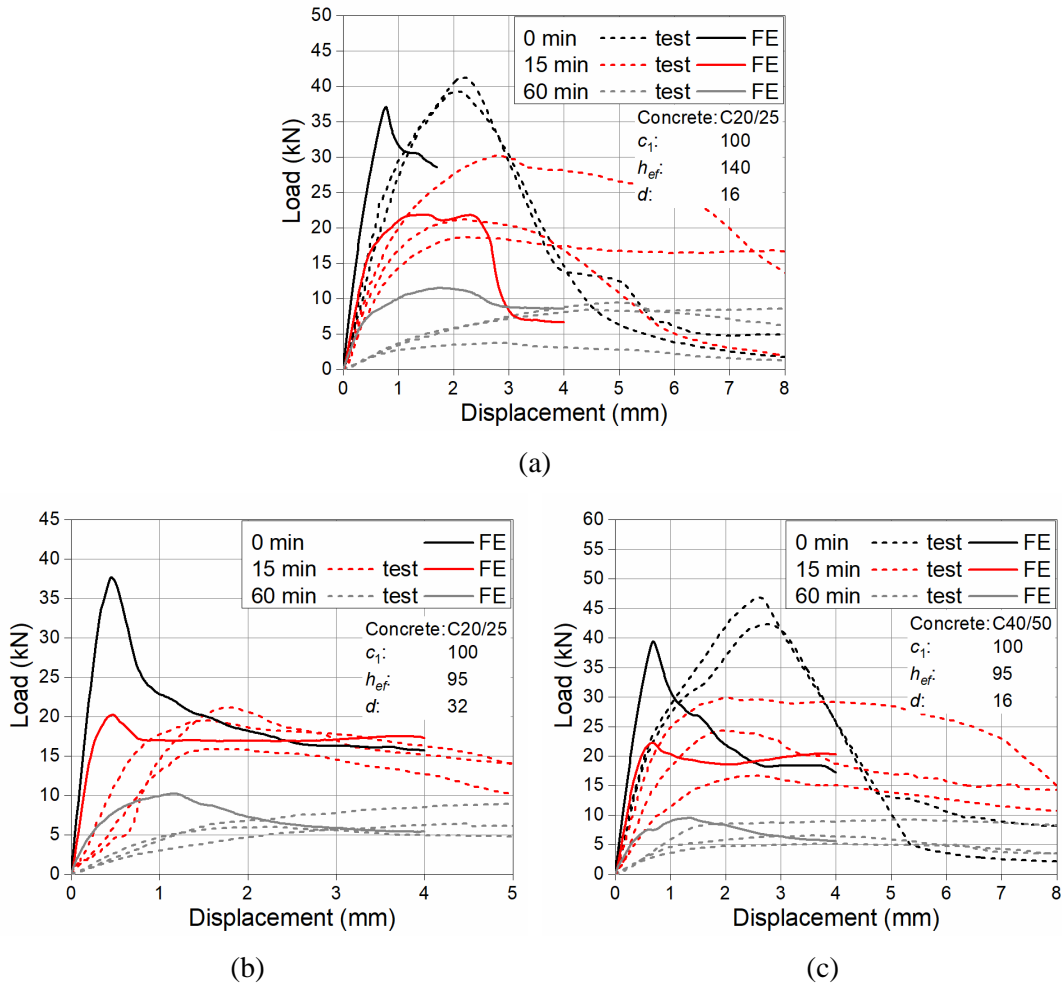
Figure 5.41 Comparison between numerical and experimental load-displacement curves at ambient temperature, after 15 min and 60 min of fire exposure. (a) 2c100h140d16, large embedment depth; (b) 2c100h95d32, large diameter; (c) 2c100h95d16, concrete grade C40/50.

5.7.6.2. FE curves in the cold and hot state

The resistance of anchor in case of concrete edge failure after fire exposure of 90 min was found to be higher for the hot state than the cold state by both experimental and numerical programs in

Chapter 4. Representative load-displacement curves for anchorage configurations in Table 5.3 are presented in this section to show comparisons between the load-bearing behaviour in the cold and hot states.

It is know the concrete edge failure resistance is mainly dependent on the edge distance. After fire exposure, the embedment depth and concrete strength may play a significant role since the location of anchors matters with respect to the heat penetration and the original concrete strength determines the concrete strength after fire exposure. Therefore, in the following the numerical load-displacement curves regarding these factors are presented.

Figure 5.42 shows the load-displacement curves obtained numerically for single headed stud anchors in both the hot and cold states after 15 min, 30 min, 60 min and 90 min of fire exposure. The concrete grade is C12/15. Figure 5.42a, b and c are for anchors with different embedment depth, and Figure 5.42d, e and f are for anchors with different edge distance.
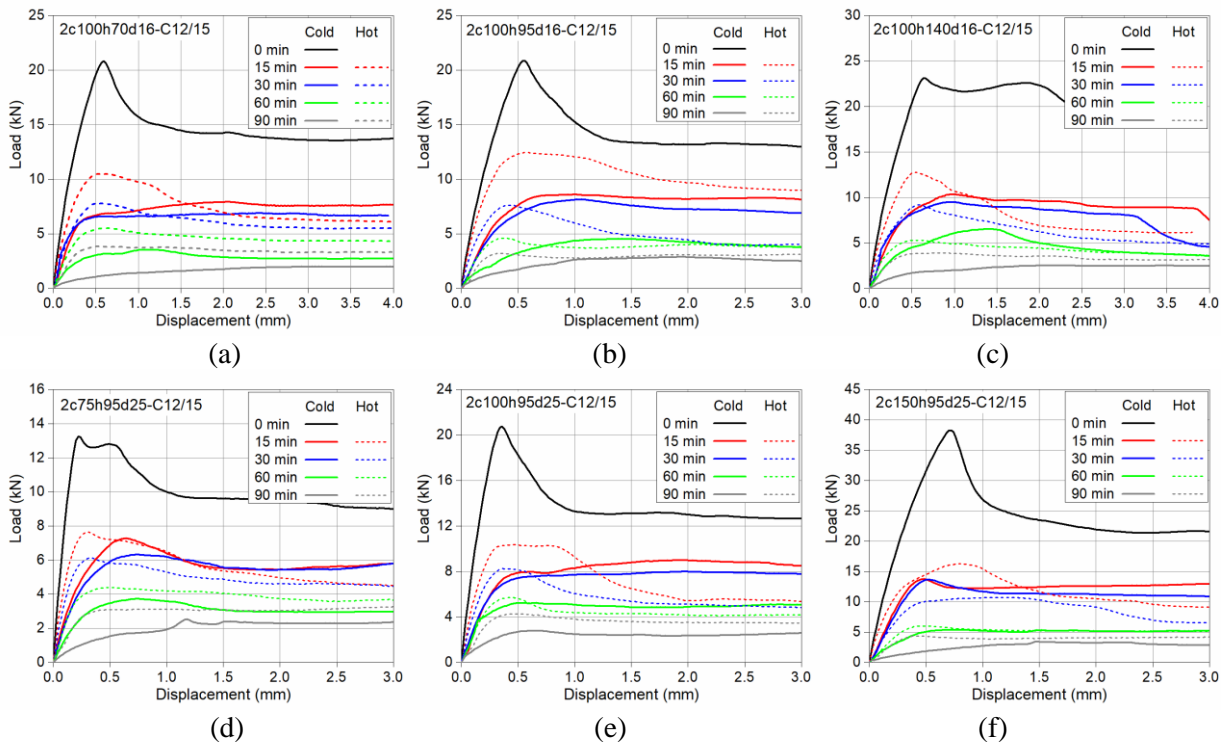
Figure 5.42 Numerical load-displacement curves of single headed stud anchors in the cold and hot state after fire exposure. Concrete grade: C12/15. (a) 2c100h70d16; (b) 2c100h95d16; (c) 2c100h140d16; (d) 2c75h95d25; (d) 2c100h95d25; (d) 2c150h95d25.

For all configurations it can be seen that the load-displacement response for the hot state is remarkably stiffer than for the cold state. In the hot state the peak load is higher comparing to that in the cold state. It is worth noting that hot state resistance after 60 min and 90 min of fire exposure is obviously higher than that in the cold state, which is consistent with the findings for

90 min of fire exposure in Chapter 4. However, for short period of fire exposure the difference between the hot state and the cold state is not always distinct. This may due to the concrete property after fire load. After long duration of fire exposure with temperature over 900 °C, the cooling process leads to severe damage to concrete, resulting low tensile strength. For short period of fire exposure and lower temperature, the damage due to cooling is not pronounced.

Figure 5.43 shows the numerical load-displacement curves of single headed stud anchors in both the hot and cold states after 15 min, 30 min, 60 min and 90 min of fire exposure for concrete grade C20/25. Basically the same phenomenon can be seen as that for anchors in concrete C12/15.
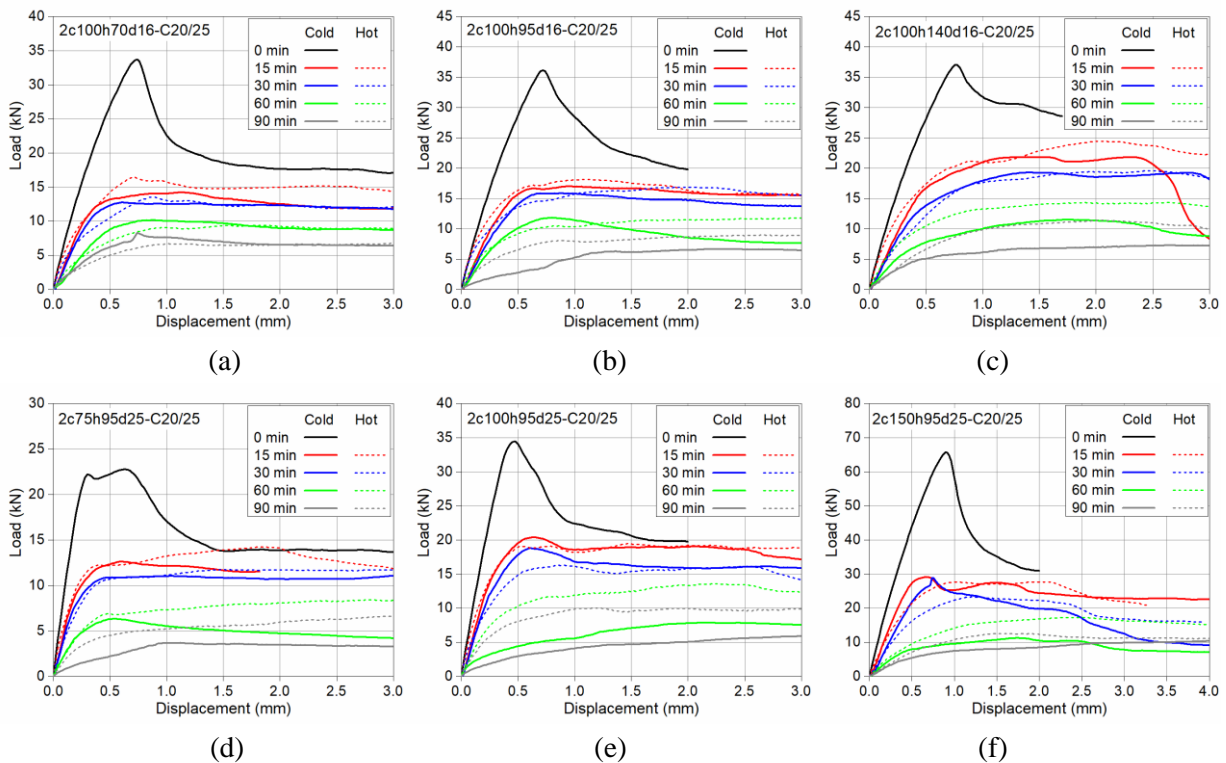
Figure 5.43 Numerical load-displacement curves of single headed stud anchors in the cold and hot state after fire exposure. Concrete grade: C20/25. (a) 2c100h70d16; (b) 2c100h95d16; (c) 2c100h140d16; (d) 2c75h95d25; (d) 2c100h95d25; (d) 2c150h95d25.

5.7.7. Resistance

Peak loads obtained from numerical analysis are summarized in Annex B Table B.2 . The numerical results are firstly verified based on experimental results. Then a prediction formula is developed according to the evaluation of numerical results.

5.7.7.1. Comparison between numerical and experimental resistance

The numerically obtained peak loads are firstly compared with experimental results. From Figure 5.44 it is seen that FE results can replicate the peak load obtained experimentally well. As already noticed in the load-displacement curves, the reduction of resistance from 15 min to 30 min of fire is not strong. Otherwise a continuous decrease of resistance can be observed. Detailed comparisons between the numerical and experimental results are shown in Figure 5.45.

(a)   (b)
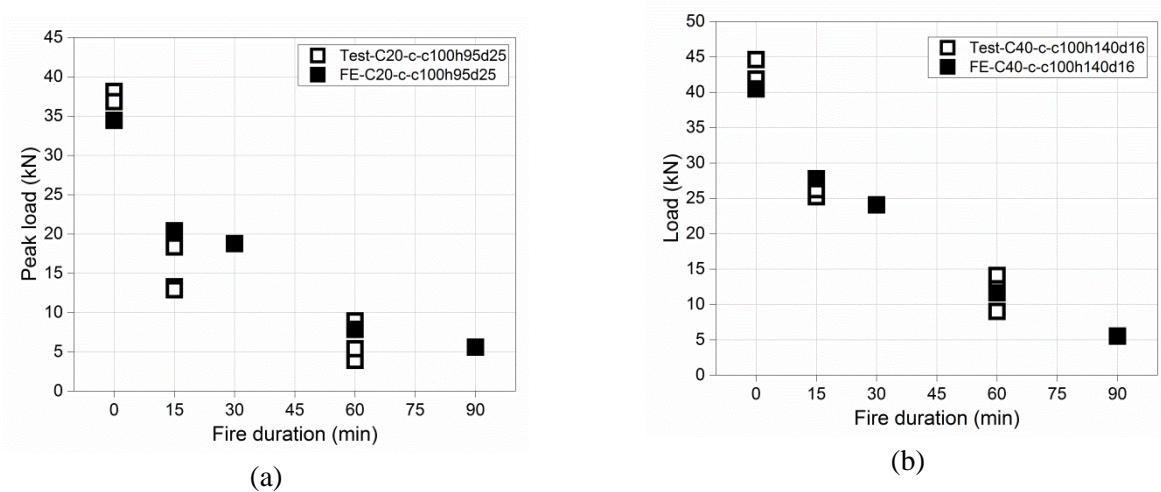
Figure 5.44 Examples of experimental and numerical results.

From Figure 5.45a and b, it can be demonstrated that the numerical and experimental results agrees with each other very well. The ratio of experimental results to numerical results has a mean value of 0.93 with SD = 0.15 and 0.99 with SD = 0.19 for ambient condition and 15 min of fire exposure, respectively. After 60 min of fire, the scatter of the data is becoming larger. The mean of the ratio is 0.81 with SD = 0.26 (Figure 5.45c). After 90 min of fire, the mean is 0.91 but with a relatively large SD equalling 0.37. Since the number of experimental results is rather limited, it is therefore concluded that the calculated peak loads are reasonably well to represent the experimental resistances.
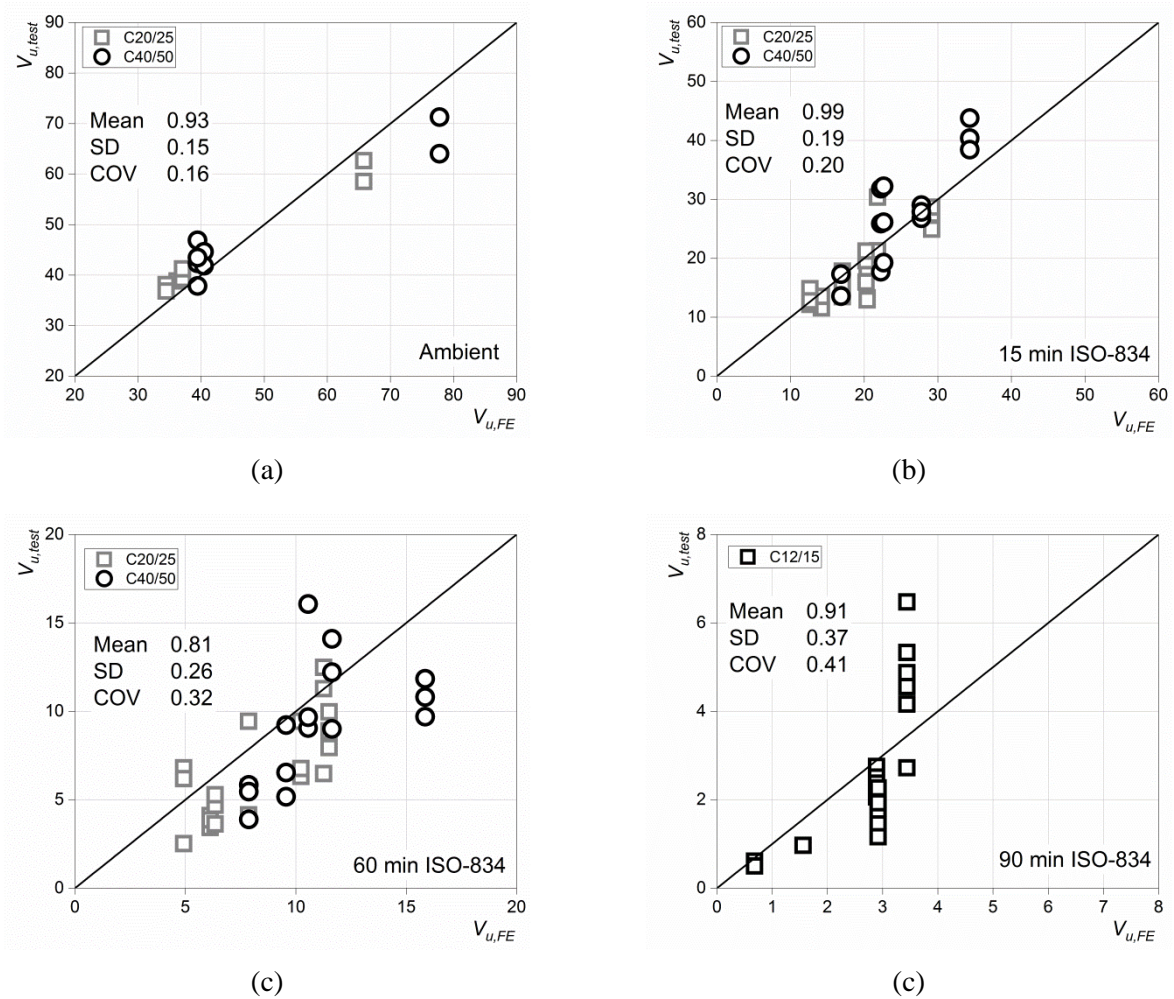
Figure 5.45 Comparison between experimental and numerical results after (a) 0 min, (b) 15 min, (c) 60 min, and (d) 90 min ISO-834 fire.

5.7.7.2. Prediction formula

From previous sections it is evident that the anchors loaded in shear perpendicular to free edge after exposing to fire behave differently compared to their behaviour under ambient conditions. The anchor diameter d and embedment depth h_{ef}, which play little role in the resistance at ambient temperature, show a significant influence on the concrete edge failure resistance after fire exposure. On the other hand, the edge distance c_1, which is one of the main factors affecting the concrete edge resistance at ambient temperature, becomes relatively less important in the post-fire resistance.

Based on the experimental and numerical results, a model for predicting the cold state capacity corresponding to concrete edge failure after fire exposure is proposed as:

$$V_{u,c}^{fi} = k_{fi(t)} \cdot d_{nom}^{\alpha_{fi(t)}} \cdot h_{ef}^{\beta_{fi(t)}} \cdot f_{cm}^{\gamma_{fi(t)}} \cdot c_1^{\varepsilon_{fi(t)}} \tag{5.6}$$

110

where d_{nom}, h_{ef}, f_{cm} and c_1 are the same as in Equation (2.7), $fi(t)$ represents fire duration of heating defined by the standard fire curve ISO 834. Thus, the following parameters are required to be obtained as a function $\phi()$ of fire duration $fi(t)$:

$$k_{fi(t)} = k_0\phi(fi(t)) \text{ where } k_0 = 3.27 \text{ at ambient temperature} \qquad (5.7)$$

$$\alpha_{fi(t)} = \alpha_0\phi(fi(t)) \text{ where } \alpha_0 \text{ is the same as in Equation } (2.7) \qquad (5.8)$$

$$\beta_{fi(t)} = \beta_0\phi(fi(t)) \text{ where } \beta_0 \text{ is the same as in Equation } (2.7) \qquad (5.9)$$

$$\gamma_{fi(t)} = \gamma_0\phi(fi(t)) \text{ where } \gamma_0 = 0.5 \text{ at ambient temperature} \qquad (5.10)$$

$$\varepsilon_{fi(t)} = \varepsilon_0\phi(fi(t)) \text{ where } \varepsilon_0 = 1.5 \text{ at ambient temperature} \qquad (5.11)$$

The basic form of Equation (5.6) maintains the basic format of the equation according to EN1992-4 (refer to Equation (2.6) or (2.7)). In order to consider the influence of fire, the exponents used in Equation (2.7) are modified to consider the fire duration in Equation (5.6). The derivations of the expressions for these exponents as a function of the fire exposure duration ($fi(t)$, in minutes) are depicted in the following.

All numerically obtained resistances for anchor configurations in Table 5.3 are evaluated. The influences of concrete strength f_{cm}, diameter d, concrete edge distance c_1 and embedment depth h_{ef} on the resistance of anchors respectively at ambient temperature, after 15min, 30 min, 60 min and 90 min of fire exposure are obtained by analogy with analyses from Chapters 5.6.5–5.6.7. The variations of parameters as a function of fire duration are presented in Figure 5.46 and Figure 5.47.

Figure 5.46a shows the variation of the exponent $\alpha_{fi(t)}$ to consider the influence of the shaft diameter on the ultimate load as a function of the duration of fire, $fi(t)$. Based on the fitting of the numerical data, the exponent $\alpha_{fi(t)}$ follows an exponential function as:

$$\alpha_{fi(t)} = \alpha_0 + 0.44 - 0.44 \times 0.98^{fi(t)} \qquad (5.12)$$

where α_0 is the initial value of the exponent $\alpha_{fi(t)}$ at ambient temperature (refer to Equation (2.6)). The exponent $\alpha_{fi(t)}$ which considers the influence of anchor diameter accounts for the bearing stress distribution (*Eligehausen et al.*, 2006) on the anchor shaft. Larger shaft diameter means greater contact area between concrete and anchor. When the shear load is applied, the stress concentration at the upside of the shaft, where the cracks initiate, is less for large shaft diameter, which leads to a relatively large fracture body. With increasing duration of fire, more damage occurs in the concrete and the effect of this stress distribution due to shear loading will be

enhanced. Moreover, with increase of anchor diameter the anchor gets stiffer and the transfer of load deeper into the concrete, that is less damaged, is more pronounced.

Figure 5.46b shows the variation of the exponent $\beta_{fi(t)}$ to consider the influence of embedment depth on the peak load after fire exposure. Similar to the exponent $\alpha_{fi(t)}$, the value of the exponent $\beta_{fi(t)}$ increases with increasing fire duration. This tendency is as follows:

$$\beta_{fi(t)} = \beta_0(8.5 - 7.5 \times 0.96^{fi(t)})$$ (5.13)

where β_0 is the initial value of the exponent $\beta_{fi(t)}$ at ambient temperature (refer to Equation (2.6)). The fracture surfaces obtained from experiments reveal that the fracture angle for anchors with large embedment depths (θ_2 in Figure 5.46b) is greater than the fracture angle for anchors installed with shallow embedment depths (θ_1 in Figure 5.46b). This effect is especially prominent for longer fire exposure, due to severely damaged concrete. Subsequently, the influence of h_{ef} increases remarkably with increasing fire duration, which is considered through the exponent $\beta_{fi(t)}$ as a function of fire duration.
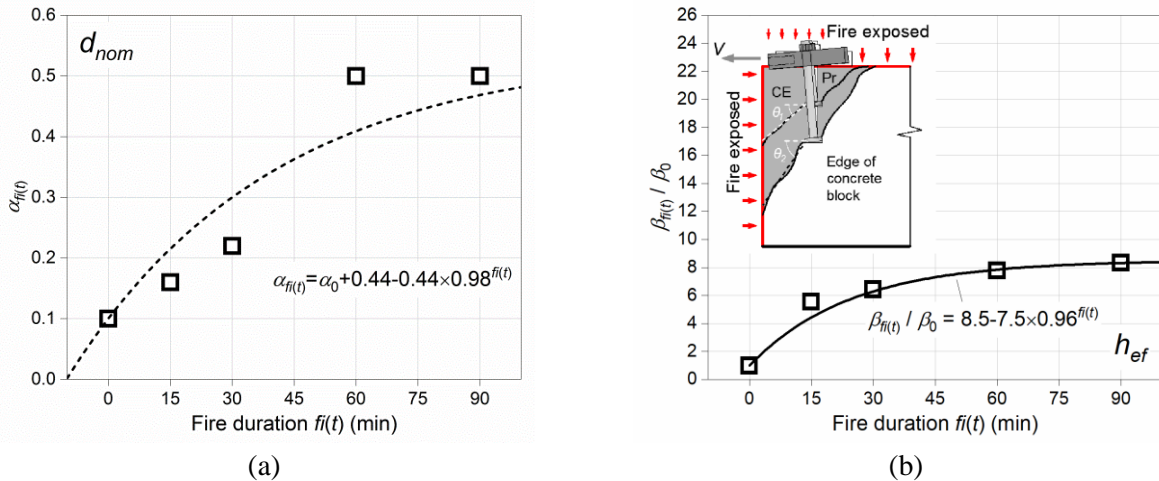
Figure 5.46 The variation of (a) exponent $\alpha_{fi(t)}$ to consider the influence of nominal diameter and (b) exponent $\beta_{fi(t)}$ to consider the influence of embedment depth on the ultimate load of anchors after fire duration $fi(t)$ according to numerical results.

Figure 5.47a shows the variation of the exponent $\gamma_{fi(t)}$ to consider the influence of concrete compressive strength on the ultimate load after fire duration $fi(t)$. The variation can be expressed as:

$$\gamma_{fi(t)} = \gamma_0(1.5 - 0.5 \times 0.9^{fi(t)})$$ (5.14)

where γ_0 is the initial value of the exponent $\gamma_{fi(t)}$ at room temperature and is equal to 0.5 as given in (2.6). Equation (5.14) suggests that concrete strength has an obviously high influence on the

112

concrete edge failure load after fire exposure, however, with prolonged fire exposure the influence is likely to keep constant.

Figure 5.47b shows the variation of the exponent $\varepsilon_{fi(t)}$ to consider the influence of edge distance c_1 on concrete failure load after fire exposure. It can be seen that the influence of the edge distance is slightly reduced with increasing fire exposure $fi(t)$. This reduction is obvious already after 15 min of fire. Beyond 15 min it is almost constant up to 60 min of fire. This reduction can be expressed as follows:

$$\varepsilon_{fi(t)} = \varepsilon_0(0.78 + 0.22 \times 0.92^{fi(t)}) \tag{5.15}$$

where ε_0 is the initial value of the exponent $\varepsilon_{fi(t)}$ at room temperature and is equal to 1.5. The decreasing effect of the edge distance can be attributed to the pronounced reduction of the peak load after fire exposure. Nevertheless, it still plays a significant role in the load carrying capacity of concrete edge failure.

(a)   (b)
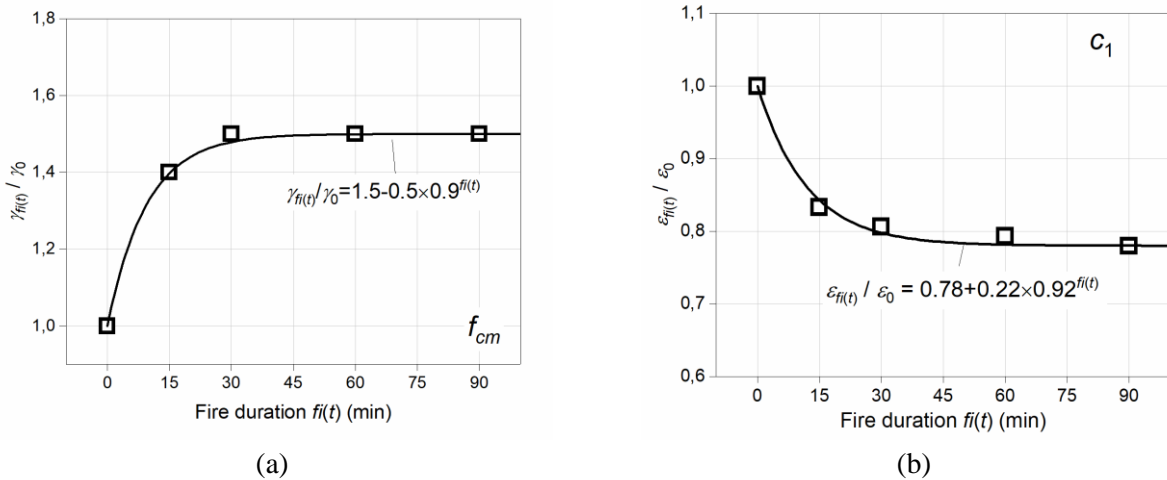
Figure 5.47 The variation of (a) exponent $\gamma_{fi(t)}$ to consider the influence of concrete compressive strength and (b) exponent $\varepsilon_{fi(t)}$ to consider the influence of edge distance on the ultimate load of anchors after fire duration $fi(t)$ according to numerical results.

By substituting Equations (5.12)–(5.15) into Equation (5.6) the following equation is obtained for the shear resistance of anchors as a function of fire duration:

$$V^0_{u,c,fi(t)} = k_{fi(t)} \cdot d_{nom}^{\alpha_0+0.44-0.44\times0.98^{fi(t)}} \cdot h_{ef}^{\beta_0(8.5-7.5\times0.96^{fi(t)})} \cdot f_{cm}^{\gamma_0(1.5-0.5\times0.9^{fi(t)})} \cdot$$
$$c_1^{\varepsilon_0(0.78+0.22\times0.9^{fi(t)})} \tag{5.16}$$

By inserting the numerical peak loads together with parameters accounting for the anchor configurations into Equation (5.16), from regression analyses the factor $k_{fi(t)}$ can be expressed as a function of fire duration as follows:

$$k_{fi(t)} = 3.3(1 + fi(t)/20)^{-2.9} \tag{5.17}$$

In Figure 5.48, comparisons between the calculated (Equation (5.16)) and numerical peak loads are shown. With respect to different concrete edge distance in Figure 5.48a, it is seen that the Equation (5.16) can predict the results very well. At ambient temperature the peak load differences is large. With prolonged fire duration, the peak loads are gradually unifying. Figure 5.48b, c and d show that Equation (5.16) can realistically reflect the influence of diameter, embedment depth and concrete strength on the resistance with increasing fire duration, respectively. It is obvious that the influence of diameter and embedment depth is relatively small, while the concrete strength plays an important role in determining the resistance after fire.
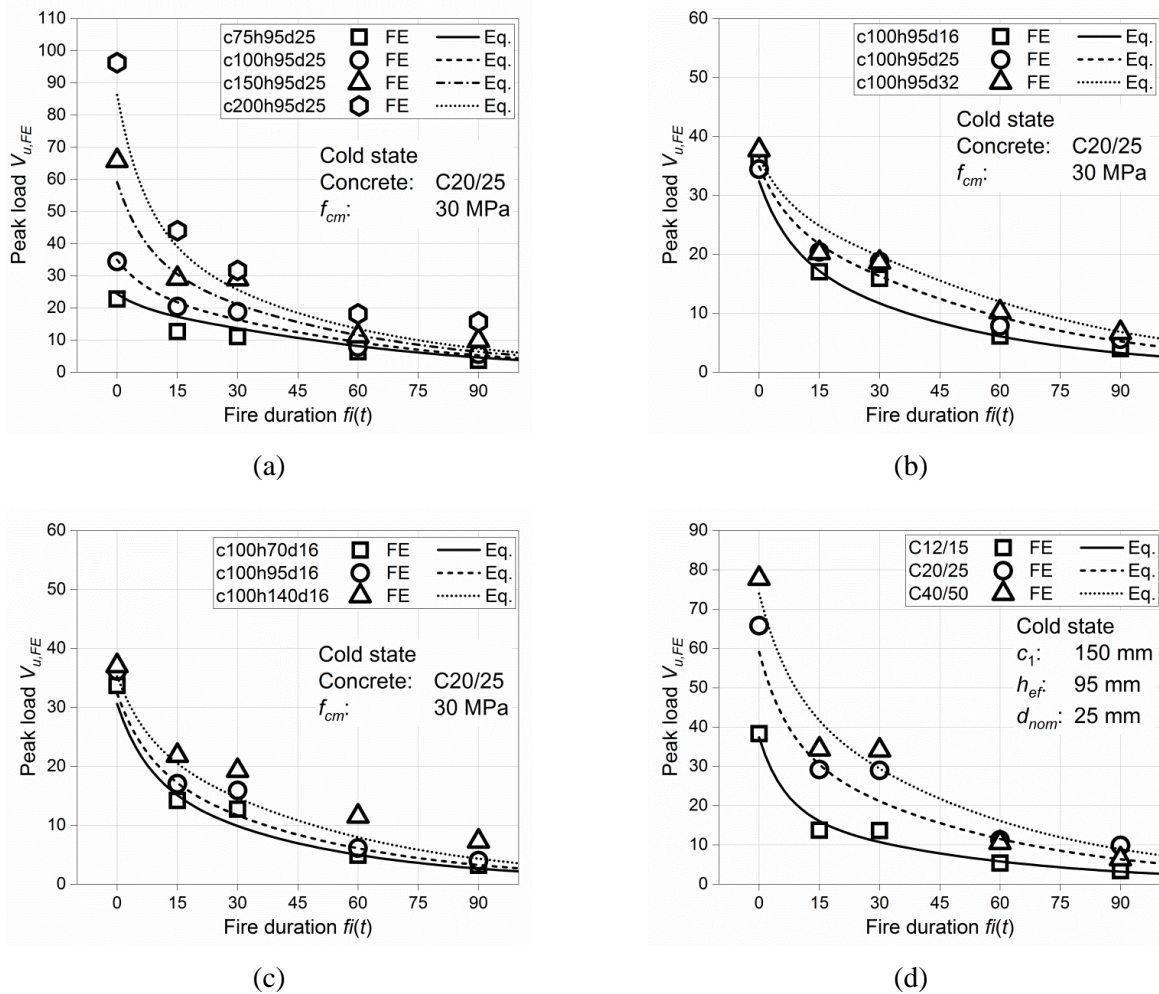
Figure 5.48 Comparison between the numerical results and calculated results according to Equation (5.16) with respect to different (a) edge distance, (b) diameter, (c) embedment depth and (d) concrete strength.

It can also be seen that just after 15 minutes of fire exposure, the resistance of the anchorages against concrete edge failure reduces by around 50%. After 60 min of fire, anchors have a remaining resistance of only 15% of the reference resistance, irrespective of the configuration of the anchors, which implies almost unified reduction due to severely thermally damaged concrete, i.e. strongly reduced tensile strength and fracture energy of concrete. It may be noted that this reduction corresponds to approximately the same as given for the fire exposure up to 90 min in the current Eurocode 2 (*European Committee for Standardization*, 2018), as shown in Equation (2.26).

Figure 5.49 presents the numerical and experimental peak loads versus the calculated peak loads according to Equation (5.16) after different fire durations. Note that no experimental result for 30 min of fire exposure is available. It is seen that at ambient temperature, after 15 min and 30 min of fire exposure, Equation (5.16) can very well take into account all the influential parameters. Only after 60 min and 90 min of fire, the comparison shows a relative large scatter. Nevertheless, Equation (5.16) is appropriate on predicting the concrete edge failure load of single stud anchors after fire exposure, considering the complex parameters involved in such problem and limited data base.

(a)

(b)   (c)

(d)   (e)
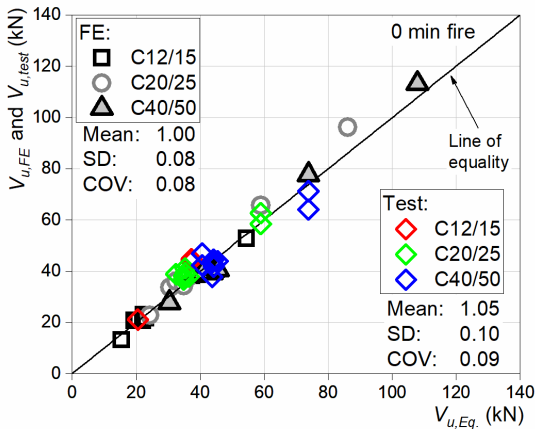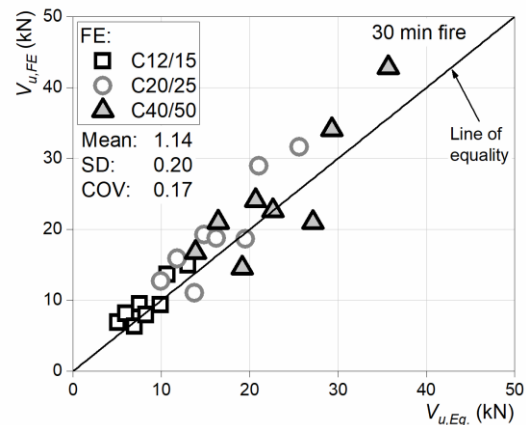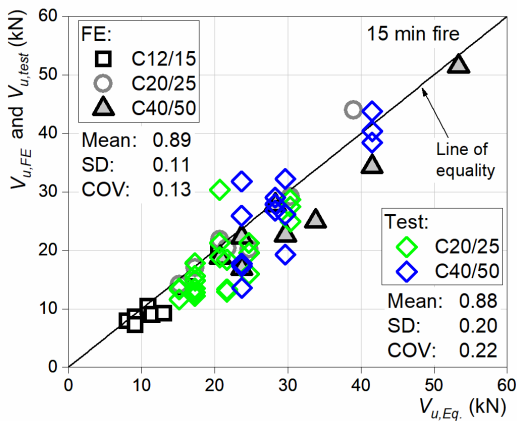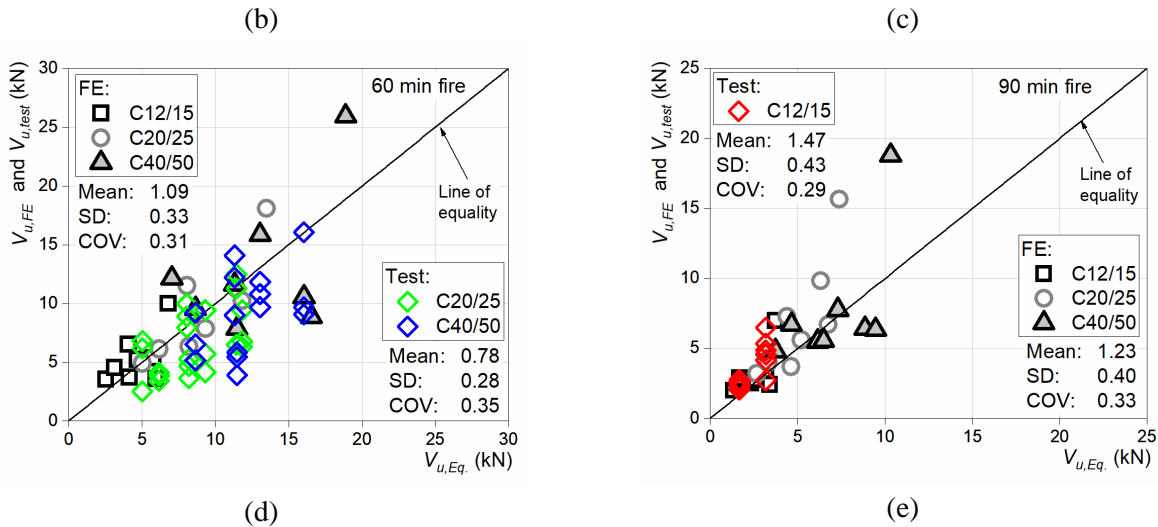
Figure 5.49 Numerical and experimental peak loads versus calculated peak loads according to Equation (5.16) after different fire durations. (a) 0 min; (b) 15 min; (c) 30 min; (d) 60 min; (e) 90 min.

5.8.   Summary

In this chapter the results of experimental investigations carried out on single headed stud anchors installed in concrete grade C20/25 and C40/50 located close to an edge and loaded perpendicular to free edge in shear at ambient temperature, after 15 min and 60 min of ISO 834 fire are presented and discussed. A series of parametric analyses has been performed to investigate the influence of various parameters on the resistance of anchors after fire exposure by concrete edge failure. These parameters include anchor diameter d_{nom}, embedment depth h_{ef}, edge distance c_1 and the concrete strength f_{cm} on the load-bearing behaviour of anchors for each time period of fire duration. Afterwards, numerical analyses are performed to verify the finite element models according to the experimental results. Parametric analyses are numerically conducted based on the verified finite element models involving more parameters. The following conclusions can be drawn:

(1) The failure mechanism and failure pattern of anchors loaded in shear after fire are rather different from that at ambient temperature. Instead of a standard concrete edge breakout, as observed at ambient temperature, after fire exposure the failure pattern is observed to be concrete edge failure in combination with pry-out failure. This is attributed to the thermally damaged concrete on the rear side of the anchor. Nevertheless, the peak load is governed by the concrete edge failure and the pry-out failure occurs after the peak load is already reached. Numerical analyses confirm this observation.

116

(2) The anchor diameter governs the shear stiffness of the anchor at ambient temperature; however, after fire the edge distance and concrete strength become the dominant factors. The diameter and embedment depth do not influence the shear stiffness strongly after exposure to fire. With increasing fire duration, the shear stiffness is reduced remarkably.

(3) The load ratio between the load at the initiation of the crack and the ultimate load is from 41% to 57% for anchors at ambient temperature, which agrees with previous research data by *Grosser* (2012). After 15 min of fire exposure, the load ratio is reduced dramatically to from 17% to 27%. After 60 min of fire, this ratio is about 10%. The crack width at the ultimate load is seen to increase from 0.28 mm to 0.63 mm to 1.99 on average for increase of fire duration 0 min to 15 min to 60 min, respectively.

(4) It is found that the anchor diameter d_{nom}, the embedment depth h_{ef} and the concrete compressive strength f_{cm} become progressively more influential in defining the resistance of anchors with increasing fire duration. On the contrary, the influence of the edge distance c_1 becomes less important after fire exposure. This is confirmed by both of the experimental and numerical analyses.

(5) Based on the evaluation of the experimental and numerical results, a formula to calculate the concrete edge failure load of single stud anchors as a function of fire duration $fi(t)$ is proposed. A good agreement between the calculated results according to the formula and the experimental or numerical results is obtained.

This study was undertaken in the context of lack of data and design rules for fire safety of anchorages. Note that the conclusions obtained are valid for headed stud fasteners close to edge (normally $h_{ef} \leq 8d_{nom}$) with fire exposure from two sides of the free edge only. The concrete should be normal weight concrete with strength in the range C12/15 to C40/50, considering no surface spalling under fire in the area of the anchorage. Although the results may be still limited in this paper, the influence and relations between the factors investigated are mostly distinct and meaningful for fire engineering of anchorages. Considering the fact that fire tests are expensive and time consuming, it is important that the 3D finite element models are verified to be valid for modelling the behaviour of anchorage after fire.

6. ANCHOR GROUPS LOADED TOWARDS FREE EDGE IN THE COLD STATE

In the current Eurocode 2 and ACI 318 design codes, at ambient temperature the concrete edge failure load of anchor groups is calculated according to the projected areas of the individual studs, according to Equation (2.9). However, it is not clear if this provision can be applied to anchor groups after fire exposure. The study in Chapter 5 shows that cracking of concrete for single anchors after fire exposure is different from that at ambient temperature. Therefore, it is necessary to examine the concrete edge failure of anchor groups with respect to the corresponding projected areas after fire exposure, experimentally and numerically.

The casting of the concrete slab and the fire test procedure are the same as described in Chapters 5.3 and 5.4, respectively.

6.1. Anchors

In the experimental program, two- and four-stud anchor groups were used as representative to examine the resistance and crack development of anchor groups loaded in shear towards free edge after fire exposure. The two-stud anchor group consists of a steel plate with two studs welded to it (Figure 6.1). The steel plate is $200 \times 100 \times 30$ mm (length $\times$ width $\times$ thickness) in dimension. All the studs are 25 mm in diameter with embedment depth of 95 mm. The distance s_2 between the studs is 100 mm. Thus, a distance of 50 mm is kept for each stud to its nearest edge of the steel plate. In the front middle of the steel plate, a hole with internal thread is prepared for connecting the hydraulic loading cylinder.

(a) (b)
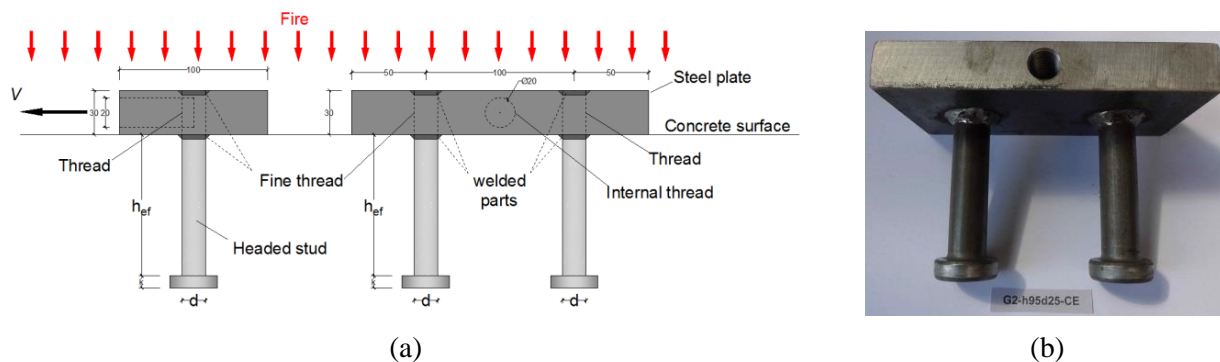
Figure 6.1 Example of two-stud anchor groups used for fire test.

For four-stud anchor group, the edge distance $c_{1,1}$ is 100 mm. The distance s_1 and s_2 between the adjacent studs are 100 mm. Thus, the steel plate is 200 × 200 × 30 mm (length × width × thickness) in dimension (Figure 6.2).

(a)   (b)
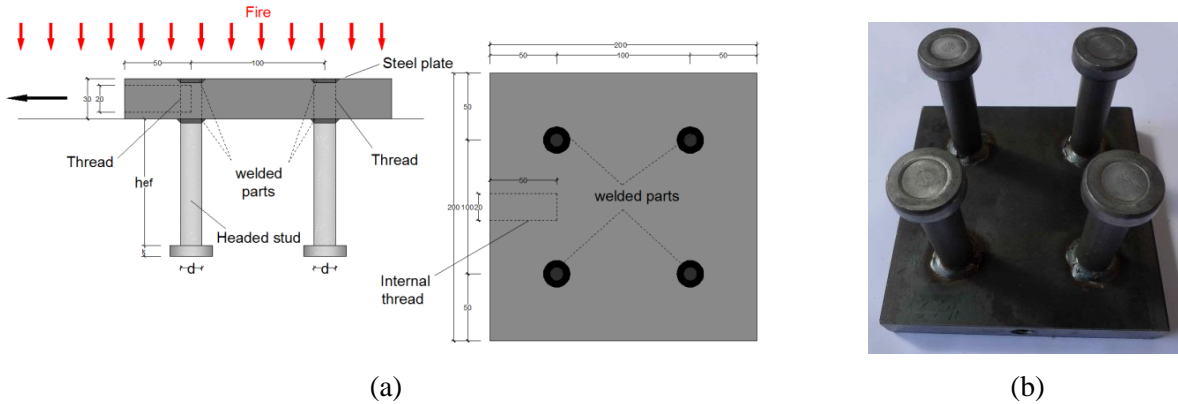
Figure 6.2 Example of four-stud anchor groups used for fire test.

The configurations of anchor groups are listed in Table 6.1. At ambient temperature, two tests were repeated, and after 15 min and 60 min of fire, three tests were performed for each case.

Table 6.1 Anchor groups configurations

Identification	Number of stud	c_1 (mm)	h_{ef} (mm)	d (mm)	Concrete grade	Fire duration $fi(t)$ (min)
G2-2c100h95d25	2	100	95	25	C20/25	0; 15; 60
G4-2c100h95d25	4	100	95	25	C20/25	0; 15; 60

6.2.   Setup and loading

As mentioned previously, the corresponding concrete edges of anchor groups were subjected to fire on two sides and the anchor groups were heated without pre-load. The installed anchor groups were loaded perpendicular to concrete edge after cooling the concrete specimens. The configuration of the loading equipment is the same as illustrated in Figure 4.6. As shown in Figure 6.3, LVDT-0 was used to monitor the horizontal movement of the steel plate, LVDT-1 and -2 were employed to monitor the crack opening during loading.

(a)

(b)
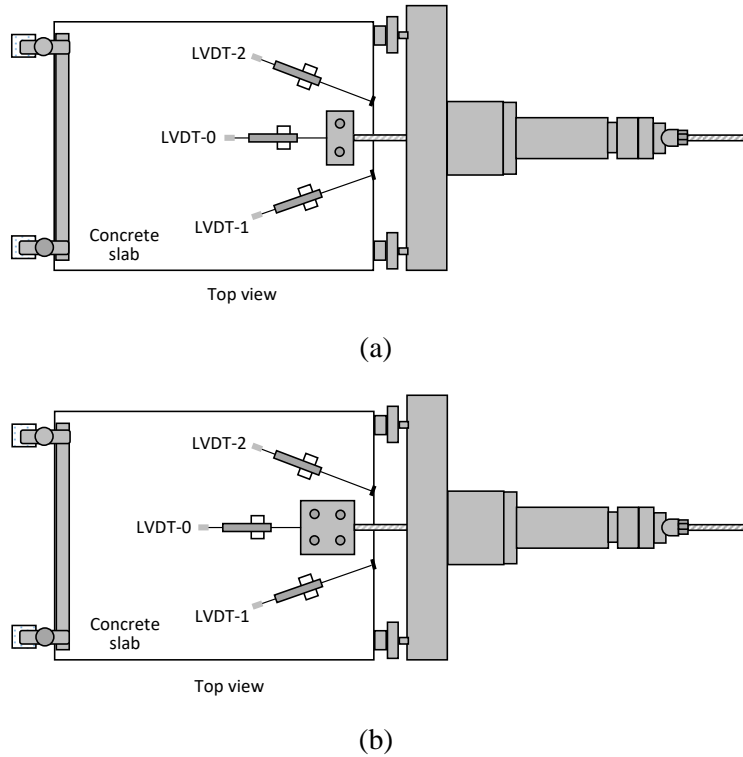
Figure 6.3 Loading setup for anchor groups with (a) two studs and (b) four studs.

6.3. Test results and discussion

The experimental results are summarized in Annex A Table A.3 . In the following the failure mode, cracking and load-displacement response after fire exposure are discussed.

6.3.1. Fracture patterns

In Figure 6.4 are shown the fracture patterns of two-stud anchor groups loaded towards free edge after fire exposure. At ambient temperature and after 15 min of fire, it was observed that the crack passing through the axes of the studs were developed when the peak load was reached, which leads to the concrete edge failure. Afterwards the rear crack appeared, which is due to the pry-out type of failure (Figure 6.4a and b). It should be noted that at ambient temperature only one anchor group exhibited the rear crack and after 15 min of fire for all anchor groups the rear crack was observed. After 60 min of fire exposure, as shown in Figure 6.4c, only one crack was developed at the back side of the anchor group. It seems that at ambient temperature and after 15 min of fire, the fracture is a combination of concrete edge failure and pry-out failure, however, the concrete edge failure is corresponding to the peak load. After 60 min of fire, the pulling force at the upper side of the shaft towards free edge and the "kicking back" force at the rear side of the stud head are activated at the same time. Considering thermally induced damage of concrete, this

may result in the integral crack development, with an intact failure body enclosed by both the studs.

(a)　　　　　　　　　　　　　　(b)　　　　　　　　　　　　　　(c)
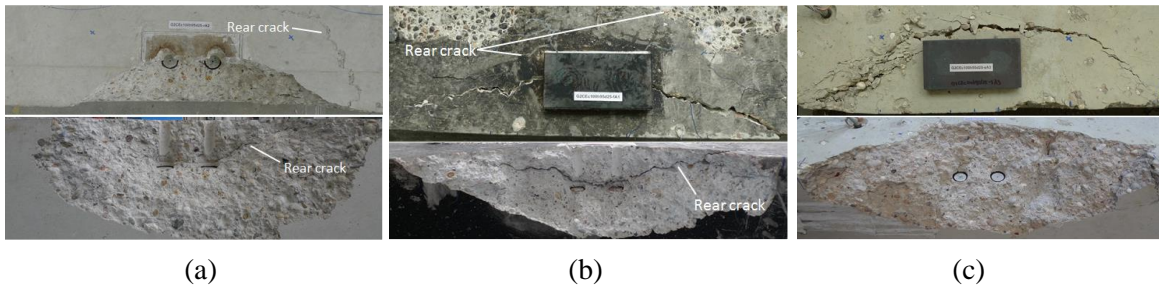
Figure 6.4 Fracture pattern of two-stud anchor group after fire exposure. (a) 0 min; (b) 15 min; (c) 60 min.

The fracture patterns of four-stud anchor groups with increasing fire exposure are generally the same as that for two-stud anchor groups (see Figure 6.5). The rear crack appeared only for one anchor group at ambient temperature. After 15 min of fire, the fracture patterns are the combination of concrete edge failure and pry-out failure (Figure 6.5b). After 60 min of fire, for all three tests, the integral cracks propagate by the back side of the anchor group with the integral concrete edge failure block being formed (Figure 6.5c). In all the tests, no cracks were observed to develop from the front studs.

(a)　　　　　　　　　　　　　　(b)　　　　　　　　　　　　　　(c)
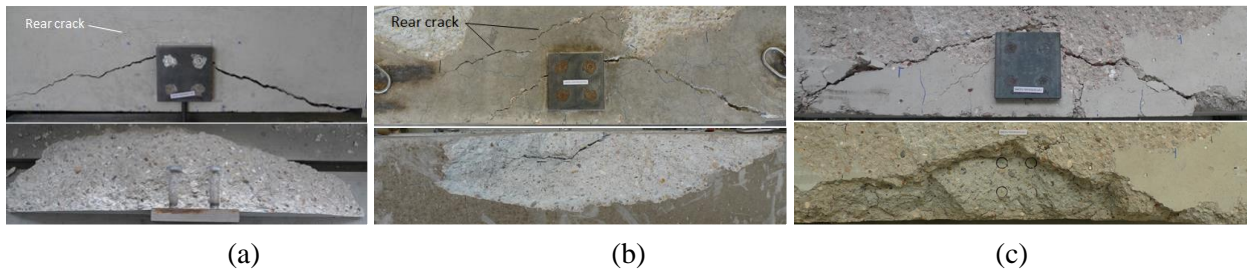
Figure 6.5 Fracture pattern of four-stud anchor group after fire exposure. (a) 0 min; (b) 15 min; (c) 60 min.

6.3.2. Crack propagation

The displacement and crack width development of two-stud anchor group after fire exposure are illustrated against load in Figure 6.6. It is shown that the measured crack widths w_1 and w_2 at each side of the anchor group are almost identical. At ambient temperature, the load-displacement and -crack width response is rather brittle. The load is increased quickly with increasing crack width and reduced rapidly after reaching the peak load. After 15 min and 60 min of fire, rather ductile responses can be seen. At each load level, the crack width is distinctly smaller than the displacement of the anchor plate.

As for single anchor, the crack width $\Delta w = 0.006$ mm is taken as the critical value for the initiation of cracking. It is useful to know the ratio between the load at crack onset and ultimate load of the anchor group after different fire durations.
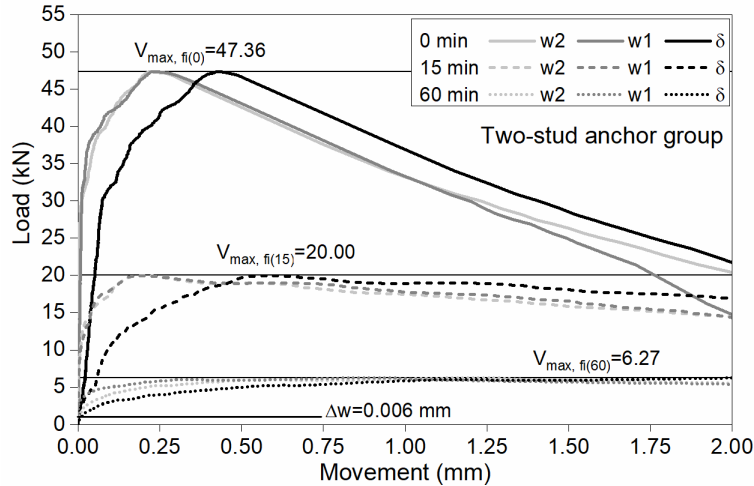
Figure 6.6 Movement and crack width development of two-stud anchor group after fire exposure.

(a)   (b)
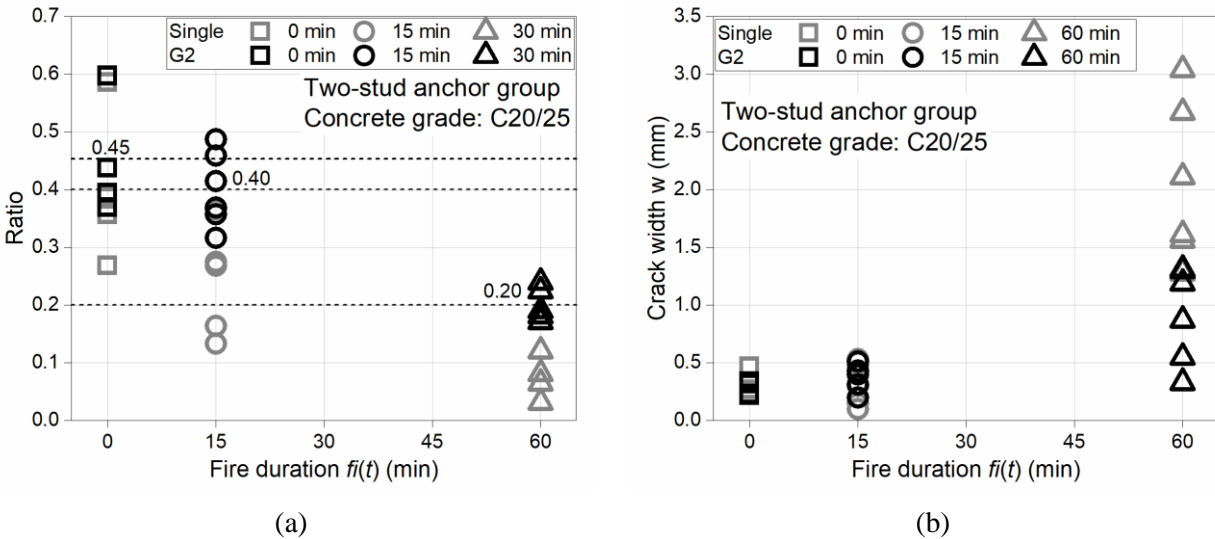
Figure 6.7 (a) Load ratio of two-stud anchor groups at the onset of crack and (b) the crack width at the peak load as function of fire duration.

Figure 6.7a shows the ratio of load at crack onset for two-stud anchor group. The same ratio for single headed stud anchor is depicted as reference. At ambient temperature, on average 45% of ultimate load is reached when the cracking starts, which is almost the same as for a single stud anchor (40%). After 15 min and 60 min of fire exposure, 40% and 20% of the ultimate loads are gained by the initiation of the cracking, respectively, which are obviously higher than that for single anchors (24% and 14%, respectively). In Figure 6.7b, the crack widths at the peak loads

are presented. As can be seen, this crack width increases with prolonged fire duration, which reflects the more ductile property of concrete after fire exposure. The values are 0.35 mm, 0.35 mm and 2.05 mm on average for single stud anchors after 0 min, 15 min, 60 min of fire, respectively. For two-stud anchor groups they are 0.28 mm, 0.34 mm and 0.93 mm after 0 min, 15 min, 60 min of fire, respectively. Therefore, at ambient and after 15 min of fire they are almost the same, however, after 60 min of fire, two-stud groups have strongly reduced crack widths.

By analogy with the two-stud anchor group, Figure 6.8 shows the displacement and crack width development of four-stud anchor group loaded towards free edge after fire exposure. The measured two crack widths w_1 and w_2 are identical at ambient temperature, however, after 15 min and 60 min of fire considerable difference can be seen between w_1 and w_2. For the cracking at ambient temperature the concrete shows more uniformity than after fire exposure. Due to the temperature load, the inhomogeneity of concrete increases with the consequence that the crack patterns becoming non-symmetric.
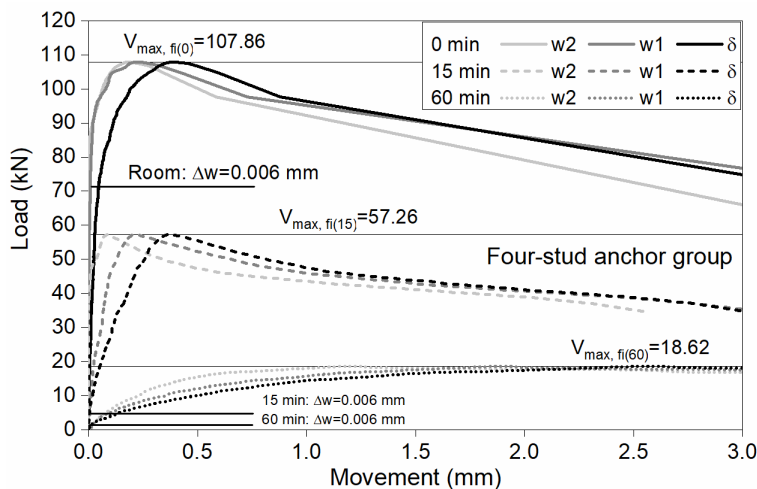
Figure 6.8 Movement and crack width development of four-stud anchor group after fire exposure.

Figure 6.9a shows the ratio between the load at crack onset and the ultimate load. The load ratio for single stud anchor is also presented as a reference. At ambient temperature, on average 53% of ultimate load is reached at crack onset, which is slightly higher than that for single stud anchors (40%). After 15 min and 60 min of fire exposure, 21% and 6% of the ultimate loads are reached, respectively, which are very close to that of single stud anchors (24% and 14%, respectively). In Figure 6.9b, the crack widths at the peak loads are presented. The crack width increases with prolonged fire duration. The crack widths for four-stud anchor groups are similar to that for single stud anchors. The values are 0.20 mm, 0.23 mm and 1.35 mm for four-stud anchor groups after 0 min, 15 min, 60 min of fire, respectively (for single anchors: 0.35 mm, 0.35 mm and 2.05 mm on average).

123
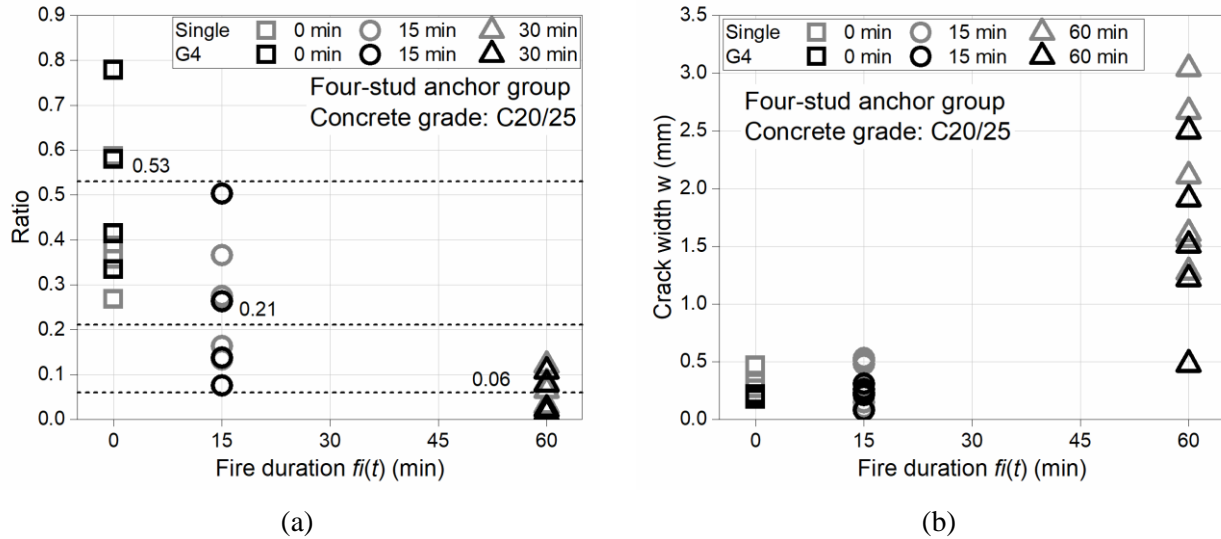
Figure 6.9 (a) Load ratio of four-stud anchor groups at crack onset and (b) the crack width at the peak load as function of fire duration.

6.3.3. Load-displacement behaviour and shear stiffness
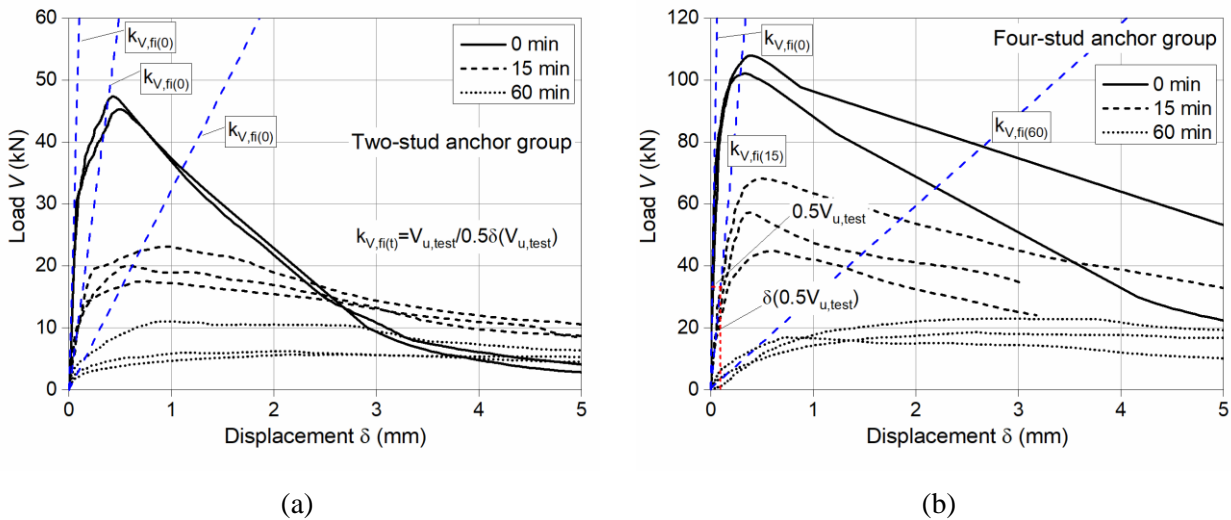
Figure 6.10 Load-displacement curves of anchor groups with (a) two and (b) four studs after different fire exposures.

The load-displacement response of anchor group is supposed to be stiffer than that of single stud anchors. Figure 6.10 shows the load-displacement curves of two- and four-stud anchor groups before and after fire exposure. According to these curves, the initial shear stiffness of the anchor groups can be reasonably defined in the same way as that for single anchors, which is $k_{V,fi(t)} = 0.5 Vu,fi(t)/\delta(0.5Vu,fi(t))$. The reduction of the shear stiffness is significant, especially

124

after 60 min of fire. It is also seen the failure is converted from brittle at ambient temperature to ductile after fire exposure, for both anchor groups. Anchor group with four studs compared to the anchor group with two studs have relatively smaller movement at ultimate load.

It is worthy to compare the change in shear stiffness when the number of studs increases. Figure 6.11a shows the shear stiffness of single stud anchors, two- and four-stud anchor groups as a function of fire duration. At ambient temperature, the difference between the shear stiffness is large, which is seen to be at different scales. They are on average 55.97 kN/mm, 423.68 kN/mm and 1537.40 kN/mm for single anchor, two- and four-stud anchor groups, respectively. After fire exposure the difference is remarkably reduced. The shear stiffnesses are on average 15.52 kN/mm, 120.83 kN/mm and 283.50 kN/mm, respectively. After 60 min of fire, they are further reduced to 3.53 kN/mm, 24.23 kN/mm and 29.39 kN/mm, respectively. In Figure 6.11b, the reduction ratios are shown for the anchors after different fire durations. It is interesting to observe that they follow almost the same reduction rate, which are on average 25% and 5% of original shear stiffness after 15 min and 60 min of fire exposure, respectively.
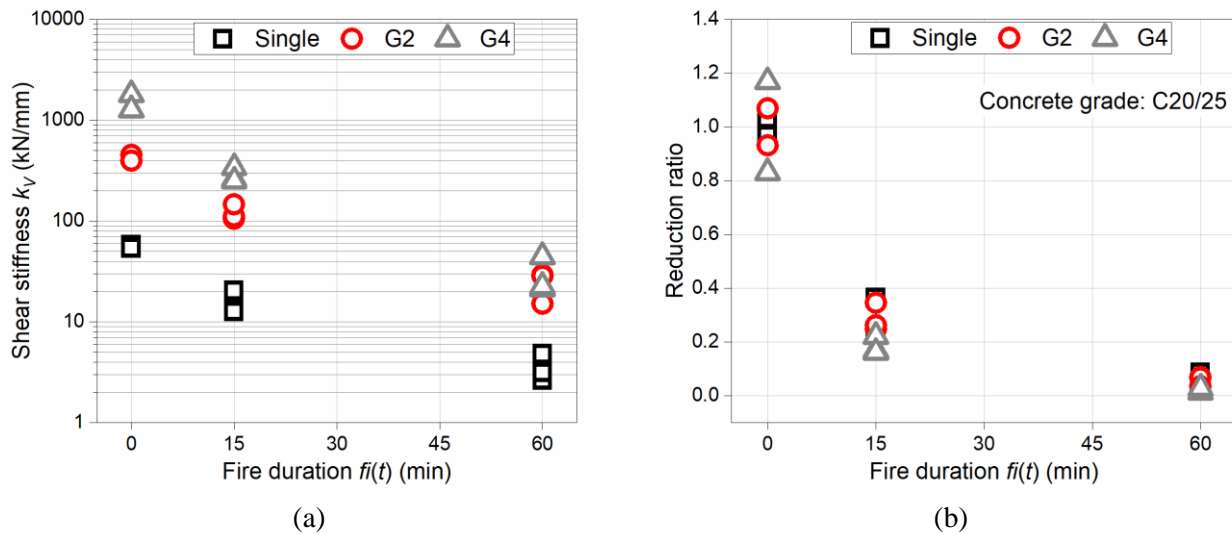
Figure 6.11 Shear stiffness (a) and its reduction ratio (b) of anchor groups with two and four studs as a function of fire duration. Note: in (a) the vertical axis is in logarithmic scale.

6.3.4. Resistance

The experiments for two- and four-stud anchor groups were only performed for concrete grade C20/25 before and after fire load. According to Chapters 5.6.6 and 5.6.7 for single stud anchors, the resistance is proportional to the concrete strength to the power of 0.75 and 0.8 after 15 min and 60 min of fire exposure, respectively. For the anchor groups after fire, the difference is mainly due to the number of studs and so the projected area of fracture. Therefore, the exponents

0.75 and 0.8 are used to normalize the experimental results of anchor groups after 15 min and 60 min of fire exposure, respectively, due to the difference in concrete strength.

Figure 6.12 shows the peak loads of single anchors, two- and four-stud anchor groups as a function of fire duration. The reduction of the peak loads with increasing fire exposure is obvious. The peak loads of two-stud anchor groups are slightly larger than that of single headed stud anchors, except that they have almost the same value after 60 min of fire. Four-stud anchor groups have distinctly higher peak loads than the others for every fire condition. It can be seen that all peak loads are almost reduced to the level less than 20 kN, regardless of their reference resistance at ambient temperature.
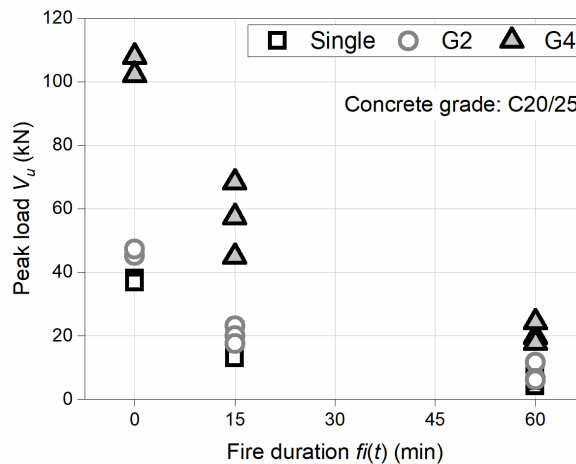
Figure 6.12 Peak loads of single anchors, two- and four-stud anchor groups as a function of fire duration.

Although the absolute values of peak loads are different, Figure 6.13a shows that the reduction rates for single anchor and anchor groups are quite similar. Four-stud anchor group presents a slightly smaller reduction after 15 min of fire exposure by comparing to that of two-stud anchor groups and single anchors, which are 46%, 56% and 60% of reduction for four-stud anchor group, two-stud anchor group and single anchor, respectively. The same as for single anchors, further away from the edge the anchor is, the lower is the reduction of the resistance after fire. However, after 60 min of fire duration, the load capacity for all anchor configurations remains about 18% of the reference value at ambient temperature.
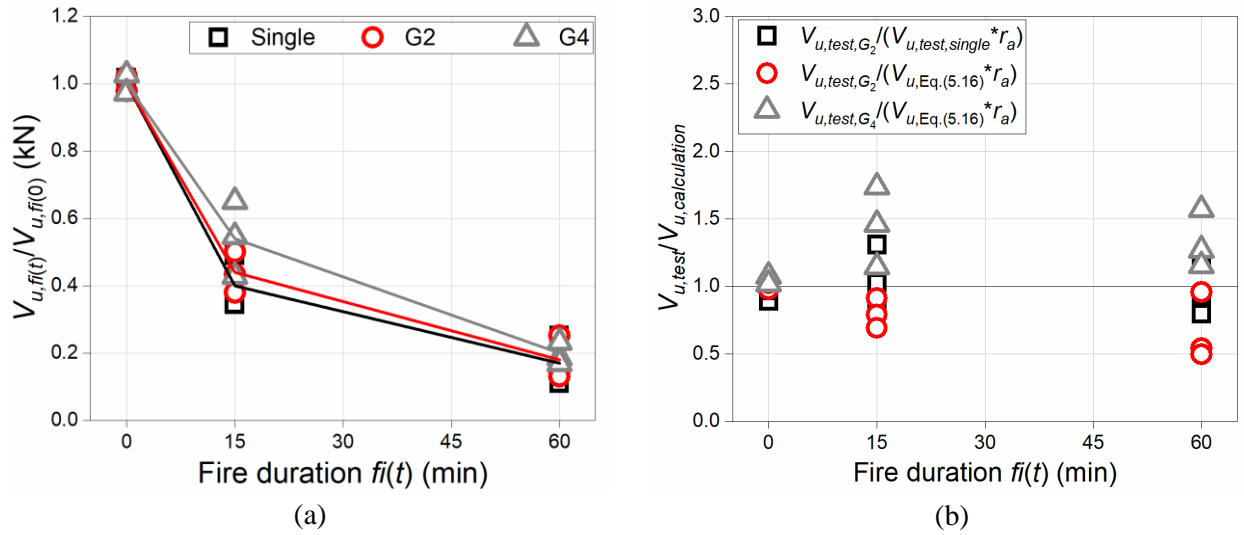
Figure 6.13 (a) Reduction rate of single anchors and anchor groups; (b) validation of calculation according to the projected area.

At ambient temperature, the resistance of anchor group is taken into account by using the projected area ratio $r_a = A_{c,V}/A_{c,V}^0$, according to the concrete capacity design approach. Since the load capacity of anchors mainly depends on the tensile strength of concrete, the projected area ratio should also be valid for anchors subjected to fire. In Table 6.2 and Table 6.3 evaluations of the validity of the projected area ratio on anchor groups after different fire exposure periods are conducted. The single anchor capacities, which are $V_{u,test,single}$ and $V_{u,Eq.,single}$ for tested and calculated according to Equation (5.16), respectively, are multiplied by the corresponding projected area ratio to get the load capacities of anchor groups. Thus the ratios between the tested results and the calculated results can be obtained for anchor groups with two studs and four studs and they are presented in Figure 6.13b. It shows that the method of using the projected area ratio works well for anchor group with two studs after 15 min and 60 min of fire duration. It also works for anchor group with four studs, however, the calculated results are noticeably lower than the tested results, especially after 60 min of fire. Thus it is likely the following equation can be drawn and it will be further verified by numerical analyses.

$$V_{u,c,fi} = \frac{A_{c,V}}{A_{c,V}^0} V_{u,c,fi}^0 \qquad (6.1)$$

where $A_{c,V}/A_{c,V}^0$ is defined as r_a.

127

Table 6.2 Evaluation of the validity of the projected area ratio for anchor group with two studs, i.e. G2-2c100h95d25. Note: "Eq." in the table indicates Equation (5.16)

$fi(t)$ (min)	$V_{u,test,G2}$ (kN)	$V_{u,test,single}$ (kN)	Proj. Area ratio $A_{c,V}/A_{c,V}^0$	$V_{u,cal.,G2}$ (kN)	$V_{u,test,G2}/V_{u,cal.,G2}$	$V_{u,Eq.,single}$ (kN)	$V_{u,test,G2}/V_{u,Eq.,single}$
0	45.27	38.13	1.33	50.71	0.89	46.29	0.98
0	47.36	36.83	1.33	48.98	0.97	46.29	1.02
15	23.17	13.30	1.33	17.69	1.31	25.37	0.91
15	20.05	18.38	1.33	24.45	0.82	25.37	0.79
15	17.60	12.93	1.33	17.20	1.02	25.37	0.69
60	11.71	9.45	1.33	12.56	0.93	12.22	0.96
60	6.63	4.15	1.33	5.51	1.20	12.22	0.54
60	6.05	5.71	1.33	7.60	0.80	12.22	0.50

Table 6.3 Evaluation of the validity of the projected area ratio for anchor group with four studs, i.e. G4-2c100h95d25. Note: "Eq." in the table indicates Equation (5.16)

$fi(t)$ (min)	$V_{u,test,G4}$ (kN)	$V_{u,Eq.,single}$ (kN)	Proj. Area ratio A_v/A_{v0}	$V_{u,Eq.,G4}$ (kN)	$V_{u,test,G4}/V_{u,Eq.,G4}$
0	107.86	85.65	1.17	100.21	1.08
0	102.17	85.65	1.17	100.21	1.02
15	57.40	33.58	1.17	39.29	1.46
15	68.36	33.58	1.17	39.29	1.74
15	44.98	33.58	1.17	39.29	1.14
60	19.70	13.25	1.17	15.50	1.27
60	24.36	13.25	1.17	15.50	1.57
60	17.87	13.25	1.17	15.50	1.15

6.3.5. Summary

The presented fracture patterns of anchor groups reveal that at ambient temperature the fracture due to pry-out at the back side of the anchor may occur, however, after 15 min of fire it is obvious that the failure is a combination of concrete edge and pry-out failure. After 60 min of fire, due to the severely damaged concrete, it leads to the integral crack to the back side of the anchor group. For four-stud anchor groups, no crack can be seen at the front studs.

The shear stiffness between single stud anchor and multiple studs anchor at ambient temperature is, as expected, largely different. Anchor groups show obviously stiffer load-displacement respond when loading. However, this difference decreases with increase of fire duration. The reduction rate of the shear stiffness is seen to be the same for anchors with single stud or multiple studs.

For the peak loads of the anchor groups with different number of studs, distinct difference can be seen at ambient temperature. However, this difference is remarkably reduced with increasing fire duration. After 60 min of fire, all anchors have the peak loads around or under 20 kN, which indicates a reduction rate of about 82% of reference resistance.

The comparative analyses between the resistance of single stud anchor and anchor groups with multiple anchors show that the projected area ratio is basically valid before and after fire exposure. However, after 60 min of fire, it is seen that the calculated resistance tends to be lower.

6.4.   Numerical study

It is obvious that the parameters taken by the experimental program for anchor groups are very limited. In this chapter numerical computations are conducted to verify if the numerical models can replicate the experimental results for anchor groups. Based on the verification analysis, parameters like the influence of edge distance, number of studs, fire duration, hot vs. cold state, are numerically investigated (results see Annex B Table B.3). In the framework of numerical study, a close examination of the fracturing process is also performed.

6.4.1.   Finite element model

Figure 6.14 shows the finite element models for anchor groups with two, three and four studs loaded in shear. The two- and three-stud anchor groups are employed to investigate the influence of the number of studs in a row along the free edge on the resistance in case of concrete edge failure after fire (see Figure 6.14a and b). In Figure 6.14c the four-stud anchor group is used to investigate the initiation of cracks and also the influence of the projected area on the resistance according to CC-Method. The models are verified based on the experimental results firstly. The geometry, boundary conditions and finite element discretization are the same as that for the single headed stud anchors in Chapter 5.7.1. The difference is that the space between studs has to be taken into account for the geometry of anchor groups.

| (a) | (b) | (c) |
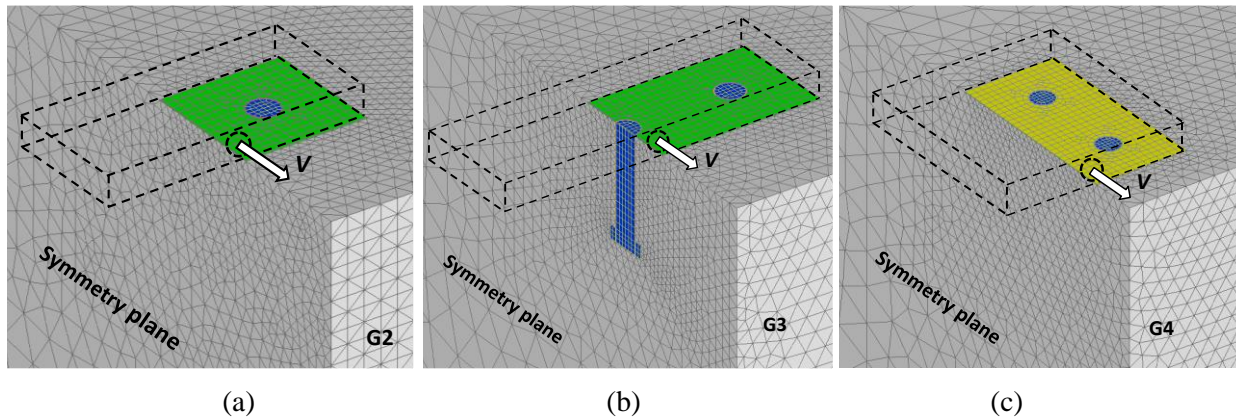
Figure 6.14 Finite element models for simulating anchor groups with (a) two suds, (b) three studs and (c) four studs loaded towards free edge after different fire durations.

In Table 6.4 are summarized the configurations investigated in the numerical studies. The same embedment depth of 95 mm and shaft diameter of 25 mm were selected for all anchor groups. For two-stud anchor groups, three different edge distances of 75 mm, 100 mm and 150 mm were

considered. The edge distance of 150 mm is applied for three-stud anchor group. For four-stud anchor group, the edge distance is 100 mm, which is the same as in the experiment.

Table 6.4 Numerically investigated geometries, materials and fire durations

Number of studs n	$c_{1,1}$ (mm)	h_{ef} (mm)	d (mm)	Concrete grade	Fire duration $fi(t)$ (min)
	75				
2	100	95	25	C20/25; C40/50	0; 15; 30; 60; 90
	150				
3	150	95	25	C20/25	0; 15; 30; 60; 90
4	100	95	25	C20/25; C40/50	0; 15; 30; 60; 90

6.4.2. Temperature profile

$fi(t)$ (min)	(a) G2-2c75h95d25; C20/25	(b) G2-2c150h95d25; C20/25
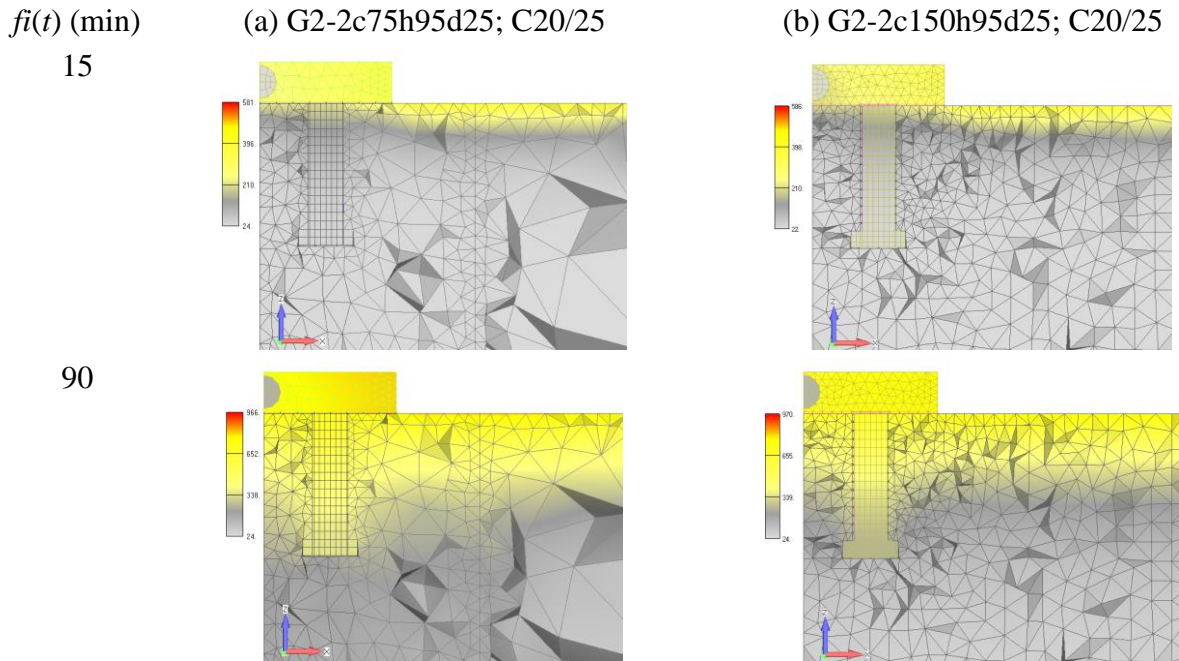
Figure 6.15 Temperature distributions of anchor groups with two studs in concrete C20/25 after different fire durations. (a) Edge distance $c_1 = 75$ mm; (b) edge distance $c_1 = 150$ mm.

Figure 6.15 shows temperature distribution for two-stud anchor groups in concrete C20/25 after fire exposure. The pictures show sections parallel to the front face of the concrete edge, passing through the axis of the studs. Note that the direction of the shear force is perpendicular to the plane. Here only the temperature distribution for 15 min and 90 mm are shown. It can be seen that the temperature distribution is the same for short period of fire exposure. However, after 90

min of fire, the anchor group with edge distance of 75 mm shows much stronger heat penetration, comparing to that for anchor group with edge distance of 150 mm. On the right side of the headed stud, the concrete has reached temperature of 250 ℃ for edge distance of 75 mm and 150 ℃ for edge distance of 150 mm.

$fi(t)$ (min)	(a)	(b)
15		
30		
60		
90		
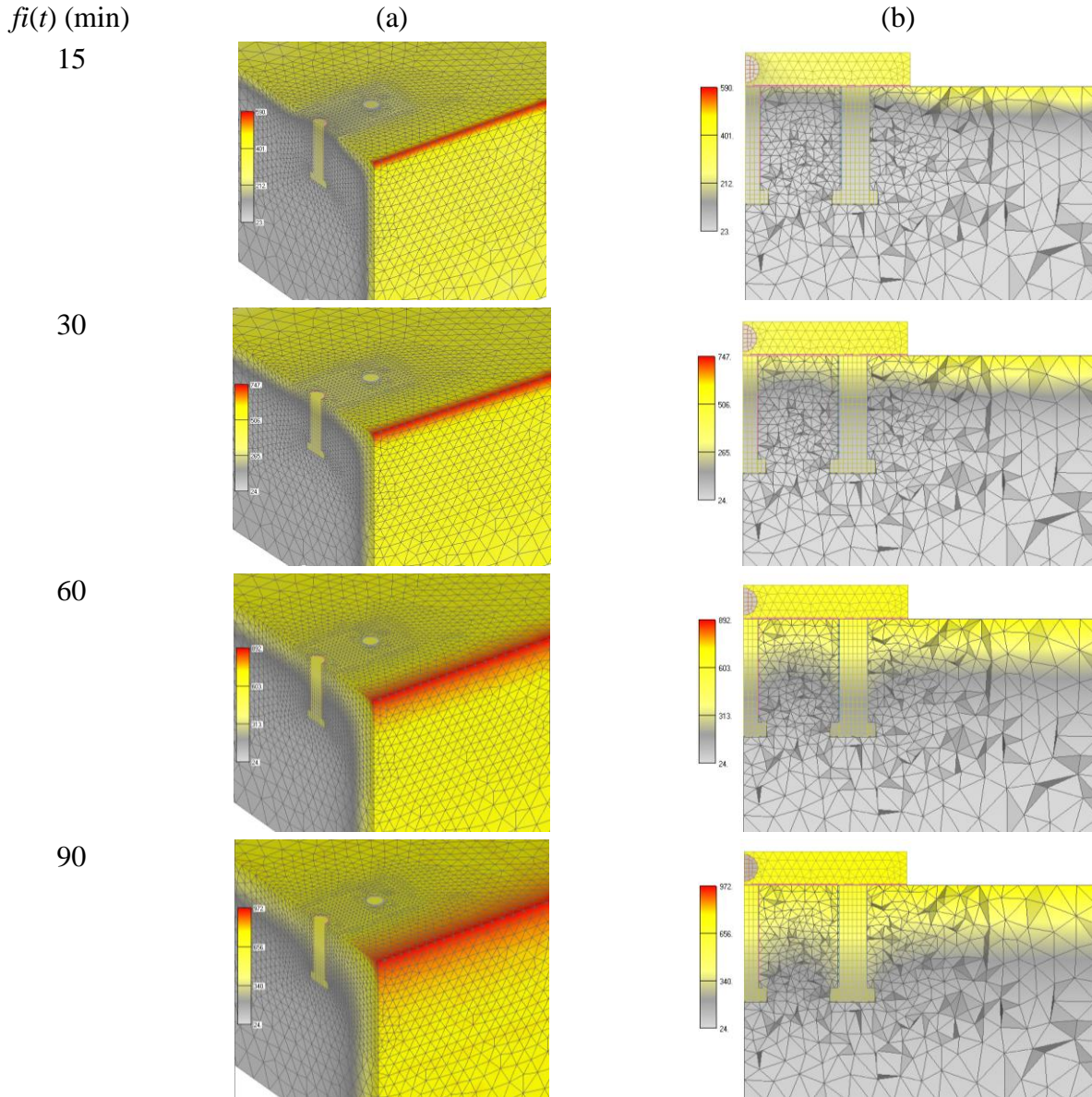
Figure 6.16 Temperature distributions of anchor group with three studs in concrete C20/25 after different fire durations (G3-2c150h95d25).

Figure 6.16 presents the temperature distribution for anchor group with three studs after different fire durations. As can be seen, the temperature distribution along the axes of stud and perpendicular to the front face is basically the same as for single headed stud anchor with the same edge distance (see Figure 6.16a and Figure 5.38). Parallel to the front face and along the

axes of the studs, for short period of fire, the temperature under the steel plate is relatively low; for long period of fire exposure, the temperature distributes in the shape of an arch under the steel plate, which is due to the influence of the anchor plate and anchors on the transport of heat (see Figure 6.16b).

Figure 6.17 shows the temperature distribution of anchor group with four studs after different fire durations. Due to the large size of anchor plate, the temperature under the central area of the steel plate is very low for 15 min of fire. With increase of fire duration, the temperature distributes in dome shape under the steel plate (see Figure 6.17 for 90 min), which may have influence on the crack propagation.
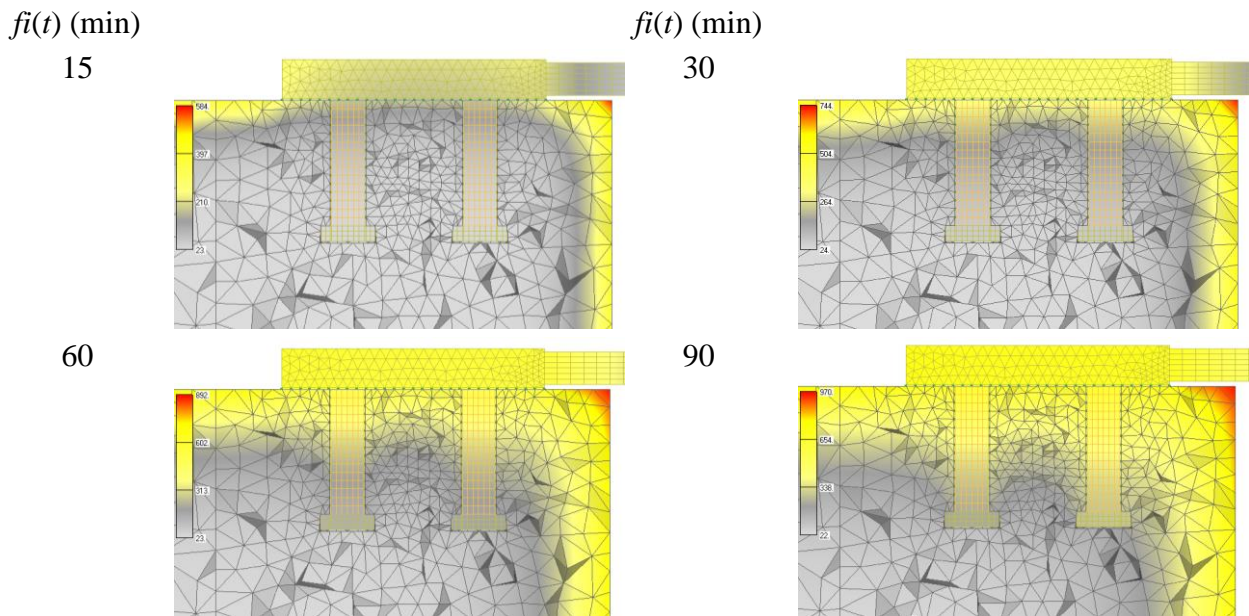
Figure 6.17 Temperature distributions of anchor group with four studs in concrete C20/25 after different fire durations (G4-2c100h95d25).

6.4.3. Fracture

Figure 6.18 shows the fracture patterns obtained numerically for two-stud anchor groups loaded towards free edge after fire exposure at peak loads. It can be seen that the concrete is more damaged in the cold state than in the hot state. In all cases, one crack propagates passing through the axes of the studs. Between the two studs, the crack is parallel to the free edge; to the side of the studs, the crack propagates towards the free edge at distances of about 2 to 3.5 times of the edge distance. In general, with increase of fire duration number of cracks and their width and length increase. It can also be seen that the damage is higher for the cold state, especially for longer fire duration. It is worth noting that the crack propagates to larger distance to the sides in the cold state than in the hot state. For short period of fire, the cracks propagate also wider than

133

for longer period of fire. A crack can be observed to develop at the back side of the anchor group, which is seen to be critical for long period of fire. At ambient or for short period of fire, the crack passing through the axes of studs dominates the failure.

$fi(t)$ (min)	(a) Cold state	(b) Hot state
0		
15		
30		
60		
90		
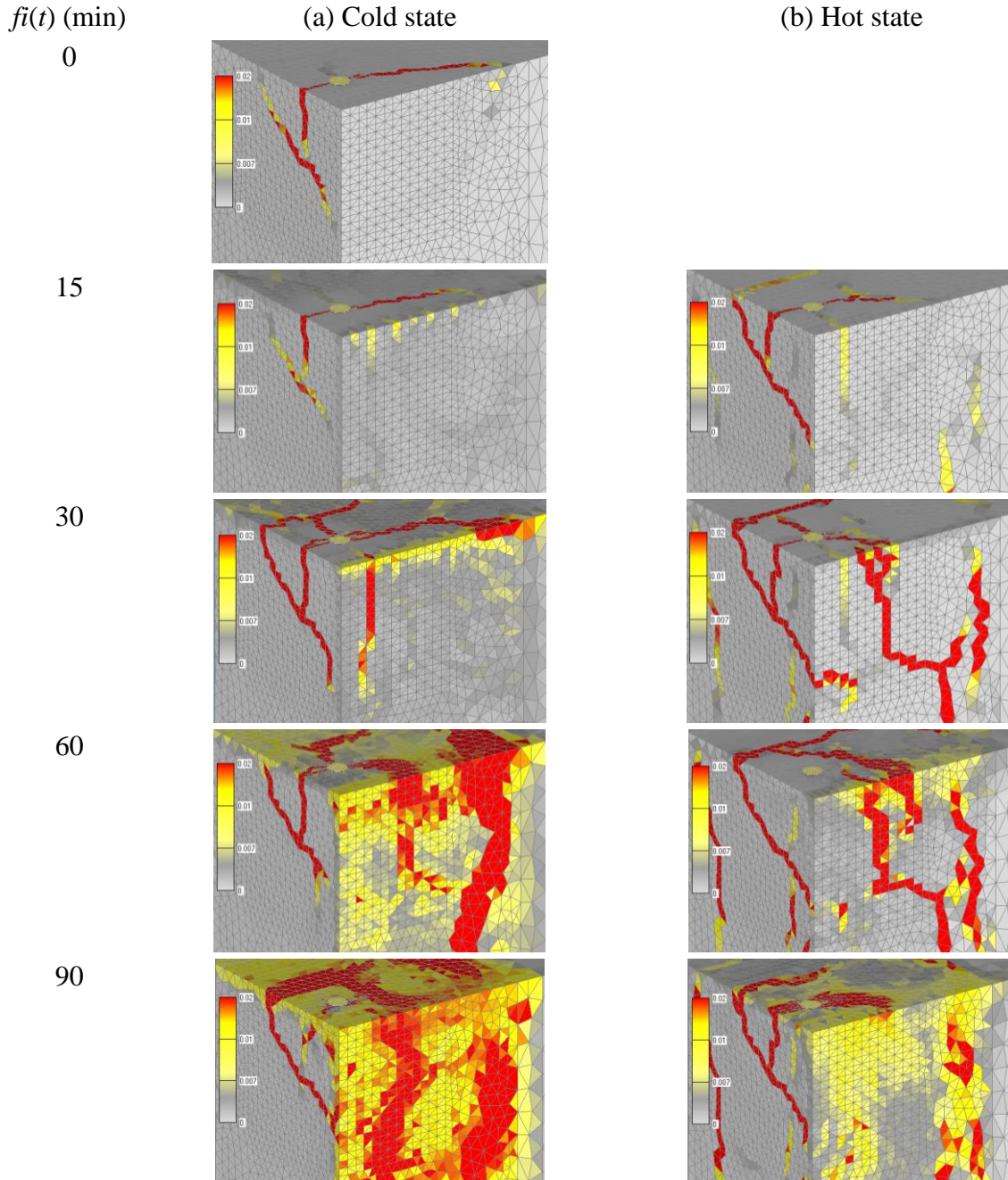
Figure 6.18 Fracture patterns of anchor group G2-2c75h95d25 loaded in shear at peak load in concrete C20/25 after different fire durations. (a) Cold stat; (b) hot state. Loading direction: towards free edge.

For the three-stud anchor group, the fracture patterns are shown in Figure 6.19. Basically the same phenomena can be observed as that for two-stud anchor group after fire exposure. It seems

134

that the crack propagating through the studs dominates the failure of the anchor group. For short period of fire duration, a single crack clearly appears between the studs; after 90 min of fire, the cracks in between are randomly oriented, i.e. damage of concrete is more distributed, especially for the cold state.

$fi(t)$ (min)	(a) Cold state	(b) Hot state
0		
15		
90		
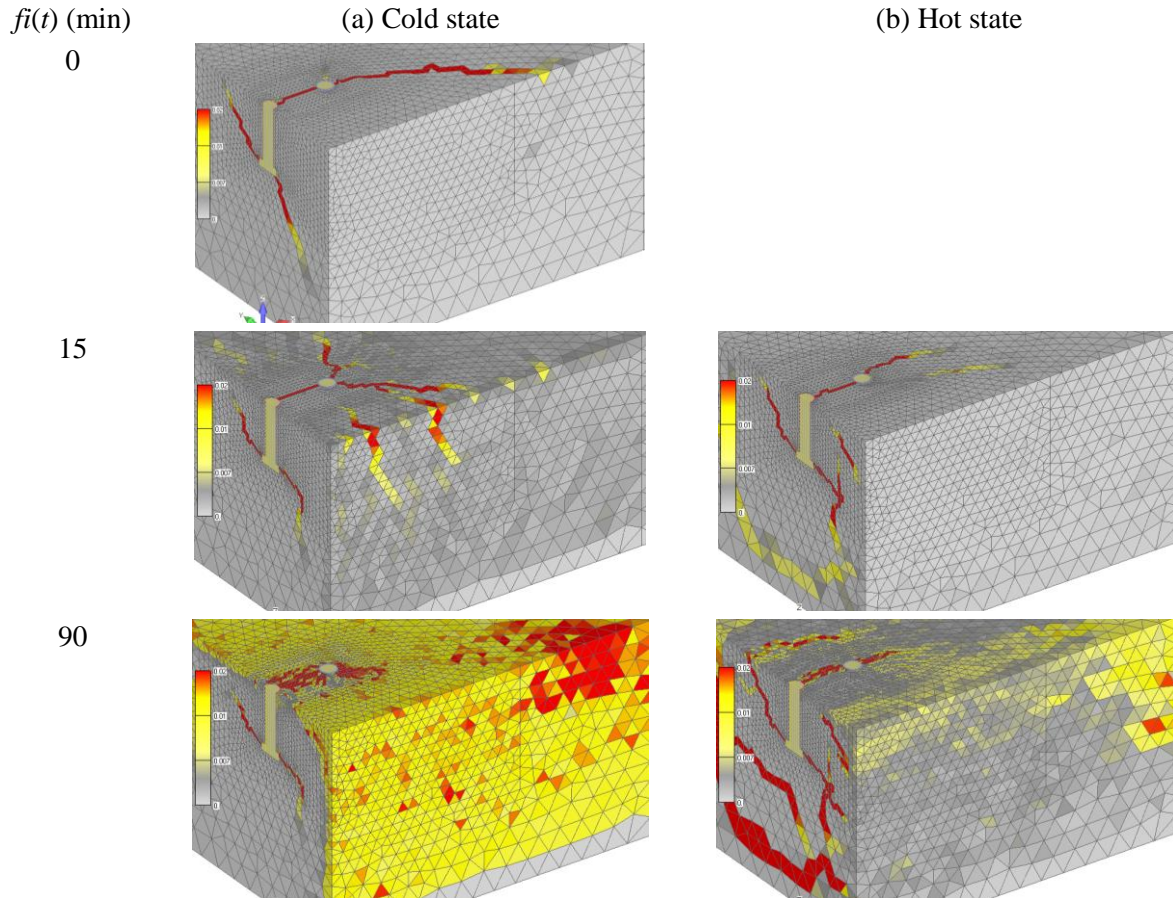
Figure 6.19 Fracture patterns of anchor group G3-2c150h95d25 loaded in shear at peak load in concrete C20/25 after different fire durations. (a) Cold state; (b) hot state. Loading direction: towards free edge.

Figure 6.20 shows the fracture patterns of four-stud anchor groups loaded towards free edge after different fire exposures. For all loading scenarios, no crack propagation can be observed at the front studs. At ambient temperature and after 15 min of fire, the cracks, initiating at the rear stud planes and subsequently propagating toward the free edge, dominate the failure. The crack propagates widely along the free edge comparing to the crack propagation after prolonged fire duration. For 60 min of fire exposure, the back side of the rear studs presents severe damage. It can be seen that with increase of fire duration, there are a number of differently oriented cracks. The same as shown above, damage tends to be more distributed over the concrete for the cold

state. These observations are in good agreement with the experimental observations (see Figure 6.5).

$fi(t)$ (min)	(a) Cold state	(b) Hot state
0		
15		
60		
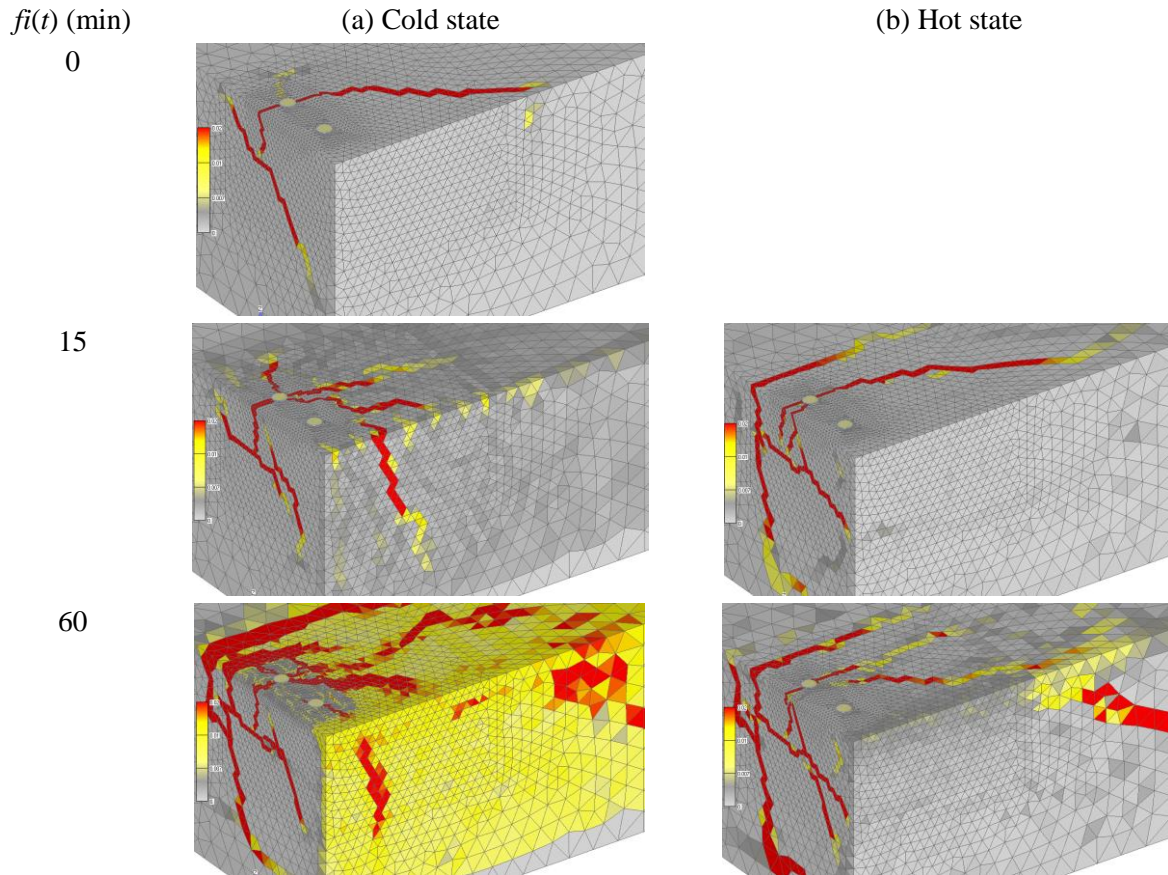
Figure 6.20 Fracture patterns of anchor group G4-2c100h95d25 loaded in shear in concrete C20/25 after different fire durations at peak loads. (a) Cold state; (b) hot state. Loading direction: towards free edge.

Figure 6.21 shows the initiation of the crack propagation for anchor group with four studs after different fire durations. At ambient temperature, the crack originates from the head of the rear studs row, which dominates the failure of the anchor. The crack does not crossing through the front studs (see Figure 6.21a). However, after 15 min of fire exposure, the development of the internal crack between the studs can be seen. The cracks mainly propagate towards the back side of the anchor group. It is worth nothing the numerical simulation shows that the crack initiates almost at the same time at the head of the front and rear studs (see Figure 6.21b). Similar crack development is observed for the fire duration of 60 min (see Figure 6.21c). These numerical results are in very good agreement with experimental observations (see Figure 6.5).

(a)   (b)   (c)
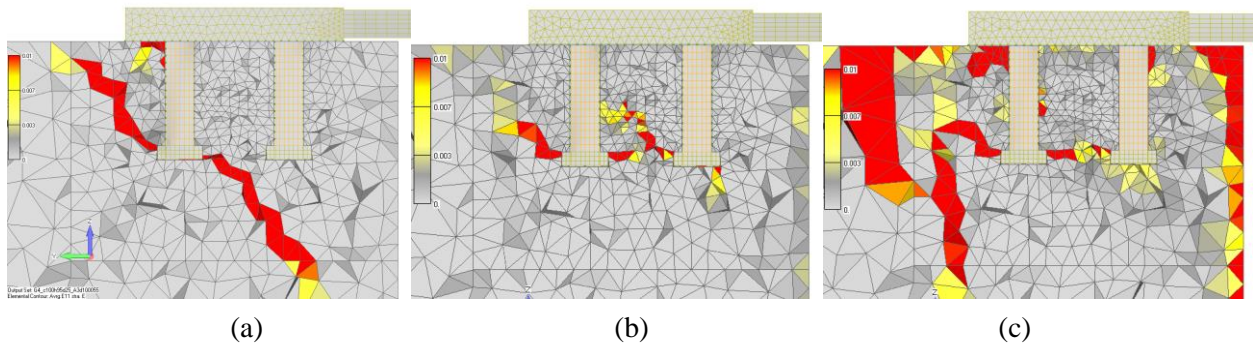
Figure 6.21 Crack propagation of four-stud anchor group loaded in the cold state after fire exposure. (a) 0 min; (b) 15 min; (c) 60 min.

6.4.4. Load-displacement curves

Figure 6.22a shows the comparison between numerically and experimentally obtained load-displacement curves for two-stud anchor group with edge distance of 100 mm in concrete C20/25. A very good agreement between numerical and experimental results can be seen at ambient temperature, after 15 min and 60 min of fire exposure.

Figure 6.22b, c and d show the numerical load-displacement curves of two-stud anchor groups loaded in shear after fire exposure. In general, with increase of fire duration resistance decreases and the response becomes more ductile. For short period of fire duration, i.e. 15 min and 30 min, it shows that only anchor group with edge distance of 150 mm reaches obviously higher resistance in the hot state than in the cold state. After 60 min of fire exposure, it can be seen that load-displacement response is stiffer in the hot state than in the cold state and the resistance in the hot state is higher than in the cold state.

137

(a)

(b)

(c)

(d)
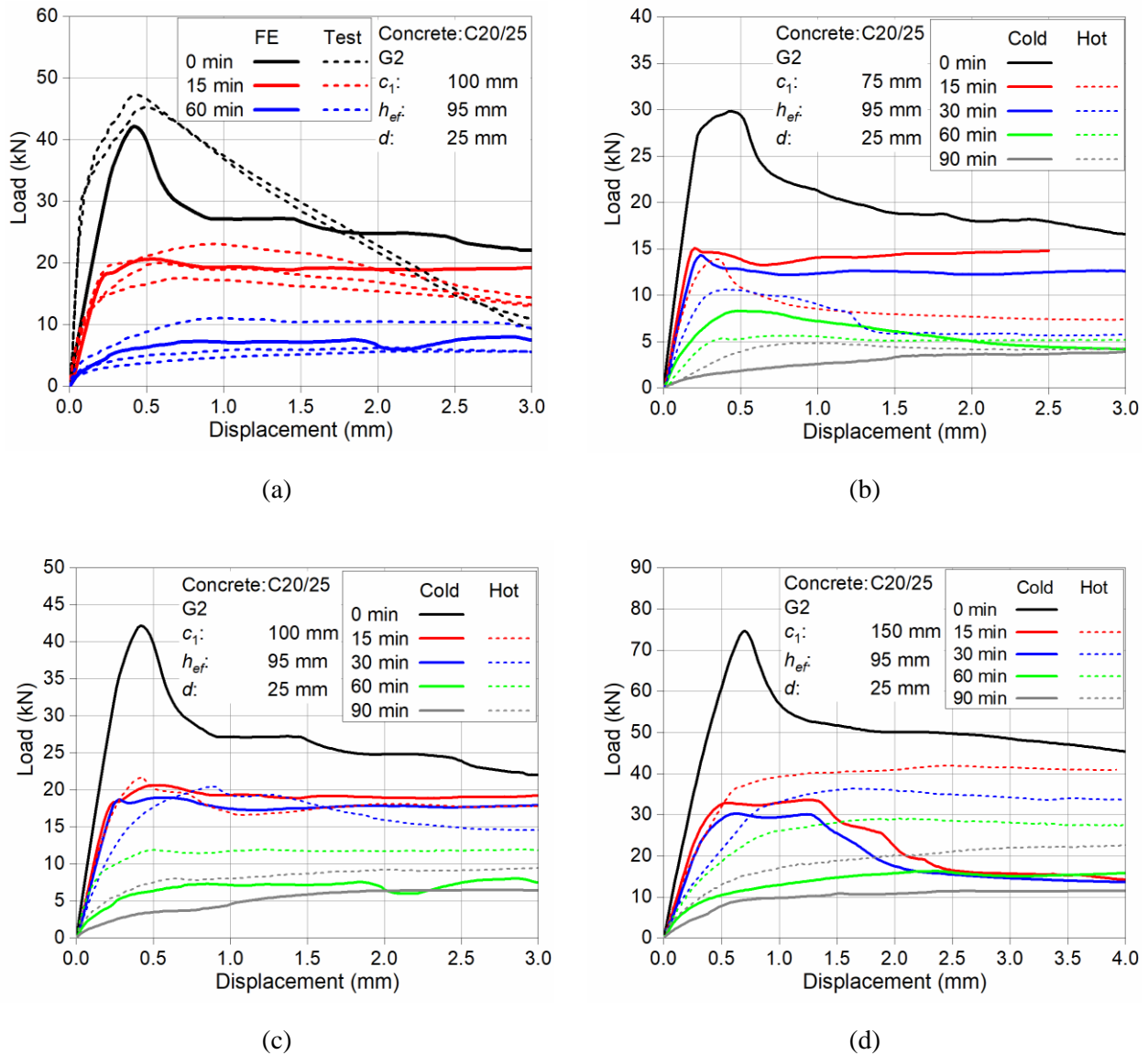
Figure 6.22 Load-displacement curves of two-stud anchor groups loaded in shear after fire: (a) comparison between numerical and experimental curves; numerical curves for (b) $c_1 = 75$ mm, (c) $c_1 = 100$ mm and (d) $c_1 = 150$ mm.

Figure 6.23a and b show the load-displacement curves of anchor groups with three studs and four studs after fire exposure, respectively. It can be seen the initial stiffness for loading in the hot state and in the cold state does not present obvious difference for each time period of fire exposure. The reason may attribute to the position of the dominating studs during the loading. The general trend is the same as discussed before. More ductile load-displacement response is presented with increase of fire duration and the resistance for the hot state can be seen to be higher than for the cold state.

(a)   (b)
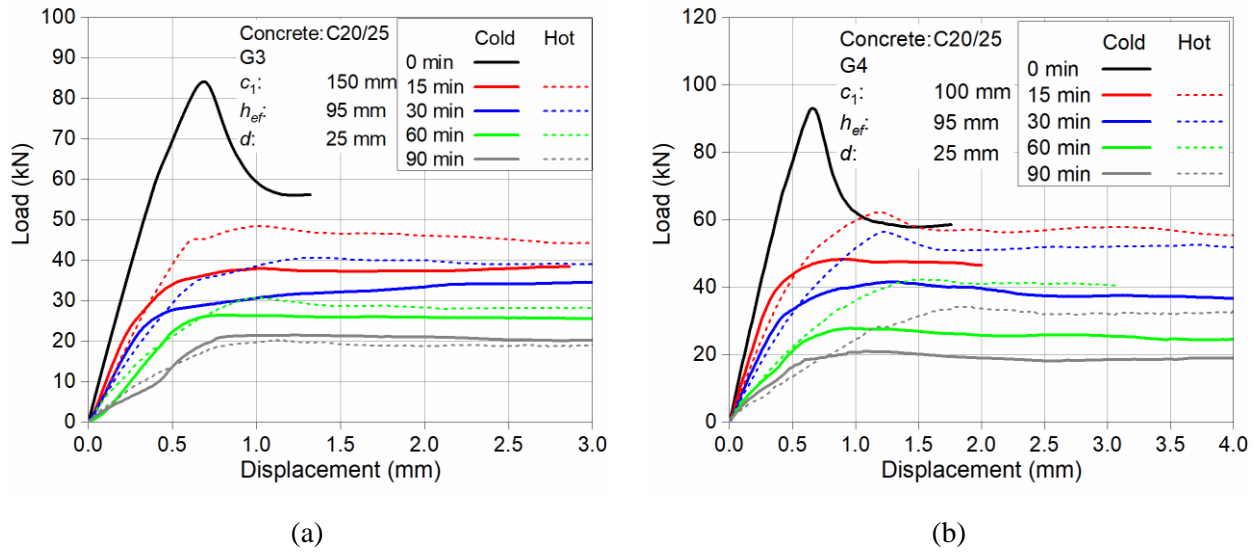
Figure 6.23 Load-displacement curves of anchor groups with (a) three studs and (b) four studs loaded in shear after fire exposure.

6.4.5. Resistance

(a)   (b)
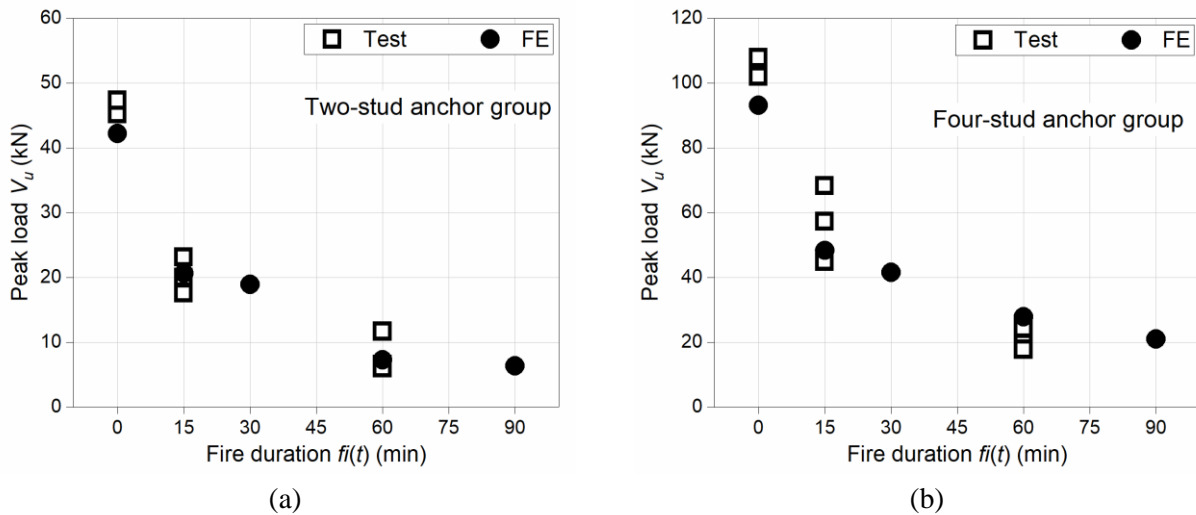
Figure 6.24 Comparison of peak loads of anchor groups obtained numerically and experimentally. (a) Two-stud anchor group; (b) four-stud anchor group.

Figure 6.24 shows numerically and experimentally obtained peak loads for anchor groups. It can be seen that numerical results agree well with experimental results, for both anchor groups with two and four studs. The numerical results show that the peak loads decrease gradually with prolonged fire duration. The reduction of the peak load is strong after 15 min of fire exposure. Especially for two-stud anchor group, the reduction from 15 min to 30 min of fire is slight. For both anchor groups, after 60 min of fire, the reduction of resistance is seen to be small.

6.5.   Verification of the CC–Method

Further numerical peak loads were analysed considering different edge distance c_1, anchor groups with two, three and four studs (see Table 6.4 and Figure 0.1) to verify the method of using the projected area ratio $A_{c,V}/A_{c,V}{}^0$ to calculate the load capacity of anchor groups by concrete edge failure.
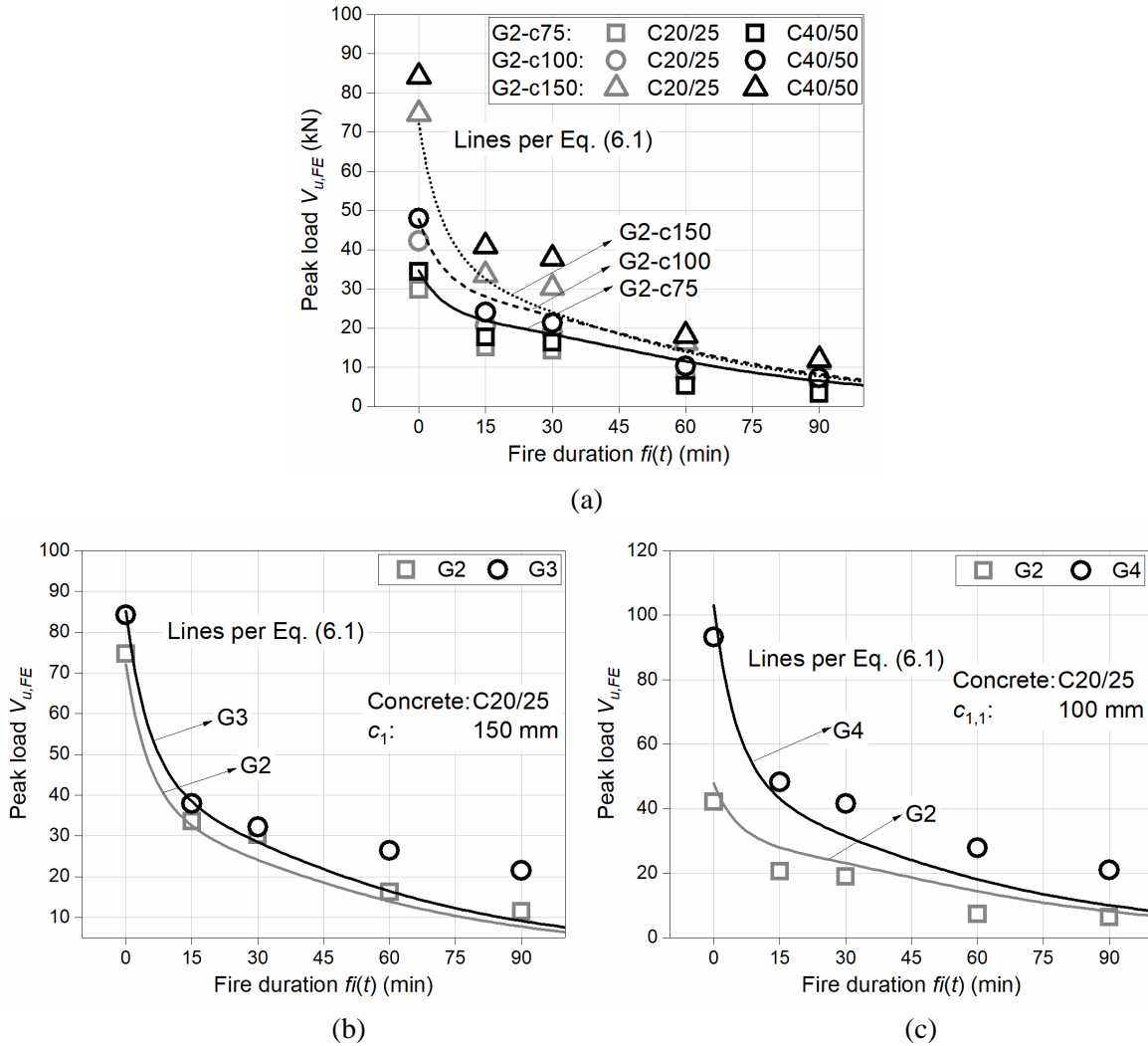
Figure 6.25 Verification analysis by using the projected area ratio for (a) two-stud anchor groups with three different edge distances, (b) two- and three-stud anchor groups and (c) two- and four-stud anchor groups.

As shown in Figure 6.25, it is clear for anchor groups with either increasing edge distance or with increasing number of studs in a row, Equation (6.1) can generally realistically predict the load capacities of anchor groups after fire exposure. It is worthy noticing that for G3 and G4 in Figure

6.25b and c, respectively, the predicted load capacities are on the conservative side and noticeably lower than the numerical results after long durations of fire (60 min and 90 min).

6.6. Summary

The fracture patterns of anchor groups obtained experimentally show that with the increase of fire duration the failure mechanism is changing. The numerical analysis confirms the experimental observations and reproduces the evolution of fracturing for anchor groups loaded towards free edge after different fire exposure.

According to Chapter 6.3.1 and 6.4.3, the fracture pattern and mechanism of anchor groups with one row of studs can be depicted as in Figure 6.26. At ambient temperature and after relatively short fire duration, the first crack, responsible for the peak load, propagates through the axes of the studs and extends towards the free edge. The second crack, due to the kicking back effect of the stud head, leads to the pry-out failure of the anchor group (see Figure 6.26a). However, after 60 min of fire, the force along the shaft and the kicking effect towards the back side of the anchor group work simultaneously and an integral concrete edge failure cone is formed (see Figure 6.26b).

(a)   (b)
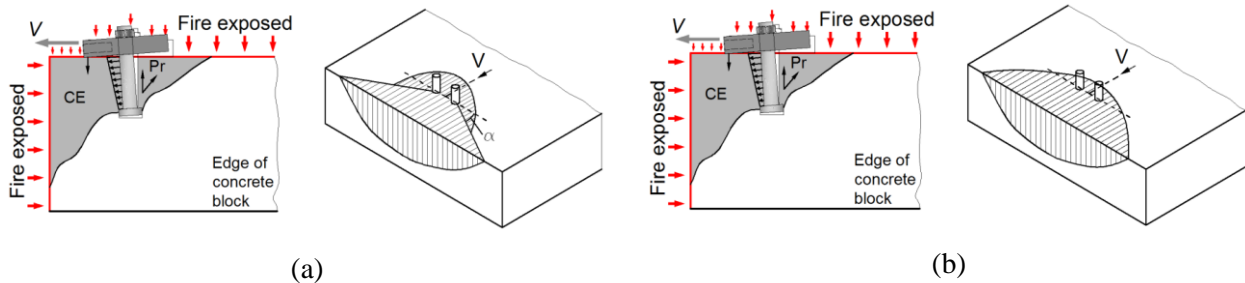
Figure 6.26 Fracture pattern and mechanism of two-stud anchor group after (a) 15 min and (b) 60 min of ISO 834 fire.

The fracture pattern and mechanism for concrete failure of four-stud anchor group after fire exposure is depicted according to both experimental and numerical study (see Figure 6.27). At ambient condition and short period of fire exposure, the failure mode is a combination of concrete edge failure and the pry-out failure of concrete. The rear studs row controls the failure (Figure 6.27a). After 60 min and longer duration of fire, the failure is due to concrete edge failure. However, the crack does not initiate from the axes of the studs, the fracture block is starting from the back side of the anchor group. This is due to the kicking back effect of the rear studs row (Figure 6.27b). At ambient temperature or for short period of fire exposure, this kicking back effect cannot dominate the failure since the concrete strength is relatively high. However, after 60 min of fire the concrete edge area is severely damaged with a number of randomly distributed

cracks (diffuse damage) and extremely low tensile strength of concrete. It should be noted that this failure is not the same as pry-out failure due to very close distance to free edge.

(a)   (b)
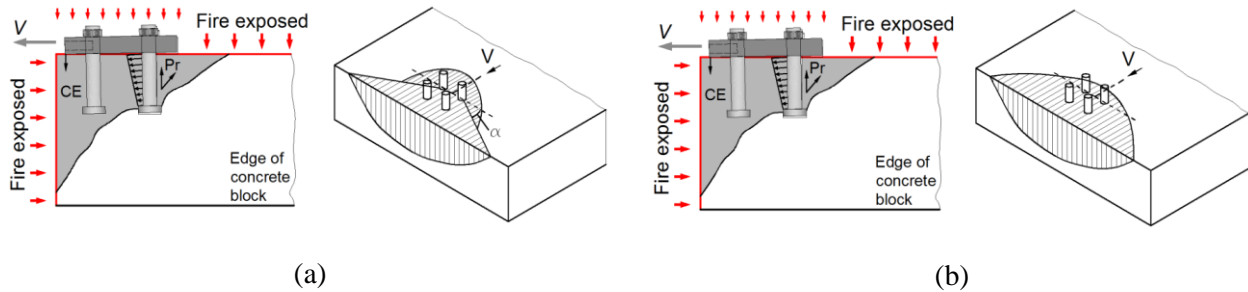
Figure 6.27 Fracture pattern and mechanism of a four-headed stud anchor group after (a) 15 min and (b) 60 min of ISO 834 fire.

At ambient condition, the shear stiffness of anchor groups increases with increasing number of studs. However, for anchor groups exposed to fire, the difference of the shear stiffness between anchor groups with different number of studs is relatively small. Anchor groups with different number of studs show very similar reduction rate of shear stiffness.

The reduction of resistance of anchor groups is the highest after 15 min of fire. After 60 min of fire, the anchor groups with different number of studs show almost the same relative resistance. The experimental and numerical analyses demonstrate that the projected area ratio according to CC-method can be used to calculate the resistance of anchor groups from resistance of single anchor after different fire exposures. However, further studies with more anchor configurations and data are needed for verification.

7. PRY-OUT FAILURE OF SINGLE HEADED STUD ANCHORS IN THE COLD STATE

7.1. Scope

Concrete pry-out failure mode usually occurs for anchors embedded relatively shallowly in the central region of concrete slab—free from all edge effects—and loaded in shear. It was considered as the result of "kicking back" concrete behind the stud. At ambient condition, the pry-out failure mechanism and prediction formulas are discussed in Chapter 2.2.3. According to Equation (2.12), the failure load is mainly influenced by the embedment depth and concrete strength. The resistance of anchor is proportional to the embedment depth to the power of 1.5 and to the compressive strength to the power of 0.5. However, it is not clear if these relations are still valid for anchors after fire exposure and what is the load-bearing behaviour of anchors after fire exposure due to pry-out failure.

In this chapter, the pry-out failure of single headed stud anchors after fire exposure is investigated firstly by experiments. The anchors, with three different embedment depths, for pry-out failure tests were cast in the central region of concrete slabs (with two different concrete grades: C20/25 and C40/50). Note that the concrete slabs were the same as those used for concrete edge failure tests described in Chapter 5. Therefore, the fire tests for pry-out failure are referring to the same fire tests as for concrete edge failure tests in the cold state. Numerical models were then verified based on the experimental results. Moreover, more parameters were considered to investigate the effect of fire exposure on the pry-out failure capacity.

7.2. Anchors and configurations

The headed stud anchor used for pry-out failure test is shown in Figure 7.1. It consists of a steel plate and a headed stud. A half groove was made at the loading side of the steel plate, which prevents the sliding of the loading device (see Figure 7.1a). Because the loading device may slide out after the steel plate rotates towards the shear loading direction if the contact surface is flat. This setup ensures that a full concrete breakout failure can be developed.

For all the anchors, the same diameter (25 mm) and size of the head were used. Three embedment depths ($h_{ef} = 70$ mm, 85 mm and 100 mm) were considered. The anchors with $h_{ef} = 70$ mm and 85 mm were produced using structural steel S235J2. The anchors with $h_{ef} = 100$ mm were produced by stainless steel type 1.4301 (*European Committee for Standardization*, 2014) for its higher mechanical properties than S235J2. The dimensions of the headed studs were taken

according to ISO 13918 (*International Organization for Standardization*, 2008). The anchorage configurations are listed in Table 7.1.

(a)   (b)
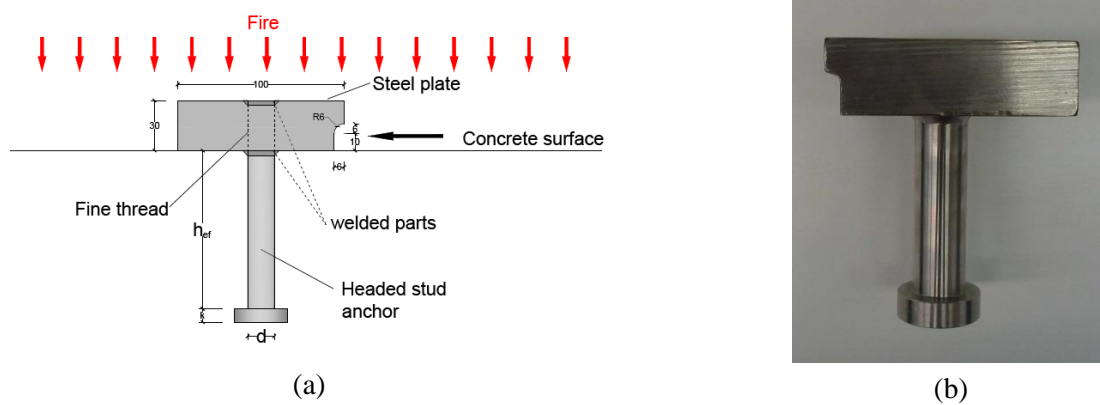
Figure 7.1 Headed stud anchor for pry-out failure test.

Table 7.1 Anchorage configurations for pry-out failure tests

Identification	h_{ef}	d	ISO 834 fire duration	Concrete grade	Number of tests
h70d25	70	25	0 min	C20/25; C40/50	2; 2
h85d25	85	25	0 min	C20/25; C40/50	2; 2
h100d25	100	25	-	-	-
h70d25	70	25	15 min	C20/25; C40/50	3; 3
h85d25	85	25	15 min	C20/25; C40/50	3; 3
h100d25	100	25	15 min	C20/25; C40/50	3; 3
h70d25	70	25	60 min	C20/25; C40/50	3; 3
h85d25	85	25	60 min	C20/25; C40/50	3; 3
h100d25	100	25	60 min	C20/25; C40/50	3; 3

7.3. Concrete specimen

The mixture and casting of concrete specimens are the same as for concrete edge failure test. Details on the production of concrete can be referred to Chapter 5.3. Two concrete grades C20/25 and C40/50 were used. The anchors were fixed at the bottom of the wooden mould, as shown in Figure 5.2, circled number 3.

7.4. Test setups

The test setup is shown in Figure 7.2, which is basically the same as that for concrete edge failure. The loading plate fits with the groove at the back side of the steel plate of the anchor. The anchors were loaded by pulling the tension rod using the hydraulic cylinder, which has a maximum capacity of 400 kN. The pry-out capacities of different anchors were first calculated according to Equation (2.11), based on which the corresponding loading cell was applied for measuring the load. LVDT-0 was used to measure the horizontal movement of the steel plate at the front side of the anchor. LVDT-1 and -2 were used to measure the vertical movement of the steel plate in the middle and at the back side of the anchor. The load and displacement were all recorded on a computer by using data logger.
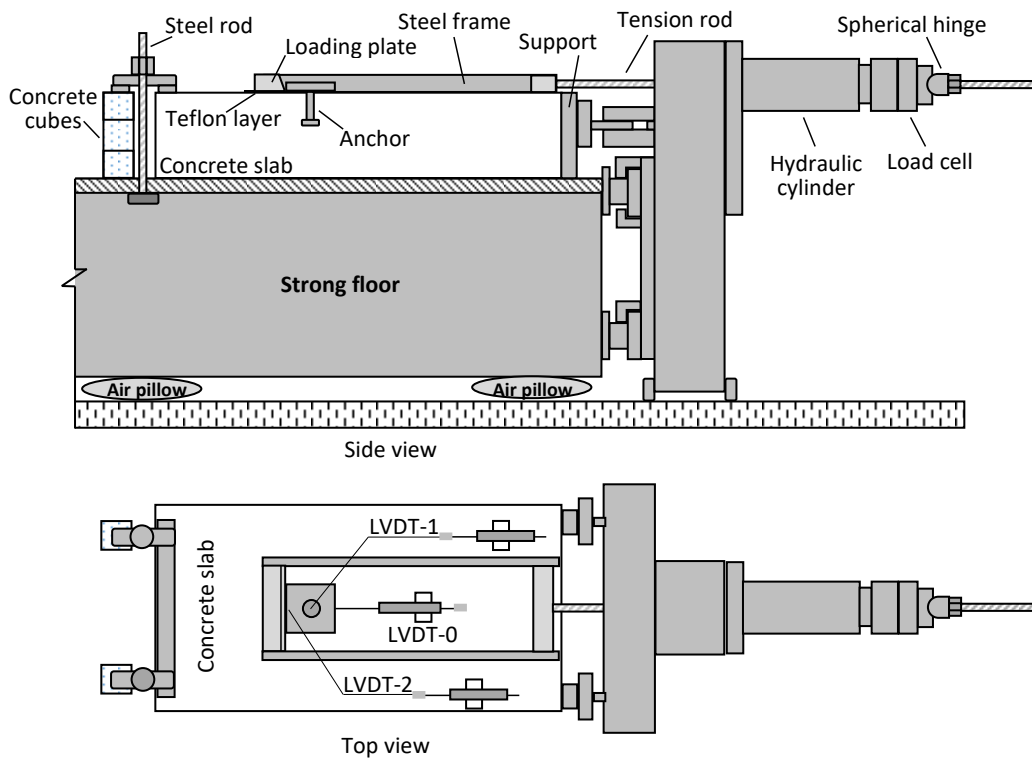
Figure 7.2 Pry-out test setup and configuration.

7.5. Test result and discussion

7.5.1. Failure pattern

Figure 7.3a shows the concrete breakout patterns for different fire durations. After 15 min and 60 min of fire, the spalling of concrete surface outside the fracturing zone can be seen (the surface spalling in the central region of concrete slabs is also presented in Figure 5.6). The failure patterns are basically the same except that the size of fracture zone becomes smaller for fire exposure of 60 min, which will be analysed in the following. Figure 7.3b shows the deformation of the anchor shaft. It was observed that only anchors with embedment depth of 85 mm at ambient temperature present deformation at the upside of the shaft. For other cases, the anchors were stiff enough against the concrete break out capacity. Detailed description of failure modes is given in Appendix A Table A.4 .

(a)

(b)
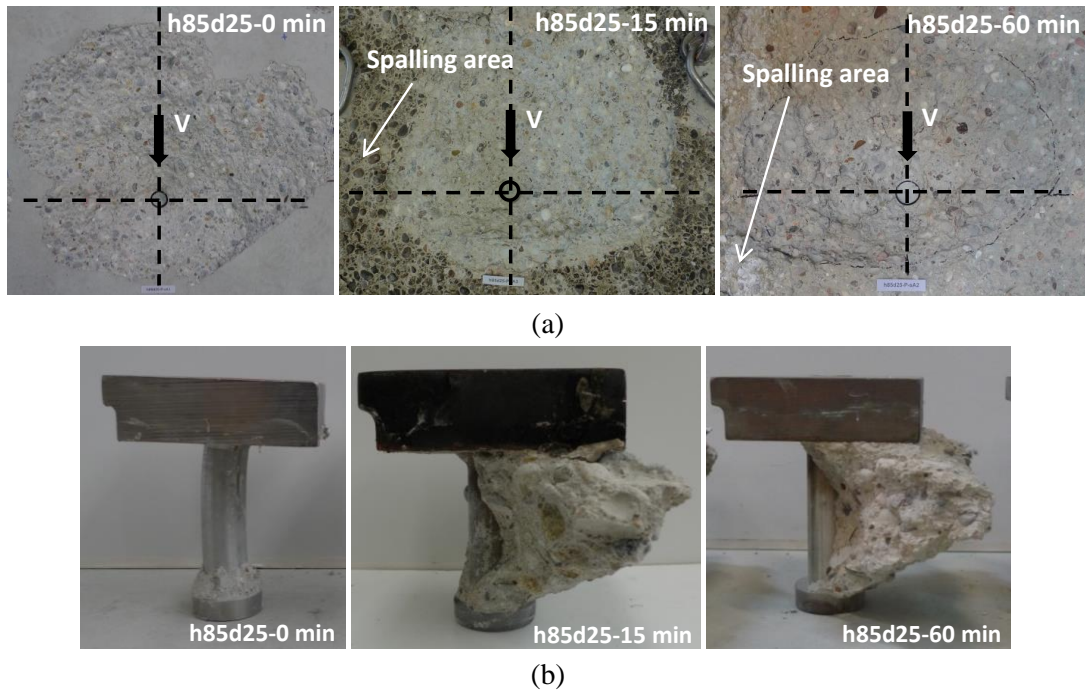
Figure 7.3 Failure patterns of pry-out tests after fire. (a) Concrete breakout; (b) anchor.

As shown in Figure 7.4a, the failure patterns can be illustrated as symmetrical about the b-b axis. The rear part (under tension during loading) is typically much larger than the front part (under compression). After fire exposure, the concrete surface spalling depth h_1 is formed around the anchor plate, which reduces the volume of concrete that resists the loading (see Figure 7.4b).
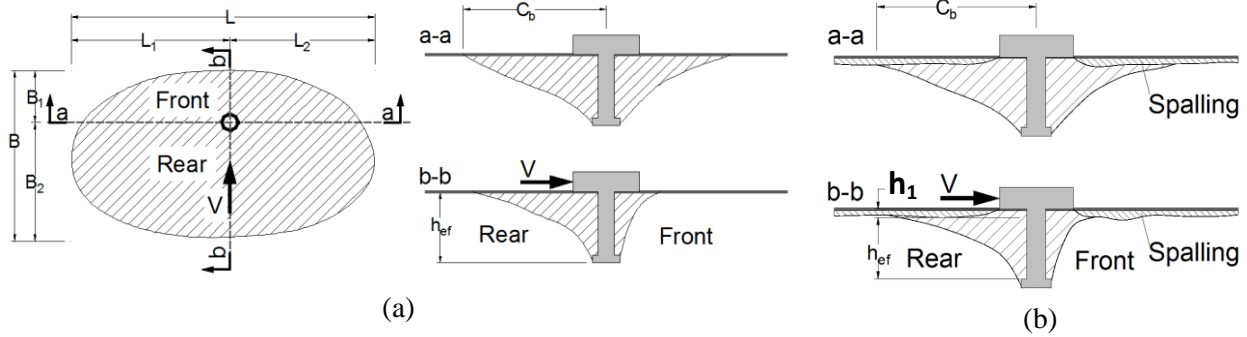
Figure 7.4 Sketch of pry-out failure patterns.

According to *Eligehausen et al.* (2006) the fracture surface of single anchor with large spacing and edge distance can be idealised as a square with side length $s_{cr,N} = 2 \cdot 1.5 h_{ef}$ at ambient temperature (see Figure 2.1). Therefore, an effective size factor $s_{fi(0)} = 1.5$ is named. However, this conclusion may have to be changed for anchors due to pry-out failure after fire exposure, as mentioned above referring to Figure 7.3a, the fracture size was observed to become smaller after especially long duration of fire.
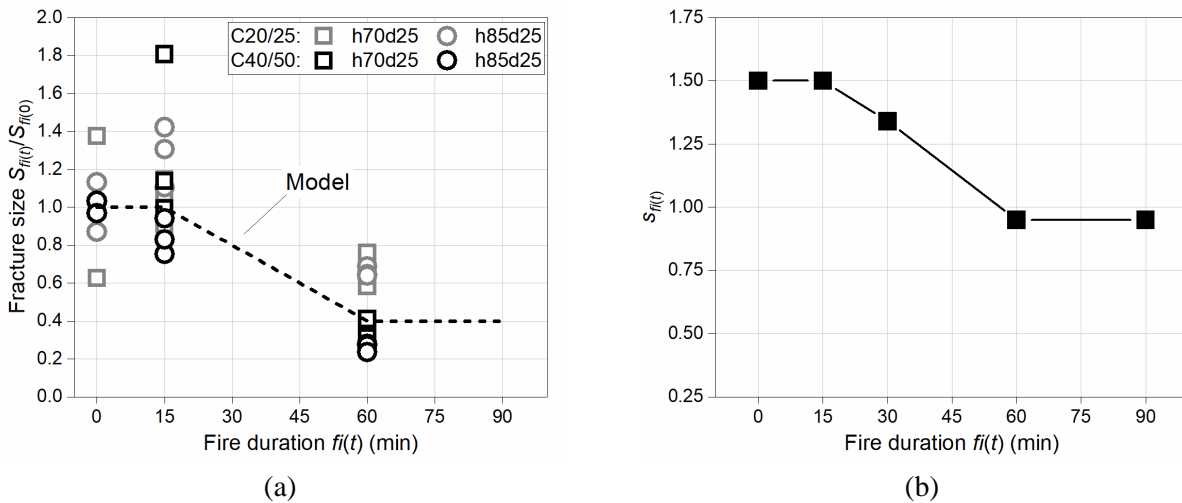
Figure 7.5 Variation of (a) fracture surface size and (b) effective size factor s_1.

Figure 7.5a shows the variation of the relative size of fracture ($S_{fi(t)} = L \times B$) measured on single stud anchors h70d25 and h85d25 by pry-out failure in concretes C20/25 and C40/50, which indicates that the fracture surface after 15 min of fire exposure keeps the same as that at ambient temperature. However, it is distinctly reduced for 60 min of fire duration. Since it has been noticed that the change of load-bearing behaviour for anchors mainly occurred between the ambient condition and 60 min of fire exposure and tends to be constant afterwards, the relative

fracture size is assumed to decrease linearly from 15 min to 60 min and then keep constant for 90 min of fire. Taking this effect into account the effective size factor $s_{fi(t)}$ is gradually decreased from 1.5 at ambient temperature to 1.5, 1.34, 0.95 and 0.95 after 15 min, 30 min, 60 min and 90 min of fire duration, respectively (see Figure 7.5b). Therefore, the idealised projection area, considering fire exposure, can be taken according to Equation (7.1).

$$A_{c,N,fi(t)}^{0} = (2s_{fi(t)} \cdot h_{ef})^2 \tag{7.1}$$

7.5.2. Load-displacement behaviour

The load-displacement curves for different fire exposures for both concrete grades C20/25 and C40/50 are shown in Figure 7.6.
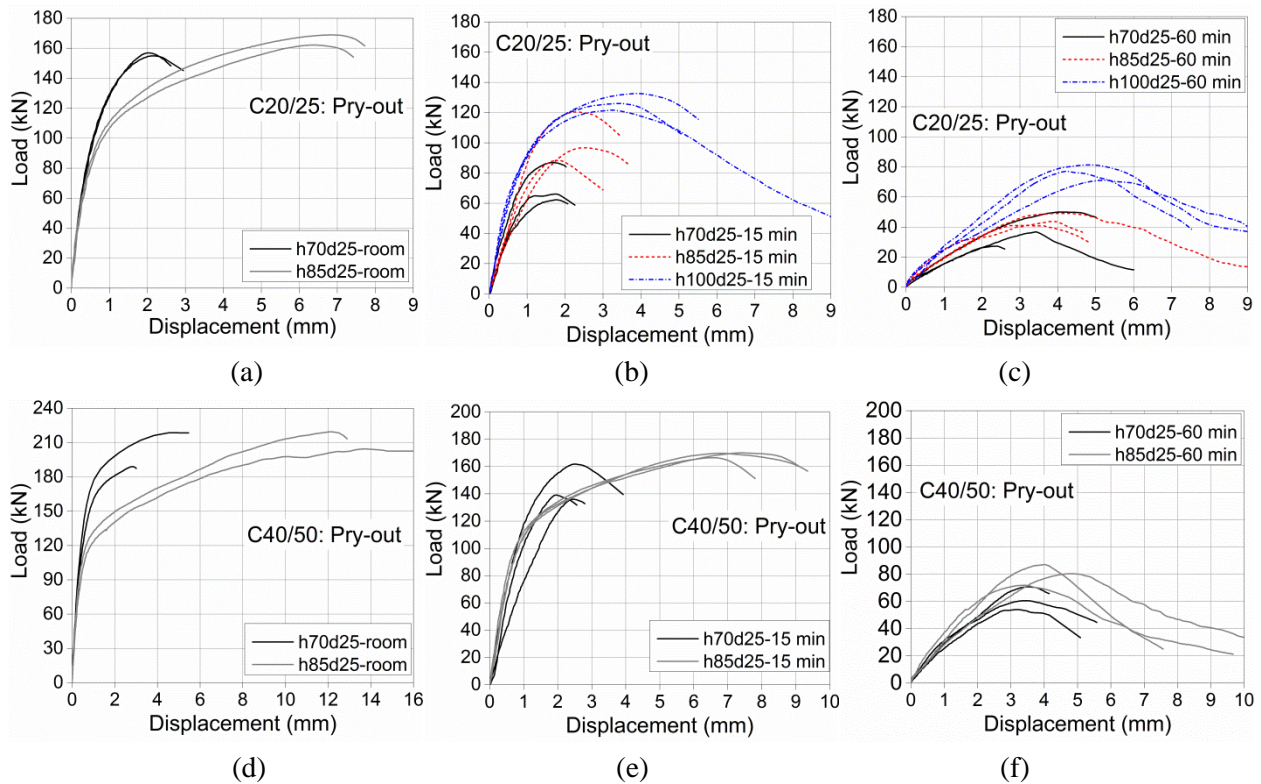
Figure 7.6 Load-displacement curves of anchors after different fire exposures for ambient temperature in concrete (a) C20/25 and (d) C40/50, 15 min of fire exposure in concrete (b) C20/25 and (e) C40/50, and 60 min of fire exposure in concrete (c) C20/25 and (f) C40/50.

The pry-out capacity at ambient temperature is mainly dependent on the embedment depth h_{ef} (*Anderson and Meinheit*, 2005; *Jebara et al.*, 2016), which is demonstrated in Figure 7.6a and d. In both concrete grades C20/25 and C40/50, the increase of embedment depth results in higher

148

capacity and also obviously more ductile load-displacement behaviour. Smaller h_{ef}/d ratio leads to stiffer response. After 15 min of fire exposure, the increase of embedment depth results in significantly higher capacity for concrete grade C20/25, whereas it is not so obvious for concrete grade C40/50 (see Figure 7.6b and e). After 60 min of fire, the peak load is largely reduced. In concrete C20/25 larger embedment depth still results in higher peak load, however, there is almost no difference in load-displacement curves for two different embedment depth in concrete grade C40/50. It is worthy to note that at ambient temperature shorter embedment depth shows stiffer load-displacement behaviour but after fire exposure deeper embedment depth shows stiffer load-displacement behaviour, which can be attributed to the fire-damaged concrete surface.
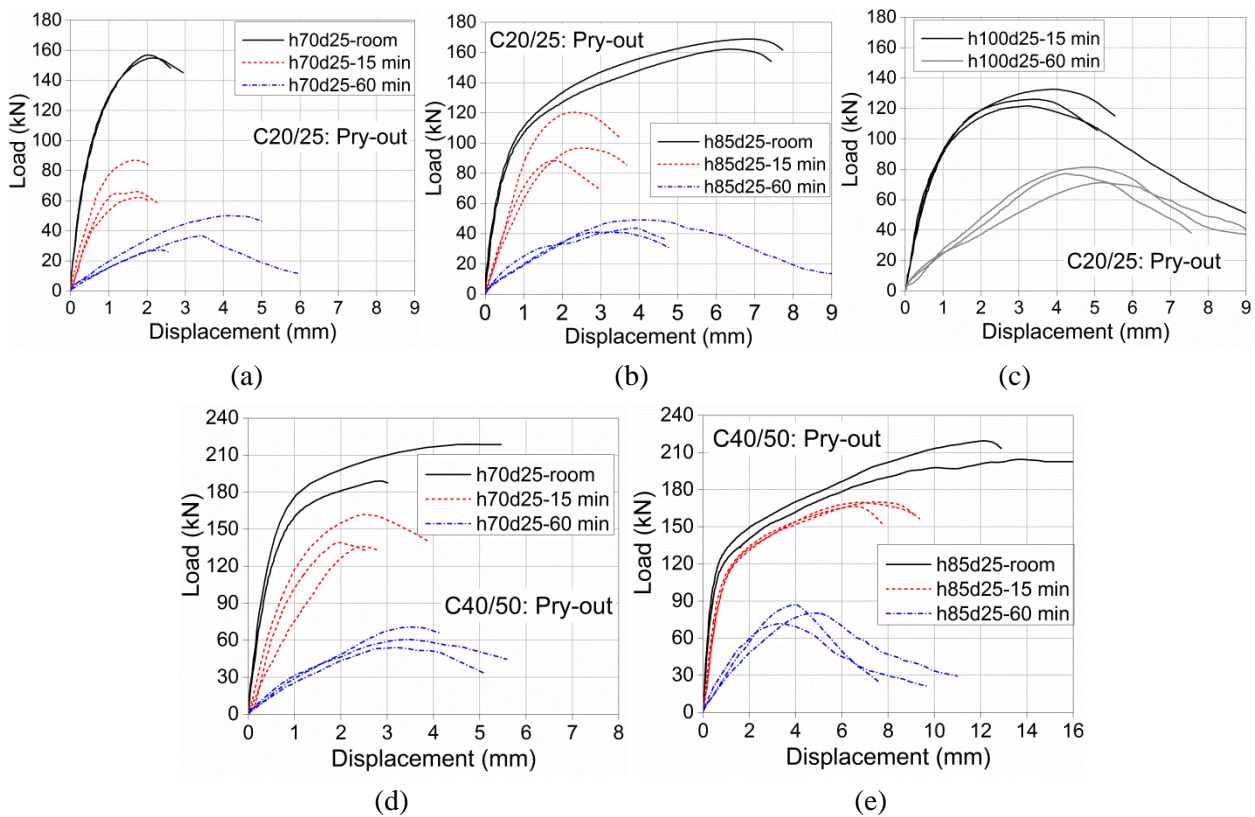
Figure 7.7 Influence of fire exposure on the load-displacement curves of anchors with different h_{ef} for h75d25 in concrete (a) C20/25 and (d) C40/50, h85d25 in concrete (b) C20/25 and (e) C40/50, and h100d25 in concrete (c) C20/50.

Figure 7.7 shows the influence of fire exposure on the load-displacement curves of anchors with different embedment depth for both concrete grades C20/25 and C40/50. It is seen that the influence of fire exposure on the load-displacement behaviour is significant in all anchorage configurations. After very short fire exposure the peak loads are largely reduced, especially after 60 min of fire the reduction is prominent. Similar as in the case of concrete edge failure, with increase of fire duration the response becomes more ductile.

Figure 7.8 shows the influence of concrete grade on the load-displacement behaviour of anchors after different durations of fire exposure. At ambient temperature, the influence of concrete grade is obvious on the peak load and also on the initial stiffness. Higher concrete strength results in larger displacement at the peak load $\delta(V_{u,cp})$. After 15 min of fire exposure, for anchor with short embedment depth of 70 mm, the influence of concrete grade is mainly on the peak load. The influence on the ductility is very limited (Figure 7.8b). However, for larger embedment depth of 85 mm the higher concrete grade leads to higher peak load and also more ductile response (Figure 7.8c). After 60 min of fire, the concrete grade has obvious influence on the peak load but almost no influence on ductility.
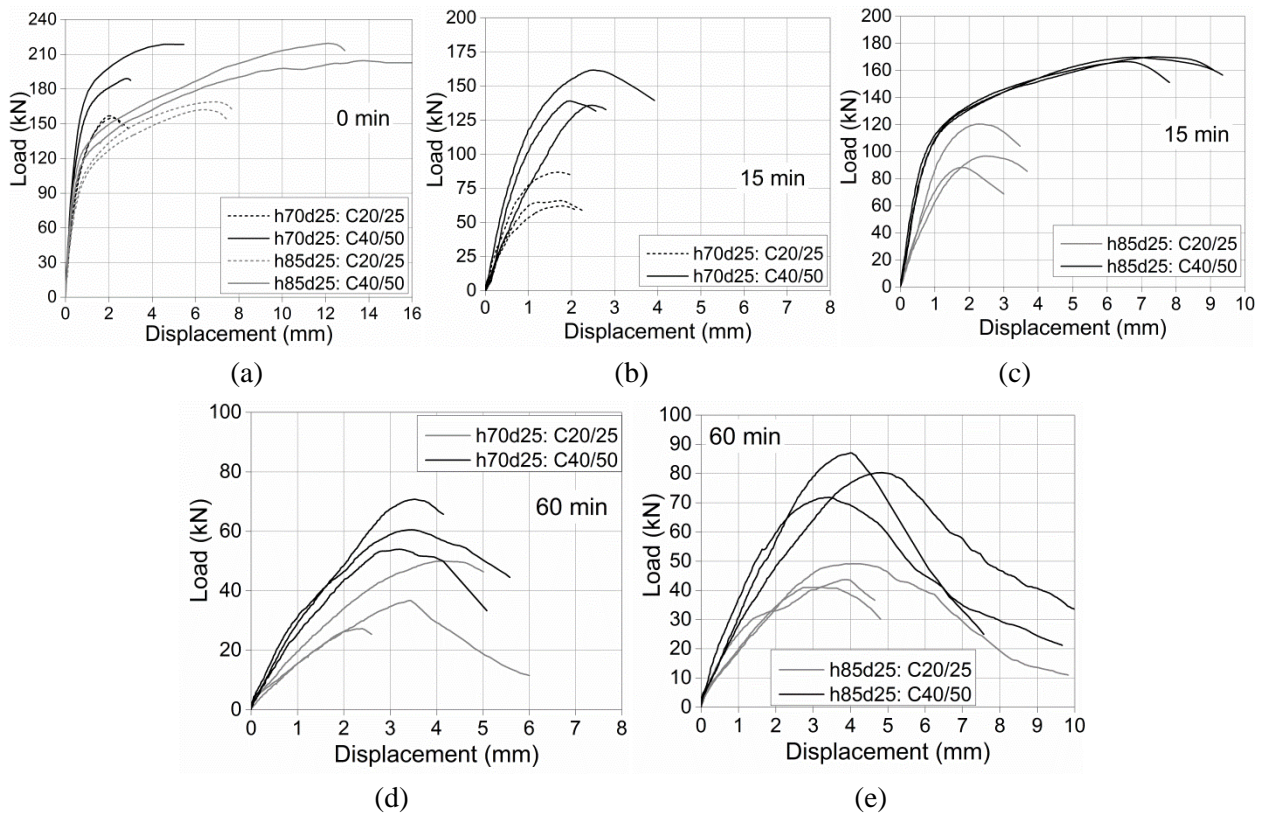
Figure 7.8 Influence of concrete grade on the load-displacement behaviour of anchors: (a) h70d25 and h85d25 at ambient temperature; (b) h70d25 and (c) h85d25 after 15 min of fire exposure; (d) h75d25 and (e) h85d25 after 60 min of fire exposure.

7.5.3. Stiffness of the response

The same as in Chapter 5.6.3 for the stiffness of concrete edge failure load-displacement curve, the stiffness of the pry-out response is evaluated as the ratio of the half peak load to the corresponding displacement: $k_{V,fi(t)} = 0.5V_{u,cp,fi(t)}/\delta(0.5V_{u,cp,fi(t)})$. Figure 7.9 shows the variation of stiffness of anchors failed in pry-out after different fire durations. As already mentioned in

Chapter 7.5.2, at ambient temperature the shorter embedment depth leads to stiffer load-displacement response (Figure 7.9a). However, from Figure 7.9b and c it is seen that the shear stiffness increases with increasing embedment depth both after 15 min and 60 min of fire duration. Figure 7.9d shows the reduction of the shear stiffness as a function of fire duration. The reduction is significant after 15 min of fire. For both of the concrete grades, the anchor with embedment depth of 70 mm presents larger reduction than that of anchor with embedment depth of 85 mm. After 60 min of fire duration, the shear stiffness reduces further and only 11% of original stiffness at ambient temperature remains for all embedment depths.

(a)

(b)

(c)

(d)
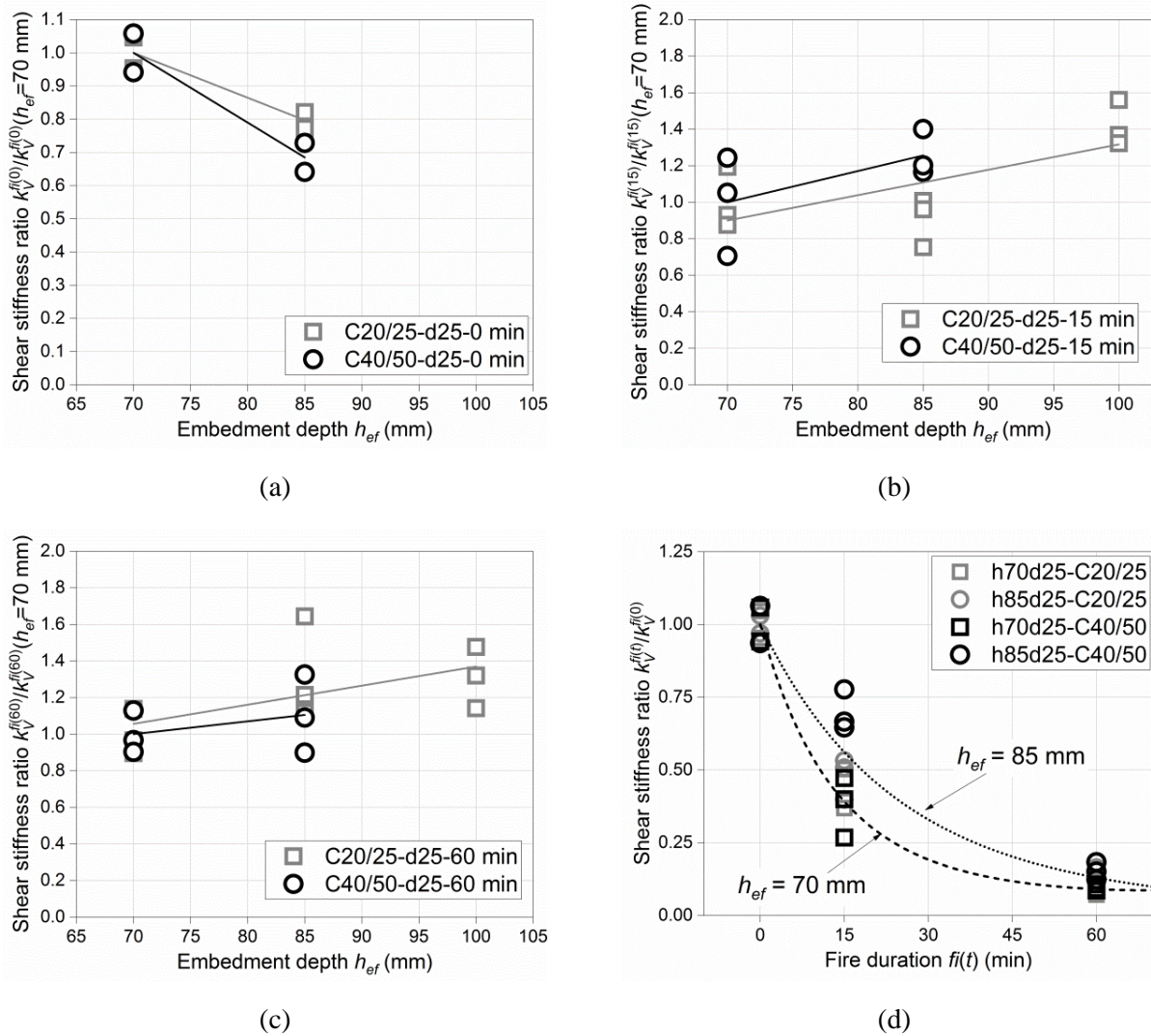
Figure 7.9 Variation of stiffness of anchors failed by pry-out. (a) At ambient temperature; (b) after 15 min of fire exposure; (c) after 60 min of fire exposure; (d) reduction of stiffness as a function of fire duration.

7.5.4. Displacement at peak load

The typical movement of the fastener is schematically shown in Figure 7.10. The displacements were recorded by the setup as described in Chapter 7.4. The anchor moves horizontally and simultaneously vertically lifted up. At peak load, the displacement δ_h, vertical displacements δ_{vm} at the middle of the steel plate and δ_{vb} at the rear end of the steel plate can be obtained.
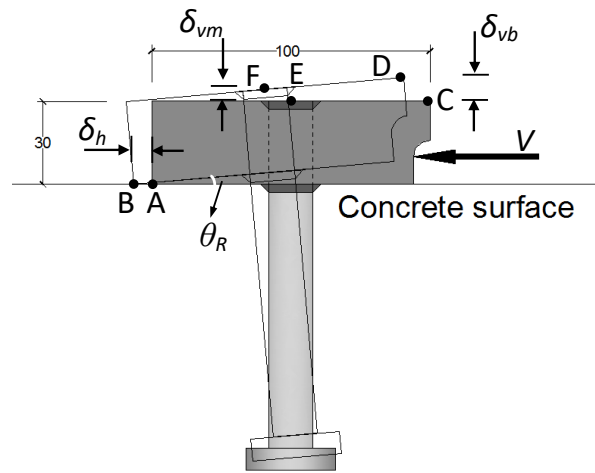
Figure 7.10 Rotation and measurement of the loaded anchor.

| (a) | (b) |
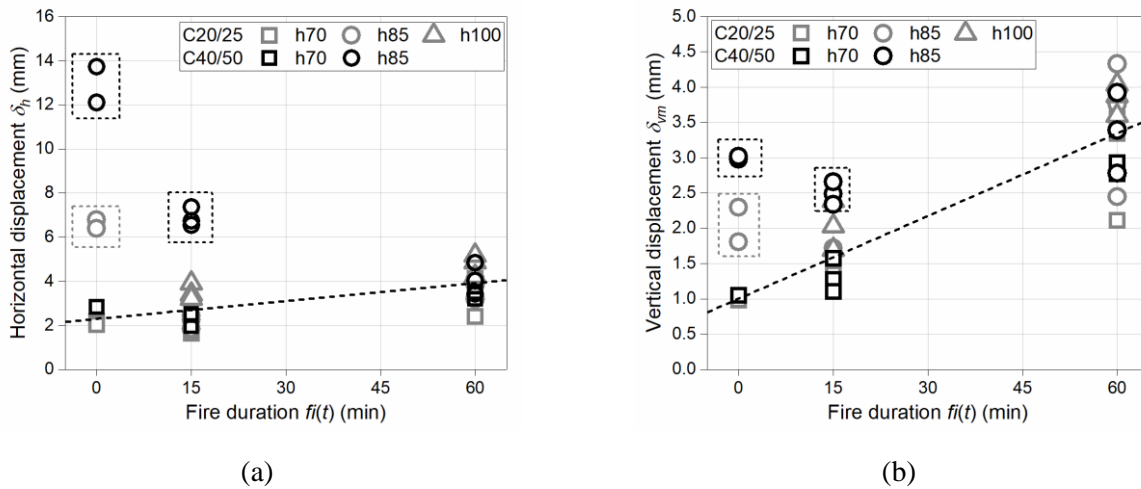
Figure 7.11 (a) Horizontal displacement; (b) vertical displacement at the middle of the steel plate.

In Figure 7.11 δ_h and δ_{vm} are shown as functions of fire duration for anchor with different embedment depths and in different concrete grades. It can be seen that anchor with relatively large embedment depth of 85 mm shows obvious large displacement before the ultimate load is reached, in concrete C20/25 and C40/50, at ambient temperature, and in concrete C40/50 after 15

min of fire exposure. This also results in large vertical movement of the steel plate. In Figure 7.11 and Figure 7.12, these data are considered as outliers because most of the deformations close to peak loads are probably related to the deformation of anchor shaft (steel).

After excluding the outliers, Figure 7.11a shows that δ_h is a linear function of fire duration. The similar linear relationship can also be seen for the vertical component of displacement (δ_{vm}) (see Figure 7.11b). Moreover, it can be seen that concrete grade and embedment depth have no strong influence on this relation.

In Figure 7.12a the ratio between δ_{vb} and δ_{vm} is shown. It is seen that the vertical movement at the rear end of the steel plate is basically about two times of that at the middle. However, after long duration of fire exposure, due to large horizontal movement this ratio is slightly decreased. Based on the above analyses, the rotation angle θ_R can be calculated and it is shown as a function of fire duration in Figure 7.12b. Angle θ_R increases linearly with increasing fire duration, which is about 1.17^o at ambient temperature and 2.98^o after 60 min of fire duration. The embedment depth can be seen to have a noticeable influence on the rotation. The anchors with deeper embedment depth show larger rotation especially after fire.

(a)

(b)
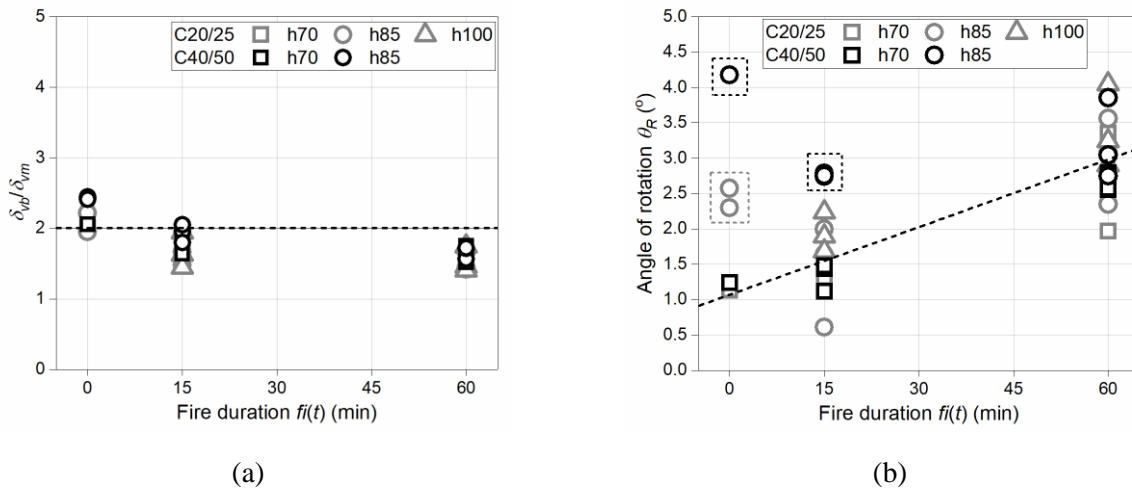
Figure 7.12 (a) Ratio between the vertical movement at the back and middle of the steel plate; (b) angle of rotation θ_R before and after fire.

7.5.5. Resistance

The direct test data of resistance is evaluated as functions of concrete strength, embedment depth and fire duration, to analyse the influence of fire exposure on the pry-out failure capacity (data are listed in Annex A Table A.4). However, as discussed above, the concrete surface spalling occurred around pry-out failure test anchors and it reduced the volume of concrete that can bear

load. Consequently, it may reduce the real resistance of corresponding anchor. Further discussion on the resistance is therefore presented in the numerical part.

7.5.5.1. Resistance at ambient temperature

The peak loads obtained experimentally at ambient temperature are only representative and are firstly compared with calculations according to the prediction Equation (2.11) for Eurocode 2 and ACI 318 code. Figure 7.13a illustrates the pry-out failure load as a function of embedment depth at ambient temperature. It can be seen that the capacity increases slightly with increasing embedment depth. Figure 7.13b shows the peak load as a function of concrete strength. The increase of resistance follows the tendency predicted by Eurocode 2 equation. However, the experimental results are on average about 20% higher than the predicted ones for both concrete grades C20/25 and C40/50. As shown in Figure 5.2, the anchors for pry-out failure tests were fixed on the bottom of the wooden mould. The bottom side of the concrete slab may have higher strength than the top side, due to its dense material structure. This may cause higher pry-out failure capacity of the anchors.
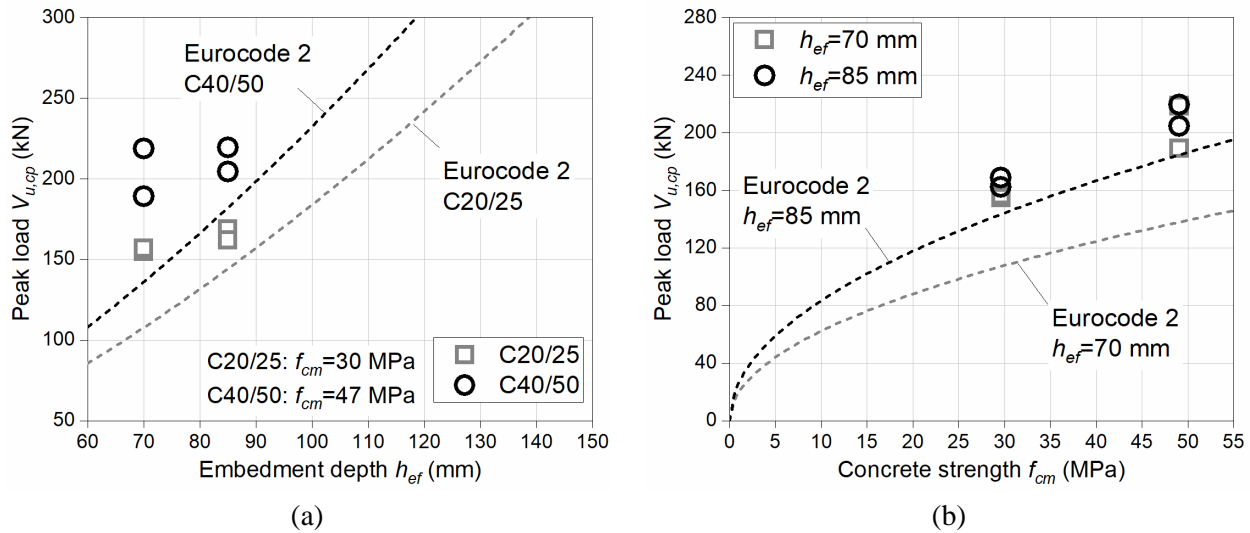
Figure 7.13 Pry-out capacity of anchors at ambient temperature as a function of (a) embedment depth and (b) concrete strength.

7.5.5.2. Influence of concrete compressive strength

Figure 7.14 shows the influence of concrete compressive strength on the relative capacity of anchors failed by pry-out after different fire durations. It can be seen that the influence of concrete strength on the peak load is proportional to the power of 0.5 at ambient temperature (Figure 7.14a), which is the same as according to Eurocode 2 and ACI 318 code. Figure 7.14b shows that the influence of concrete strength after 15 min of fire exposure is increased compared

to that at ambient temperature, which is proportional to the concrete strength to the power of about 1.6. After 60 min of fire exposure, the influence of concrete strength on the capacity is strong but relatively reduced comparing for 15 min of fire (Figure 7.14c). It seems that after fire exposure the concrete strength plays important role in the resistance. However, it should be noted that as the concrete is cracked by the heating and cooling process, especially after long duration of fire, the scatter of data is relatively large.

(a)

(b)

(c)
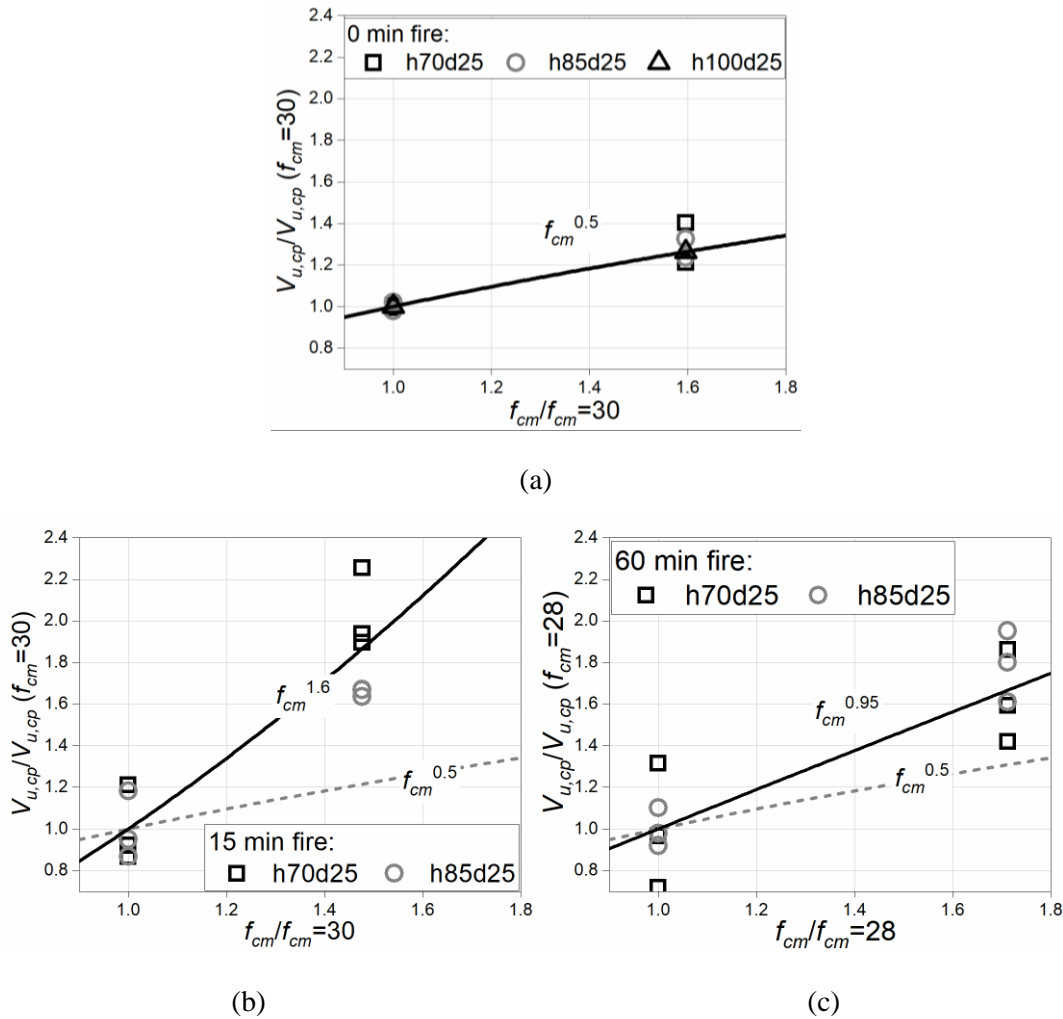
Figure 7.14 Influence of concrete strength on the relative pry-out failure load. (a) At ambient temperature; (b) after 15 min of fire duration; (c) after 60 min of fire duration.

7.5.5.3.   Influence of embedment depth

Figure 7.15 shows the influence of embedment depth on the relative resistance of pry-out failure capacity, which is the ratio between the peak loads of anchors with different h_{ef} and the peak load for anchor with $h_{ef} = 70$ mm. It is seen that the embedment depth has relatively large influence on the pry-out failure capacity of anchors, and this influence is increasing with increasing fire duration.

(a)

(b)

(c)
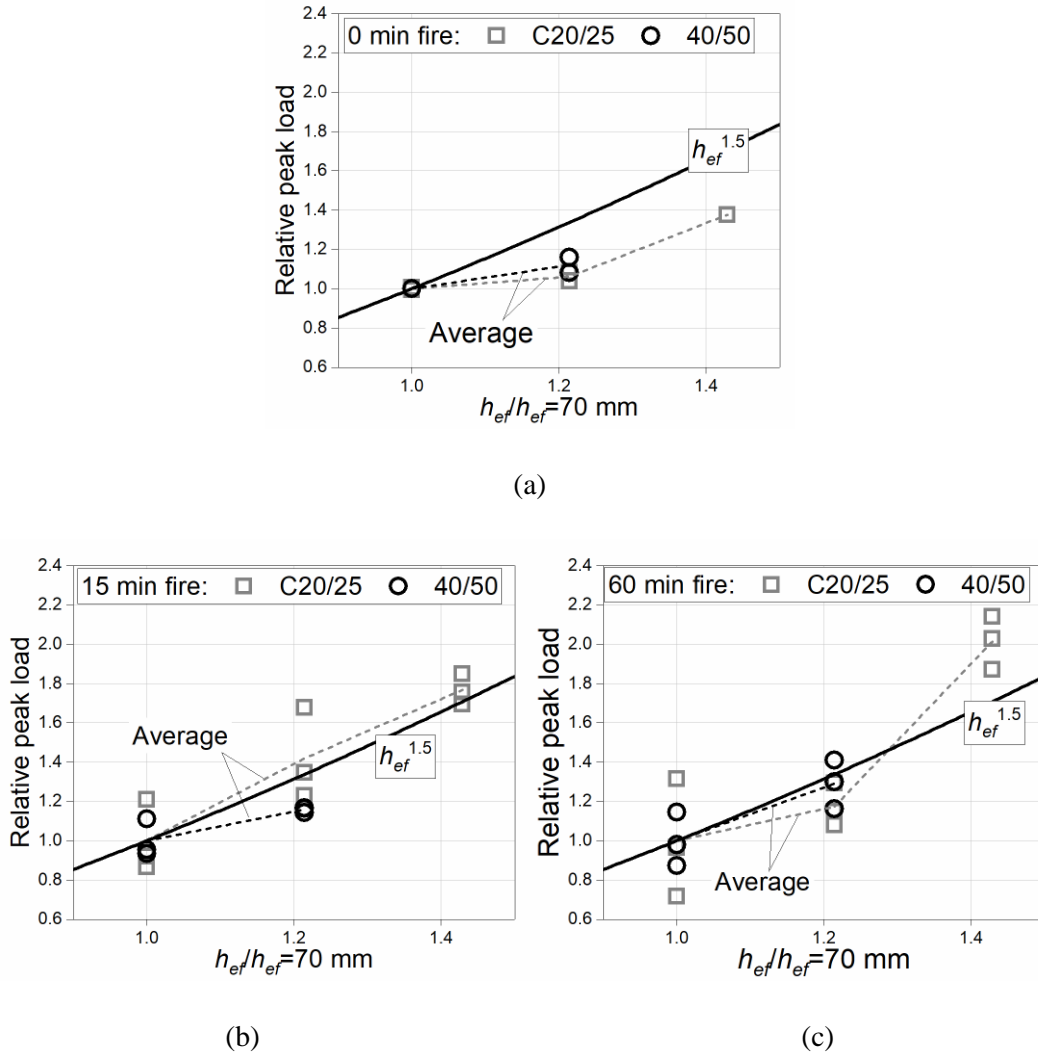
Figure 7.15 Influence of embedment depth on the relative pry-out failure load. (a) At ambient temperature; (b) after 15 min of fire duration; (c) after 60 min of fire duration.

7.5.5.4.   Influence of fire duration

Figure 7.16 presents the relative peak load as a function of fire duration. The pry-out failure resistance is strongly reduced with the increase of fire duration. After 15 min of fire exposure, the resistance of anchors in concrete C20/25 is reduced more than that in concrete C40/50. Anchors with shorter embedment depth show relatively more reduction of resistance. Anchor with $h_{ef} = 70$ mm presents on average as large as 54% reduction of reference resistance. After 60 min of fire, all anchors show very similar relative peak load to the reference at ambient temperature, which is around 30% of reference value.
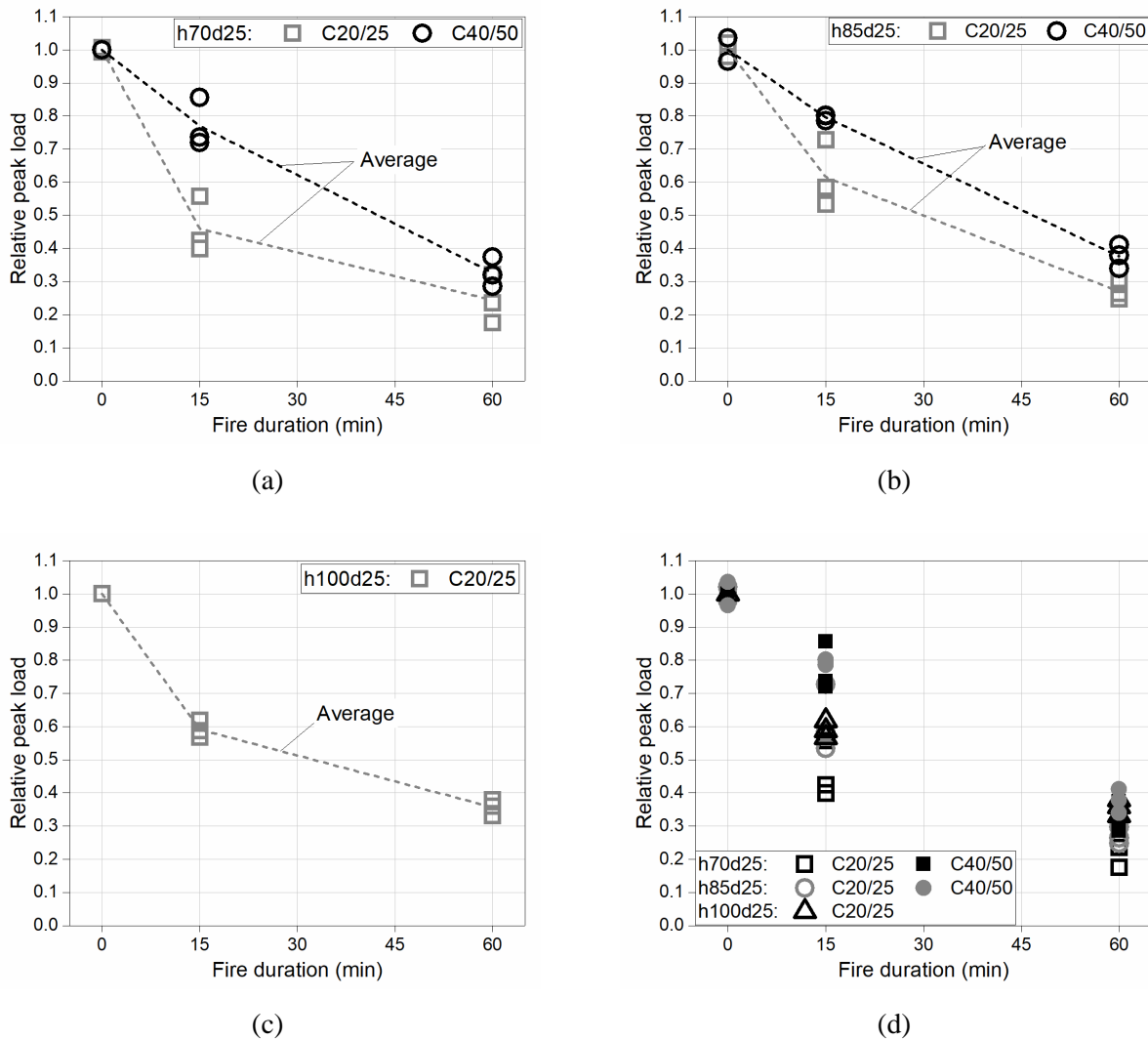
Figure 7.16 Influence of fire duration on the relative pry-out failure load. (a) h70d25; (b) h85d25; (c) h100d25; (d) all data.

7.5.6. Summary

According to current codes (*European Committee for Standardization*, 2018; *American Concrete Institute Committee 318*, 2014), the pry-out failure capacity of anchors at ambient temperature is found to be influenced by the concrete strength to the power of 0.5 and the embedment depth to the power of 1.5. However, the peak loads obtained in the performed tests are about 20% higher than the prediction.

Principally, with increasing duration of fire the resistance and stiffness decrease, however the ductility increases. As expected, with increase of embedment depth reduction of resistance due to fire decreases. Furthermore, for short period of fire, concrete strength makes a prominent

difference on the pry-out failure capacity of anchors. However, with increase of fire duration, the influence of concrete strength becomes less important.

Nevertheless, only several configurations of anchors were tested. Therefore, numerical analyses are needed to validate the finite element models and to perform parametric study.

7.6. Numerical study

In this chapter the numerical analysis is conducted to verify the finite element models and to perform parametric study in order to better understand the influence of different parameters on the pry-out failure under fire. All numerical results are summarized in Annex B Table B.4 . In particular, numerical analysis is performed to investigate the influence of surface spalling on the pry-out failure load before and after fire exposure.

7.6.1. Finite element model and material property

Figure 7.17 shows the geometry, typical finite element discretization and boundary conditions of the numerical model for simulating pry-out failure before and after fire exposure. For the sake of saving the computational time, only half of the specimen is modelled by utilising symmetry plane (see Figure 7.17a). The concrete slab has the length L which is 8 times of the embedment depth h_{ef} of the anchor plus 100 mm on each side, the width W is $4h_{ef}$ plus 100 mm, and the height H is 250 mm for all models. This is sufficient to avoid splitting of the specimen during loading. As shown in Figure 7.17b, between the concrete and fastener contact elements are employed as contact layer. The finite element discretization of concrete is performed by employing 4-node constant strain solid finite elements, while for the discretization of fastener 8-node solid finite elements are used. The model is restrained on the symmetry plane in y direction plus constraints c_1, c_2 and c_3 as shown in Figure 7.17. The surface of the concrete specimen is heated according to ISO 834 fire curve and cooled down to the ambient temperature. Fasteners are loaded up to failure by displacement control.

The configuration of anchors for numerical investigation is listed in Table 7.2. As can be seen, three different embedment depths, five different fire durations, three different concrete strength and two loading conditions are investigated.
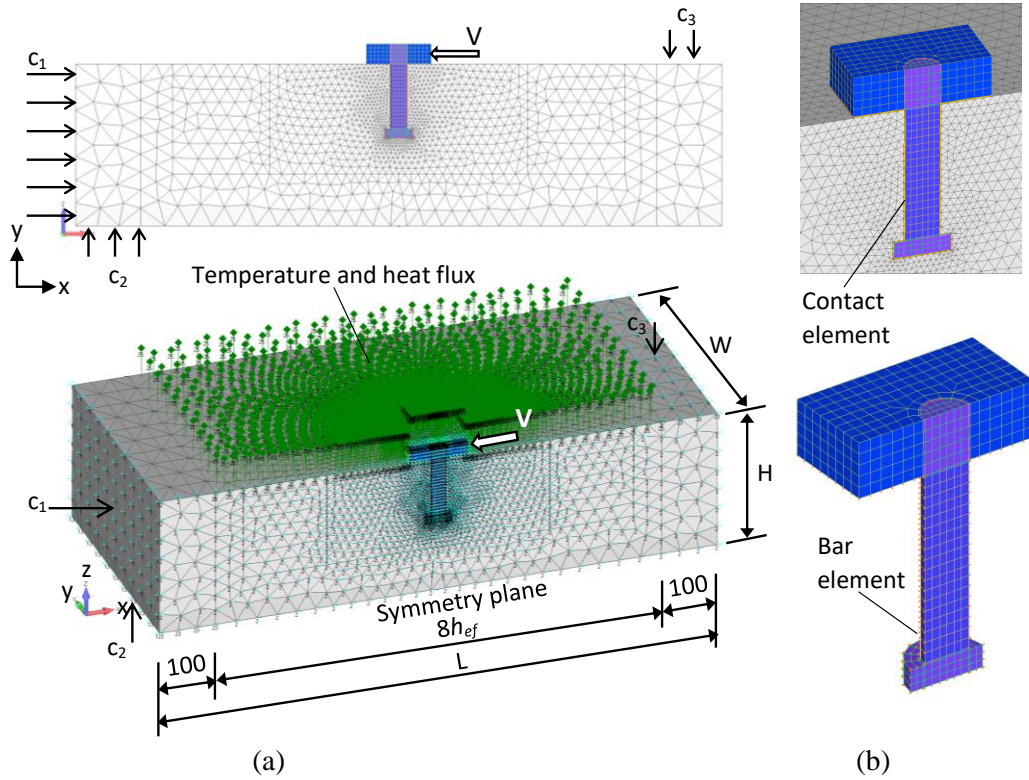
Figure 7.17 Geometry and finite element discretization of the model for pry-out failure simulation.

Table 7.2 Configuration of anchors for numerical simulation of pry-out failure

Identification	h_{ef} (mm)	d (mm)	$fi(t)$ (min)	Concrete grade	Loading condition
h70d25	70	25	0 15 30 60 90	C12/15; C20/25; C40/50	Hot state (h); Cold state (c)
h85d25	85	25	0 15 30 60 90	C12/15; C20/25; C40/50	Hot state (h); Cold state (c)
h100d25	100	25	0 15 30 60 90	C12/15; C20/25; C40/50	Hot state (h); Cold state (c)

159

The material properties of concrete are listed in Table 7.3. Since the aim of the analysis was to investigate the failure of concrete, the behaviour of steel was assumed to be linear elastic. The Young's modulus of steel in the model is 200 GPa, with Poisson's ratio being equal to 0.33. The thermal properties of material are the same as specified in Chapter 5.7.2. Therefore, the temperature rise in concrete is the same as already verified and presented in Chapter 5.7.3.

Table 7.3 Material properties for pry-out failure simulation

Concrete	Young's modulus E_C (GPa)	Poisson's ratio v_c	Tensile strength f_{ctm} (MPa)	Compressive strength f_{cm} (MPa)	Fracture energy G_f (J/m^2)
C12/15	25.00	0.18	1.60	12.00	0.03
C20/25	30.00	0.18	2.90	30.00	0.06
C40/50	34.00	0.18	3.80	47.00	0.09

7.6.2. Thermal load

Figure 7.18 shows typical temperature distribution for anchors embedded in concrete C20/25 with embedment depth of 70 mm and 85 mm, respectively, at the last step of heating (15 min, 30 min, 60 min and 90 min). It is worth noting the heat penetrates along the anchor shaft into the depth. The steel part has relatively high thermal conductivity, resulting in faster heat transfer to the concrete in the area that is close to the anchor shaft. After about 30 min of heating, the heat penetrates to the depth of the stud head of the anchor h70d25. In contrast, this happens to anchor h85d25 after about 60 min of fire exposure. In analogy, for anchor h100d25 this will take longer time period. Since the strength of concrete is temperature dependent, and the pry-out failure resistance of anchor is closely associated with the concrete strength near the stud head, the depth of temperature penetration will influence the pry-out failure capacity of anchors significantly.
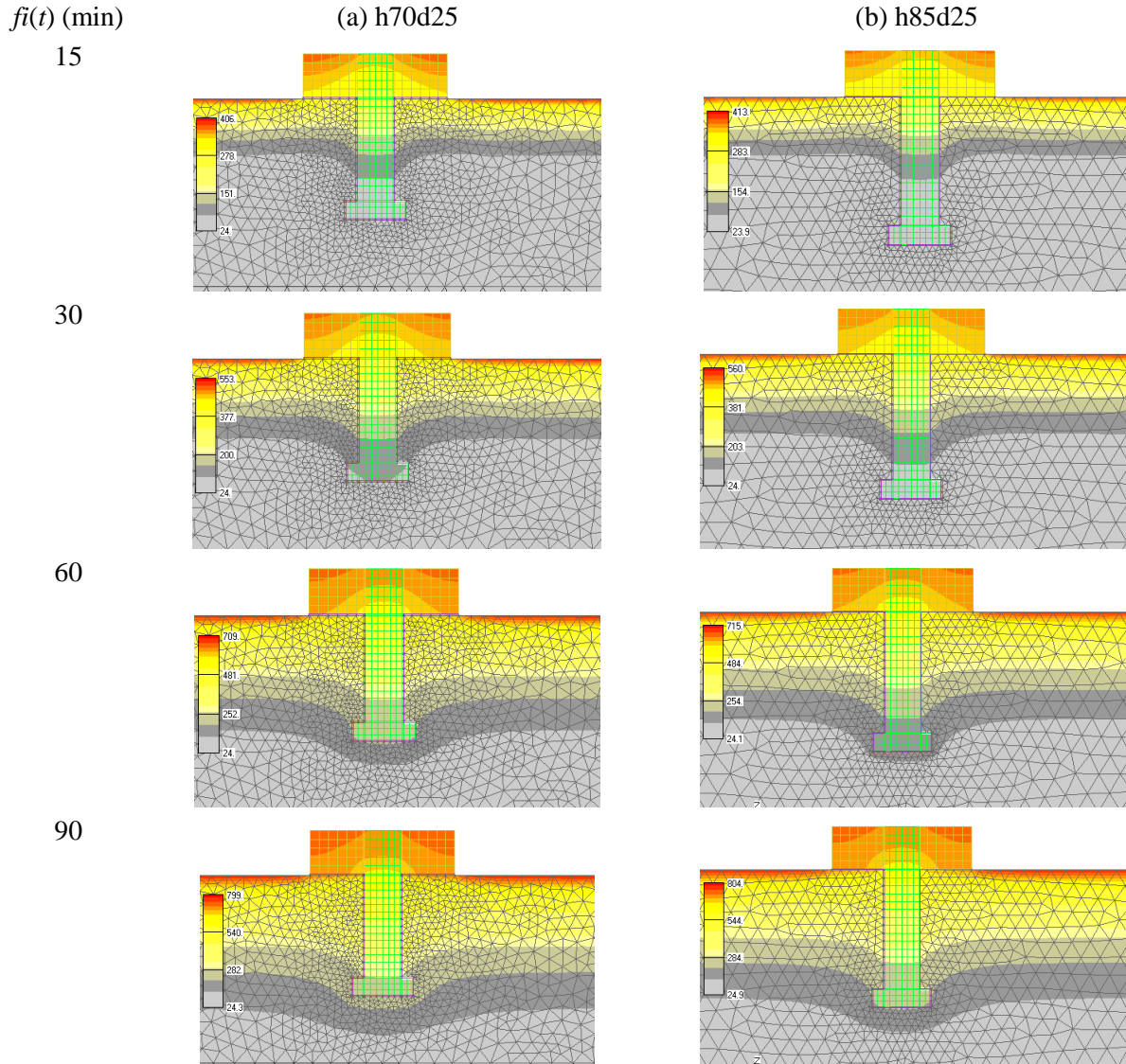
Figure 7.18 Temperature distribution of anchors embedded in concrete C20/25 after different fire durations. (a) h75d25; (b) h85d25.

7.6.3. Failure modes

Figure 7.19 shows the comparison between the fracture patterns obtained experimentally and numerically for the anchor with embedment depth of 85 mm. After 15 min and 60 min of heating, in the experiment concrete surface spalling occurred. Figure 7.19b shows the enclosed concrete block under the steel plate. This is due to the strongly compressed area at the front side of the anchor (see Figure 7.19c). Principally, there is good agreement between prediction and experiment. It can be seen that with increase of fire duration damage of concrete becomes severer and distributed over the larger volume of concrete.
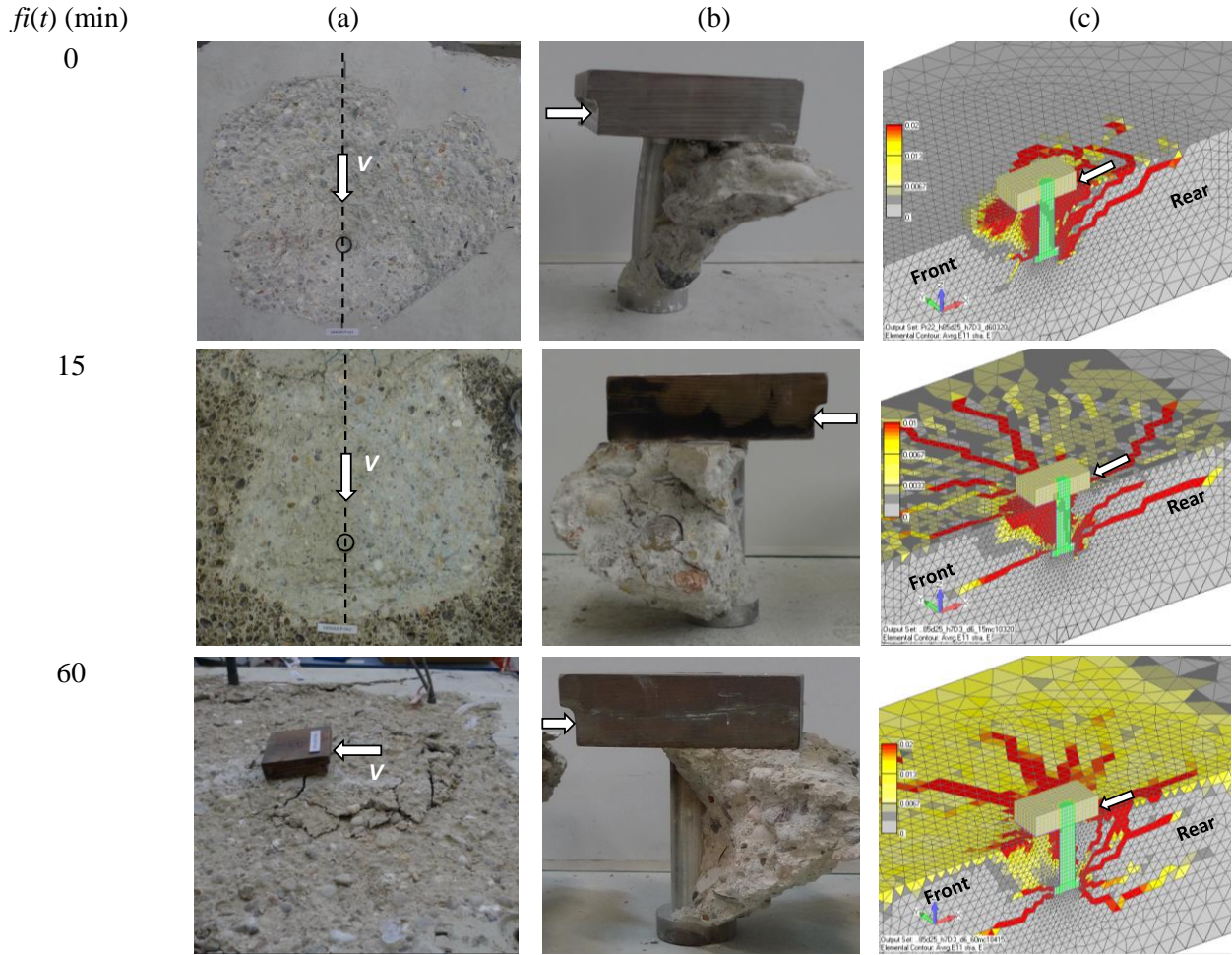
Figure 7.19 Comparison of fracture patterns obtained experimentally and numerically. Anchor: h85d25.

Typical fracture patterns at the peak load for anchor with embedment depth of 85 mm are shown for the cold and hot state in Figure 7.20. For shorter duration of fire exposure, the failure modes for the cold and hot states are similar. However, with increase of fire duration damage of concrete for the cold state is more severe and the concrete cone tends to be smaller. The main crack, due to the kicking back effect of the stud head, develops steeply, which results in a relatively small fracture size (see Figure 7.20a for 60 min and 90 min). These findings generally agree well with the experimental observation (see Figure 7.3).
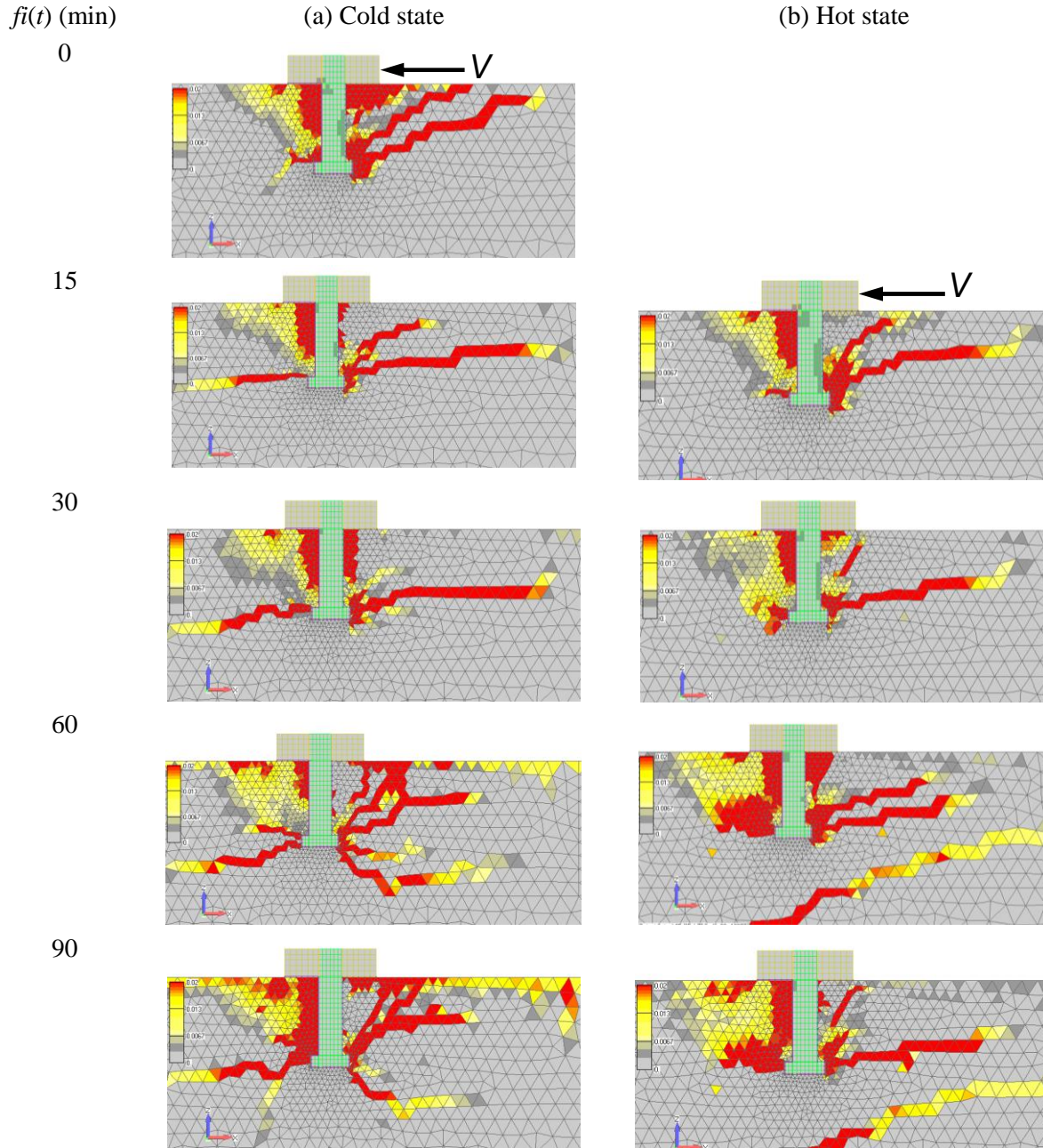
Figure 7.20 Fracture patterns of anchor h85d25 loaded in shear in concrete C20/25 after different fire durations. (a) Cold state; (b) hot state.

7.6.4. Load-displacement behaviour

To confirm the objectivity of the analysis the experimentally measured load-displacement curves are firstly compared with numerically obtained curves (see Figure 7.21). It can be seen that the numerical results are in good agreement with the experimental results, except for anchor h85d25 in concrete C40/50 at ambient temperature and after 15 min of fire. For these cases the

experimentally measured curves exhibit relatively ductile response. This is attributed to the linear behaviour of steel assumed in FE analysis.

(a)

(b)

(c)

(d)

(e)
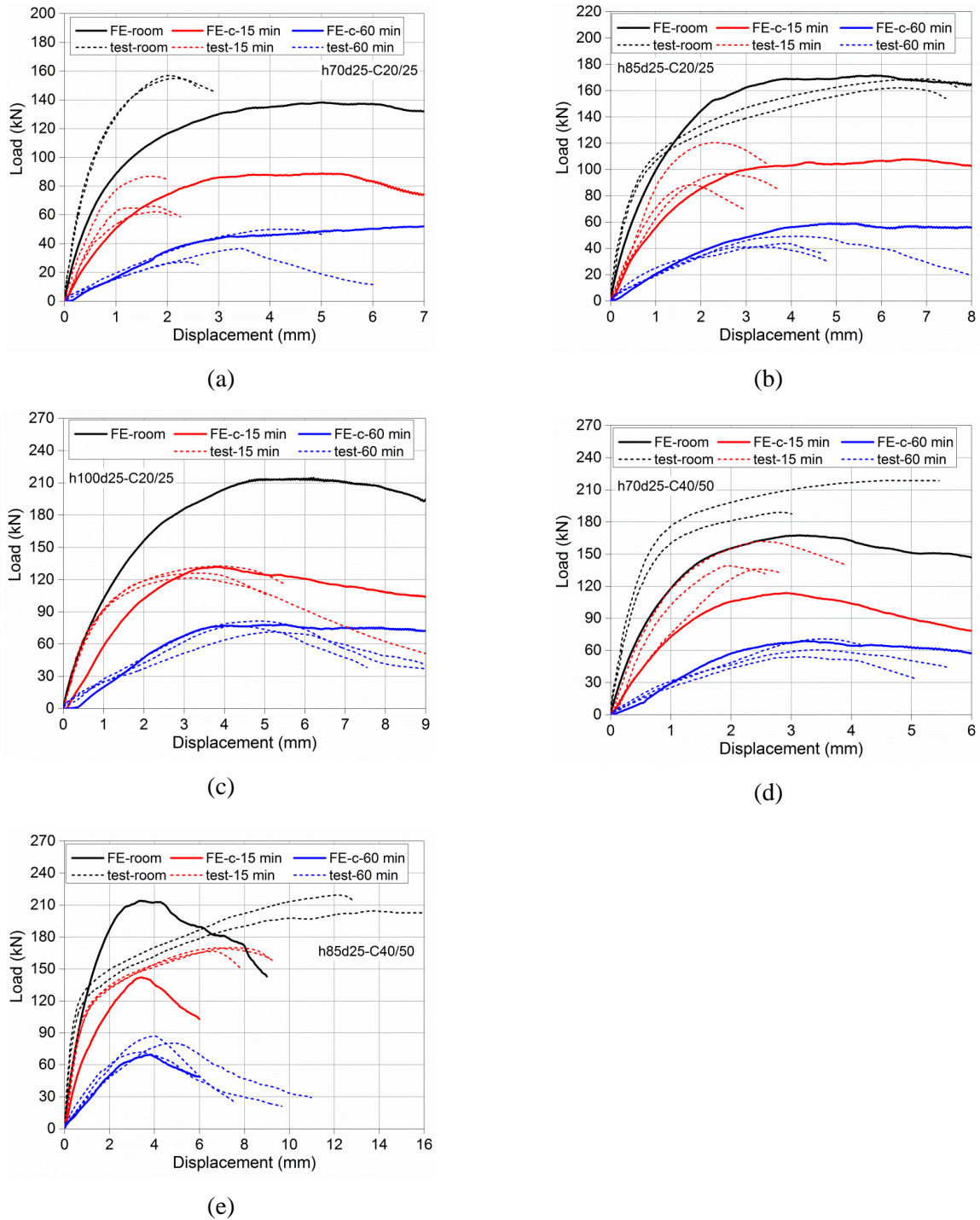
Figure 7.21 Comparison between the numerically and experimentally obtained load-displacement curves. (a) h70 in C20/25; (b) h85 in C20/25; (c) h100 in C20/25; (d) h70 in C40/50; (e) h85 in C40/50.

After verification of the model additional numerical simulations were carried out (see Table 7.2). The anchors with three different embedment depths (70 mm, 85 mm and 100 mm) are loaded in shear at various conditions, including 0 min, 15 min, 30 min, 60 min and 90 min of fire duration, three types of concrete, and both loading in the hot and cold state.

For concrete edge failure, it was shown that the resistance in the hot state is higher than that in the cold state. In the test of pry-out failure, anchors are located in the central region of the concrete slab and only exposed to fire from one side, the hot state resistance should be higher than the resistance in the cold state; however, the difference between them may be different from that of the concrete edge failure.

(a)

(b)   (c)
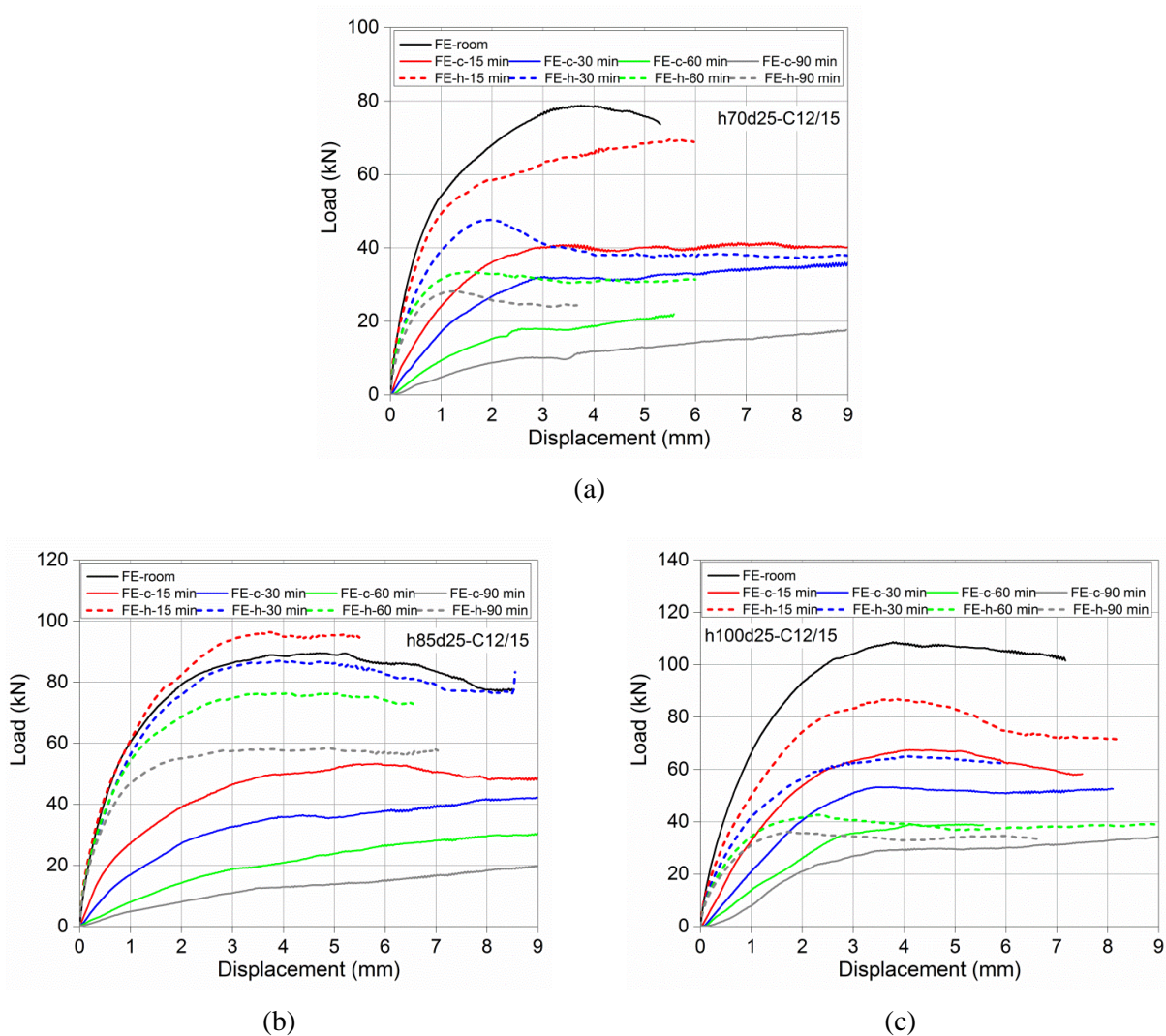
Figure 7.22 Load-displacement curves in the cold and hot states for anchors in concrete C12/15. (a) h70d25; (b) h85d25; (c) h100d25.

Figure 7.22 shows the load-displacement curves of anchors with embedment depth of 70 mm, 85 mm and 100 mm, loaded in shear, for concrete grade C12/15. It is seen that the curves for hot state exhibit stiffer response than those loaded in the cold state. Furthermore, the resistance of anchors for the hot state is also higher. However, for anchor with embedment depth of 100 mm, the difference of resistance between the hot state and cold state is seen to be reduced comparing to anchors with small embedment depth (70 mm and 85 mm).

Figure 7.23 and Figure 7.24 show the load-displacement curves of anchors with embedment depth of 70 mm, 85 mm and 100 mm loaded in shear for concrete C20/25 and C40/50, respectively. Principally, the influence of high temperature is the same as for concrete C12/15, except the peak load is higher, which is due to the higher concrete strength.

(a)

(b)

(c)
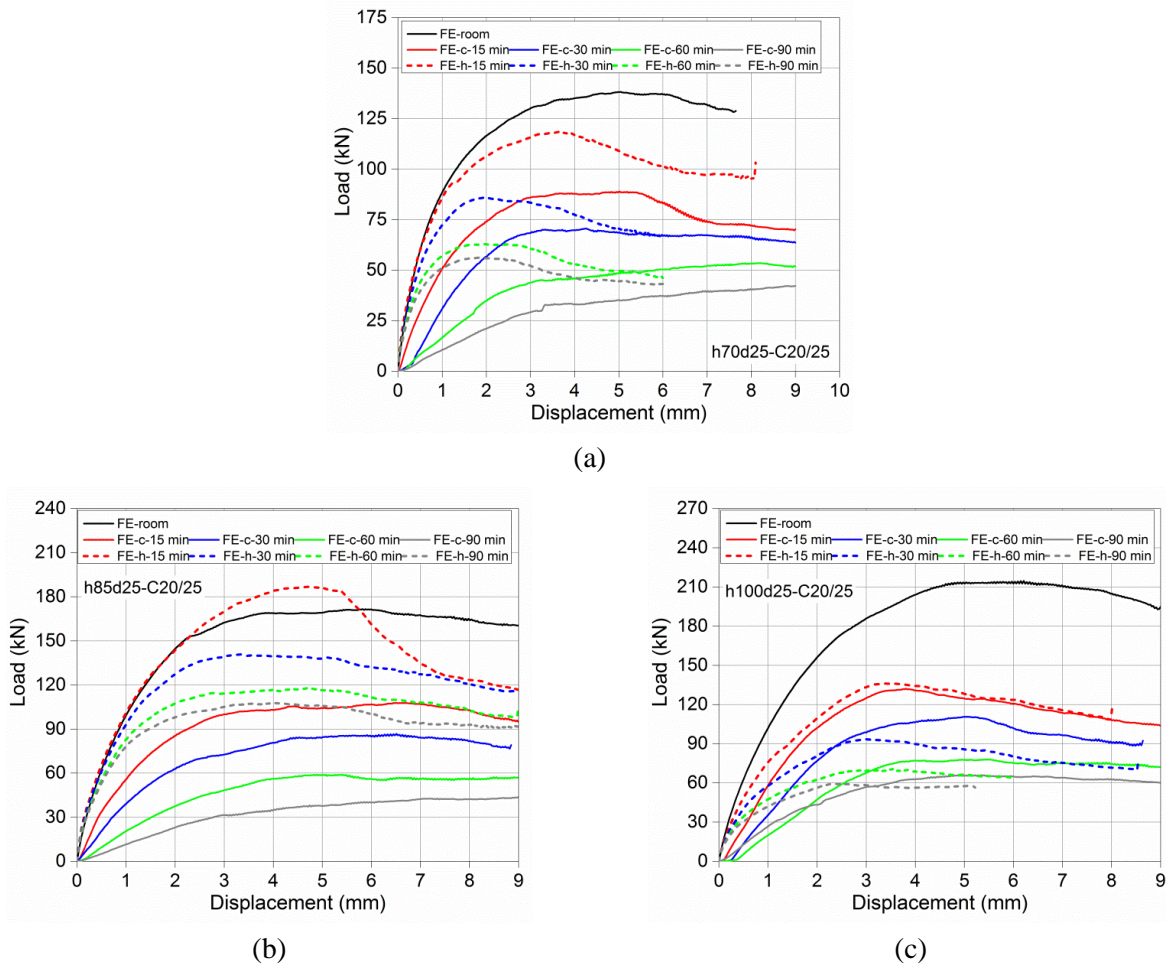
Figure 7.23 Load-displacement curves in the cold and hot states for anchors in concrete C20/25. (a) h70d25; (b) h85d25; (c) h100d25.

According to the load-displacement curves, it can be concluded that the load-displacement response is always stiffer for the hot state loading, regardless of the embedment depth and concrete quality. The resistance is shown to be higher for the hot state. However, this difference

166

is decreasing with the increase of embedment depth. For the ductility of pry-out failure mode in the cold and hot states, no obvious difference is observed.

(a)

(b)   (c)
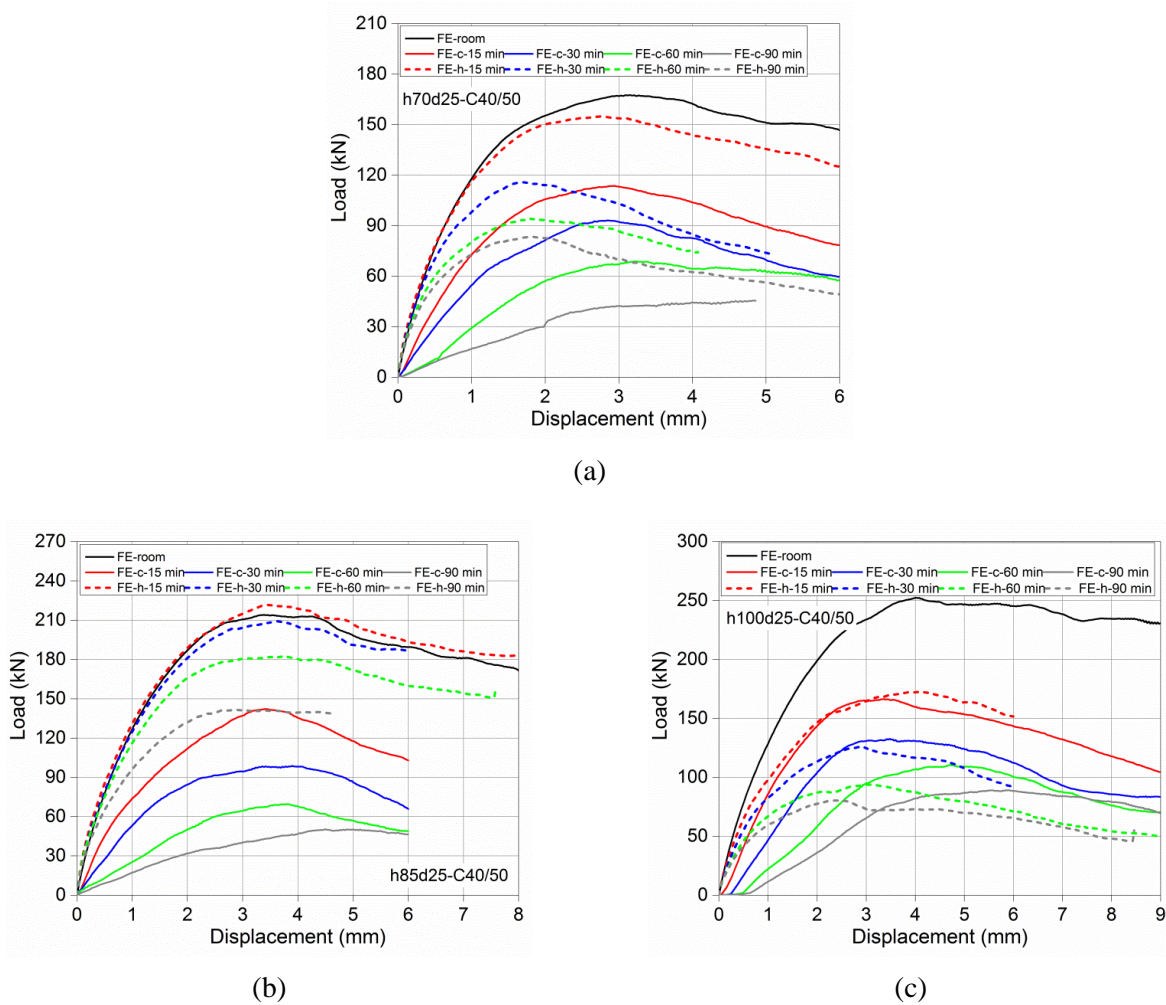
Figure 7.24 Load-displacement curves in the cold and hot states for anchors in concrete C40/50. (a) h70d25; (b) h85d25; (c) h100d25.

7.6.5. Resistance

As mentioned in the experimental part, the concrete surface spalling occurred widely after fire exposure for concrete specimen C20/25 (Figure 7.3). This reduces the volume of concrete that resists the loading and consequently may have influence on the actual pry-out failure load of the anchor. Numerical analysis was conducted to investigate the effect of surface spalling before and after fire exposure. Therefore, the direct failure loads from tests are normalized to their actual values. The resistance obtained numerically are verified according to normalized experimental data and finally both numerical and experimental data are used to evaluate the influence of fire exposure on resistance.

7.6.5.1. Influence of concrete surface spalling

Numerical investigation on the influence of surface spalling was conducted by finite element models with different spalling depth h_1 (see Figure 7.25). The same embedment depth ($h_{ef} = 70$ mm, 85 mm and 100 mm) as in the pry-out failure tests were considered. For each h_{ef}, different values of h_1 (0 mm, 10 mm, 20 mm and 30 mm) were separately applied to simulate the spalling depth of concrete surface. The distance between the edge of anchor plate and area of surface spalling was kept as 18 mm (Figure 7.25a), which was according to the measurement in the experiment. Fire durations of 0 min, 15 min and 60 min, the same as in the tests, were used. The material property, discretization and loading regime were the same as described in Chapter 7.6.1.
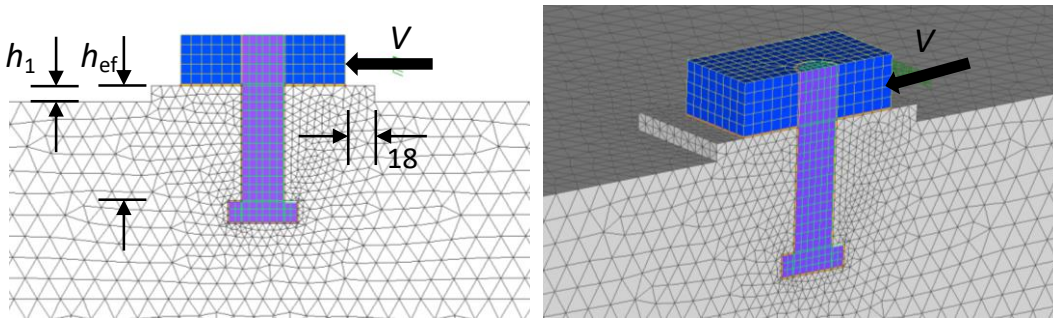
Figure 7.25 Numerical modelling of the effect of spalling depth h_1 on the pry-out failure capacity.

In Figure 7.26a, the peak loads obtained numerically at ambient temperature are compared with that obtained experimentally. It can be seen that the numerical results agree with the experimental results very well. Figure 7.26b shows the relative pry-out capacity of anchors after different durations of fire as a function of the spalling depth h_1. As can be seen the concrete surface spalling (h_1) has considerable influence on the pry-out failure capacity. The resistance is reduced with increase of h_1 for all studied fire durations. The embedment depth of anchor does not show great influence on the reduction rate, however, different durations of fire make remarkable differences. The longer is the fire exposure, the more is the reduction for each spalling depth h_1. The decrease of the pry-out capacity for different fire duration can be expressed as functions of h_1 as follows:

$$V_{u,cp,h_1}^{fi(0)}/V_{u,cp}^{fi(0)} = -0.017h_1 + 1 \text{ for ambient condition} \tag{7.2}$$

$$V_{u,cp,h_1}^{fi(15)}/V_{u,cp}^{fi(0)} = -0.019h_1 + 1 \text{ for 15 min of fire duration} \tag{7.3}$$

$$V_{u,cp,h_1}^{fi(60)}/V_{u,cp}^{fi(0)} = -0.022h_1 + 1 \text{ for 60 min of fire duration} \tag{7.4}$$

Based on Equations (7.2), (7.3) and (7.4), the direct experimental results are normalized to eliminate the effect of the surface spalling and the results are presented in the following with numerical results.

(a)

(b)
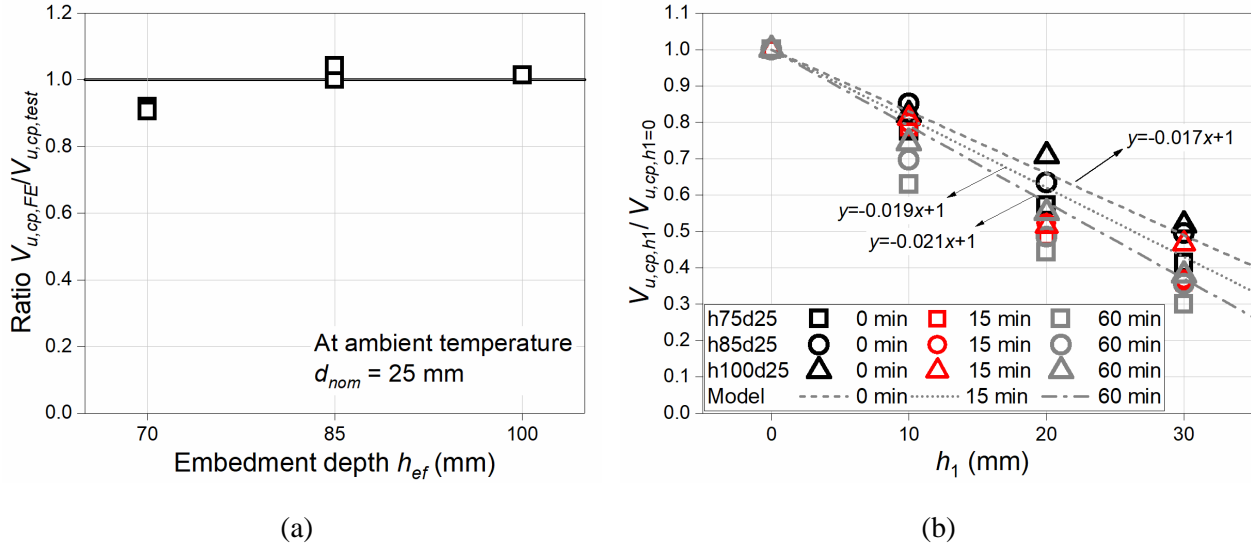
Figure 7.26 (a) Comparison of experimental and numerical results for three different embedment depth at ambient condition (spalling depth $h_1 = 0$ mm); (b) influence of spalling depth h_1 on the pry-out capacity of anchors after different fire durations.

7.6.5.2. Influence of fire duration

(a)

(b)

(c)
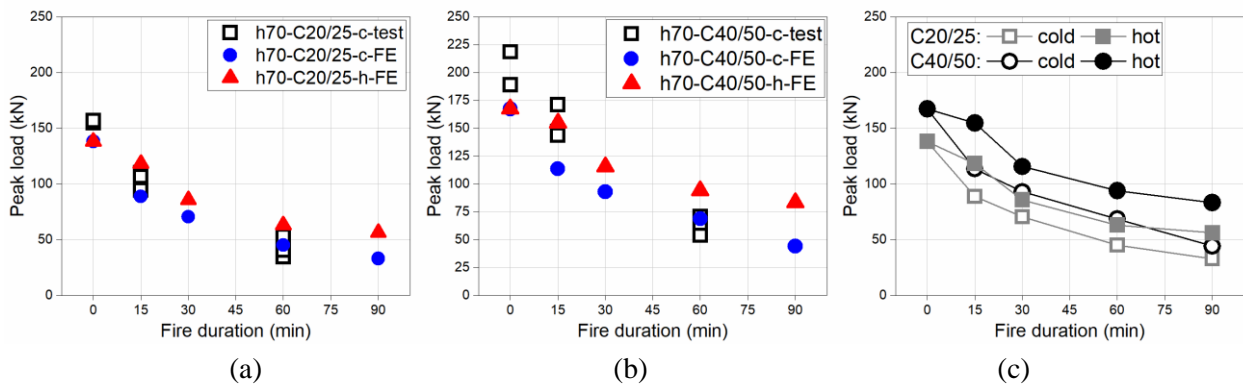
Figure 7.27 Comparison of peak loads obtained experimentally and numerically for anchor with $h_{ef} = 70$ mm in concrete (a) C20/25 and (b) C40/50. (c) Difference of peak loads between the cold and hot states loading obtained numerically. "-c-" for cold and "-h-" for hot.

Figure 7.27 shows the resistance of anchors with $h_{ef} = 70$ mm in concrete C20/25 and C40/50. In Figure 7.27a and b, the comparison of peak loads obtained experimentally and numerically is presented. As can be seen, the numerical results agree well with experimental data for both concrete grades. In Figure 7.27c the resistance predicted numerically is shown for the cold and

hot states. It is seen that for both concrete grades, the peak load in the hot state is higher than that in the cold state. This is especially true for longer duration of fire.

Figure 7.28 shows the peak loads of anchors with h_{ef} = 85 mm in concrete C20/25 and C40/50. The same conclusions can be obtained as for anchor with h_{ef} = 70 mm. However, it can be seen that the difference between the hot and cold states becomes higher.

(a)   (b)   (c)
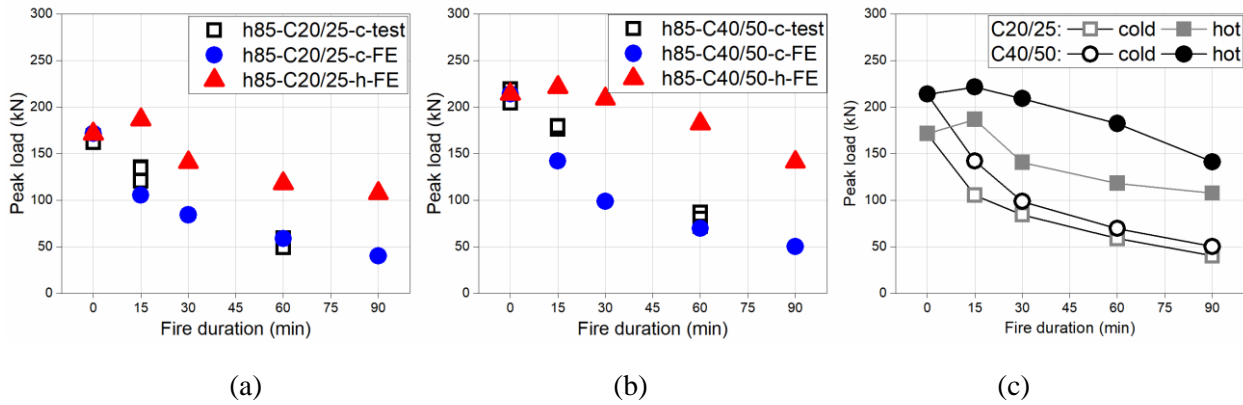
Figure 7.28 Comparison of peak loads obtained experimentally and numerically for anchor with with h_{ef} = 85 mm in concrete (a) C20/25 and (b) C40/50. (c) Difference of peak loads between the cold and hot states loading obtained numerically. "-c-" for cold and "-h-" for hot.

Figure 7.29a and b show that the experimental peak loads of anchors with h_{ef} = 100 mm in concrete C20/25 and C40/50 are very well predicted numerically. However, Figure 7.29c shows that for both concrete grades, the peak load in the hot state is basically the same as that in the cold state, which is a distinct difference from the results for anchors with h_{ef} = 70 mm and 85 mm.

(a)   (b)   (c)
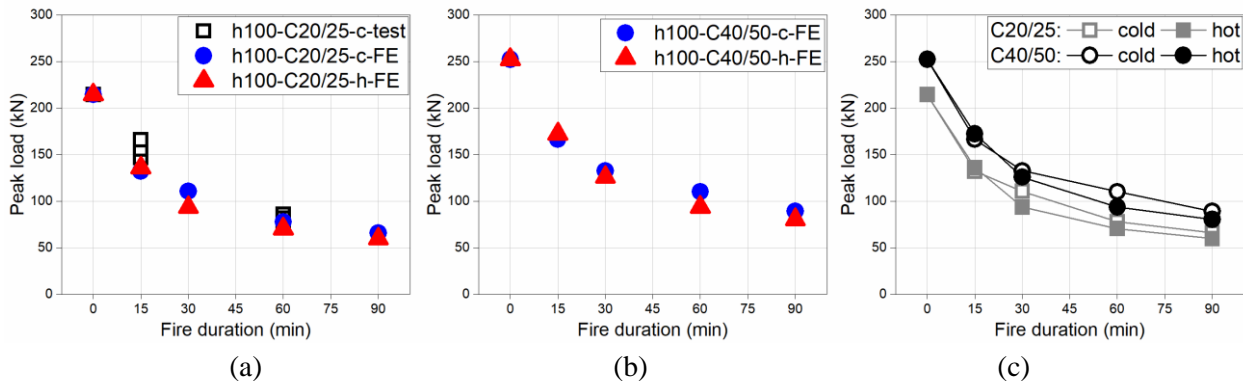
Figure 7.29 Comparison of peak loads obtained experimentally and numerically for anchor with h_{ef} = 100 mm in concrete (a) C20/25 and (b) C40/50. (c) Difference of peak loads between the cold and hot states loading obtained numerically. "-c-" for cold and "-h-" for hot.

170

The numerical results suggest that with increase of embedment depth the difference of resistance between hot and cold states becomes significantly smaller.

The relative resistances for the cold state and hot states are shown in Figure 7.30 as a function of fire duration. In Figure 7.30a is shown that the relative resistance obtained numerically agree well with the experimental results. It is shown that for all investigated case there is strong reduction of resistance with increase of fire duration. Figure 7.30b shows the relative resistance for the hot state. It varies significantly with increasing duration of fire. For anchor with relatively short embedment depth of 70 mm and 85 mm, the reduction after 15 min of fire is relatively small. The reason for relatively small reduction is due to the confinement effects, which are stronger in case of smaller embedment depths and shorter fire duration. This is observed for both concrete types.

(a)   (b)
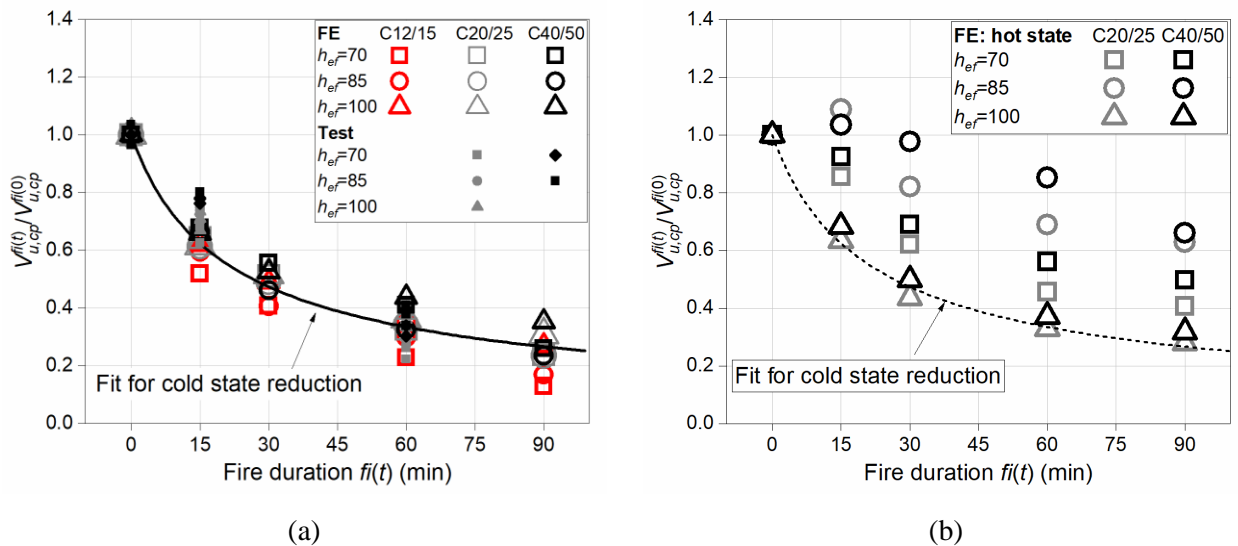
Figure 7.30 (a) Relative resistance for (a) the cold state and (b) the hot state.

The above analysis of the load-displacement curves and peak loads of anchors reveals that the pry-out failure capacity in the hot state is higher or equal to the capacity in the cold state. Thus, the cold state should be relevant for the code development and the engineering design of pry-out failure after fire exposure.

7.7. Summary

In this chapter the pry-out failure capacity of single anchors after different fire durations is investigated experimentally and numerically. The numerical models are proved to be able to replicate the pry-out failure of singe stud anchors before and after fire exposure (cold state). The ultimate loads (for the cold and hot states) and load-displacement curves are predicted numerically.

The fracture cone size of anchors failed in case of pry-out failure is found, both experimentally and numerically, to decrease with fire duration over 15 min. This can have the influence on evaluating the effect of anchor spacing on anchor group capacity.

The concrete surface spalling after fire creates the non-negligible spalling depth for the shear loaded anchor, which reduces the volume of concrete that can bear the load and is numerically demonstrated to have strong influence on the pry-out failure capacity. Numerical results on the effect of spalling depth are used to normalize the test data.

The evaluation of experimental and numerical results shows that with increase of fire duration the pry-out failure resistance decreases. The decrease is higher for the cold state, which is especially true for the larger embedment depth. Moreover, the relative decrease of resistance for the cold state is almost independent of the concrete grade and embedment depth. The same as for the concrete edge failure, for the practical applications, the load bearing behaviour due to pry-out failure in the cold state seems to be relevant.

8. PRY-OUT FAILURE OF ANCHOR GROUPS

In this Chapter, experimental and numerical investigations on the load-bearing behaviour of anchor groups with respect to the pry-out failure mode are conducted. Similar as for the single anchors, to verify the model the experimental results are compared with test data and subsequently additional parametric study is carried out. Special care is given to the influence of number of studs on the load-bearing behaviour. Furthermore, it is investigated whether the projected area ratio $A_{c,N}/A_{c,N}{}^0$ at ambient temperature according to the concrete cone design approach (CC-method) (*Fuchs et al.*, 1995) is still valid after exposing anchor groups to different durations of fire.

8.1. Anchor groups

As shown in Figure 8.1, anchor groups with two studs (Figure 8.1a) and four studs (Figure 8.1b) were tested. They have a fixed spacing of studs, i.e. $s_1 = s_2 = 100$ mm. The embedment depth is $h_{ef} = 85$ mm for all anchor groups, and the diameter of anchor shaft is $d = 25$ mm. The same as for the single anchors, the notch in the form of a half groove was made at the rear side of anchor plate, for the sake of fitting the shear loading setup in and to avoid the sliding of loading device.
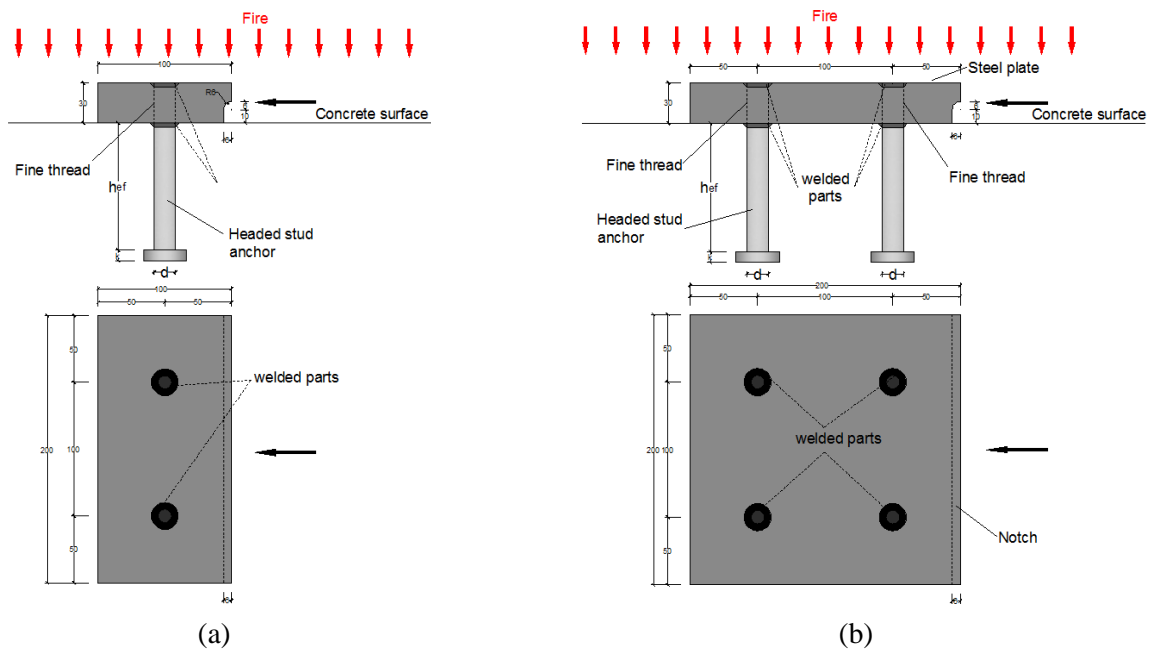
Figure 8.1 Sketch of anchor groups for pry-out failure tests: (a) two-stud anchor group G2-h85d25; (b) four-stud anchor group G4-h85d25.

All tested configurations of anchor groups are listed in Table 8.1. The main investigated parameters are the number of studs, the fire duration and the concrete strength.

Table 8.1 Configuration of anchor group for pry-out failure tests

Identification	h_{ef}	d	$fi(t)$	Concrete grade	Number of tests
G2-h85d25	85	25	Ambient	C20/25	2
				C40/50	2
G4-h85d25	85	25	Ambient	C20/25	2
G2-h85d25	85	25	15 min	C20/25	3
				C40/50	2
G4-h85d25	85	25	15 min	C20/25	3
G2-h85d25	85	25	60 min	C20/25	3
				C40/50	2
G4-h85d25	85	25	60 min	C20/25	3

8.2. Test setup

(a)   (b)
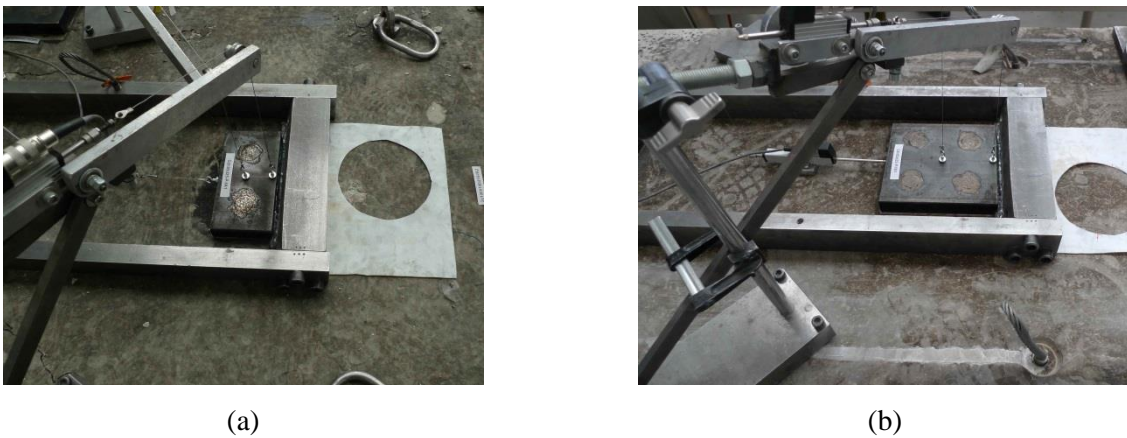
Figure 8.2 Loading setup for anchor groups: (a) two-stud anchor group; (b) four-stud anchor group.

The loading setup is the same as that used for single anchor tests, as shown in Figure 7.2. In detail, the loading condition on the anchor plate is shown in Figure 8.2. The steel plate of the anchor was placed exactly in the middle of the loading frame. Teflon sheet was used between the concrete surface and the steel plate, thus the friction force can be neglected. The same as for the single anchor, three LVDTs were used to measure the displacement of anchors. LVDT-0 in front of the steel plate is used to measure the horizontal displacement in the loading direction. LVDT-1

174

and LVDT-2 are used to measure the vertical displacement of the anchor plate at the middle and the rear side, respectively.

8.3. Test results and discussion

Experimentally obtained results are summarized in Annex A Table A.5 . The influence of fire exposure on the features like the failure mode, shear stiffness, ductility and resistance are presented in the following.

8.3.1. Failure mode

Figure 8.3–Figure 8.5 show typical fracture patterns of the two- and four-stud anchor groups loaded in shear before and after exposing to fire. At ambient temperature, anchor with four studs failed in concrete breakout, however, the anchor groups experienced three times loading-unloading cycles to finally break the concrete, which was due to unexpected high resistance of the anchor group over the capacity limit of the loading setup. Before the breakout of concrete, some hairline crack propagating to the rear side of the anchor group can be observed (see Figure 8.3). After fire exposure it is seen that the concrete surface spalling occurred for some anchor groups (see Figure 8.4a). Except in the case of four-stud anchor groups at ambient temperature, all other anchor groups failed in concrete breakout by one time loading. No steel deformation was observed in all anchor groups. All failures were somewhat explosive after reaching the ultimate load. However, the explosive breakout of concrete was much less stronger for anchor groups exposed to longer duration of fire.

(a)   (b)
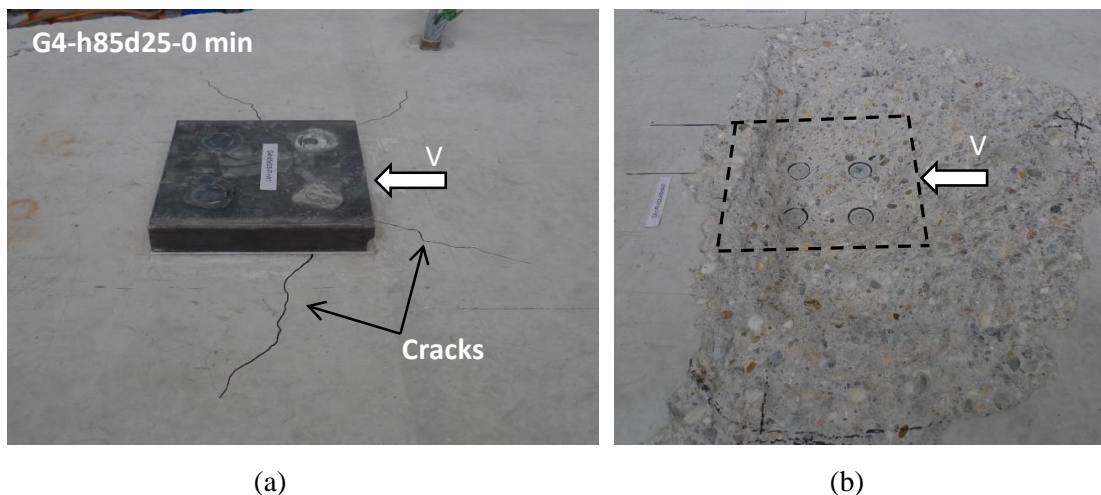
Figure 8.3 Fracture patterns for four-stud anchor group at ambient temperature. (a) Hairline cracks during loading; (b) final failure pattern.
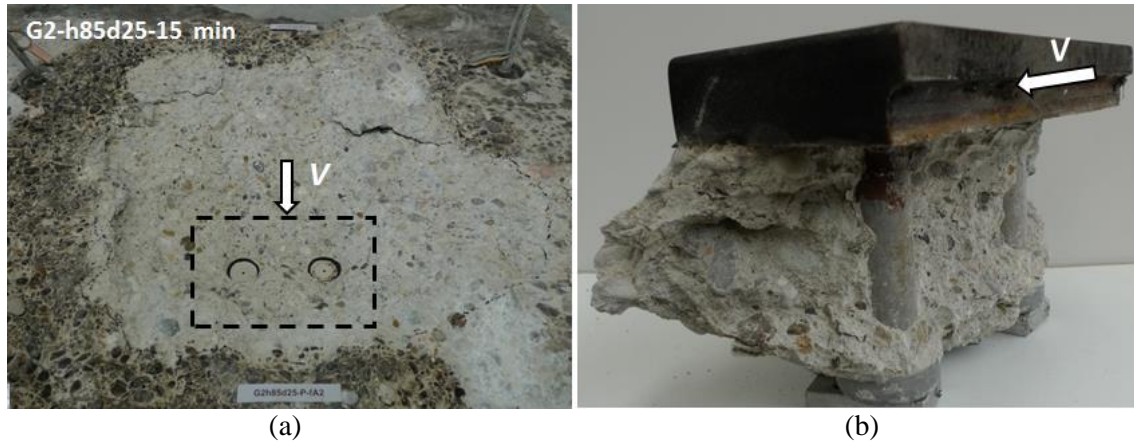
Figure 8.4 Typical fracture patterns for two-stud anchor group after 15 min of fire exposure.
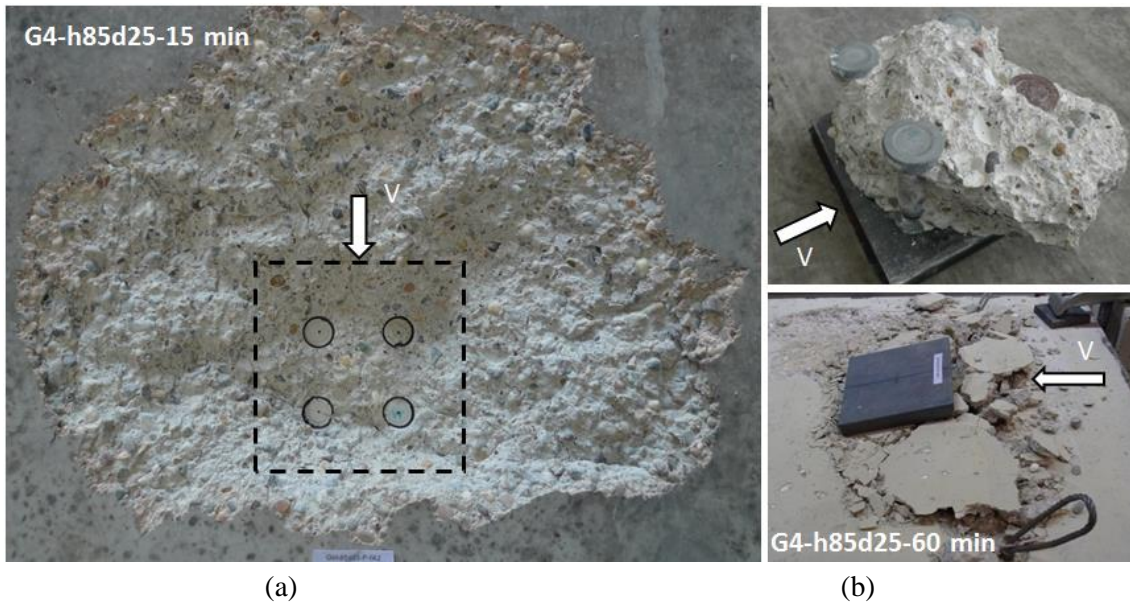
Figure 8.5 Typical fracture patterns for four-stud anchor group after fire exposure.

Based on the experimental results, the typical fracture patterns are schematically depicted in Figure 8.6. These failure patterns are similar to the patterns observed for the pry-out failure at ambient temperature. More details can be found in *Jebara* (2018). The fracture usually develops widely in the horizontal direction with large L. To the vertical direction, the value of B is relatively small; however, the value of B2 is obviously larger than that of B1. In the loading direction, the concrete under the front side of the anchor plate is crashed due to compressive force and this portion of concrete is enclosed within the studs. The main crack initiates at the head and

propagates diagonally upward to the rear side of the anchor until intersecting the concrete surface. For anchor group with two rows of studs (Figure 8.6b), concrete between front and rear studs is enclosed (also see Figure 8.5b).
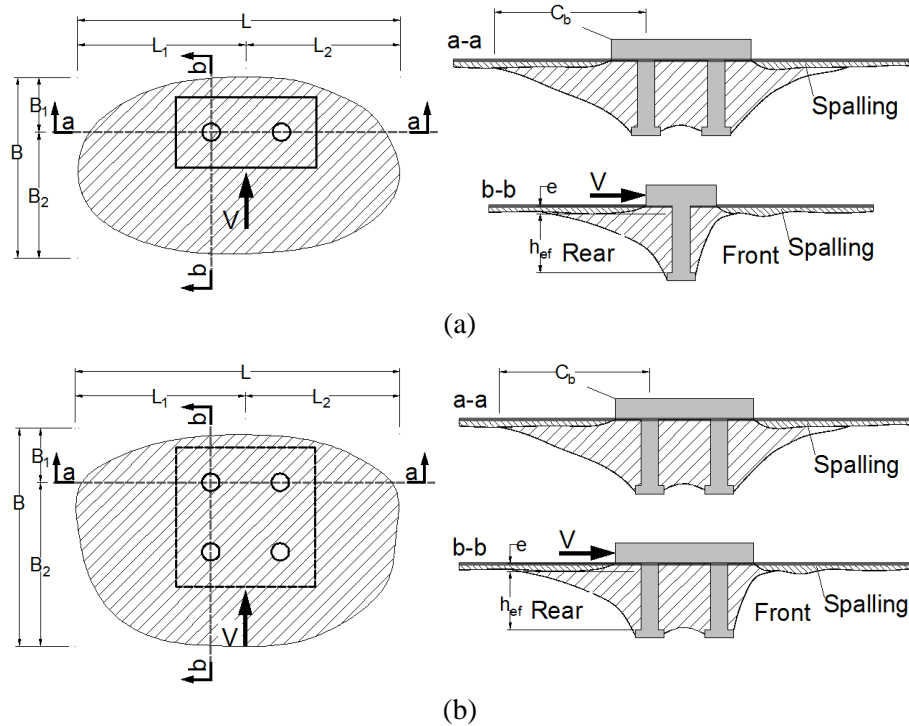
Figure 8.6 Schematic fracture patterns for (a) two- and (b) four-stud anchor groups.

8.3.2. Load-displacement behaviour

Figure 8.7 shows the load-displacement curves of two-stud anchor groups loaded until pry-out failure after fire exposure. It is seen that higher concrete strength leads to stiffer load-displacement response, which is prominent after 60 min of fire. At ambient temperature, the anchor groups show relatively brittle failure, i.e. almost no descending branch of the load-displacement curve was possible to obtain (see Figure 8.7a). After 15 min and 60 min of fire duration, the post-peak descending branch was obtained, especially after 60 min of fire, which indicates much more ductile failure mode due to temperature induced damage of concrete.
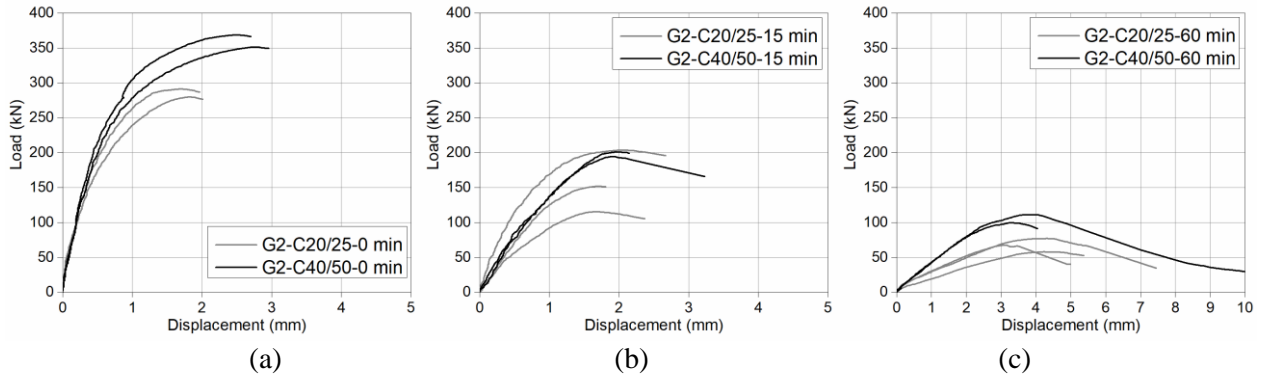
Figure 8.7 Load-displacement curves of two-stud anchor groups after fire durations of (a) 0 min, (b) 15 min and (c) 60 min.

Figure 8.8 shows the influence of fire duration on the load-displacement curves of two- and four-stud anchor groups. As can be seen, the fire exposure extremely reduces the stiffness and also the resistance. The curves show a very good consistency to all testing conditions. The transition from brittle failure to ductile failure with increase of fire duration can be clearly seen.
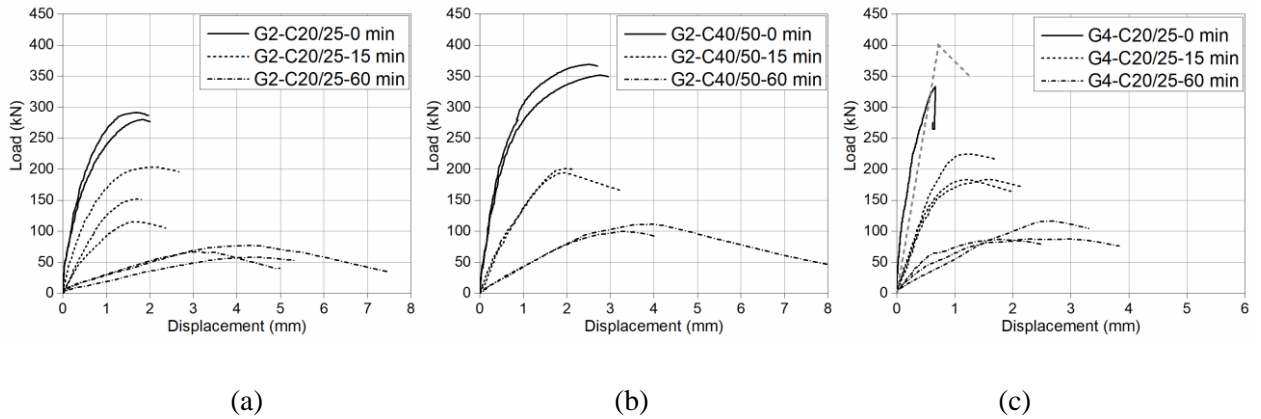
Figure 8.8 Load-displacement curves of anchor groups after fire exposure. (a) Two-stud anchor groups after different fire duration in concrete C20/25; (b) two-stud anchor groups after different fire duration in concrete C40/50; (c) four-stud anchor groups after different fire duration in concrete C20/25.

8.3.3. Stiffness

The same as for single anchors loaded in shear, the stiffness of anchor group is here defined as $k_{v,fi(t)} = 0.5V_{u,fi(t)}/\delta(0.5V_{u,fi(t)})$. In Figure 8.9a the shear stiffness is depicted as a function of fire duration. For both the two- and four-stud anchor groups, the same trend for reduction rate of the shear stiffness can be seen and expressed as:

$$k_{v,cp,fi(t)}/k_{v,cp,fi(0)} = (1 + fi(t)/20)^{-1.77} \tag{8.1}$$

Figure 8.9b and c show the influence of the number of studs on the shear stiffness of anchor groups. The shear stiffness of single anchor with the same embedment depth of 85 mm and diameter of 25 mm from Chapter 7 is taken to compare with that of two- and four-stud anchor groups. From Figure 8.9b, it is seen that at ambient temperature the number of studs has significant influence on the shear stiffness. After 15 min of fire, the influence is reduced significantly. After 60 min of fire, the number of studs only slightly increases the shear stiffness of anchor groups. The longer the fire exposure is, the lower the influence of the number of studs on the shear stiffness shows. Figure 8.9c shows the relative increase of shear stiffness, it can be seen that on average the two- and four-stud anchor groups have the shear stiffness that is 2.4 and 5.7 times of the shear stiffness at ambient temperature, respectively. After 15 min of fire, the increase of shear stiffness is about 1.7 and 3.5 times of reference for two- and four-stud anchor groups, respectively. The increase becomes about 1.2 and 3.2 times of the reference stiffness after 60 min of fire exposure.

(a)

(b)

(c)
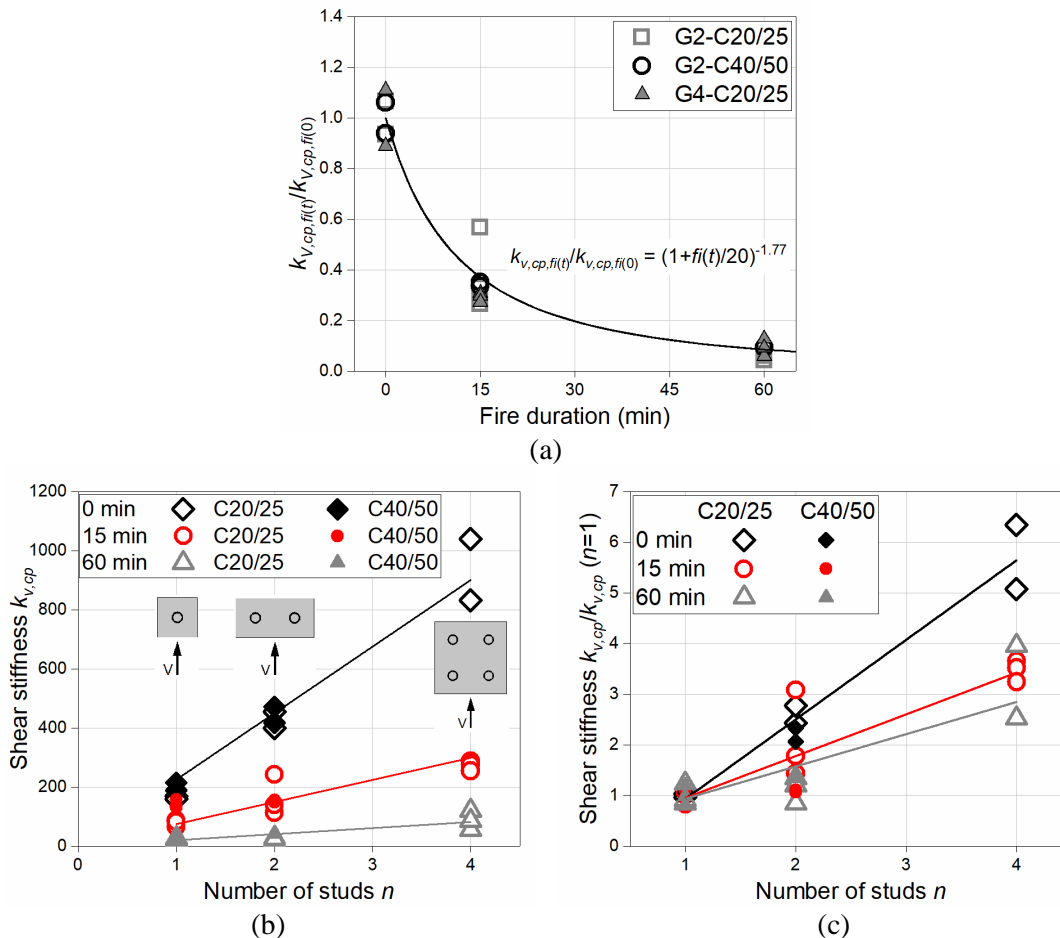
Figure 8.9 Shear stiffness of anchor groups as functions of (a) fire duration, (b) number of studs (absolute resistance) and (c) number of studs (relative resistance).

179

8.3.4. Resistance

Experiments were performed in different batches of concrete with different compressive strength. The relative peak loads obtained directly from experiments are plotted in Figure 8.10 as a function of relative concrete compressive strength. It shows that the peak loads are proportional to the concrete compressive strength to the power of 0.5, 0.65 and 0.75 for 0 min, 15 min and 60 min of fire duration, respectively. These values are the same as that for pry-out failure of single anchors and are used to normalize experimental data with respect to $f_{cm} = 30$ MPa for concrete grade C20/25 and $f_{cm} = 47$ MPa for concrete grade C40/50.
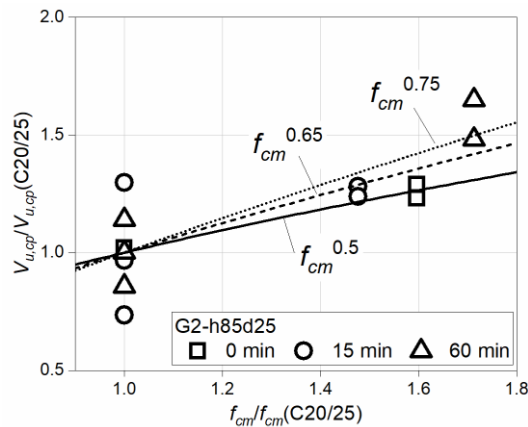
Figure 8.10 Relative peak loads of anchor groups as functions of concrete compressive strength.

The failure resistances of two- and four-stud anchor groups against fire durations are plotted in Figure 8.11 and Figure 8.12, respectively. As can be seen, higher concrete strength leads to higher resistance for every fire exposure condition (Figure 8.11a). The relative resistance seems to be independent of concrete grade (Figure 8.11b). For four-stud anchor group, significant reduction is observed for 15 min of fire exposure (see Figure 8.12).
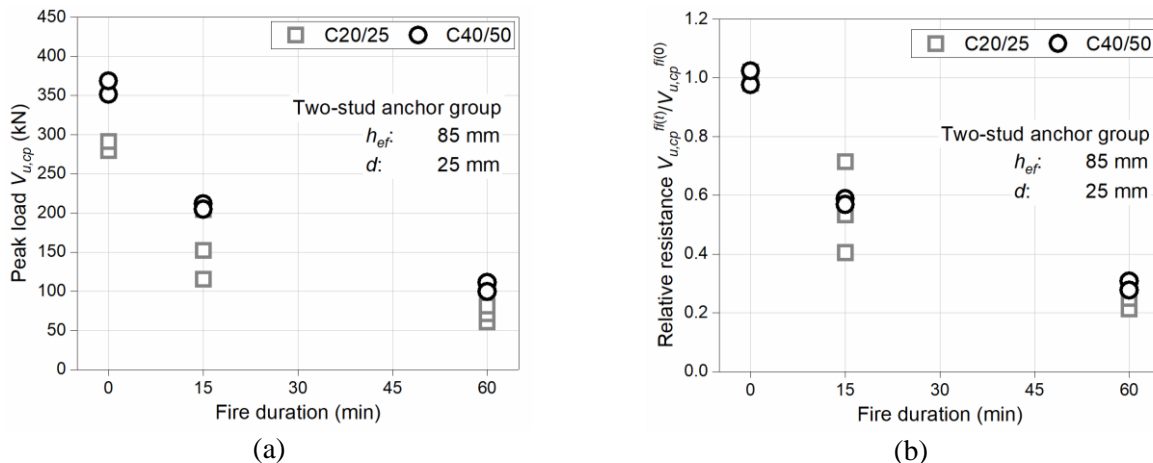
Figure 8.11 Resistance of two-stud anchor group after fire: (a) absolute value; (b) relative value.

180
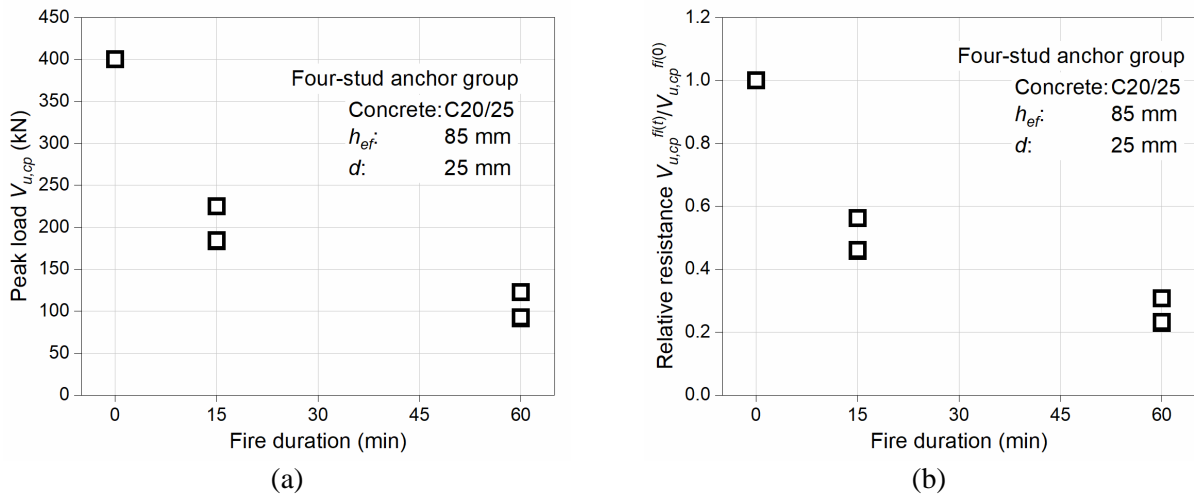
Figure 8.12 Resistance of four-stud anchor group after fire: (a) absolute value; (b) relative value.

Figure 8.13 shows the resistance of single anchor, two- and four-stud anchor groups as a function of fire duration. The difference of resistance at ambient temperature is significant. After fire exposure, especially after 60 min of fire, the difference becomes smaller (Figure 8.13a). From Figure 8.13b it can be seen the reduction of resistance due to fire exposure is very high. However, for 15 min of fire exposure single stud anchor shows relatively less reduction and four-stud anchor group shows the highest reduction. The reduction is about 20% for single stud anchor and over 50% for four-stud anchor group. After 60 min of fire, all fasteners have about 30% reference resistance left.
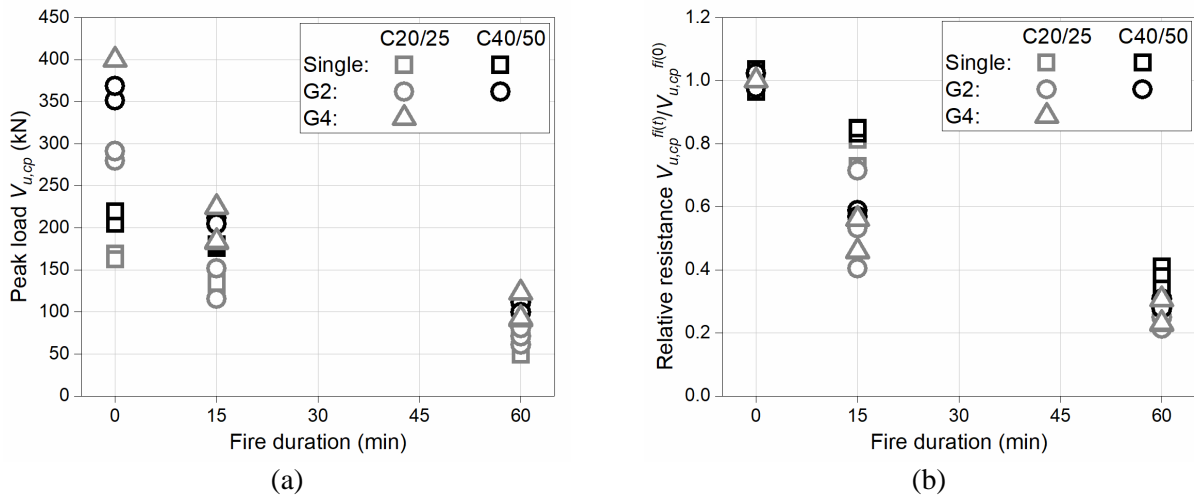
Figure 8.13 Resistance of single anchor, two- and four-stud anchor groups as a function of fire exposure: (a) absolute value; (b) relative value.

181

8.4. Numerical analysis

In this chapter numerical modelling is performed to verify the finite element model based on the experimental results. A further parametric study is focusing on the influence of the fire duration, the concrete quality and the projected area on the pry-out failure of anchor groups, mainly for the cold state.

8.4.1. Finite element model and discretization

Figure 8.14a and b present the geometry, boundary conditions and finite element discretization of anchor groups with two and four studs. To save computational time, one symmetry plane is used. The geometry, boundary conditions and loading regimes are principally the same as that for single anchors (see Figure 7.17). The area covering four times the embedment depth from each anchor has been exposed to fire according to ISO-834 fire curve.
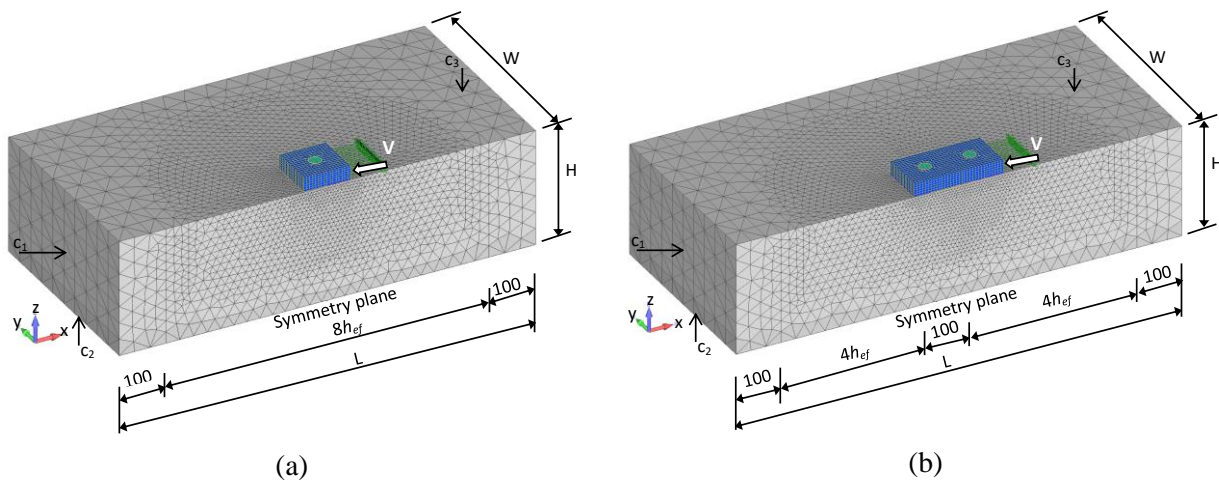
Figure 8.14 Finite element models for anchor groups with (a) two studs and (b) four studs. $h_{ef} = 85$ mm; $d = 25$ mm.

The configurations of anchor groups that are numerically investigated are summarized in Table 8.2. The same for single anchors, five different durations of fire and three concrete grades are considered. Loading in the hot state and in the cold state are conducted. The numerical results are listed in Annex B Table B.5 .

Table 8.2 Configuration of anchor groups for numerical simulation of pry-out failure

Identification	h_{ef} (mm)	d (mm)	$fi(t)$ (min)	Concrete grade	Loading condition
G2-h85d25	85	25	0 15 30 60 90	C12/15; C20/25; C40/50	Hot state (h); Cold state (c)
G4-h85d25	85	25	0 15 30 60 90	C12/15; C20/25; C40/50	Hot state (h); Cold state (c)

8.4.2. Temperature distribution

Figure 8.15 Numerical results of temperature distribution of anchor groups embedded in concrete C20/25 after different fire durations. (a) G2-h85d25; (b) G4-h85d25. Loading direction: right to left.

Figure 8.15 shows the typical temperature profiles of anchor groups for different durations of fire (concrete C20/25). Since these two anchor groups with two and four studs have the same embedment depth, it is seen the penetration depth of heat is basically the same for the both. However, the concrete temperature close to the steel stud is much higher than in the rest. From Figure 8.15b it is also seen that the concrete under the central region of the steel plate has relatively slow temperature rise for short period of heating, i.e. 15 min and 30 min, due to the effect of the anchor plate. After heating of 60 min, this effect is less.

8.4.3. Fracture pattern
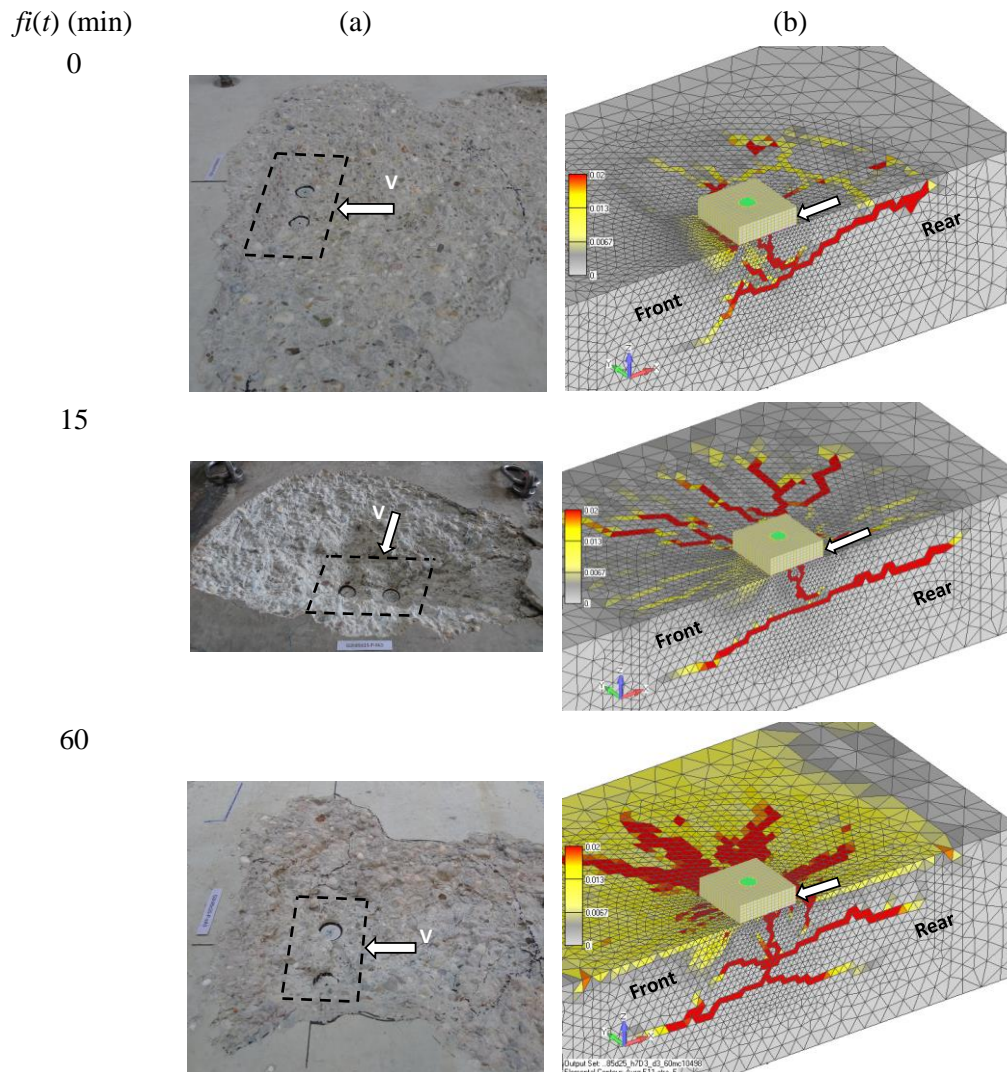
Figure 8.16 Comparison of fracture patterns obtained experimentally and numerically for anchor group G2-h85d25.

184

Figure 8.16 displays the comparison between the fracture patterns obtained experimentally and numerically for anchor groups with two studs after different duration of fire. It is seen that the predicted failure patterns represent the experimentally obtained fracture patterns favourably well. At ambient condition, the cracks mainly develop to the rear side of the anchor. However, after fire duration of 60 min, it is seen the surface of the specimen is severely damaged and the front side of the anchor suffers also severe damage due to compressive action. At ambient temperature and for shorter fire duration the failure cone is relatively large and forms at the rear side of the anchor plate. However, for longer durations of fire, the cone tends to be smaller but spreads also over the front side of the anchor group.

Figure 8.17 shows the comparison between the fracture patterns obtained experimentally and numerically, for anchor group with four studs, after different durations of fire. Good agreement between the experimental and numerical failure mode can be seen. Generally, the same observation as that of the two-stud anchor group is seen.
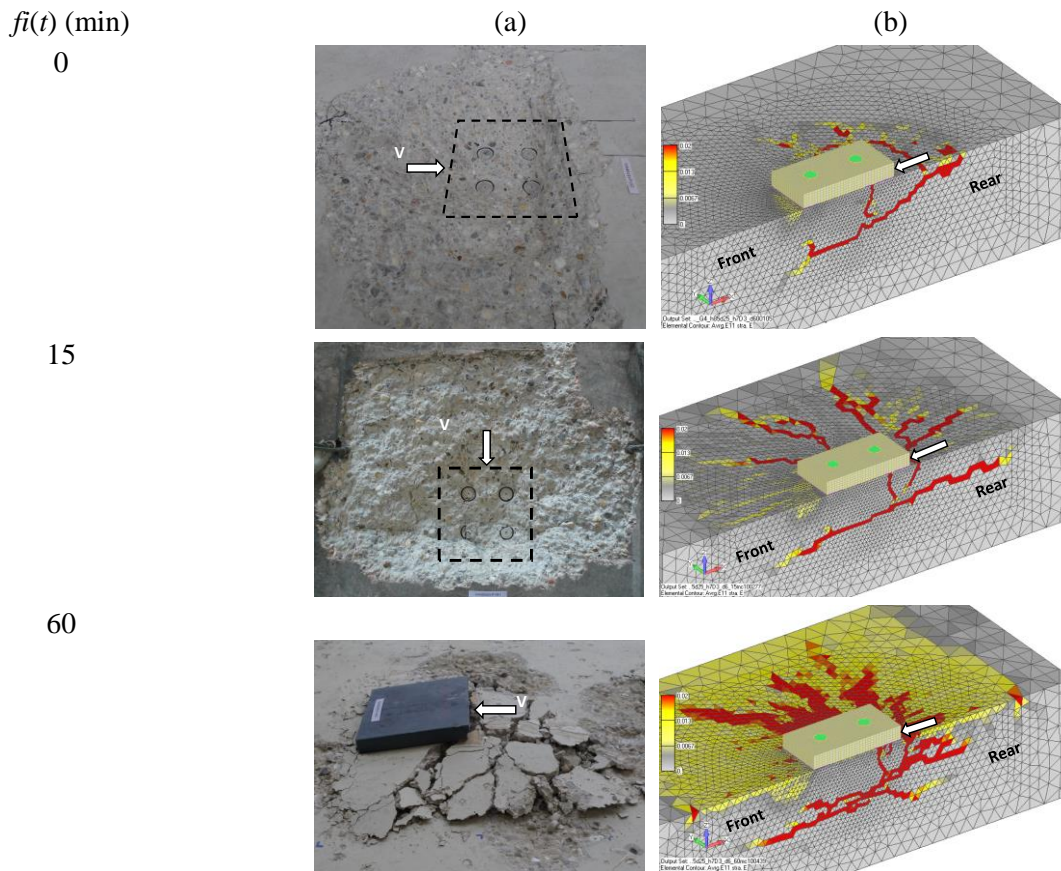
Figure 8.17 Comparison of fracture patterns obtained experimentally and numerically for anchor group G4-h85d25.

Figure 8.18 shows the fracture patterns of anchor group with four studs in concrete C20/25 after a series of fire exposure for the cold state and the hot state loading. With prolonged fire exposure,

185

more cracks can be seen for the cold state. Furthermore, for the cold state, damage under the anchor plate becomes more distributed with the increase of fire duration. This leads to the more localized cone failure and agrees well with the experiments.

For the hot state, Figure 8.18b shows no obvious difference in crack distribution, except that more damage at the front side of the anchor group due to compressive stress can be seen.
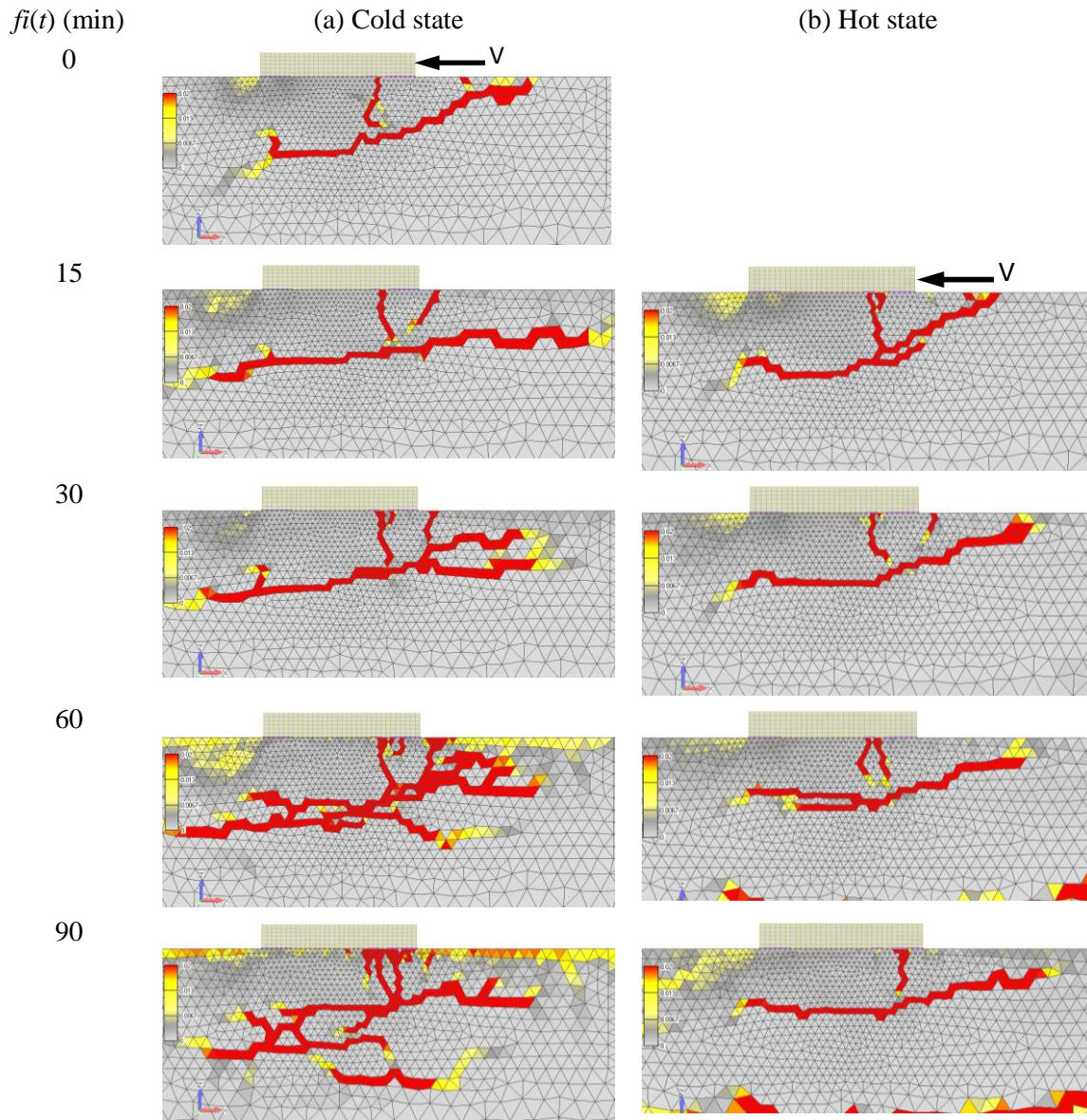
Figure 8.18 Numerical fracture patterns (symmetric plane) of anchor group G4-h85d25 in concrete C20/25 after different fire durations. (a) Cold state; (b) hot state.

Figure 8.19 shows the fracture patterns in the section plane of the studs at ambient temperature and after 90 min of fire. The internal crack between studs is not developed to intersect the anchor plate or the anchor shaft. The initiation of the crack is observed to start simultaneously at the

186

front and rear row. It can be seen that after fire there is more damage of concrete than in the case of ambient temperature.

(a)

(b)
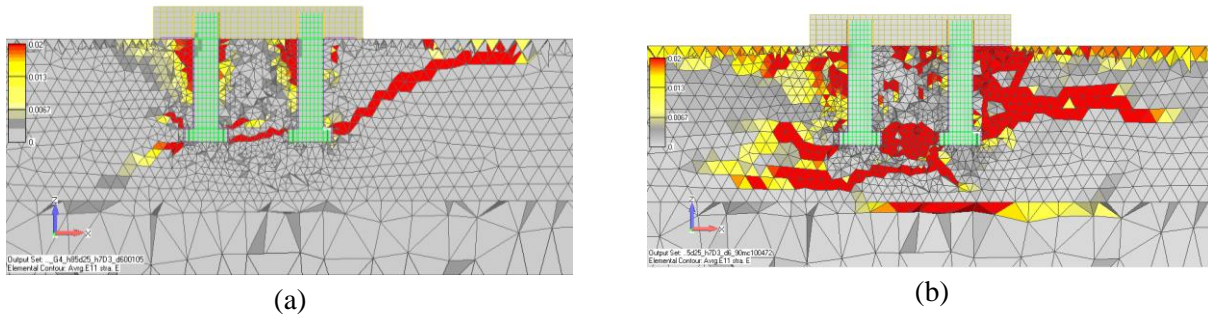
Figure 8.19 Fracture development: (a) at ambient temperature; (b) after 90 min of fire exposure.

8.4.4. Load-displacement behaviour

The experimental and numerical load-displacement curves of anchor groups are compared and illustrated in Figure 8.20. Having in mind the complex of the problem the agreement is very good. The stiffness of anchor groups before and after fire is well simulated.

(a)

(b)

(c)
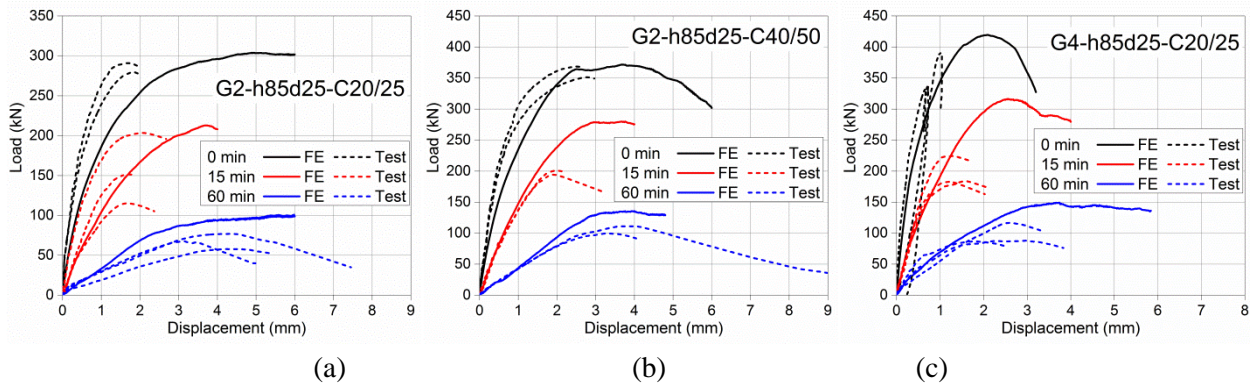
Figure 8.20 Verification of load-displacement curves of anchor groups (a) with two studs in concrete C20/25, (b) with two studs in concrete C40/50 and (c) with four studs in concrete C20/25.

8.4.5. Resistance

Concrete surface spalling occurred around some of the anchor groups (for example, Figure 8.4). The same as for the surface spalling of single stud anchors after fire (see Chapter 7.6.5.1), the surface spalling depth h_1 reduces the volume of concrete that can bear the load and has influence on the actual resistance of the anchor group. Therefore, the Equations (7.2), (7.3) and (7.4) are

187

used to normalize the experimental values to their actual values eliminating the influence of h_1. Finally the numerical and experimental results are compared and evaluated in the following.
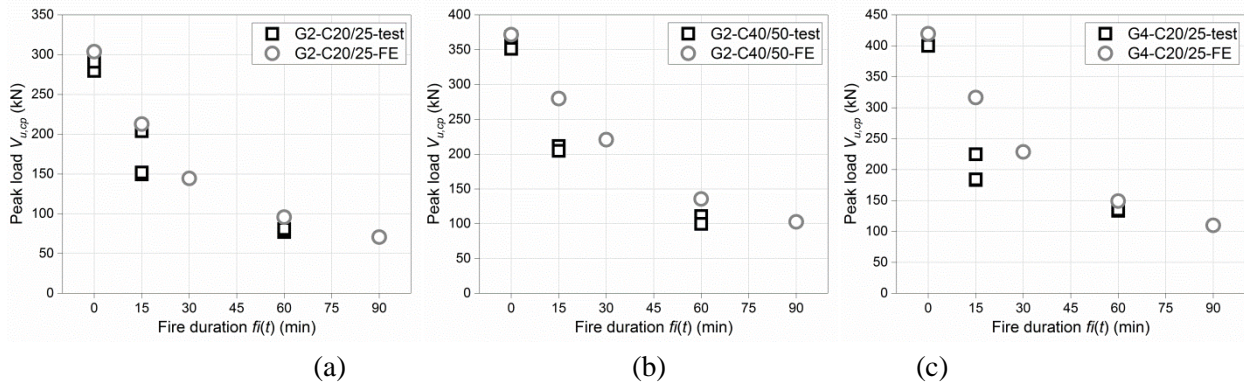
Figure 8.21 Verification of peak loads of anchor groups. (a) Two-stud anchor groups in concrete C20/25; (b) two-stud anchor group in concrete C40/50; (c) four-stud anchor group in concrete C20/25.

Figure 8.21 shows the pry-out failure load of anchor groups obtained numerically and experimentally as a function of fire duration. It can be seen that the numerical results for 15 min of fire exposure are slightly higher for all anchor groups than the corresponding experimental results. At ambient condition and after 60 min of fire, good agreement between the numerical and experimental results is obtained.

Based on the above verification analysis, numerical and experimental results of resistance for single stud anchor, two- and four-stud anchor groups (G2 and G4) for three concretes (C12/15, C20/25 and C40/50) against duration of fire are plotted in Figure 8.22. Figure 8.22a shows that higher concrete strength increases the resistance of all fasteners significantly. Four-stud anchor groups have distinctly greater resistance than that of single anchor and two-stud anchor groups. At ambient temperature the concrete strength and number of studs have significant influence on the resistance. However, with prolonged fire the influence is obviously much smaller. Figure 8.22b shows the relative resistance. The number of studs does not exhibit significant influence on the relative resistance, however, the influence of concrete strength is remarkable. The fastener in low strength concrete C12/15 shows obviously much larger reduction of resistance after fire exposure than that in concrete C20/25 and C40/50. Nevertheless, the difference is decreasing with prolonged fire exposure. On average, after 90 min of fire the anchor groups have residual capacity 16%, 25% and 28% of reference at ambient temperature in concrete C12/15, C20/25 and C40/50, respectively.

(a)   (b)
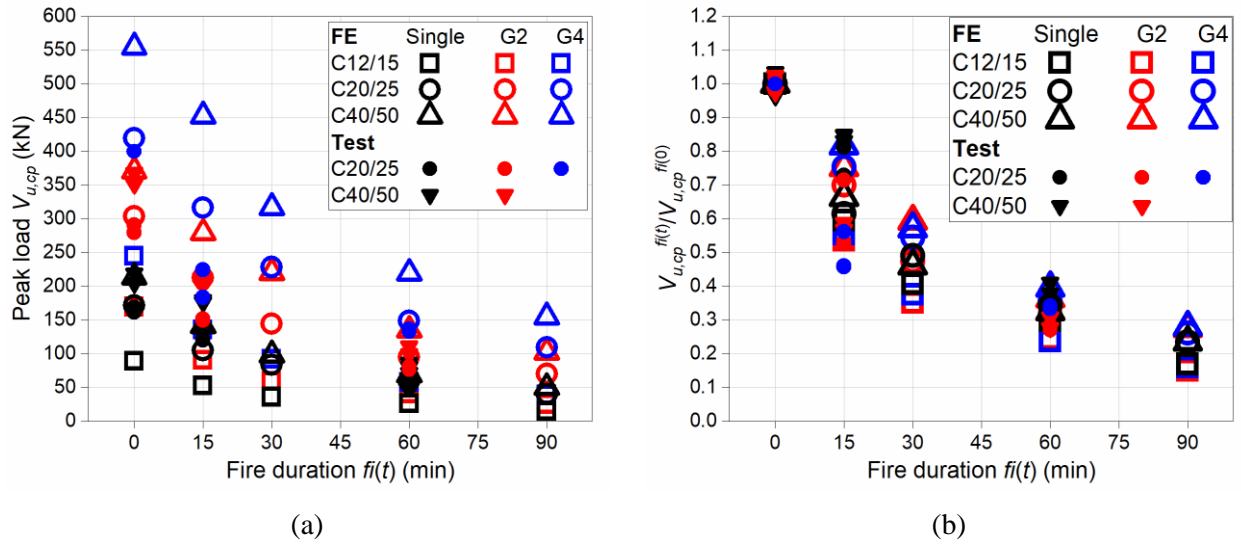
Figure 8.22 Numerical results of peak loads as functions of fire duration. (a) Absolute value; (b) relative value.

8.4.6. Influence of concrete strength

(a)   (b)
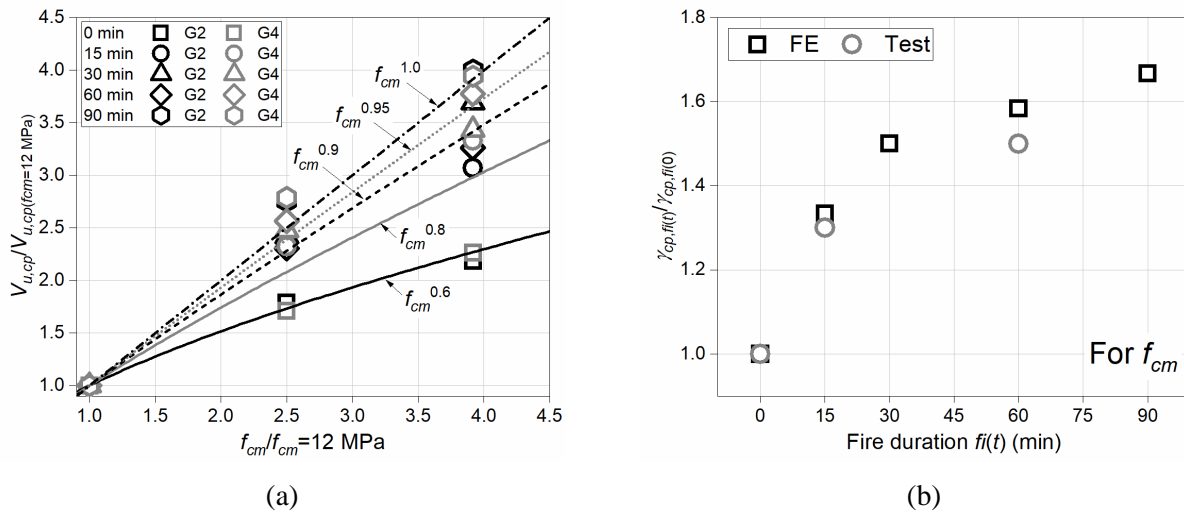
Figure 8.23 (a) Relative resistance of anchor groups as a function of concrete compressive strength; (b) relative value of $\gamma_{cp,fi(t)}$ as a function of fire duration.

The above mentioned results show that concrete strength plays important role on the resistance before and after fire exposure. The numerical peak loads of anchor groups as functions of concrete strength are depicted in Figure 8.23a. It is obvious that the influence of concrete strength is increasing with the increase of fire duration, which can be taken by the increase of the exponent of f_{cm} from 0.6, 0.8, 0.9, 0.95 and 1 after 0 min, 15 min, 30 min, 60 min and 90 min of

189

fire durations, respectively. This increase of the exponent of f_{cm} is further compared with the factor obtained experimentally. As presented in Figure 8.23b, they agree with each other well. This confirms that the normalization of peak loads with respect to different concrete compressive strength should be performed by applying different exponents $\gamma_{cp,fi(t)}$ on f_{cm} depending on the fire duration.

8.4.7. The projected area ratio

According to the CC-Method (*Fuchs et al.*, 1995), the resistance of anchor group is proportional to the projected area ratio $A_{c,N}/A_{c,N}^0$, in which the characteristic projected area of a single anchor with large spacing and edge distance is the concrete cone idealised as a pyramid of base length $s_{cr,N} = 3h_{ef}$ (see Figure 2.1). Figure 8.24a displays the peak load of anchor groups relative to that of single anchor (numerical and experimental data) versus the projected area ratio $A_{c,N}/A_{c,N}^0$, with the effective fracture size as $3h_{ef}$. The figure shows that most of the data are above the line of equality and indicates that the projected area ratio cannot take the influence of spacing into account very well. The fracture size $S_{fi(t)}$ (L×B, see Figure 8.6) of anchor groups before and after fire is therefore evaluated and plotted in Figure 8.24b. It shows that the fracture size is decreasing after fire exposure. After 15 min of fire, slight decrease can be seen. However, after 60 min of fire the reduction of fracture size is 40% on average. Therefore, the critical factor $s_{fi(t)}$ (at ambient temperature $s_{fi(0)} = 1.5$, see Chapter 7.5.1) should be revised with respect to different fire duration for anchor groups.
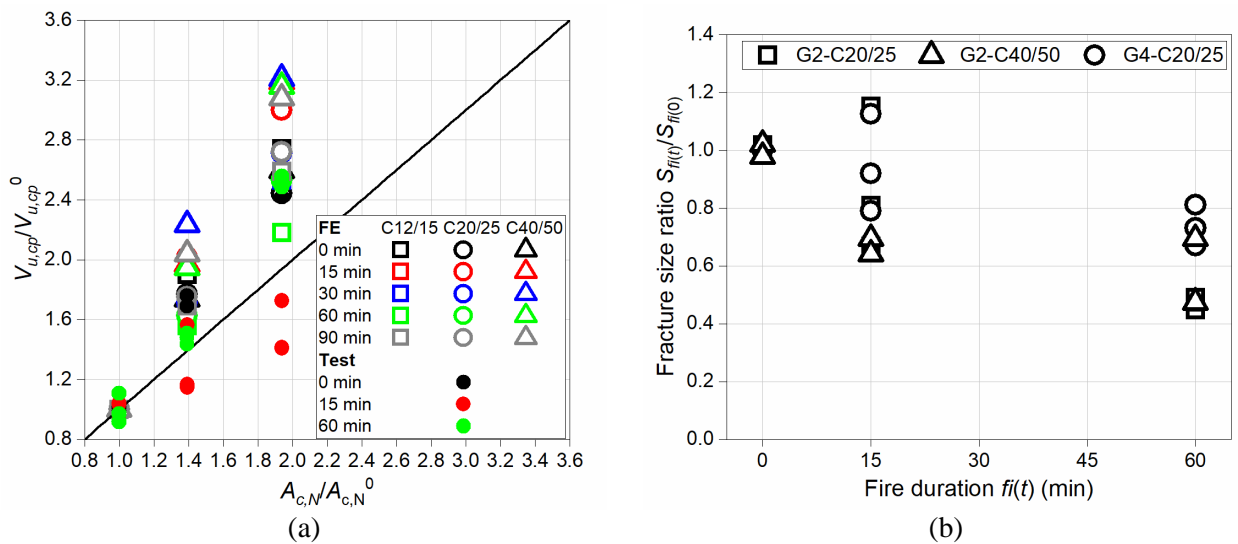
Figure 8.24 (a) Relative peak load versus the projected area ratio with original effective size factor; (b) the fracture size ratio of anchor groups versus fire duration.

Numerical and experimental results of the pry-out failure resistance of single stud anchor, anchor groups with two studs and four studs are employed to evaluate the validity of the projected area

$A_{c,N}$ before and after fire. According to conclusions from Chapter 7.5.1, the projected area ratio is calculated with factor $s_{fi(t)}$ equals 1.5, 1.5, 1.34, 0.95 and 0.95 for fire durations of 0 min, 15 min, 30 min, 60 min and 90 min, respectively. The peak load ratio versus the projected area ratio is again shown in Figure 8.25. The data plot presents a better positive correlation. However, further numerical and experimental studies are required to investigate this problem in more detail.
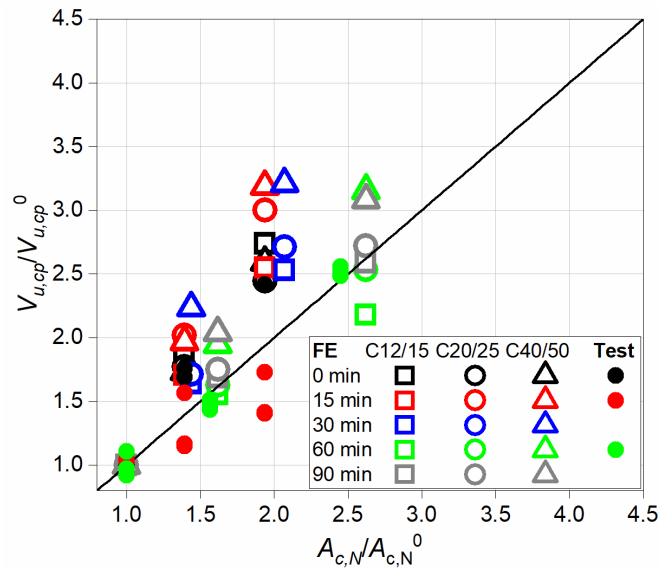
Figure 8.25 Relative peak load versus the projected area ratio depending on fire duration.

8.5. Summary

Fire exposure shows strong influence on the load-bearing behaviour of anchor groups due to pry-out failure. From single stud anchor to multiple studs anchor groups, the shear stiffness is seen to increase significantly at ambient temperature, however, after fire the reduction of the influence of the number of studs on the shear stiffness is pronounced, especially for long duration of fire (60 min). The reduction of pry-out failure resistance is about 40% and 50% for two- and four-stud anchor groups after 15 min of fire, respectively. After 60 min of fire, they have a reduction of over 70% of reference resistance. The fracture patterns can be seen similar to finding at ambient condition from previous researchers, however, the internal crack within the studs was not observed in this study. For anchor group with two rows of studs, the experimental observations indicates that the cracks initiated at the head of the front and rear studs simultaneously, which is further confirmed by the numerical examination.

It is interesting to find that the size of the failure cone after long duration of fire is reduced comparing to that at ambient temperature or short period of fire exposure. Consequently, the projected area ratio $A_{c,N}/A_{c,N}{}^{0}$ according to CC-method at ambient temperature should be modified

191

depending on the fire duration. The modification was conducted based on the measurement of the fracture size of single stud anchor and anchor groups after different fire durations. The evaluation of both experimental and numerical data shows that the modified projected area ratio can better taking the influence of spacing into account. It is worthy of further investigation on this topic.

9.   SUMMARY AND RECOMMENDATIONS

In the present thesis, previous studies on the concrete failure of fasteners at ambient and high temperature are reviewed and current fire safety design codes for fasteners in structural fire are introduced. The concrete failure of headed stud fasteners loaded in shear after fire exposure is experimentally and numerically investigated. Two typical and important failure types, concrete edge failure and pry-out failure, are studied. Both single stud anchor and multiple-stud anchor groups are considered. Finite element analysis is conducted corresponding to each experimental program and its theoretical background is briefly discussed. Numerical models are verified based on experimental results and parametric numerical studies are performed. The aim is to understand the failure mechanism of shear loaded fasteners close to and away from concrete slab edge after fire exposure. The main conclusions from the thesis are summarized as below.

1) The literature review indicates a lack of data on fasteners under fire and the current codes for fire safety design of fasteners are only informative. As a primary investigation, the concrete failure resistance is critical since it represents the ultimate capacity the fastener can sustain. For better understanding of the load-bearing behaviour of fasteners after fire, the thermophysical and thermomechanical properties of concrete are reviewed and special care is given to the difference of concrete properties in the hot and cold states. It is shown that the hot state is less significant than the cold state. From this point of view, the resistance of fasteners due to concrete failure should be analyzed separately for the cold and hot states.

2) The fire tests on the concrete edge failure of anchors in the hot state show that the confinement effect exists, especially for anchor with relatively restrained supporting distance. This effect may induce unexpected high resistance of anchors. Numerical analysis confirmed the experimental findings with the compressive struts formed against the shear load. After cooling, this confining stress is released. However, even without the confinement effect, numerical analysis shows that the concrete edge failure resistance for the cold state (over 90% reduction for 90 min of fire) is much lower than for the hot state, i.e. the cold state is relevant for fire safety design.

3) Experimental and numerical studies show that in the cold state the load-bearing behaviour of the concrete edge failure is significantly reduced. After fire, the stiffness of response is largely reduced. Consequently, much more ductile response is observed and larger cracking and displacement at peak loads are shown. The influences of diameter, embedment depth and concrete strength on the resistance are increasing with the increase of fire duration. The dependency on the compressive strength increases the power 0.5 at ambient temperature to 0.8 for 60 min of fire exposure. However, the power on c_1 is decreased from 1.5 at ambient

193

condition to 1.2 for 60 min of fire exposure. This is due to the severe damage to the concrete. The failure pattern is changed from typical concrete edge failure to the combination of concrete edge failure and pry-out failure after fire. These findings basically indicate different failure mechanism of fasteners after fire exposure. Based on the experimental and numerical results, a formula is proposed to calculate the resistance after fire exposure for the cold state.

4) Concrete edge failures of anchor groups with multiple studs are investigated. It is found that at ambient condition and after 15 min of fire the failure mode is, similar to that for single stud anchors, a combination of concrete edge failure and pry-out failure. However, after 60 min of fire, the anchor groups show an intact fracture propagating at the back side of the anchor group. Significant reduction of the stiffness of anchor groups can be seen. The number of studs has strong influence on the shear stiffness and resistance, however, the influence is much less after prolonged fire exposure. The experimental and numerical results show that the projected area ratio according to CC-method can well take the spacing effect of studs into account regarding concrete edge failure before and after fire. However, it should be noted that after long duration of fire, the prediction according to CC-method tends to be lower than the tested resistance.

5) The investigation on the pry-out failure of single stud anchors shows that the size of the fracture surface decreases after fire exposure, which is also confirmed through the numerical simulation. This eventually has influence on the evaluation of the projected area ratio to calculate the resistance of anchor groups based on the resistance of single stud anchor, according to the CC-method. The base length ($s_{cr,N} = 3h_{ef}$) of the idealized concrete cone has to be modified after fire exposure.

6) Fire exposure reduces strongly the stiffness of anchors due to pry-out failure. However, with longer fire duration, the influence of embedment depth and concrete strength on the stiffness is largely decreased. With the increase of fire exposure, the anchor presents larger displacements (vertical and horizontal) and, correspondingly, larger rotation of the anchor plate is measured.

7) In the fire tests, the concrete surface spalling occurred. The evaluation of the experimental and numerical results proves that the surface spalling reduces the actual resistance of the anchors, which is dependent on the actual spalling depth around the anchor. This is due to the fact that the volume of concrete that can bear the load is reduced. The pry-out failure resistance due to concrete failure is mainly influenced by the concrete strength and embedment depth. After fire exposure, the influence of concrete strength and embedment depth are increasing. The resistance at ambient condition is proportional to the power of 0.5

and 1.5 to the compressive strength and embedment depth, respectively. These parameters should increase with the increase of fire duration.

8) Experimental and numerical studies are conducted on anchor groups with two and four studs to investigate the spacing effect with respect to pry-out failure after fire exposure. Similar to single stud anchors, the failure surface of anchor groups becomes smaller with the increase of fire exposure and the effective size factor for the projected area should be modified.

9) Although the shear stiffness due to pry-out failure decreases significantly with increase of fire duration, from single stud to four-stud anchor groups, the shear stiffness increases most prominently at ambient temperature and after long duration of fire the increase is much less. Experimental and numerical results also show that the influence of concrete strength on the resistance is stronger with prolonged fire exposure and the tendency of increase is principally the same as that for single stud anchors. From single stud anchor to anchor groups, the influence of the number of studs on the pry-out failure resistance can be well taken into account by the modified projected area ratio according to measurement of the fracture size observed in experiments.

10) Thermo-mechanically coupled microplane model for concrete, with relaxed kinematic constraint, is found to be reliable on calculating the concrete failure of fasteners before and after fire exposure. With appropriate consideration of thermal and mechanical properties of concrete and fire load, the model can predict the temperature distribution and load-bearing response of anchors exposed to fire very well.

This thesis gives an insight into the failure mechanism and the reduction of resistance of fasteners after fire exposure. In sum, for the presented cases, experimental and numerical results indicate that the cold state resistance is generally lower than the hot state resistance, due to the larger temperature induced damage of concrete in the cold state. After fire exposure, even after only 15 min of fire exposure, the load-bearing response is obviously changed with more ductile behaviour. The failure mode can be very different due to severely thermally damaged concrete. Concrete edge failure after fire tends to have more damage initiated on the back side of the anchor and pry-out failure tends to have reduced fracture size due to steep propagation of the dominant crack. Most importantly, more than 50% of reduction of resistance has to be taken into account after only 15 min of fire. After 60 min of fire, the resistance is already very low.

Therefore, for further investigation and code development, it is recommended to have a clear differentiation between the hot and cold states behaviour. Nevertheless, for the practice the focus should be the cold state. After fire exposure, both for concrete edge failure and pry-out failure types, the influence of parameters (c_1, d, f_{cm} and h_{ef} for concrete edge failure; f_{cm} and h_{ef} for pry-out failure) are different from that at ambient condition. The experimental and numerical

conclusions from the relevant parts can be taken as reference to consider their effect on the resistance. It can also be found that for both failure types, after 60 min of fire exposure, the influence of different parameters is much less and the resistance is already quite low, especially for concrete edge failure. However, in the current code, the fire resistance of anchors is considered for 90 min and 120 min of fire. From this point of view, the most important is the mechanical behaviour of fasteners below 90 min of fire, because, beyond 90 min, the influence of different parameters is practically the same and the resistance is rather low.

REFERENCES

Abrams, M.S. (1971) Compressive strength of concrete at temperatures to 1600F. *ACI Special Publication.* 25, 33–58.

AISC Manual Committee (2001) *AISC Manual of Steel Construction: Load and Resistance Factor Design.* Third. Chicago, IL, USA.

Ali, F., Nadjai, A., Abu-Tair, A. (2011) Explosive spalling of normal strength concrete slabs subjected to severe fire. *Materials and Structures.* 44(5), 943–956.

American Concrete Institute Committee 318 (2014) *Building code requirements for structural concrete* (*ACI* 318-14) *and commentary* (*ACI* 318*R*-14). Farmington Hills, MI.

Anderberg, Y., Thelandersson, S. (1976) Stress and deformation characteristics of concrete at high temperature: 2. Experimental investigation and material behaviour model. *Bulletin of Division of Structural Mechanics and Concrete Construction, Bulletin 54*, 86.

Anderson, N.S., Meinheit, D.F. (2005) Pryout capacity of cast-in headed stud anchors. *PCI Journal.* 90-112

Association for Specialist Fire Protection, Steel Construction Institute, Group, F.T.S. (2014) *Fire protection for structural steel in buildings* (*Yellow Book*). *Fifth Edition.* UK.

Bahr, O., Schaumann, P., Bollen, B., Bracke, J. (2013) Young's modulus and Poisson's ratio of concrete at high temperatures: Experimental investigations. *Materials & Design.* 45, 421–429.

Baker, G. (1996) The effect of exposure to elevated temperatures on the fracture energy of plain concrete. *Materials and Structures.* 29(July), 383–388.

Bamonte, P.F., Gambarova, P.G., Bruni, M., Rossini, L. (2007) Ultimate capacity of undercut fasteners installed in thermally-damaged high-performance concrete. *Proceedings of the 6th International Conference on Fracture Mechanics of Concrete and Concrete Structures.* 3.

Bamonte, P., Gambarova, P.G. (2012) A study on the mechanical properties of self-compacting concrete at high temperature and after cooling. *Materials and Structures/Materiaux et Constructions.* 45(9), 1375–1387.

Bažant, Z.P., Oh, B.H. (1983) Crack band theory for fracture of concrete. *Materials and Structures.* 16(3), 155–177.

Bažant, Z.P. (1984) Size effect in blunt fracture: concrete, rock, metal. *Journal of Engineering Mechanics.* 110(4), 518–535.

Bažant, Z.P., Gambarova, P.G. (1984) Crack shear in concrete: crack band microplane model. *Journal of Structural Engineering.* 110(9), 2015–2035.

Bažant, Z.P., Oh, B.H. (1986) Efficient numerical integration on the surface of a sphere. *Journal of Applied Mathematics and Mechanics*. 66(1), 37–40.

Bažant, Z.P., Prat, P.C. (1988) Microplane model for brittle-plastic material: I. Theory. *Journal of Engineering Mechanics*. 114(10), 1672–1688.

Bažant, Z.P., Kazemi, M.T. (1990) Determination of fracture energy, process zone length and brittleness number from size effect, with application to rock and conerete. *International Journal of Fracture*. 44(2), 111–131.

Bažant, Z.P., Ožbolt, J. (1990) Nonlocal microplane model for fracture, damage, and size effect in structures. *Journal of Engineering Mechanics*. 116(11), 2485–2505.

Bažant, Z.P., Kaplan, M.F. (1996) *Concrete at High Temperatures: Material Properties and Mathematical Models*. London: Longman Addison-Wesley.

Bažant, Z.P., Adley, M.D., Carol, I., Jirásek, M., Akers, S.A., Rohani, B., Cargile, J.D., Caner, F.C. (2000) Large-strain generalization of microplane model for concrete and application. *Journal of Engineering Mechanics*. 126(9), 971–980.

Bažant, Z.P., Becq-Giraudon, E. (2002) Statistical prediction of fracture parameters of concrete and implications for choice of testing standard. *Cement and Concrete Research*. 32(4), 529–556.

Bošnjak, J. (2014) *Explosive spalling and permeability of high performance concrete under fire – numerical and experimental investigations*, PhD thesis. University of Stuttgart.

Brühwiler, E., Wittmann, F.H. (1990) The wedge splitting test, a new method of performing stable fracture mechanics tests. *Engineering Fracture Mechanics*. 35(1–3), 117–125.

Cavallini, M., Papagni, M.F., Preis, F.W.B. (2007) Fire disasters in the twentieth century. *Annals of Burns and Fire Disasters*. 20(2), 101–103.

Chang, Y.F., Chen, Y.H., Sheu, M.S., Yao, G.C. (2006) Residual stress–strain relationship for concrete after exposure to high temperatures. *Cement and Concrete Research*. 36(10), 1999–2005.

DIN Deutsches Institute für Normung (2008a) *DIN 1045-1 Concrete, reinforced and prestressed concrete structures - Part 1: Design and construction.* Berlin.

DIN Deutsches Institute für Normung (2008b) *DIN 1045-2 Concrete, reinforced and prestressed concrete structures - Part 2: Concrete - Specification, properties, production and conformity - Application rules for DIN EN 206-1*. Berlin.

DIN Deutsches Institute für Normung (2016) *DIN 4102-4 Fire behaviour of building materials and building components - Part 4: Synopsis and application of classified building materials, components and special components*. Berlin.

Driscoll, G.G., Slutter, R.G. (1961) Research on composite design at Lehigh University. *Proceedings of the National Engineering Conference, American Institute of Steel Construction*. 180(61–8), 18–24.

Elfgren, L., Broms, C.E., Cederwall, K., Gylltoft, K. (1982) Fatigue of anchor bolts in reinforced concrete foundations. In: IABSE Report Vol. 37, Fatigue of Steel and Concrete Structures. *International Association for Bridges and Structural Engineering*. Zurich, Switzerland.

Elfgren, L., Ohlsson, U. (1986) *Modelling of hook anchors, in: Fracture Mechanics of Concrete*. Report TVBM-3025. Lund.

Eligehausen, R., Clausnitzer, W. (1983) *Analytisches Modell zur Beschreibung des Tragverhaltens von Befestigungselementen* (*Analytical model to describe the load-bearing behaviour of fixing elements*) Report No. 4/1-83/3.

Eligehausen, R., Mallée, R., Silva, J.F. (2006) *Anchorage in Concrete Construction*. Berlin: Ernst & Sohn.

European Committee for Standardization (1999) *EN 10095 Heat resisting steels and nickel alloys*. Brussels, Belgium.

European Committee for Standardization (2002) *EN 1990: Basis of structural design.* Brussels, Belgium.

European Committee for Standardization (2003) *Eurocode 1 1991-1-2: Actions on structures - Part 1-2: General actions - Actions on structures exposed to fire*. Brussels, Belgium

European Committee for Standardization (2004a) *Eurocode 2 1992-1-2: design of concrete structures. Part 1-2: general rules-structural fire design.* Brussels, Belgium.

European Committee for Standardization (2004b) *Eurocode 4 EN 1994-1-1 Design of composite steel and concrete structures - Part 1-1: General rules and rules for buildings.* Brussels, Belgium.

European Committee for Standardization (2005a) *Eurocode 3 EN 1993-1-2 Design of steel structures - Part 1-2: General rules - Structural fire design.* Brussels, Belgium.

European Committee for Standardization (2005b) *Eurocode 4 EN 1994-1-2 Design of composite steel and concrete structures - Part 1-2: General rules - Structural fire design.* Brussels, Belgium.

European Committee for Standardization (2009a) *CEN/TS 1992-4-2 Design of fastenings for use in concrete - Part 4-2: Headed Fasteners.* Brussels, Belgium.

European Committee for Standardization (2009b) *CEN - EN 12390-3 Testing hardened concrete - Part 3: Compressive strength of test specimens.* Brussels, Belgium.

European Committee for Standardization (2009c) *CEN - EN 12390-7 Testing hardened concrete - Part 7: Density of hardened concrete.* Brussels, Belgium.

European Committee for Standardization (2010) *CEN - EN 12390-6 Testing hardened concrete - Part 6: Tensile splitting strength of test specimens.* Brussels, Belgium.

European Committee for Standardization (2011) *Eurocode 2 1992-1-1: Design of concrete structures - Part 1-1: General rules and rules for building*. Brussels, Belgium.

European Committee for Standardization (2012) *EN 1363-1 Fire resistance tests - Part 1: General Requirements.* Brussels, Belgium.

European Committee for Standardization (2013a) *CEN - EN 12390-13 Testing hardened concrete - Part 13: Determination of secant modulus of elasticity in compression.* Brussels, Belgium.

European Committee for Standardization (2013b) *EN 206 Concrete - Specification, performance, production and conformity.* Brussels, Belgium.

European Committee for Standardization (2014) *EN 10088-3 Stainless steels - Part 3: Technical delivery conditions for semifinished products, bars, rods, wire, sections and bright products of corrosion resisting steels for general purposes.* Brussels, Belgium.

European Committee for Standardization (2016) *EN 13501-2: Fire classification of construction products and building elements - Part 2: Classification using data from fire resistance tests, excluding ventilation services.* Brussels, Belgium.

European Committee for Standardization (2018) *Eurocode 2 EN 1992-4 Design of concrete structures - Part 4 Design of fastenings for use in concrete.* Brussels, Belgium.

European Organisation for Technical Approvals (2004) *TR 020 Technical Report-Evaluation of Anchorage in Concrete concerning Resistance to Fire.* Brussels, Belgium.

European Organisation for Technical Approvals (2012) *ETAG 001 Guideline for European technical approval of metal anchors for use in concrete.* Brussels, Belgium.

fédération internationale du béton (fib) (1993) *CEB-FIP Model Code 1990.* London: Thomas Telford Ltd.

fédération internationale du béton (fib) (2007) *CEB-FIP bulletin 38: Fire design of concrete structures - materials, structures and modelling.* Lausanne, Switzerland.

fédération internationale du béton (fib) (2008) *CEB-FIP bulletin 46. Fire design of concrete structures - structural behaviour and assessment*. Lausanne, Switzerland.

Felicetti, R., Gambarova, P.G., Sora, M.P.N., Khoury, G.A. (2000) Mechanical behaviour of HPC and UHPC in direct tension at high temperature and after cooling. *Fifth International RILEM Symposium on Fibre-Reinforced Concrete* (*FRC*). (2000), 749–758.

Felicetti, R., Meda, A. (2005) *Residual behaviour of reinforcing steel bars after fire. In Proceeding of Keep Concrete Attractive. Hungarian Group of fib.* Budapest University of Technology and Economics. Budapest, Hungary, pp. 1148–1156.

Fuchs, W., Eligehausen, R., Breen, J.E. (1995) Concrete capacity design (CCD) approach for fastening to concrete. *Structural Journal*. 92(1).

Gernay, T. (2012) *A multiaxial constitutive model for concrete in the fire situation including transient creep and cooling down phases*, PhD thesis. University of Liège.

Grosser, P.R. (2012) *Load-bearing behavior and design of anchorages subjected to shear and torsion loading in uncracked concrete,* PhD thesis. University of Stuttgart, Germany.

Hager, I. (2004) *Comportement à haute température des bétons à haute performance: évolution des principales propriétés mécaniques.* École nationale des ponts et chaussées.

Harada, T., Takeda, J., Yamane, S., Furumura, F. (1972) Strength, elasticity and thermal properties of concrete subjected to elevated temperatures. *ACI Special Publication*. 34, 377–406.

Harmathy, T.Z. (1970) Thermal properties of concrete at elevated temperatures. *Journal of Materials.* 5(1), 47–74.

Harmathy, T.Z., Allen, L.W. (1973) Thermal Properties of Selected Masonry Unit Concretes. *ACI Journal Proceedings*. 70(2), 132–142.

Harmathy, T.Z. (1993) *Fire Safety Design and Concrete*. Longman Scientific & Technical.

Hlavička, V., Lublóy, É. (2018) Concrete cone failure of bonded anchors in thermally damaged concrete. *Construction and Building Materials*. 171, 588–597.

Hofmann, J., Fuchs, W., Eligehausen, R. (2004) Quertragfähigkeit randnaher Befestigungsmittel mit Belastung senkrecht zum Bauteilrand-Einfluß von Durchmesser und Verankerungstiefe (Resistance of fasteners close to the edge under shear load perpendicular to the edge-Influence of the parameters diameter). *Beton- und Stahlbetonbau*. 99(10), 806–812.

Hofmann, J. (2005) *Tragverhalten und Bemessung von Befestigungen unter beliebiger Querbelastung in ungerissenem Beton* (*Behaviour and design of anchorages under arbitrary shear load direction in uncracked concrete),* PhD thesis. University of Stuttgart, Germany.

International Organization for Standardization (1999) *ISO 834-1 Fire resistance tests - Elements of building construction - Part 1: General requirements.* Geneva, Switzerland.

International Organization for Standardization (2008) *ISO 13918 Welding - Studs and ceramic ferrules for arc stud welding.* Geneva, Switzerland.

Jebara, K., Ožbolt, J., Hofmann, J. (2016) Pryout failure capacity of single headed stud anchors. *Materials and Structures/Materiaux et Constructions*. 49(5), 1775–1792.

Jebara, K. (2018) *Pryout capacity and bearing behavior of stocky headed stud anchorages*, PhD thesis. University of Stuttgart.

Ju, Y., Tian, K., Liu, H., Reinhardt, H.-W., Wang, L. (2017) Experimental investigation of the effect of silica fume on the thermal spalling of reactive powder concrete. *Construction and Building Materials*. 155, 571–583.

Kalifa, P., Menneteau, F.-D., Quenard, D. (2000) Spalling and pore pressure in HPC at high

temperatures. *Cement and Concrete Research.* 30(12), 1915–1927.

Khoury, G.A. (1983) *Transient thermal creep of nuclear reactor pressure vessel type concretes.* University of London.

Khoury, G.A. (2000) Effect of fire on concrete and concrete structures. *Progress in Structural Engineering and Materials*. 2(4), 429–447.

Khoury, G.A., Majorana, C.E., Pesavento, F., Schrefler, B.A. (2002) Modelling of heated concrete. *Magazine of Concrete Research*. 54(2), 77–101.

Khoury, G.A. (2006) Strain of heated concrete during two thermal cycles. Part 1: strain over two cycles, during first heating and at subsequent constant temperature. *Magazine of Concrete Research*. 58(6), 367–385.

Kluwer Academic Publishers (1985) *Determination of the fracture energy of mortar and concrete by means of three-point bend tests on notched beams*.

Kordina, K., Meyer-Ottens, C. (1981) *Beton-Brandschutz-Handbuch*. Düsseldorf: Beton-Verlag.

Kosmatka, S.H., Kerkhoff, B., Panarese, W.C. (2002) *Design and Control of Concrete Mixture*. 14th ed. Illinois, USA: Portland Cement Association.

Lee, J.S., Xi, Y., Willam, K. (2007) Strength and stiffness of concrete under heating and cooling treatments. *Proceedings of the 6th International Conference on Fracture Mechanics for Concrete and Concrete Structures*, Catania, Italy, 1709-1714.

Li, L., Purkiss, J. (2005) Stress-strain constitutive equations of concrete material at elevated temperatures. *Fire Safety Journal*. 40(7), 669–686.

Lie, T.T. (1992) *Structural Fire Protection*. American Society of Civil Engineers.

Luccioni, B.M., Figueroa, M.I., Danesi, R.F. (2003) Thermo-mechanic model for concrete exposed to elevated temperatures. *Engineering Structures.* 25(6), 729–742.

Mashiri, F.R., Mirza, O., Canuto, C., Lam, D. (2017) Post-fire behaviour of innovative shear connection for steel-concrete composite structures. *Structures*. 9, 147–156.

Mindeguia, J.-C., Pimienta, P., Noumowé, A., Kanema, M. (2010) Temperature, pore pressure and mass variation of concrete subjected to high temperature - Experimental and numerical discussion on spalling risk. *Cement and Concrete Research*. 40(3), 477–487.

Mirza, O., Uy, B. (2009) Behaviour of headed stud shear connectors for composite steel–concrete beams at elevated temperatures. *Journal of Constructional Steel Research*. 65(3), 662–674.

Mohr, O. (1900) Welche Umstände bedingen die Elasstizitätsgrenze und den Bruch eines Materials. *Zeitschrift des Vereins deutscher Ingenieure*. 46, 1524–1530.

National Precast Concrete Association (2012) *Architectural Precast Concrete Wall Panels Connection Guide*. Carmel, IN, USA.

Neuenschwander, M., Knobloch, M., Fontana, M. (2017) Generic model stress-strain relationship for concrete in compression at elevated temperatures. *ACI Materials Journal*. 114(1), 3–15.

Ollgaard, J. G.; Slutter, R. G.; Fisher, J.W. (1971) Shear strength of stud connectors in lightweight and normal weight concrete, AISC Eng'g Jr., April 1971 (71-10). *AISC Engineering Journal*, 55–64.

Ožbolt, J. (1995) *Maßtabseffekt und Duktilität von Beton- und Stahlbetonkonstruktionen* (*Size effect and ductility of concrete and reinforced concrete structures*). Tech. Habil. University of Stuttgart.

Ožbolt, J. (1998) *MASA-macroscopic space analysis, Internal Report.* Institute of Construction Materials, University of Stuttgart, Germany.

Ožbolt, J., Li, Y., Kožar, I. (2001) Microplane model for concrete with relaxed kinematic constraint. *International Journal of Solids and Structures*. 38(16), 2683–2711.

Ožbolt, J., Kožar, I., Eligehausen, R., Periškić, G. (2005a) Instationäres 3D Thermo-mechanisches Modell für Beton (Transient 3D thermo-mechanical model for concrete). *Beton- und Stahlbetonbau.* 100(1), 39–51.

Ožbolt, J., Kožar, I., Eligehausen, R., Periškić, G. (2005b) Three-dimensional FE analysis of headed stud anchors exposed to fire. *Computers and Concrete*. 2(4), 249–266.

Ožbolt, J., Periškić, G., Reinhardt, H.-W., Eligehausen, R. (2008) Numerical analysis of spalling of concrete cover at high temperature. *Computers and Concrete*. 5(4), 279–293.

Ožbolt, J., Sharma, A., Reinhardt, H.-W. (2011) Dynamic fracture of concrete – compact tension specimen. *International Journal of Solids and Structures*. 48(10), 1534–1543.

Ožbolt, J., Bošnjak, J., Periškić, G., Sharma, A. (2014) 3D numerical analysis of reinforced concrete beams exposed to elevated temperature. *Engineering Structures*. 58, 166–174.

Periškić, G. (2009) *Entwicklung eines 3D thermo-hygro-mechanischen Modells für Beton unter Brandbeanspruchung und Anwendung auf Befestigungen unter Zuglasten* (*Development of a thermo-hydro-mechanical model for concrete under fire and application to fastenings loaded in tension*) (*in German*), PhD thesis. University of Stuttgart.

Persson, B. (2003) *Self-compacting concrete at fire temperatures.* (Report TVBM; Vol. 3110).

Reick, M. (2001) *Brandverhalten von Befestigungen mit großem Randabstand in Beton bei zentrischer Zugbeanspruchung* (*Fire resistance of anchors far from an edge in concrete with axial loading*) (*in German*), PhD thesis. University of Stuttgart.

Sawade, G. (1994) *Ein energetisches Materialmodell zur Berechnung des Tragverhaltens von*

zugbeanspruchtem Beton (*Energetic material model to describe the load-bearing behaviour of concrete under tension*) (*in German*), PhD thesis. University of Stuttgart.

Schneider, U. (1976) Behaviour of concrete under thermal steady state and non-steady state conditions. *Fire and Materials*. 1, 103–115.

Schneider, U. (1982) Verhalten von Beton bei erhöhten Temperaturen (Behaviour of concrete at high temperatures) (in German). *Deutsche Ausschuß für Stahlbeton*. 337.

Schneider, U. (1988) Concrete at high temperatures — A general review. *Fire Safety Journal*. 13(1), 55–68.

Shaikh, A.F., Yi, W. (1985) In-place strength of welded headed studs. *PCI Journal*. 30(2), 56–81.

Shariati, A., Ramlisulong, N.H., Suhatril, M., Shariati, M. (2012) Various types of shear connectors in composite structures: A review. *International Journal of the Physical Sciences*. 7(22), 2876–2890.

Sharma, A., Bošnjak, J. (2017) Residual tensile capacity of post-installed anchors after exposure to fire. *In 3rd International Symposium on Connections between Steel and Concrete*. Stuttgart, pp. 1270–1279.

Shin, K.-Y., Kim, S.-B., Kim, J.-H., Chung, M., Jung, P.-S. (2002) Thermo-physical properties and transient heat transfer of concrete at elevated temperatures. *Nuclear Engineering and Design*. 212(1), 233–241.

Silva, J.F. (2007) Open questions in the field of anchorage to concrete. *Beton- und Stahlbetonbau.* 102(S1), 2–6.

Stabler, J.T. (2000) *Computational modelling of thermomechanical damage and plasticity in concrete.* University of Queensland.

Standard Australia Limited (2003) Australian Standard AS2327.01-2003, *Composite Structures, Part 1 Simply Supported Beams*. Sydney, Australia.

Takeuchi, M., Hiramoto, M., Kumagai, N., Yamazaki, N., Kodaira, A., Sugiyama, K. (1993) Material properties of concrete and steel bars at elevated temperatures. *In Transactions of the 12. international conference on Structural Mechanics in Reactor Technology (SMiRT).* Volume H: Concrete and concrete structures.

Taylor, G.I. (1938) Plastic strains in metals. *Journal of the Institute of Metals*. 62, 307–324.

Tian, K., Ožbolt, J., Periškić, G. (2016) Concrete edge failure of headed stud anchors under fire and post-fire conditions : verification of a 3D FE code. *In 9th International Conference on Structures in Fire*. Princeton, pp. 20–27.

Tian, K., Ožbolt, J., Periškić, G., Hofmann, J. (2018) Concrete edge failure of single headed

stud anchors exposed to fire and loaded in shear: Experimental and numerical study. *Fire Safety Journal.* 100, 32–44.

Tian, K., Ožbolt, J., Sharma, A., Hofmann, J. (2018) Experimental study on concrete edge failure of single headed stud anchors after fire exposure. *Fire Safety Journal*. 96, 176–188.

Torić, N., Boko, I., Peroš, B. (**2013**) Reduction of postfire properties of high-strength concrete. *Advances in Materials Science and Engineering*, 1–9.

Viest, I.M. (1956) Investigation of stud shear connectors for composite concrete and steel T-beams. *Journal of the American Concrete Institute*. 52(4), 875–892.

Wang, A.J. (2012) Numerical Investigation into Headed Shear Connectors under Fire. *Journal of Structural Engineering*. 138(1), 118–122.

Wittmann, F.H. (2002) Crack formation and fracture energy of normal and high strength concrete. *Sadhana*. 27(4), 413–423.

Yu, K., Yu, J., Lu, Z. (2013) Average fracture energy for crack propagation in post-fire concrete. *Advances in Materials Science and Engineering*, 1–13.

Zhang, B., Bicanic, N. (2002) Residual fracture toughness of normal- and high-strength gravel concrete after heating to 600 ℃. *ACI Materials Journal.* 99(3), 217–226.

Zhao, G. (1993) *Tragverhalten von randfernen Kopfbolzenverankerungen bei Betonbruch* (*Behaviour of headed stud anchors remote to an edge at concrete failure*) (*in German*), PhD thesis. University of Stuttgart.

Zienkiewicz, O.C., Pande, N. (1977) Time-dependent multilaminate model of rocks—a numerical study of deformation and failure of rock masses. *International Journal for Numerical and Analytical Methods in Geomechanics*. 1, 219–247.

APPENDICES

Appendix A: Experimental results

Appendix B: Numerical results

APPENDIX A

Table A.1 Experimental results of concrete edge failure for concrete C12/15

Condition	c_1/mm	h_{ef}/mm	d/mm	$f_{cc,150}$ /MPa	$fi(t)$/min	$V_{u,test}$ /kN	δ_h/mm	fm
Ambient	50	95	16	14.61	0	7.80	3.01	CE
Ambient	50	95	16	14.61	0	5.68	0.75	CE
Hot state 1	50	95	16	15.95	90	11.78	NA[3]	CE
Hot state 1	50	95	16	15.95	90	10.03	NA[3]	CE
Hot state 1	50	95	16	15.95	90	12.68	NA[3]	CE
Hot state 2	50	95	16	21.71	90	9.30	NA[3]	CE
Hot state 2	50	95	16	21.71	90	10.77	NA[3]	CE
Hot state 2	50	95	16	21.71	90	11.92	NA[3]	CE
Cold state	50	95	16	15.95	90	0.64	7.43	CE
Cold state	50	95	16	15.95	90	0.53	8.70	CE
Ambient	50	95	25	14.61	0	7.77	0.61	CE
Ambient	50	95	25	14.61	0	7.01	0.70	CE
Hot state 1	50	95	25	14.61	90	10.65	NA[3]	CE
Hot state 1	50	95	25	14.61	90	12.93	NA[3]	CE
Hot state 1	50	95	25	14.61	90	10.23	NA[3]	CE
Cold state	50	95	25	14.61	90	0.95	5.77	CE
Ambient	100	95	16	14.61	0	21.13[1]	2.20[1]	CE
Ambient	100	95	16	14.61	0	21.13[1]	2.20[1]	CE
Hot state 1	100	95	16	15.11	90	26.65	NA[3]	CE[2]
Hot state 1	100	95	16	15.11	90	24.60	NA[3]	CE[2]
Hot state 1	100	95	16	14.61	90	22.55	NA[3]	CE[2]
Hot state 2	100	95	16	17.54	90	19.05	NA[3]	CE[2]
Hot state 2	100	95	16	17.54	90	18.04	NA[3]	CE[2]
Hot state 2	100	95	16	14.61	90	15.60	NA[3]	CE[2]
Cold state	100	95	16	15.11	90	2.67	7.13	CE
Cold state	100	95	16	15.11	90	2.77	6.26	CE
Cold state	100	95	16	14.61	90	2.46	4.50	CE
Cold state	100	95	16	17.54	90	2.34	10.87	CE
Cold state	100	95	16	17.54	90	2.63	9.34	CE
Cold state	100	95	16	17.54	90	2.69	13.75	CE
Ambient	100	95	25	14.61	0	44.69	6.66	CE
Ambient	100	95	25	14.61	0	43.98	5.68	CE
Hot state 1	100	95	25	15.95	90	33.85	NA[3]	CE
Hot state 1	100	95	25	15.95	90	32.39	NA[3]	CE
Hot state 1	100	95	25	15.95	90	29.31	NA[3]	CE
Hot state 2	100	95	25	21.71	90	28.90	NA[3]	CE
Hot state 2	100	95	25	21.71	90	31.30	NA[3]	CE
Hot state 2	100	95	25	21.71	90	32.77	NA[3]	CE

Appendix A

Condition	c_1/mm	h_{ef}/mm	d/mm	$f_{cc,150}$ /MPa	$fi(t)$/min	$V_{u,test}$ /kN	δ_h/mm	fm
Cold state	100	95	25	15.95	90	6.80	4.19	CE
Cold state	100	95	25	15.95	90	5.12	7.34	CE
Cold state	100	95	25	15.95	90	4.79	4.83	CE
Cold state	100	95	25	21.71	90	5.60	6.31	CE
Cold state	100	95	25	21.71	90	3.66	5.52	CE
Cold state	100	95	25	21.71	90	7.17	4.69	CE
Ambient	100	45	25	14.61	0	31.37	1.63	CE
Ambient	100	45	25	14.61	0	23.91	2.25	Pr
Hot state 1	100	45	25	14.61	90	16.67	NA[3]	CE
Hot state 1	100	45	25	14.61	90	18.91	NA[3]	CE
Hot state 1	100	45	25	14.61	90	19.89	NA[3]	CE
Cold state	100	45	25	14.61	90	1.65	3.77	CE
Cold state	100	45	25	14.61	90	1.43	1.06	CE
Cold state	100	45	25	14.61	90	2.22	3.40	CE
Cold state	100	45	25	14.61	90	1.73	5.80	CE
Cold state	100	45	25	14.61	90	1.89	2.58	CE
Cold state	100	45	25	14.61	90	1.14	6.49	CE

Hot state 1: fire on one side; Hot state 2: fire on two sides; Cold state: fire on two sides; CE: concrete edge failure; Pr: pryout failure.

[1] Calculated results based on the capacity of c50h95d16 and c150h95d16, and the equation in Eurocode 2 1992-4:2015

[2] Concrete edge failure with yield of anchor shaft

[3] Not available due to safety reasons in the hot state

Table A.2 Experimental results of concrete edge failure for the cold state: single stud anchors

c_1 [mm]	h_{ef} [mm]	d [mm]	$f_{cc,150}$ [MPa]	$fi(t)$ [min]	$V_{u,test}$ [kN]	$\delta_{u,test}$ [mm]	$\delta(0.5V_{u,test})$ [mm]	k_V [kN/mm]	fm
100	95	16	37.04	0	38.84	1.68	0.49	39.63	CE
100	95	16	37.04	0	38.84	1.51	0.41	47.37	CE
100	140	16	37.04	0	39.33	2.07	0.58	33.91	CE
100	140	16	37.04	0	41.24	2.20	0.72	28.64	CE
150	95	25	37.04	0	38.13	1.11	0.33	57.77	CE
100	95	25	37.04	0	36.83	1.15	0.34	54.16	CE
150	95	25	37.04	0	58.55	2.54	0.72	40.67	CE
150	95	25	37.04	0	62.64	n/a	n/a	n/a	CE
100	95	16	59.12	0	42.34	2.72	0.63	33.60	CE
100	95	16	59.12	0	46.89	2.61	0.67	34.99	CE
100	140	16	59.12	0	44.61	3.00	0.85	26.24	CE
100	140	16	59.12	0	41.86	2.22	0.47	44.53	CE
100	95	25	59.12	0	43.48	1.21	0.28	77.64	CE
100	95	25	59.12	0	37.86	1.26	0.35	54.09	CE
150	95	25	59.12	0	71.27	2.08	0.60	59.39	CE
150	95	25	59.12	0	64.04	1.82	0.45	71.16	CE
100	70	16	36.92	15	13.30	1.86	0.44	15.11	CE
100	70	16	36.92	15	11.54	1.73	0.39	14.79	CE
100	70	16	36.92	15	13.49	1.95	0.59	11.43	CE
100	95	16	36.92	15	13.44	3.27	0.64	10.50	CE
100	95	16	36.92	15	15.58	3.19	0.66	11.80	CE
100	95	16	36.92	15	17.76	2.33	0.71	12.51	CE
100	140	16	36.92	15	21.22	2.16	0.50	21.22	CE
100	140	16	36.92	15	30.29	2.78	0.66	22.95	CE
100	140	16	36.92	15	18.77	2.21	0.55	17.06	CE+S
75	95	25	36.92	15	12.15	2.09	0.60	10.13	CE
75	95	25	36.92	15	14.80	1.37	0.41	18.05	CE
75	95	25	36.92	15	12.74	1.20	0.41	15.54	CE
100	95	25	36.92	15	13.27	1.68	0.49	13.54	CE
100	95	25	36.92	15	18.34	1.30	0.45	20.38	CE
100	95	25	36.92	15	12.90	2.05	0.51	12.65	CE
150	95	25	36.92	15	24.87	1.98	0.54	23.03	CE
150	95	25	36.92	15	27.42	2.21	0.56	24.48	CE
150	95	25	36.92	15	28.62	1.83	0.62	23.08	CE
100	95	32	36.92	15	15.92	1.60	0.62	12.84	CE
100	95	32	36.92	15	19.53	1.54	0.43	22.71	CE
100	95	32	36.92	15	21.19	1.76	0.81	13.08	CE
100	95	16	54.52	15	16.67	2.48	0.61	13.66	CE
100	95	16	54.52	15	29.94	2.02	0.49	30.55	CE
100	95	16	54.52	15	24.36	2.02	0.57	21.37	CE+S
100	140	16	54.52	15	27.30	2.09	0.44	31.02	CE
100	140	16	54.52	15	25.22	4.41	0.85	14.84	CE+S

c_1 [mm]	h_{ef} [mm]	d [mm]	$f_{cc,150}$ [MPa]	$fi(t)$ [min]	$V_{u,test}$ [kN]	$\delta_{u,test}$ [mm]	$\delta(0.5V_{u,test})$ [mm]	k_V [kN/mm]	fm
100	140	16	54.52	15	26.23	3.70	0.57	23.01	CE+S
75	95	25	54.52	15	12.80	2.38	0.24	26.67	CE
75	95	25	54.52	15	12.77	1.97	0.31	20.60	CE
75	95	25	54.52	15	16.28	1.83	0.41	19.85	CE
100	95	25	54.52	15	18.12	1.67	0.39	23.23	CE
100	95	25	54.52	15	24.59	2.35	0.45	27.32	CE
100	95	25	54.52	15	30.32	1.24	0.42	36.10	CE
150	95	25	54.52	15	41.21	1.74	0.58	35.53	CE
150	95	25	54.52	15	38.00	1.50	0.55	34.55	CE
150	95	25	54.52	15	36.17	1.21	0.44	41.10	CE
100	70	16	34.53	60	2.38	1.91	0.59	2.02	CE
100	70	16	34.53	60	6.44	3.35	0.77	4.18	CE
100	70	16	34.53	60	5.86	3.39	1.03	2.84	CE
100	95	16	34.53	60	3.88	2.61	0.72	2.69	CE
100	95	16	34.53	60	3.24	4.38	0.92	1.76	CE
100	95	16	34.53	60	3.65	5.93	0.96	1.90	CE
100	140	16	34.53	60	9.43	4.98	1.57	3.00	CE
100	140	16	34.53	60	7.52	n/a	n/a	n/a	CE
100	140	16	34.53	60	8.42	4.46	1.17	3.60	CE
75	95	25	34.53	60	3.43	7.32	1.51	1.14	CE
75	95	25	34.53	60	4.43	4.61	0.81	2.73	CE
75	95	25	34.53	60	4.99	4.77	0.70	3.56	CE
100	95	25	34.53	60	8.93	3.79	0.93	4.80	CE
100	95	25	34.53	60	3.92	3.13	0.74	2.65	CE
100	95	25	34.53	60	5.40	5.15	0.86	3.14	CE
150	95	25	34.53	60	10.67	3.65	1.09	4.89	CE
150	95	25	34.53	60	6.13	1.88	0.77	3.98	CE
150	95	25	34.53	60	11.81	2.30	0.83	7.11	CE
100	95	32	34.53	60	5.98	2.26	0.54	5.54	CE
100	95	32	34.53	60	6.40	4.45	1.08	2.96	CE
100	95	32	34.53	60	8.93	4.99	1.05	4.25	CE+S
100	95	16	59.12	60	6.54	3.61	0.63	5.19	CE
100	95	16	59.12	60	5.17	3.96	0.59	4.38	CE
100	95	16	59.12	60	9.22	5.49	0.80	5.76	CE
100	140	16	59.12	60	14.10	4.45	1.42	4.96	CE
100	140	16	59.12	60	9.01	5.13	1.03	4.37	CE
100	140	16	59.12	60	12.21	2.96	1.11	5.50	CE
75	95	25	59.12	60	3.89	2.83	0.65	2.99	CE
75	95	25	59.12	60	5.84	4.11	0.59	4.95	CE
75	95	25	59.12	60	5.46	3.83	0.95	2.87	CE
100	95	25	59.12	60	10.81	4.27	0.95	5.69	CE
100	95	25	59.12	60	11.84	3.42	0.90	6.58	CE
100	95	25	59.12	60	9.70	2.12	0.74	6.55	CE
150	95	25	59.12	60	9.06	2.94	0.80	5.66	CE

c_1 [mm]	h_{ef} [mm]	d [mm]	$f_{cc,150}$ [MPa]	$fi(t)$ [min]	$V_{u,test}$ [kN]	$\delta_{u,test}$ [mm]	$\delta(0.5V_{u,test})$ [mm]	k_V [kN/mm]	fm
150	95	25	59.12	60	9.67	3.48	0.84	5.76	CE
150	95	25	59.12	60	16.07	2.28	0.66	12.17	CE

Table A.3 Experimental results of concrete edge failure for the cold state: anchor groups

Anchor	$c_{1,1}$ [mm]	$c_{1,2}$ [mm]	$f_{cc,150}$ [MPa]	$fi(t)$ [min]	$V_{u,test}$ [kN]	$\delta_{u,test}$ [mm]	$\delta(0.5V_{u,test})$ [mm]	k_V [kN/mm]	fm
G2-c100h95d25	100	-	37.04	0	45.27	0.49	0.05	452.70	CE
G2-c100h95d25	100	-	37.04	0	47.36	0.43	0.06	394.67	CE+Pr
G4-c100h95d25	100	200	37.04	0	107.86	0.38	0.03	1797.67	CE
G4-c100h95d25	100	200	37.04	0	102.17	0.33	0.04	1277.13	CE+Pr
G2-c100h95d25	100	-	36.92	15	23.11	0.95	0.11	105.05	CE+Pr
G2-c100h95d25	100	-	36.92	15	20	0.57	0.09	111.11	CE+Pr
G2-c100h95d25	100	-	36.92	15	17.56	0.75	0.06	146.33	CE+Pr
G4-c100h95d25	100	200	36.92	15	57.26	0.38	0.11	260.27	CE+Pr
G4-c100h95d25	100	200	36.92	15	68.19	0.48	0.10	340.95	CE+Pr
G4-c100h95d25	100	200	36.92	15	44.87	0.60	0.09	249.28	CE+Pr
G2-c100h95d25	100	-	34.53	60	11.07	0.98	0.19	29.13	CE+Pr
G2-c100h95d25	100	-	34.53	60	6.27	2.08	0.11	28.50	CE+Pr
G2-c100h95d25	100	-	34.53	60	5.72	2.19	0.19	15.05	CE+Pr
G4-c100h95d25	100	200	34.53	60	18.62	2.60	0.44	21.16	CE+Pr
G4-c100h95d25	100	200	34.53	60	23.03	2.91	0.51	22.58	CE+Pr
G4-c100h95d25	100	200	34.53	60	16.89	0.74	0.19	44.45	CE+Pr

Table A.4 Experimental results of pry-out failure for the cold state: single stud anchors

h_{ef} [mm]	d [mm]	$f_{cc,150}$ [MPa]	$fi(t)$ [min]	$V_{u,test}$ [kN]	δ_h [mm]	$\delta(0.5V_{u,test})$ [mm]	k_V [kN/mm]	δ_{vm} [mm]	δ_{vb} [mm]	fm
70	25	37.04	0	154.88	2.17	0.36	215.11	0.98	1.97	Pr
70	25	37.04	0	156.88	2.02	0.40	196.10	0.99	1.98	Pr
85	25	37.04	0	168.84	6.78	0.50	168.84	2.30	4.49	Pr+S1
85	25	37.04	0	162.11	6.39	0.51	158.93	1.81	4.01	Pr+S1
70	25	59.12	0	189.05	2.84	0.34	278.01	1.05	2.16	Pr
70	25	59.12	0	218.66	n/a	0.35	312.37	n/a	n/a	Pr+S1
85	25	59.12	0	204.44	13.73	0.54	189.30	2.98	7.28	Pr+S2
85	25	59.12	0	219.40	12.10	0.51	215.10	3.02	7.28	Pr+S2
70	25	36.92	15	86.86	1.64	0.42	103.40	1.43	2.30	Pr
70	25	36.92	15	66.08	1.74	0.41	80.59	n/a	n/a	Pr
70	25	36.92	15	62.24	1.76	0.41	75.90	1.54	2.58	Pr
85	25	36.92	15	120.37	2.25	0.69	87.22	1.72	2.86	Pr+S1
85	25	36.92	15	96.70	2.44	0.74	65.34	2.35	3.48	Pr+S1
85	25	36.92	15	88.25	1.85	0.53	83.25	0.00	1.06	Pr+S1
100	25	36.92	15	132.69	3.91	0.56	118.47	1.70	3.31	Pr+S1
100	25	36.92	15	126.04	3.41	0.55	114.58	2.39	3.90	Pr+S1
100	25	36.92	15	121.67	3.21	0.45	135.19	2.03	2.94	Pr+S1
70	25	54.52	15	161.75	2.50	0.58	139.44	1.27	2.51	Pr
70	25	54.52	15	139.06	1.96	0.59	117.85	1.10	1.95	Pr
70	25	54.52	15	135.97	2.47	0.86	79.05	1.57	2.58	Pr
85	25	54.52	15	166.47	6.55	0.53	157.05	2.49	4.86	Pr+S1
85	25	54.52	15	169.96	7.37	0.65	130.74	2.66	4.78	Pr+S1
85	25	54.52	15	169.73	6.74	0.63	134.71	2.34	4.80	Pr+S1
70	25	34.53	60	27.27	2.40	0.86	15.85	2.11	3.43	Pr
70	25	34.53	60	36.73	3.42	1.25	14.69	3.34	4.74	Pr
70	25	34.53	60	49.99	4.11	1.34	18.65	3.56	5.84	Pr
85	25	34.53	60	49.13	4.08	1.34	18.33	3.76	5.34	Pr
85	25	34.53	60	41.03	3.19	1.03	19.92	2.45	4.10	Pr
85	25	34.53	60	43.66	3.84	0.81	26.95	4.33	6.21	Pr
100	25	34.53	60	81.38	4.87	1.68	24.22	3.88	5.66	Pr
100	25	34.53	60	71.14	5.17	1.90	18.72	4.04	7.06	Pr
100	25	34.53	60	77.10	4.21	1.78	21.66	3.60	5.06	Pr
70	25	59.12	60	70.77	3.51	1.31	27.01	2.93	4.45	Pr
70	25	59.12	60	60.53	3.45	0.96	31.53	2.78	4.87	Pr
70	25	59.12	60	53.98	3.19	1.07	25.22	2.77	4.49	Pr
85	25	59.12	60	87.07	4.02	1.43	30.44	3.39	5.31	Pr
85	25	59.12	60	80.30	4.83	1.60	25.09	3.92	6.72	Pr
85	25	59.12	60	71.82	3.42	0.97	37.02	2.78	4.79	Pr

Table A.5 Experimental results of pry-out failure for the cold state: anchor groups

Anchor	$f_{cc,150}$ [MPa]	$fi(t)$ [min]	$V_{u,test}$ [kN]	δ_h [mm]	$\delta(0.5V_{u,test})$ [mm]	k_V [kN/mm]	δ_{vm} [mm]	δ_{vb} [mm]	fm
G2h85d25	37.04	0	279.58	1.81	0.35	399.40	1.09	1.73	Pr
G2h85d25	37.04	0	291.05	1.69	0.32	454.77	0.91	1.87	Pr
G4h85d25	37.04	0	400*	n/a	0.24	832.53	n/a	n/a	n/a
G4h85d25	37.04	0	400*	n/a	0.19	1040.27	n/a	n/a	Pr
G2h85d25	59.12	0	351.26	2.77	0.42	418.17	1.11	2.17	Pr
G2h85d25	59.12	0	368.41	2.49	0.39	472.32	1.09	2.18	Pr
G2h85d25	36.92	15	203.42	2.06	0.42	242.17	1.37	2.76	Pr
G2h85d25	36.92	15	115.17	1.68	0.51	112.91	2.07	2.98	Pr
G2h85d25	36.92	15	151.62	1.69	0.54	140.39	2.19	3.05	Pr
G4h85d25	36.92	15	224.29	1.30	0.39	287.55	2.20	3.33	Pr
G4h85d25	36.92	15	182.78	1.18	0.33	276.94	1.57	2.66	Pr
G4h85d25	36.92	15	183.76	1.57	0.36	255.22	2.70	4.26	Pr
G2h85d25	54.52	15	200.86	2.01	0.64	156.92	2.63	3.34	Pr
G2h85d25	54.52	15	194.12	1.90	0.65	149.32	2.15	3.06	Pr
G2h85d25	34.53	60	57.74	4.21	1.57	18.39	4.81	7.05	Pr
G2h85d25	34.53	60	67.48	3.09	1.15	29.34	3.05	2.84	Pr
G2h85d25	34.53	60	76.82	4.29	1.47	26.13	4.05	6.04	Pr
G4h85d25	34.53	60	116.43	2.64	1.06	54.92	2.87	5.01	Pr
G4h85d25	34.53	60	86.66	1.85	0.36	120.36	2.22	3.66	Pr
G4h85d25	34.53	60	87.83	2.96	0.51	86.11	3.99	6.86	Pr
G2h85d25	59.12	60	111.02	3.65	1.34	41.43	3.54	5.15	Pr
G2h85d25	59.12	60	99.73	3.27	1.19	41.90	3.40	4.76	Pr

APPENDIX B

Table B.1 FE results of concrete edge failure

c_1/mm	h_{ef}/mm	d/mm	f_{cm}/MPa	$fi(t)$/min	Condition	$V_{u,FE}$/kN	fm
50	95	16	15	0	Ambient	7.86	CE
50	95	16	15	90	verification: hot 1	9	CE
50	95	16	15	90	verification: hot 2	8.31	CE
50	95	16	15	90	prediction: hot 1	5.99	CE
50	95	16	15	90	prediction: hot 2	3.78	CE
50	95	16	15	90	cold state	0.8	CE
100	95	16	15	0	Ambient	20.87	CE
100	95	16	15	90	verification: hot 1	19.3	CE
100	95	16	15	90	verification: hot 2	16.92	CE
100	95	16	15	90	prediction: hot 1	12.08	CE
100	95	16	15	90	prediction: hot 2	8.52	CE
100	95	16	15	90	cold state	2.47	CE
150	95	16	15	0	Ambient	35.28	CE
150	95	16	15	90	verification: hot 1	29.72	CE
150	95	16	15	90	verification: hot 2	23.63	CE
150	95	16	15	90	prediction: hot 1	15.84	CE
150	95	16	15	90	prediction: hot 2	13.06	CE
150	95	16	15	90	cold state	4.63	CE
150	45	25	15	0	Ambient	27.89	CE
150	45	25	15	90	verification: hot 1	20.86	CE
150	45	25	15	90	verification: hot 2	NA	CE
150	45	25	15	90	prediction: hot 1	13.02	CE
150	45	25	15	90	prediction: hot 2	11.68	CE
150	45	25	15	90	cold state	1.68	CE
150	95	25	15	0	Ambient	37.4	CE
150	95	25	15	90	verification: hot 1	31.5	CE
150	95	25	15	90	verification: hot 2	NA	CE
150	95	25	15	90	prediction: hot 1	16.79	CE
150	95	25	15	90	prediction: hot 2	13.84	CE
150	95	25	15	90	cold state	4.91	CE

Table B.2 FE results of concrete edge failure for the cold state: single stud anchors

c_1 [mm]	h_{ef} [mm]	d[mm]	Concrete grade	f_{cm} [MPa]	$fi(t)$ [min]	$V_{u,FE}$[kN] Cold	$V_{u,FE}$[kN] Hot	fm
100	70	16	C12/15	12	0	20.80	20.80	CE
100	70	16	C12/15	12	15	7.93	10.51	CE+Pr
100	70	16	C12/15	12	30	6.91	7.79	CE+Pr
100	70	16	C12/15	12	60	3.55	5.51	CE+Pr
100	70	16	C12/15	12	90	2.01	3.85	CE+Pr
100	95	16	C12/15	12	0	20.88	20.88	CE
100	95	16	C12/15	12	15	8.62	12.46	CE+Pr
100	95	16	C12/15	12	30	8.16	7.63	CE+Pr
100	95	16	C12/15	12	60	4.55	4.61	CE+Pr
100	95	16	C12/15	12	90	2.89	3.22	CE+Pr
100	140	16	C12/15	12	0	23.13	23.13	CE
100	140	16	C12/15	12	15	10.36	12.78	CE+Pr
100	140	16	C12/15	12	30	9.49	9.21	CE+Pr
100	140	16	C12/15	12	60	6.54	5.30	CE+Pr
100	140	16	C12/15	12	90	2.52	3.91	CE+Pr
75	95	25	C12/15	12	0	13.27	13.27	CE
75	95	25	C12/15	12	15	7.28	7.65	CE+Pr
75	95	25	C12/15	12	30	6.33	6.14	CE+Pr
75	95	25	C12/15	12	60	3.73	4.41	CE+Pr
75	95	25	C12/15	12	90	2.53	3.14	CE+Pr
100	95	25	C12/15	12	0	20.76	20.76	CE
100	95	25	C12/15	12	15	8.99	10.38	CE+Pr
100	95	25	C12/15	12	30	7.99	8.26	CE+Pr
100	95	25	C12/15	12	60	5.24	5.71	CE+Pr
100	95	25	C12/15	12	90	2.79	4.28	CE+Pr
150	95	25	C12/15	12	0	38.32	38.32	CE
150	95	25	C12/15	12	15	13.75	16.26	CE+Pr
150	95	25	C12/15	12	30	13.67	10.74	CE+Pr
150	95	25	C12/15	12	60	5.37	6.03	CE+Pr
150	95	25	C12/15	12	90	3.44	4.37	CE+Pr
200	95	25	C12/15	12	0	52.82	52.82	CE
200	95	25	C12/15	12	15	20.00	27.16	CE+Pr
200	95	25	C12/15	12	30	15.00	22.40	CE+Pr
200	95	25	C12/15	12	60	10.00	15.87	CE+Pr
200	95	25	C12/15	12	90	7.00	11.30	CE+Pr
100	95	32	C12/15	12	0	21.70	21.70	CE
100	95	32	C12/15	12	15	9.22	10.32	CE+Pr
100	95	32	C12/15	12	30	9.39	8.10	CE+Pr
100	95	32	C12/15	12	60	3.61	5.41	CE+Pr
100	95	32	C12/15	12	90	2.42	4.12	CE+Pr
100	70	16	C20/25	30	0	33.70	33.70	CE
100	70	16	C20/25	30	15	14.20	16.45	CE+Pr

c_1 [mm]	h_{ef} [mm]	d [mm]	Concrete grade	f_{cm} [MPa]	$fi(t)$ [min]	$V_{u,FE}$ [kN] Cold	$V_{u,FE}$ [kN] Hot	fm
100	70	16	C20/25	30	30	12.73	13.54	CE+Pr
100	70	16	C20/25	30	60	4.92	9.43	CE+Pr
100	70	16	C20/25	30	90	3.20	6.71	CE+Pr
100	95	16	C20/25	30	0	36.18	36.18	CE
100	95	16	C20/25	30	15	17.03	18.16	CE+Pr
100	95	16	C20/25	30	30	15.90	16.91	CE+Pr
100	95	16	C20/25	30	60	6.12	11.49	CE+Pr
100	95	16	C20/25	30	90	3.98	8.69	CE+Pr
100	140	16	C20/25	30	0	37.05	37.05	CE
100	140	16	C20/25	30	15	21.82	24.45	CE+Pr
100	140	16	C20/25	30	30	19.27	19.62	CE+Pr
100	140	16	C20/25	30	60	11.51	14.36	CE+Pr
100	140	16	C20/25	30	90	7.27	11.41	CE+Pr
75	95	25	C20/25	30	0	22.76	22.76	CE
75	95	25	C20/25	30	15	12.64	14.23	CE+Pr
75	95	25	C20/25	30	30	11.05	11.75	CE+Pr
75	95	25	C20/25	30	60	6.34	8.11	CE+Pr
75	95	25	C20/25	30	90	3.70	6.31	CE+Pr
100	95	25	C20/25	30	0	34.45	34.45	CE
100	95	25	C20/25	30	15	20.40	19.49	CE+Pr
100	95	25	C20/25	30	30	18.79	16.30	CE+Pr
100	95	25	C20/25	30	60	7.86	13.60	CE+Pr
100	95	25	C20/25	30	90	5.60	10.01	CE+Pr
150	95	25	C20/25	30	0	65.78	65.78	CE
150	95	25	C20/25	30	15	29.17	27.75	CE+Pr
150	95	25	C20/25	30	30	28.98	23.31	CE+Pr
150	95	25	C20/25	30	60	11.26	17.33	CE+Pr
150	95	25	C20/25	30	90	9.84	12.61	CE+Pr
200	95	25	C20/25	30	0	96.27	96.27	CE
200	95	25	C20/25	30	15	44.00	44.76	CE+Pr
200	95	25	C20/25	30	30	31.63	36.29	CE+Pr
200	95	25	C20/25	30	60	18.09	26.31	CE+Pr
200	95	25	C20/25	30	90	15.66	17.70	CE+Pr
100	95	32	C20/25	30	0	37.72	37.72	CE
100	95	32	C20/25	30	15	20.25	18.50	CE+Pr
100	95	32	C20/25	30	30	18.65	16.26	CE+Pr
100	95	32	C20/25	30	60	10.23	10.18	CE+Pr
100	95	32	C20/25	30	90	6.70	7.67	CE+Pr
100	70	16	C40/50	47	0	38.38	38.38	CE
100	70	16	C40/50	47	15	18.78	17.24	CE+Pr
100	70	16	C40/50	47	30	16.76	13.75	CE+Pr
100	70	16	C40/50	47	60	12.16	9.54	CE+Pr
100	70	16	C40/50	47	90	4.83	7.00	CE+Pr
100	95	16	C40/50	47	0	39.42	39.42	CE

c_1 [mm]	h_{ef} [mm]	d[mm]	Concrete grade	f_{cm} [MPa]	$fi(t)$ [min]	$V_{u,FE}$[kN] Cold	$V_{u,FE}$[kN] Hot	fm
100	95	16	C40/50	47	15	22.26	20.67	CE+Pr
100	95	16	C40/50	47	30	21.02	16.06	CE+Pr
100	95	16	C40/50	47	60	9.56	11.09	CE+Pr
100	95	16	C40/50	47	90	6.72	6.98	CE+Pr
100	140	16	C40/50	47	0	40.46	40.46	CE
100	140	16	C40/50	47	15	27.76	30.31	CE+Pr
100	140	16	C40/50	47	30	24.08	21.84	CE+Pr
100	140	16	C40/50	47	60	11.64	14.33	CE+Pr
100	140	16	C40/50	47	90	5.51	8.48	CE+Pr
75	95	25	C40/50	47	0	27.81	27.81	CE
75	95	25	C40/50	47	15	16.85	13.34	CE+Pr
75	95	25	C40/50	47	30	14.57	11.81	CE+Pr
75	95	25	C40/50	47	60	7.87	8.42	CE+Pr
75	95	25	C40/50	47	90	5.56	6.17	CE+Pr
100	95	25	C40/50	47	0	39.43	39.43	CE
100	95	25	C40/50	47	15	22.64	21.45	CE+Pr
100	95	25	C40/50	47	30	22.65	18.91	CE+Pr
100	95	25	C40/50	47	60	15.86	12.21	CE+Pr
100	95	25	C40/50	47	90	7.77	9.12	CE+Pr
150	95	25	C40/50	47	0	77.79	77.79	CE
150	95	25	C40/50	47	15	34.35	36.61	CE+Pr
150	95	25	C40/50	47	30	34.10	30.79	CE+Pr
150	95	25	C40/50	47	60	10.56	20.78	CE+Pr
150	95	25	C40/50	47	90	6.43	14.97	CE+Pr
200	95	25	C40/50	47	0	113.33	113.33	CE
200	95	25	C40/50	47	15	51.52	41.89	CE+Pr
200	95	25	C40/50	47	30	42.85	35.42	CE+Pr
200	95	25	C40/50	47	60	25.96	25.95	CE+Pr
200	95	25	C40/50	47	90	18.78	16.73	CE+Pr
100	95	32	C40/50	47	0	40.70	40.70	CE
100	95	32	C40/50	47	15	24.98	19.16	CE+Pr
100	95	32	C40/50	47	30	20.99	15.71	CE+Pr
100	95	32	C40/50	47	60	8.89	11.38	CE+Pr
100	95	32	C40/50	47	90	6.34	8.85	CE+Pr

Table B.3 FE results of concrete edge failure for the cold state: anchor groups

Anchor	c_1 [mm]	h_{ef} [mm]	d [mm]	Concrete grade	f_{cm} [MPa]	$fi(t)$ [min]	$V_{u,FE}$ [kN] Cold	$V_{u,FE}$ [kN] Hot	fm
G2	75	95	25	C20/25	30	0	29.84	29.84	CE+Pr
G2	75	95	25	C20/25	30	15	15.07	13.90	CE+Pr
G2	75	95	25	C20/25	30	30	14.32	10.62	CE+Pr
G2	75	95	25	C20/25	30	60	8.32	5.66	CE+Pr
G2	75	95	25	C20/25	30	90	3.63	4.87	CE+Pr
G2	100	95	25	C20/25	30	0	42.22	42.22	CE+Pr
G2	100	95	25	C20/25	30	15	20.64	21.71	CE+Pr
G2	100	95	25	C20/25	30	30	18.94	20.48	CE+Pr
G2	100	95	25	C20/25	30	60	7.30	11.99	CE+Pr
G2	100	95	25	C20/25	30	90	6.38	8.69	CE+Pr
G2	150	95	25	C20/25	30	0	74.66	74.66	CE+Pr
G2	150	95	25	C20/25	30	15	33.56	41.90	CE+Pr
G2	150	95	25	C20/25	30	30	30.26	36.33	CE+Pr
G2	150	95	25	C20/25	30	60	16.28	29.15	CE+Pr
G2	150	95	25	C20/25	30	90	11.44	22.11	CE+Pr
G2	75	95	25	C40/50	47	0	34.42	34.42	CE+Pr
G2	75	95	25	C40/50	47	15	17.74	19.69	CE+Pr
G2	75	95	25	C40/50	47	30	16.33	15.62	CE+Pr
G2	75	95	25	C40/50	47	60	5.37	10.52	CE+Pr
G2	75	95	25	C40/50	47	90	3.28	6.86	CE+Pr
G2	100	95	25	C40/50	47	0	47.98	47.98	CE+Pr
G2	100	95	25	C40/50	47	15	24.06	23.24	CE+Pr
G2	100	95	25	C40/50	47	30	21.30	17.36	CE+Pr
G2	100	95	25	C40/50	47	60	10.32	11.80	CE+Pr
G2	100	95	25	C40/50	47	90	7.34	8.84	CE+Pr
G2	150	95	25	C40/50	47	0	84.19	84.19	CE+Pr
G2	150	95	25	C40/50	47	15	40.89	46.46	CE+Pr
G2	150	95	25	C40/50	47	30	37.80	41.81	CE+Pr
G2	150	95	25	C40/50	47	60	18.12	29.03	CE+Pr
G2	150	95	25	C40/50	47	90	11.93	24.18	CE+Pr
G3	150	95	25	C20/25	30	0	84.19	84.19	CE+Pr
G3	150	95	25	C20/25	30	15	37.96	48.52	CE+Pr
G3	150	95	25	C20/25	30	30	32.17	40.77	CE+Pr
G3	150	95	25	C20/25	30	60	26.45	30.83	CE+Pr
G3	150	95	25	C20/25	30	90	21.53	20.46	CE+Pr
G4	100	95	25	C20/25	30	0	93.19	93.19	CE+Pr
G4	100	95	25	C20/25	30	15	48.35	62.31	CE+Pr
G4	100	95	25	C20/25	30	30	41.56	56.46	CE+Pr
G4	100	95	25	C20/25	30	60	27.84	42.38	CE+Pr
G4	100	95	25	C20/25	30	90	20.99	34.38	CE+Pr
G4	100	95	25	C40/50	47	0	105.06	105.06	CE+Pr
G4	100	95	25	C40/50	47	15	52.55	65.94	CE+Pr

Anchor	c_1 [mm]	h_{ef} [mm]	d [mm]	Concrete grade	f_{cm} [MPa]	$fi(t)$ [min]	$V_{u,FE}$ [kN] Cold	$V_{u,FE}$ [kN] Hot	fm
G4	100	95	25	C40/50	47	30	47.13	55.44	CE+Pr
G4	100	95	25	C40/50	47	60	32.66	38.11	CE+Pr
G4	100	95	25	C40/50	47	90	20.42	26.00	CE+Pr

Table B.4 FE results of pry-out failure for the cold state: single stud anchors

h_{ef} [mm]	d [mm]	Concrete grade	f_{cm} [MPa]	$fi(t)$ [min]	$V_{u,FE}$ [kN] Cold	$V_{u,FE}$ [kN] Hot	fm
70	25	C12/15	12	0	78.82	78.82	Pr
70	25	C12/15	12	15	40.9	69.53	Pr
70	25	C12/15	12	30	32.15	47.69	Pr
70	25	C12/15	12	60	18	33.6	Pr
70	25	C12/15	12	90	10.21	28.13	Pr
85	25	C12/15	12	0	89.56	89.56	Pr
85	25	C12/15	12	15	53.31	96.4	Pr
85	25	C12/15	12	30	36.47	87.09	Pr
85	25	C12/15	12	60	26.68	76.55	Pr
85	25	C12/15	12	90	15.18	58.6	Pr
100	25	C12/15	12	0	108.62	108.62	Pr
100	25	C12/15	12	15	67.47	86.91	Pr
100	25	C12/15	12	30	53.26	65.12	Pr
100	25	C12/15	12	60	39.98	42.66	Pr
100	25	C12/15	12	90	29	36.16	Pr
70	25	C20/25	30	0	138.23	138.23	Pr
70	25	C20/25	30	15	88.93	118.39	Pr
70	25	C20/25	30	30	70.6	85.84	Pr
70	25	C20/25	30	60	45.21	63.15	Pr
70	25	C20/25	30	90	33	56.29	Pr
85	25	C20/25	30	0	171.59	171.59	Pr
85	25	C20/25	30	15	105.49	186.79	Pr
85	25	C20/25	30	30	84.29	140.74	Pr
85	25	C20/25	30	60	58.88	118.22	Pr
85	25	C20/25	30	90	40.35	107.66	Pr
100	25	C20/25	30	0	214.56	214.56	Pr
100	25	C20/25	30	15	132.19	136.08	Pr
100	25	C20/25	30	30	110.68	93.69	Pr
100	25	C20/25	30	60	77.91	70.59	Pr
100	25	C20/25	30	90	66.04	59.81	Pr
70	25	C40/50	47	0	167.55	167.55	Pr
70	25	C40/50	47	15	113.63	154.84	Pr

h_{ef} [mm]	d [mm]	Concrete grade	f_{cm} [MPa]	$fi(t)$ [min]	$V_{u,FE}$ [kN]		fm
					Cold	Hot	
70	25	C40/50	47	30	93.12	115.71	Pr
70	25	C40/50	47	60	68.74	94.06	Pr
70	25	C40/50	47	90	44.32	83.43	Pr
85	25	C40/50	47	0	214.02	214.02	Pr
85	25	C40/50	47	15	142.05	221.56	Pr
85	25	C40/50	47	30	98.76	209.22	Pr
85	25	C40/50	47	60	69.59	182.38	Pr
85	25	C40/50	47	90	50.32	141.37	Pr
100	25	C40/50	47	0	252.4	252.4	Pr
100	25	C40/50	47	15	166.4	172.35	Pr
100	25	C40/50	47	30	132.72	125.98	Pr
100	25	C40/50	47	60	110.37	93.84	Pr
100	25	C40/50	47	90	89.14	80.44	Pr

Table B.5 FE results of pry-out failure for the cold state: anchor groups

Anchor	h_{ef} [mm]	d [mm]	Concrete grade	f_{cm} [MPa]	$fi(t)$ [min]	$V_{u,FE}$ [kN] Cold	$V_{u,FE}$ [kN] Hot	fm
G2	85	25	C12/15	12	0	170.11	170.11	Pr
G2	85	25	C12/15	12	15	91.15	164.01	Pr
G2	85	25	C12/15	12	30	59.78	147.66	Pr
G2	85	25	C12/15	12	60	41.55	132.44	Pr
G2	85	25	C12/15	12	90	25.65	111.58	Pr
G2	85	25	C20/25	30	0	303.84	303.84	Pr
G2	85	25	C20/25	30	15	212.82	308.7	Pr
G2	85	25	C20/25	30	30	144.41	279.48	Pr
G2	85	25	C20/25	30	60	95.78	210.68	Pr
G2	85	25	C20/25	30	90	70.68	181.04	Pr
G2	85	25	C40/50	47	0	371.66	371.66	Pr
G2	85	25	C40/50	47	15	279.82	396.52	Pr
G2	85	25	C40/50	47	30	220.74	381.92	Pr
G2	85	25	C40/50	47	60	135.54	306.74	Pr
G2	85	25	C40/50	47	90	102.63	266.9	Pr
G4	85	25	C12/15	12	0	245.40	245.4	Pr
G4	85	25	C12/15	12	15	136.05	232.84	Pr
G4	85	25	C12/15	12	30	92.34	192.04	Pr
G4	85	25	C12/15	12	60	58.18	162.11	Pr
G4	85	25	C12/15	12	90	39.33	143.11	Pr
G4	85	25	C20/25	30	0	419.46	419.46	Pr
G4	85	25	C20/25	30	15	316.46	422.14	Pr
G4	85	25	C20/25	30	30	228.58	384.98	Pr
G4	85	25	C20/25	30	60	149.18	302.04	Pr
G4	85	25	C20/25	30	90	109.71	263.5	Pr
G4	85	25	C40/50	47	0	555.02	555.02	Pr
G4	85	25	C40/50	47	15	452.96	602.26	Pr
G4	85	25	C40/50	47	30	317.16	555.5	Pr
G4	85	25	C40/50	47	60	219.70	434.6	Pr
G4	85	25	C40/50	47	90	155.07	373.24	Pr